Molecular basis of membrane stability and dynamics

Moiset Coll, Gemma

Molecular basis of membrane stability and dynamics

Gemma Moiset Coll

Cover artist impression by Eduard Madrid.

university of groningen / faculty of mathematics and natural sciences / zernike institute for advanced materials

This Ph.D. study was carried out in the Biochemistry Department of the Groningen Biomolecular Sciences and Biotechnology Institute, and was finantially supported by the Zernike Institute for Advanced Marerials (University of Groningen, the Netherlands).

Printed by: PrintPartners Ipskamp, Enschede, The Netherlands.

Zernike Institute Ph.D. thesis series 2013-23

ISSN: 1570-1530

ISBN: 978-90-367-6527-5 (printed)

ISBN: 978-90-367-6528-2 (electronic)

rijksuniversiteit
groningen

Molecular basis of membrane stability and dynamics

Proefschrift

ter verkrijging van het doctoraat in de
Wiskunde en Natuurwetenschappen
aan de Rijksuniversiteit Groningen
op gezag van de
Rector Magnificus, dr. E. Sterken,
in het openbaar te verdedigen op
vrijdag 29 november 2013
om 9:00 uur

door

Gemma Moiset Coll

geboren op 26 november 1985

te Girona, Spain

Promotor: Prof. dr. B. Poolman

Beoordelingscommissie: Prof. dr. S.J. Marrink
Prof. dr. A.M. van Oijen
Prof. dr. M. Baldus

Contents

Chapter 1

General introduction to biological membranes

Cell membranes

The cell membrane plays a vital role in any species from all three domains of life – Eukarya, Eubacteria, and Archaea. This two dimensional arrangement of lipids and proteins separates the internal contents of the cell from the outside medium. Moreover, the membrane pursues the multiple reactions needed to keep the cell alive, incl. energy and signal transduction, solute transport and enzymatic catalysis. The formation of the lipid bilayer has its origin in the amphipathicity of the lipid molecules (1). Eukaryotic cell membranes contain hundreds of different lipids, which are distributed asymmetrically over the two leaflets of the bilayer. To synthesize those lipids cells use about 5 % of their genes and invest a substantial amount of energy resources (2). It is thought that the complexity of the membrane serves to buffer the external perturbations and ensures matching of the spaces at the protein-lipid interfaces to avoid ion and solute leakage (1).

Lipids are classified in different categories: e.g. glycerophospholipids, sphingolipids, and sterols. Compared to most prokaryotes, eukaryotic cells contain two extra lipid categories, i.e. sterols and sphingolipids. These lipids are also known to be key players in the trafficking of membrane vesicles in eukaryotes. In fact, the sterol composition increases along the secretory pathway, i.e. from 5% in the endoplasmic reticulum (ER) to more than 40 % in the plasma membrane (PM), and intermediate amounts in the Golgi complex (2). Cholesterol, the sterol of mammalian cells, increases the stiffness and the thickness of the membrane. These characteristics are important since the transmembrane domains (TMDs) of plasma membrane proteins of yeast and vertebrates are predicted to be somewhat longer than those of proteins resident in the ER and Golgi complex (3). Thus, cholesterol is able to induce protein sorting in those bilayers where the thickness and stiffness differ. Even more, it has been shown in yeast that ergosterol and sphingolipids play a role in the trans-Golgi network (TGN) sorting machinery by enriching for so-called 'rafts' lipids, which results in a higher lipid order in the secretory vesicles compared to the late Golgi membrane (4). All together there is a lot of evidence that cholesterol and ergosterol are responsible for the organization of membrane proteins in the biosynthetic secretory pathway.

Membrane organization: 'Rafts'

Cell membranes are not only complex in composition but also in the organization of the lipid and protein molecules. Initially, it was thought that the proteins were the key factors of membrane functionality, with the lipids serving as a 2D fluid mosaic in which the proteins were embedded (5). Later, the lateral segregation of sphingolipids and cholesterol together with some proteins in the plasma membrane of epithelial cells was observed. Those protein-lipid platforms could be isolated by solubilization of the cell membrane with cold detergent (Triton X-100), resulting in the so-called Detergent Resistant Membranes (DRMs). Herewith, the 'raft' concept as a functional organization of the membrane was introduced (6), even though the existence of lipid domains in cell membranes was suggested in several earlier studies (7). In parallel, the lateral segregation of lipids (and proteins) has also been studied in model membranes, giant unilamellar vesicles (GUVs), containing glycerophospholipids, sphingolipids and cholesterol. In those three-component mixtures the lipids separate in two relevant phases: liquid-ordered (L_o) phase, enriched in sphingolipids, cholesterol or saturated phospholipids, and the liquid-disordered (L_d) phase containing most of the unsaturated glycerophospholipids (8, 9). The domains are dynamic and dependent on the lipid composition and temperature (10, 11). The coexistence of two different lipid domains has also been seen in Giant Plasma Membrane Vesicles (GPMVs), lipids isolated from rat kidney membranes at low temperatures or at physiological temperatures in the presence

of cholera toxin; the latter induces clustering of ganglioside GM1 (12-14). However, the demonstration of membrane rafts in biological membranes is difficult due to their small size, and the introduction of artifacts upon detergent extraction and GM1 clustering (15). Consequently, the lipid raft concept has been highly debated (16, 17). Finally, with the development of new microscopy techniques, there is now some consensus on the nature of rafts and membrane organization (18). Membrane rafts are defined as dynamic, nanoscale, sterol-sphingolipid-enriched, ordered assemblies of proteins and lipids. Those assemblies can merge into larger raft domains by specific lipid-lipid, protein-lipid and protein-protein oligomerizing interactions (Figure 1) (19). The nanoscale rafts are supported by NMR measurements in GMPVs, which indicated an increased relaxation time in the lipid chain resonance at temperatures around the phase miscibility transition. GPMVs contain two liquid phases at low temperatures (comparable to L_o and L_d) and one liquid phase at high temperatures. However, slightly above the transition temperature, heterogeneity can be observed that corresponds to < 50 nm-sized membrane regions (20). This implies that cell membranes reside close to a critical point where small membrane compartments exist at a very low energetic cost.

Opposite to the protein enrichment in rafts (seen in DRMs), polytopic membrane proteins and transmembrane peptides have been shown to partition into the L_d phase in model membranes (21, 22), whereas palmitoylated single membrane spanners have been observed in membrane rafts (23). However, palmitoylation is not the only factor to associate proteins with rafts, also length of the transmembrane segments and amino acid sequence plays a role (1).

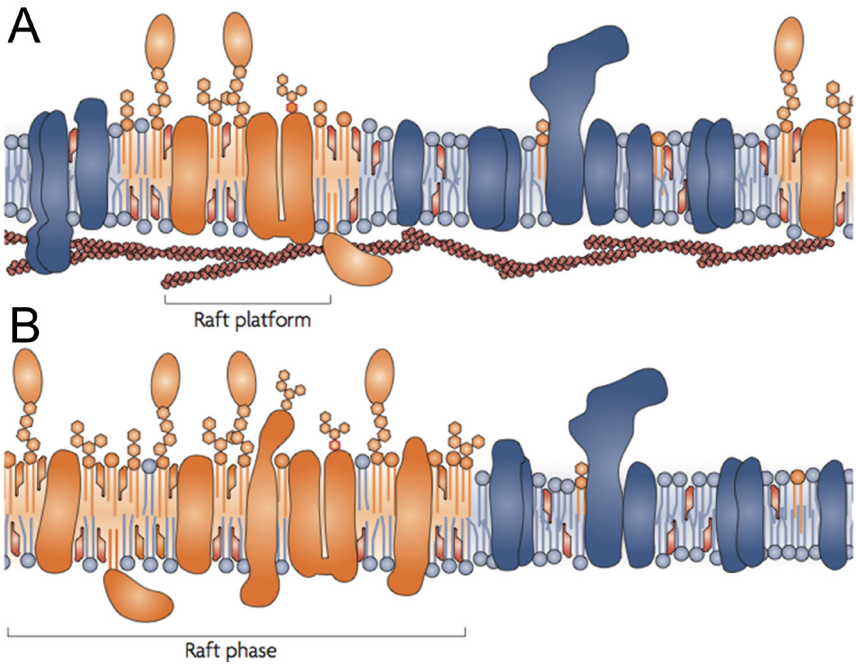

Figure 1. *Raft-based heterogeneity in cell membranes*. (A) Raft platforms formed, in response to external signals, from nanoscale assemblies of sterols, sphingolipids, glycolipids and proteins in the plasma membrane. (B) Micrometre-sized raft ‚phases' induced at equilibrium usualy seen in GUVs. Figure modified with permission from K. Simons (19).

Interaction of small molecules with membranes: Amphipathic pore-forming peptides

Cell membranes are complex in composition and dynamic in nature, and the interaction of small hydrophobic or amphipathic molecules with the lipid bilayer can have important consequences for the stability and barrier function of the membrane. Important examples are the antimicrobial peptides (AMPs) (24). They are produced by living organisms of all types in order to protect themselves against microbes (25). In fact, the gene-encoded antimicrobial peptides serve as part of their innate immune system (26, 27). Despite the huge variety of AMPs, they share similar features such as a cationic nature and amphipathicity. Their diversity in sequence classifies them in different structural groups: α-helical, β-sheet, extended and looped (28, 29). Figure 2 shows two examples of AMPs, with different structure, studied in this thesis, the cyclic BPC194 and the linear Alamethicin.

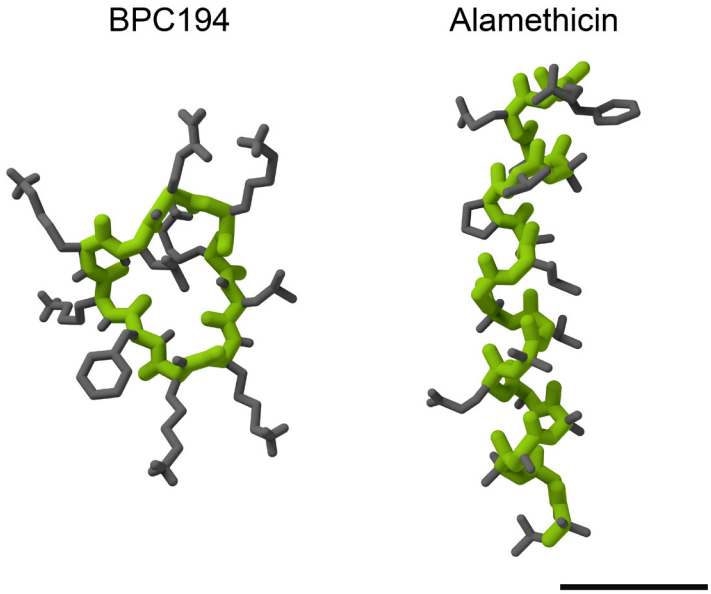

Figure 2. Illustrations of BPC194, form the MD simulations of Chapter 2, and Alamethicin, from the crystal structure by R. Fox and F. M. Richards (30). Scale bar represents 1 nm.

What is still under debate is whether their main target is the cell membrane or some metabolic function after accessing the cytoplasm (24). However, the interaction of AMPs with cell membranes and the impact on the function of biological membranes makes them important targets of study, and several modes of membrane disruption have been demonstrated. In the 'barrel-stave' model, peptides associate and align perpendicular to the bilayer forming the pore (31). In the 'carpet model', peptides are attracted and then oriented parallel to the membrane surface (32). Once a threshold concentration is reached peptides disrupt the bilayer in a detergent-like fashion by forming micelles. In this case, specific peptide-peptide interactions are not required. In the 'toroidal-pore model', like in the barrel-stave, peptides align perpendicular to membrane but the lipids in the vicinity of the peptides do not align parallel to the peptides (33). Membrane curvature is induced in such a way that the lumen of the pore is formed by both, peptides and the phospholipid head groups. The 'disordered-toroidal pore model' is a recent modification of the regular toroidal-pore model (34, 35). Peptides adopt a less-rigid conformation/orientation, and the pore lumen is

only aligned by the phospholipids. There are other peptides, named cell-penetrating peptides (CPPs), which are able to translocate across the cell membrane with very low toxicity. They can serve as drug carriers by mediating cellular uptake of proteins and other molecules like drugs. Methods have been described to assess the interaction of peptides with membranes, both *in vitro* and *in vivo,* which facilitates the classification of CPPs (36) and AMPs (37-39). Even more, to predict the active concentration ranges *in vivo* and to aid the design of new antibiotics, correlations have been made between the minimum inhibitory concentration of AMPs *in vivo*, and their partition constants and threshold concentrations in model membranes (40).

There is increasing evidence that the classification of antimicrobial peptides on the basis of a single mode of action is often not correct, as the interaction of AMPs with the cell membrane is complex and the different models are not mutually exclusive. Also, the distinction AMPs and CPPs is not unambiguous, and the classification is often biased by the type of experiment(s) or molecular dynamics simulation done to characterize the molecules (34, 35, 41, 42). There is experimental evidence that peptides can undergo a dual mode of action to disrupt the membranes. For example, the G13A mutant of the N-terminal 20 residue-peptide of the influenza hemagglutinin promotes contents leakage but also fuses membranes as a way of entering the host cell (43). The antimicrobial cryptdin-4 found in mice induces hemi-fusion and contents leakage in model membranes (44). The prototypic CPP derived from the human immunodeficient virus (HIV)-1 TAT protein residues 48-60, known as TAT, causes leaky fusion of liposomes with a lipid composition mimicking that of late endosome (45). The human salivary antimicrobial peptide Histatin 5 causes temporary damage to the plasma membrane of the parasites and acts as a CPP and is translocated to the cytoplasm (46). A recent *in vivo* study revealed how the human antimicrobial, LL-37, acts on Gram-negative bacteria *Escherichia coli.* The action mechanism involves two stages. Initially, the peptide binds and quickly saturates the outer membrane, containing the lipopolysaccharide and O-antigen. Subsequently, it enters the periplasmic space and shortly after this step the cell growth is arrested. Well after the cell growth is inhibited the peptide reaches and permeabilizes the cytoplasmic membrane (39). This work also shows that *in vitro* methods may not reveal the full complexity of the action mechanism of AMPs. Importantly, the complex and multiple interactions of the AMPs with cells may be the cause for the difficulty of target cells to develop resistance. As a result, an increased interest in the understanding of the mechanism of action of those peptides has emerged in the past decade. Their selectivity for bacterial *versus* mammalian cells makes AMPs important pharmacological agents to treat infections against drug-resistant pathogens and, thus, a good alternative to the conventional antibiotics.

Interaction of small molecules with membranes: reducing *versus* non-reducing sugars

Saccharides are synthesized in large amounts when yeast or plant cells enter into an anhydrobiotic state, where the amount of water in the organism is reduced and the metabolism is slowed or stopped (47, 48). Upon entering this state, a common physiological response of the cells is the synthesis of high amounts of sugars such as sucrose and trehalose. Membranes are stabilized by these sugars, but the molecular mechanism behind it is not fully understood.

In model membranes it has been shown how sugars are bound by hydrogen bonding with the lipid head groups. However, the only sugars found in nature that are synthesized by the organisms undergoing dehydration are the two non-reducing sugars sucrose and trehalose. For that reason those two have been studied extensively in dryed membrane systems (49-55). It has been suggested that these

sugars intercalate in between the lipid/water interface, resulting in the spreading of the lipids, thinning of the bilayer and decreasing of the transition phase temperature (T_m) during dehydration. The reason for the decrease in the T_m is the ability of the sugars to keep the lipid molecules separated from each other when the amount of water molecules is extremely low, which avoids a tight packing of the acyl chains and the transition from the liquid to the gel phase of the membrane. Several mechanisms have been described to explain this phenomenon, such as the replacement of water molecules by the sugars at the lipid/water interface, formation of amorphous glasses to protect the membrane, the concentration of water molecules close to the membranes preserving its native properties or the exclusion of the sugars from the surface reducing the compressive stress in the membrane upon dehydration (51, 52, 55-60).

There are also some studies on fully hydrated systems and here the mechanisms via which sugars stabilize membranes have been explained in the following way. At low amounts of sugars, the saccharides bind the lipids and replace the water molecules of the lipid/water interface resulting in an increase of the membrane area. However, at high sugar concentrations the sugars are expelled from the membrane due to the domination of the kosmotropic effect of the sugars. Consequently, the sugar concentration in the bulk solution is higher than in the hydration zone of the lipids. However, the sugar molecules that were already bound at lower sugar concentrations are still in the membrane causing the same changes in membrane area as at low concentrations (55, 59, 61, 62).

To study the membrane organization, the whole system needs to be hydrated to mimic the *in vivo* membrane environment. To study the membrane organization and formation of lipid rafts, GUVs or GPMVs are often used as model systems even though they lack the complexity of native plasma membranes. For instance, artificial membranes are not asymmetric in composition of the two bilayer leaflets, they are not connected to active processes within the cell, and they exclude interactions of membrane proteins skeletal components. These are all factors that can influence the distribution of membrane components and likely contribute to the fact that macroscopic phase separation is readily observed in model systems but not in living cells (63). However, to study specific parameters of biological membranes, GUVs and GPMVs serve as perfect simplified membrane model systems. For example, the physical basis underlying the diffusion of proteins and lipids in membranes could only be delineated in GUVs (64). Similarly, the effect of small antimicrobial peptides and other molecules like saccharides on membranes can be addressed with greater detail in GUVs than would be possible *in vivo*.

Design of novel membrane pores: Applications in synthetic biology

Ion transport across membranes of the cells and organelles is an important process to provide organisms with co-factors, to generate ion gradients, to regulate cell volume and others. To fulfill this function ion pumps and ion channels are embedded in the cell membrane. The ion transporters are driven by ATP or electrochemical ion gradients, and they pump ions against their concentration gradient (65). In general, they are specific for one or a few ions, e.g. the P-type Na^+/K^+-ATPase. The ion channels either display a high ion selectivity, e.g. the voltage-gated ion channels of our central nervous system, or are ion or solute indifferent, e.g. the mechanosensitive channels involved in cell volume regulation (66). Ion channels allow the passive transport of ions down the concentration gradient (65). Ion channels have served as models to create new and easy to control synthetic channels. The applications include the use of small synthetic ion channels in drug (antibiotics) release (drug

delivery systems), and the engineering of *in vitro* catalysts, detectors and sensors (67). However, it is not trivial to work with channels outside their native environment, the cell membrane, and their insertion into the membrane is a complicated protein-mediated process. Moreover, the functions of membrane proteins are highly regulated by the surrounding lipids and/or they have co-evolved with other proteins. A way to overcome this limitation is the use of simpler channels, such as peptide-based pores that auto insert into the membrane and have less specific lipid demands. However, their structures and functions are often ill defined, which is a challenge for subsequent engineering (68). After all there are some peptide-based pores that have been engineered, such as alamethicin, gramicidin A, melittin, and amphiphilic peptides made of leucine-serine or leucine-arginine-alanine repeats (69). Arguably, alamethicin is the best-characterized and "most-modified" antimicrobial peptide, containing 2-aminoisobutyric acid in addition to natural amino acids. Alamethicin is thought to form 'barrel-stave' type pores (see also previous section). This 20-residue α-helical peptide assembles perpendicular to the bilayer with the hydrophilic residues aligning the pore and the hydrophobic amino acids shielding the aliphatic lipid chains (70-75). The peptide has been tethered covalently with different kinds of linkers to create preferred oligomeric states (76, 77). It has also been linked to other molecules to control the assembly by extramembrane segments (78, 79), protein ligand interactions (80, 81) or by metals (82).

DNA as a template has been used to control chemical reactions (83), to perform asymmetric catalysis (84, 85), to modulate protein activity (86) and even to create entire channels with high analyte selectivity (87). The high selectivity of base-pairing gives a very robust control over the assembly process, which is attractive in the design of synthetic channels. Therefore, DNA might serve as a useful building block to regulate and give control to new synthetic channels.

Saccharomyces cerevisiae as model system

A key achievement in the evolution of eukaryotic cells has been the compartmentalization of cellular processes within membrane-enclosed organelles. The increased complexity of higher organisms relates to the need to differentiate cell types, to perform inter- and intracellular signaling and to compartmentalize specific functions. *Saccharomyces cerevisiae* serves as a model organism for eukaryotic cells with around 30 % of the total proteome being membrane proteins, very similar to that of other eukaryotes, bacteria and archaea (88). Moreover, yeast is easily susceptible to genetic, biochemical and microscopic studies. Yeast possesses a great variety of lipids. Compared to the PM of mammalian cells with about 30-40 % cholesterol and 10-20 % sphingomyelin, yeast has about 30 % sphingolipids (from which 80 to 100 % are in the PM), which may function as the mammalian sphingomyelin; most of the phosphosphingolipids in yeast have a inositol headgroup. In addition, yeast possesses ergosterol, instead of cholesterol, in amounts comparable to those of the glycerophospholipids (89, 90). Ergosterol together with complex sphingolipids have been shown to form functional rafts, and they have been isolated as detergent-insoluble glycolipid-enriched complexes (DIGs) or DRMs (91, 92). Together with ergosterol and sphingolipids some polytopic proteins have been co-purified such as the plasma membrane H^+-ATPase Pma1p, the glycosylphosphatidylinositol (GPI) anchor Gas1p, the general amino acid permease Gap1p, the hexose transport facilitator Hxt1p, the H^+/uracil symporter Fur4p and the H^+/Tryptophan symporter permease Tat2p (91-96). The importance of ergosterol and sphingolipids in the formation of rafts in the yeast PM is evident from the fact that all these proteins require either ergosterol or sphingolipids or both to get properly targeted to the PM. For example, Pma1p and Gas1p are no longer associated with lipid rafts in cells lacking ergosterol or in *lcb1-100* cells, which are unable to synthesize sphingolipids. Sphingolipids are also

required for the oligomerization of Pma1p in the ER, which is crucial for the delivery of the protein to the cell surface (97). Arginine uptake via the H^+/ Arginine symporter Can1p was decreased 3-fold in cells with decreased ergosterol (*erg24* and *erg6*) and the protein was degraded in the vacuolar lumen in *lcb1-100* cells (98). Another example is Tat2p, an integral membrane that is no longer delivered to the PM in the absence of ergosterol (94, 99).

Several micro compartments have been described for yeast, frequently denominated lipid rafts due to their lipid/protein segregation but they seem to function differently from the mammalian cells rafts (100). On the basis of the lateral segregation of membrane proteins, three main compartments have been described for yeast. The membrane compartment occupied by Can1p (MCC), the membrane compartment occupied by Pma1p (MCP), and the membrane compartment occupied by the rapamycin kinase complex 2, TORC2 (MCT). Cells contain 50-80 of the patch-like MCC domains, furrow-like invaginations in the cell surface, with dimension of around 300 nm long and 50 nm deep. MCPs are described as a network percolated by the MCCs and MCTs (98, 101-104). The MCC domain has been shown to accommodate several proteins apart from Can1p, namely the tetraspan proteins of unknown function Nce102p, Sur7p, Ynl194p, Ydl222p, Ylr414p and Ygr131p (101, 105, 106), and the transport proteins Fur4p and Tat2p (96, 107). Even though, the function of the Sur7p family proteins is not fully understood, the sphingolipid composition and sporulation of yeast were altered in cells lacking Sur7p, Ynl194p and Ydl222p (105). There are also indications that Sur7p interacts with the cell wall since digestion of the wall caused the Sur7p patches to disappear. However, there is some controversy on this topic since Malinska *et al.* showed the maintenance of the Sur7p patches after cell wall digestion (101). The extracellular regions of Sur7p-family proteins have the highest sequence conservation and homologues are present in several fungi and higher plant but not in organisms lacking a cell wall (105). The actin cytoskeleton does not appeared to be directly involved in the maintenance of the patchy localization of MCC proteins as treatment of cells with lantrunculin A, which depolymerizes F-actin, showed no effect (98, 101, 107). The membrane potential has been shown to play an important role in the maintenance of the MCC domains. By dissipating the membrane potential with FCCP (carbonyl cyanide 4-(trifluoromethoxy)phenylhydrazone), all proteins from the MCC domain, except Sur7p, and ergosterol lost their patchy localization at the cell periphery. Surprisingly, pretreatment of cells with filipin, to stain ergosterol, and then FCCP, to dissipate the membrane potential, locked Can1p in the MCCs (107). Filipin is also known to disrupt membrane rafts by sequestering the sterols to some extent (108). There are a number of proteins that are not localized in patches but distributed homogenously over the PM, incl. the hexose transport facilitator, Hxt1p and the yeast general amino acid permease, Gap1p (98, 109). Interestingly, Gap1p also requires sphingolipid biosynthesis for proper localization at the PM (109). The fact that both MCC and MCP contain raft lipids, sphingolipids and ergosterol, is consistent with the localization of Gap1p in both compartments.

In close vicinity to the PM and right underneath the MCC domain, reside the so-called 'eisosomes' (from the Greek '*eis*', meaning portal, and '*soma*', meaning body) (110, 111). Their constituents are all cytosolic proteins that interact with the MCC domain. They were initially described as endocytic sites with Pil1p as main fundamental component. Deletion of *PIL1* leads to miss-localization of Lsp1p, another protein associated with eisosomes, and the MCC protein Sur7p. On the contrary, deletion of *LSP1* or *SUR7* did not have any effect on the localization of Pil1p. The eisosomes are surprisingly static and after photo-bleaching of Pil1p-GFP no recovery of fluorescence was observed (107, 110). Pkh-kinases were also found to co-localize with eisosomes, i.e. Lsp1p. Pkh-kinases, Pkh1 and Pkh2 are regulated by the Long-Chain Bases (LCB), which form the metabolic precursors of sphingolipids. Mutations

in these kinases or in sphingolipid biosynthetic enzymes block endocytosis. Those LCBs regulate the assembly of Pil1p since higher levels of LCBs or ceramides increase the amounts of Pil1p in the plasma membrane and make the eisosome patches more elongated. Pkh-kinases are also responsible for the phosphorylation and localization of Pil1p in the eisosomes (112). The idea that eisosomes serve as endocytic points has been questioned by Grossmann and coworkers, who found that the proteins of the endocytic machinery are excluded from the MCC/eisosomes (106). They showed 21 proteins co-localizing with the MCCs, nine of them being polytopic with 4 or 12 TMDs; the other twelve, all cytosolic, were assigned to the eisosomes. However, deletion of *PIL1* gene resulted in complete dissipation of all MCC markers analyzed (HUP1, Can1p, Sur7p and ergosterol). When deleting the *PIL1* or *NCE102* genes, thus dissipating the MCCs, the endocytosis of Can1p (and Fur4p) was increased either by adding an excess of substrate or protein synthesis inhibitor cycloheximide. The data suggest that proteins are protected when localized in the MCC/eisosome patches (106). This is in agreement with the fact that Pil1p down-regulates pathways involved in endocytosis (Pkc1-mitogen-activated protein and Ypk1). In other words, the eisosomes/MCCs would represent an area that is protected from endocytosis. This idea is reinforced by experiments from Brach *et al*., who showed that only 30 % of the total Can1p resides in the MCCs and the endo- and exocytosis occurs outside those domains (113). Recently, another study pointed out the fact that the reported compartmentalization of yeast PM is not so strict (114). They studied 46 PM proteins and none of them were fully co-localizing with each other. They concluded that the yeast PM might be organized in numerous partially overlapping domains.

Protein dynamics in the plasma membrane of *Saccharomyces cerevisiae*

As mentioned heretofore, the total amount of sphingolipids and ergosterol increases along the secretory pathway (2), and these lipids also play an important role in the TGN-sorting machinery for the targeting of the proteins to the PM via secretory vesicles (4). Interestingly, the lateral diffusion of proteins and lipids in the yeast PM is very slow (115-118). This slow diffusion is a particular feature of the PM because the diffusion in internal membranes seems faster. The SNARE Sso1 protein in the PM of yeast has a diffusion constant of ~0.0025 $\mu m^2/s$, which is two orders of magnitudes slower than in mammalian cells (0.1 $\mu m^2/s$). The same protein was targeted to the vacuolar membrane by fusing it to the N-terminal domain of SNARE Pep2. The resulting diffusion in the vacuolar membrane was much higher, similar to that in mammalian membranes. However, the fraction of the chimera that localized to the PM of yeast had again an anomalously slow diffusion. The diffusion of the two PM proteins analyzed, Sso1 and Snc1, did not depend on the presence of the cell wall or the actin cytoskeleton, but it was 2-fold faster in the *erg6* mutant (115). Besides membrane proteins, lipid probes have also been shown to diffuse slowly at the PM of yeast. The cell wall had no influence on the diffusion, but removal of surface proteins by trypsinization of spheroplasting of cells resulted in a significant increase of the diffusion coefficients (117). A difference in diffusion speed of PM and vacuolar membrane residents was observed for the lipid-anchored Ras2, albeit with only a 4-fold slower diffusion in the PM (119). In addition, the diffusion of membrane reporters in the ER was found to be 5-6 times faster than in the inner nuclear membrane (120, 121). One of the causes for the slow mobility in the PM could be the high fraction of sphingolipids and ergosterol as compared to the organellar membranes or vesicles in the secretory pathway.

The exceptionally slow diffusion of membrane proteins together with the endocytic cycling of proteins has been proposed as means to maintain the membrane polarity (115, 122, 123). Maintenance of membrane polarity is a fundamental feature of the yeast cell cycle. Two signaling pathways can regulate the polarized distributions: immobilization via scaffolds (e.g. cytoskeleton) or through dynamic recycling of membrane proteins (123). The dynamic maintenance of the polarity is strongly influenced by the lateral diffusion of membrane proteins. In fact, polarity is achieved by balancing of three different mechanisms. First, the delivery of membrane proteins via vesicle transport. Second, the lateral diffusion of membrane proteins. Third, the redistribution from the PM to the cytoplasm via endocytosis (124). It has been shown that the delivery of proteins via vesicle trafficking, 50-80 nm in size (97, 125), and the recycling via endocytosis occur at restricted sites that are non-randomly distributed over the PM In fact, those sites are excluded from the cortical ER and are also free of MCC/eisosome domains. The MCC invaginations are thought be responsible for the local perforations of the cortical ER (126). Taken collectively, the PM is a complex structure with tight regulation of the spatial and functional organization of its constituents.

Chapter 2

Structural basis for the enhanced activity of cyclic antimicrobial peptides: The case of BPC194

Jacek T. Mika*, Gemma Moiset*, Anna D. Cirac, Lidia Feliu, Eduard Bardají, Marta Planas, Durba Sengupta, Siewert J. Marrink and Bert Poolman

(*) Shared first authorship

Published in *Biochimica et Biophysica Acta: Biomembranes* (2011) 1808: 2197-2205

We report the molecular basis for the differences in activity of cyclic and linear antimicrobial peptides. We iteratively performed atomistic molecular dynamics simulations and biophysical measurements to probe the interaction of a cyclic antimicrobial peptide and its inactive linear analogue with model membranes. We establish that, relative to the linear peptide, the cyclic one binds stronger to negatively-charged membranes. We show that only the cyclic peptide folds at the membrane interface and adopts a beta-sheet structure characterized by two turns. Subsequently, the cyclic peptide penetrates deeper into the bilayer while the linear peptide remains essentially at the surface. Finally, based on our comparative study, we propose a model characterizing the mode of action of cyclic antimicrobial peptides. The results provide a chemical rationale for enhanced activity in certain cyclic antimicrobial peptides and can be used as a guideline for design of novel antimicrobial peptides.

Introduction

Antimicrobial peptides (AMPs) are currently in the spotlight as potential candidates to overcome bacterial resistance to conventional antibiotics. These peptides are natural weapons produced by a variety of organisms, including insects, animals and plants (127, 128). While displaying a wide spread in primary structures, most antimicrobial peptides exhibit common basic features (129-131). The linear α-helical peptides have been shown to be unstructured in water and adopt a secondary structure upon association with the membrane (132, 133). Though acquiring structure upon membrane binding is an important feature of these AMPs, short peptides lacking a well-defined secondary structure are also active (134). Cyclic AMPs are amongst the most effective antimicrobial agents (25, 135) and some members of the family have been shown to adopt a structure even in water (136). One of the best studied examples is gramicidin S, whose structure in aqueous media, an anti-parallel β-sheet characterized by two turns, is important for its activity (137). Comparative studies between related peptides with differing activities, though not yet been undertaken, would help us rationalize the essential structural properties vital for function and will help us design more potent antimicrobial peptides.

Besides acquiring structure at the membrane interface, the partitioning behavior of the peptides, i.e. the membrane-aqueous medium partition coefficient and the membrane penetration depth also contribute to their efficacy and action and selectivity (138). In fact, the local concentrations of AMPs in the membrane can be up to 10,000 times higher than in the aqueous phase (40), therefore the understanding of partitioning behaviour is of importance to unravel mechanisms of action of these peptides. Again, undertaking comparative studies would help us distinguish between essential and non-essential differences in partitioning and help to extract only the critical features.

The focus of our work is a cyclic peptide, BPC194 [c(KKLKKFKKLQ)], which, from a library of *de novo* designed cyclic decapeptides, proved most active against plant pathogens such as *Erwinia amylovora, Pseudomonas syringae* and *Xanthomonas vesicatoria* (139, 140); its linear analogue is poorly active. Here, we present a combined MD and biophysical study of the cyclic peptide interacting with anionic lipid bilayers to understand its mechanism of action. The linear analogue, BPC193 has been studied to contrast the behavior of the two related peptides and extract the molecular basis for antimicrobial activity. We show how the cyclic and linear peptides differ both in their partitioning behavior and their folding state upon interaction with membranes. We speculate that these differences are related to differences in pore forming activity.

Materials and methods

Biophysical characterization

Materials

The 9-fluorenylmethoxycarbonyl (Fmoc)-protected amino acid derivatives, coupling reagents, and 4-methylbenzhydrylamine (MBHA) resin hydrochloride (0.4 mmol/g) were obtained from Iris Biotech (Marktredwitz, Germany). Trifluoroacetic acid (TFA), N,N-dimethylformamide (DMF), N-methyl-2-pyrrolidinone (NMP), $Pd(PPh_3)_4$, sodium N,N-diethyldithiocarbamate, triisopropylsilane (TIS), tetrahydrofuran and $CHCl_3$ were from Sigma-Aldrich Corporation (Madrid, Spain). Piperidine, N-methylmorpholine (NMM), and N,Ndiisopropylethylamine (DIEA) were purchased from Fluka (Buchs, Switzerland). Acetic acid (AcOH), diethyl ether and CH_2Cl_2 were from Panreac (Castellar del Vallès, Spain). Solvents for reverse-phase high-performance liquid chromatography (RP-HPLC) were obtained from

Scharlau (Sentmenat, Spain). H_2O was de-ionized and filtered using a COT Millipore Q-gradient. The 4-(2-hydroxyethyl)piperazine-1-ethanesulfonic acid (HEPES) and 2-amino-2-(hydroxymethyl)-1,3-propanediol (Tris-HCl) were from Roche Diagnostics GmbH (Germany), sodium chloride, sodium fluoride and Triton-X100 were from Merck (Germany). Phospholipids 1,2-dioleoyl-sn-glycero-3-phosphatidylcholine (DOPC), 1,2-dioleoyl-sn-glycero-3-phosphatidylglycerol (DOPG) and 1,2-dioleoyl-sn-glycero-3-phosphatidyl-ethanolamine (DOPE) were from Avanti Polar Lipids.

Peptide synthesis

Decapeptides investigated in this study (Table 1) varied in the type of aromatic aminoacid at position 6 and included cyclic analogues: BPC194, BPC294 and BPC418, together with their linear counterparts: BPC193, BPC293 and BPC417. Peptides were synthesized from a MBHA resin by carrying out solid-phase synthesis of linear sequences followed by on-resin cyclization. A three-dimensional orthogonal Fmoc/tButyl/Allyl strategy was used (141). Side-chain protection for Lys and Trp was as tert-butyl carbamate (Boc) and as tert-butyl (tBu) for Tyr. Fmoc-Glu-OAl residue was used as trifunctional amino acid to allow peptide anchoring onto the resin, which resulted in a Gln after peptide cleavage from the support. The MBHA resin (0.4 mmol/g, 200-400 mesh) was swollen with CH_2Cl_2 (1 × 20 min), DMF (1 × 20 min), piperidine/DMF (3:7, 1 × 5 min), DMF (6 × 1 min), and CH_2Cl_2 (3 × 1 min). Then, the resin was treated with Fmoc-Rink linker (5 equiv), N-[(1H-benzotriazol-1-yl)(dimethylamino)methylene]-N-methylmethanaminium hexafluorophosphate (HBTU) and DIEA (10 equiv) with overnight stirring. The Fmoc group was removed by treating the resin with a mixture of piperidine/DMF (3:7, 2 + 8 min). Couplings were conducted using the corresponding Fmoc-protected amino acid (4 equiv), which was dissolved in DMF and preactivated for 5 min with HBTU (3.8 equiv), 1-hydroxybenzotriazole (HOBt) (4 equiv) and DIEA (7.8 equiv). The mixture was added to the resin and shaken for 1 h at room temperature. The completion of the reactions was checked by the Kaiser test. Peptide elongation was performed by repeated cycles of Fmoc group removal and coupling. After each deprotection and coupling step, the resin was washed with DMF (5 × 1 min). Once the chain assembly was completed, the C-terminal allyl ester was cleaved by treatment with $Pd(PPh_3)_4$ (3 equiv.) in $CHCl_3$/AcOH/NMM (92.5:5:2.5, 1 mL) with stirring under nitrogen for 3 h at room temperature, followed by washings with tetrahydrofuran (3 × 2 min), DMF (3 × 2 min), DIEA/CH_2Cl_2 (1:19, 3 × 2 min), sodium N,N-diethyldithiocarbamate (0.03 M in DMF, 3 × 15 min), DMF (10 × 1 min) and CH_2Cl_2 (3 × 2 min). After final Fmoc removal, the resin was divided: One portion of the resin was used to obtain the linear peptides. The rest of the resin was subjected to cyclization by treatment with benzotriazol-1-yl-N-oxytris(pyrrolidino)phosphonium hexafluorophosphate (PyBOP) (5 equiv), HOBt (5 equiv), and DIEA (10 equiv) in NMP at 25 ºC for 24 h. After this time, the resin was washed with NMP (6 × 1 min), CH_2Cl_2 (3 × 1 min), and diethyl ether (3 × 1 min), and air-dried. Cleavage of the corresponding linear and cyclic peptides was performed by treatment with TFA/H_2O/TIS (95:2.5:2.5) for 2 h at room temperature, and the cleavage cocktail was evaporated to dryness under a stream of nitrogen. Following diethyl ether extraction, peptides were dissolved in H_2O, lyophilized and analyzed by analytical HPLC performed at 1.0 ml/min using a Kromasil (4.6 × 40 mm; 3.5 μm particle size) C_{18} reverse-phase column. Linear gradients of 0.1% aqueous TFA and 0.1% TFA in CH_3CN were run from 0.98:0.02 to 0:1 over 7 min with UV detection at 220 nm. All peptides synthesized showed ~90% HPLC purity. Electrospray ionization mass spectrometry (ESI-MS) was used to confirm peptide identity.

Liposome preparation

Liposomes for calcein dequenching. Liposomes were prepared as described previously (142). Briefly, liposomes at a final concentration of 1mM of lipid molecules were prepared by rehydration of a dried lipid film with 100 mM calcein-NaOH in 10 mM HEPES, pH 7.0. The vesicles were then subjected to five cycles of flash freezing in liquid nitrogen and rapid thawing at 50°C. Subsequently, the liposomes were sonicated (5 × 10 sec. pulses at 75% amplitude with a Sonics Vibra Cell VCX 130 sonicator) to obtain unilamellar vesicles. Liposomes were separated from the non-encapsulated dye by size exclusion chromatography (Sephadex G-75, GE Healthcare). The column was equilibrated and eluted with 10 mM HEPES, pH 7.0, plus 150 mM NaCl, further refered as buffer A.

Liposomes for Circular Dichroism (CD). Liposomes were prepared similarly as described for the calcein dequenching experiments except that the dried lipid film was rehydrated with 10 mM sodium phosphate, pH 7.0, plus 150 mM NaF to a final concentration of 25 mM lipids. Sodium chloride was replaced by sodium fluoride to reduce the noise levels at wavelengths < 200 nm, which is caused by chloride ions. Furthermore, liposomes were extruded through a 30 nm polycarbonate filter (Whatman International Ltd, UK), instead of sonication, to obtain a more homogenous sample.

Liposomes for binding and tryptophan environment assays. Liposomes were prepared by rehydration of DOPG phospholipid films in buffer A to a final concentration of 25 mM and subsequently extruded through a 200 nm polycarbonate filter.

Calcein dequenching

The calcein dequenching assay was performed as reported previously (142). A 20 μl sample of liposomes (1mM of lipid), obtained as described in section 2.1.3.1 of Materials and Methods, was placed in 3 ml of buffer A, which yielded a final concentration of 6.7 μM of lipid in the cuvette. The membrane permeabilizing activity of the peptide was followed by measuring the increase in fluorescence (calcein dequenching), resulting from vesicle leakage after peptide addition addition (0-52 μM). Fluorescence emission was monitored at 520 ± 5 nm (excitation at 485 ± 2 nm) in a Cary Eclipse Fluorescence Spectrophotometer (Varian Inc.). The release of the calcein was calculated as a percentage of the total amount present in the liposomes:

$$\%\ Release = (I - I_0) / (I_{100} - I_0) \times 100$$

where I is the measured fluorescence intensity at a given time, I_0 is the initial background fluorescence intensity and I_{100} is the fluorescence intensity upon complete lysis of the liposomes, which was elicited by adding Triton X-100 (0.06% final concentration).

Circular dichroism

Far-UV circular dichroism spectra were recorded on a Jasco J-815 CD spectrometer (Jasco, UK) between 190 and 250 nm at room temperature and scanning every 1 nm, using a quartz cell of 1 mm path length. The peptide at 0.15 mM was titrated with small aliquots (1 to 10 μL) of DOPG liposomes at a concentration of 25 mM. 2,2,2-Trifluoroethanol (TFE, Janssen Chimica) was used as a secondary structure inducer. The spectra were corrected for the absorption of buffer and vesicles.

Peptide environment probed with tryptophan fluorescence

The tryptophan analogues (BPC417 and BPC418) were placed in a quartz cuvette in buffer A at 2 μM and their fluorescence was monitored with a Fluorlog-3 (Jobin Yvon) spectrofluorimeter at an excitation wavelength of 285 ± 5 nm and emission scanning from 295 to 400 nm. Different amounts of DOPG vesicles were introduced into the cuvette (at final lipid concentrations of 2.28, 28 and 275 μM, corresponding to P:L ratios of 0.88, 0.071 and 0.0073, respectively). Subsequently, NaCl was titrated into the cuvette to a final concentration of 350 mM. The emission spectra were corrected with the corresponding buffer spectra (including DOPG and salt) and fitted to a skewed Gaussian curve (143) to obtain the fluorescence emission maximum, λ_{max}.

Peptide binding by ultracentrifugation

Increasing amounts of DOPG liposomes (0-753 μM) were added to 0.5 ml of 6 μM peptide in buffer A up to a P:L ratio of 1:114 and incubated for 20 min at room temperature. The samples were spun down by ultracentrifugation (1 h at 270,000 × g) and supernatants were separated from the pellets. A control experiment with an encapsulated dye in the same vesicles was carried out and under those conditions the vesicles were quantitatively spun down. To correct for the differences in quantum yield of the tryptophan fluorescence in different environments (hydrophilic buffer A vs. hydrophobic membrane environment), 2% (w/v) of sodium dodecyl sulfate (SDS) was added to the supernatant fraction and the fluorescence was measured. A correction was made for the background signal using a reference solution of buffer A, liposomes and SDS without the peptide. The percentage of binding was calculated using the equation:

$$\% \; Binding = 100 - (I_0/I \times 100)$$

where, I_0 is the fluorescence intensity of the supernatant sample with peptide without liposomes and I is the fluorescence intensity of the samples with liposomes. The obtained data were fitted to a general binding equation to obtain the dissociation constant (K_d):

$$\% \; Binding = (B_{max} \times C_{lipid}) / (K_d + C_{lipid})$$

where, C_{lipid} is the concentration of lipid and B_{max} is the maximum value for binding. For this purpose a simple binding equilibrium was assumed where peptide interacts [P] with the membrane [M] to form a peptide-membrane complex [PM]. This approach is equivalent to what was described by Matos and coworkers (144). The affinity of peptide membrane interaction can also be expressed as partitioning coefficients (145). The relationship between the two models is discussed in the work of Matos *et al.* (144).

Molecular Dynamics Simulations

System set-up

Simulations were performed with BPC194 [c(KKLKKFKKLQ)], and the linear analogue BPC193 [H-KKLKKFKKLQ-OH]. For the cyclic peptide, a peptide bond was created between the N-terminal lysine residue and the C-terminal glutamine residue. The initial structure of the peptides was modeled using the leap module of AMBER 9 (146).

Peptide in aqueous environment

A number of systems were prepared with either one cyclic or one linear peptide solvated by water. The cyclic peptide was initially unstructured in all simulations but

different starting conformations of the linear analogue were tested: α-helix, bend and random-coil. An overview of all simulations performed is shown in Table 2 (Wa-Wk), and the details are presented in Table 3. All systems were simulated in a cubic box of length 4~5 nm and about 3000 water molecules. In a few simulations, counterions (Cl^-) were added to neutralize the system.

Peptide-membrane systems

A number of simulations were performed with peptides in a solvated DPPG (1,2-dipalmitoyl-sn-glycero-3-phosphatidylglycerol) membrane system. Simulations were performed with molar peptide: lipid (P:L) ratios of 1:128, 2:60, 4:128 and 9:128 (and 6000-8000 water molecules) for both BPC194 and BPC193 (see Table 2 for an overview and Table 3 for details). Initially, the peptides were placed in the water phase close to the membrane surface, with distances between the peptide and membrane ranging from 1.5 to 2.3 nm. The cyclic peptide was initially unstructured and different conformations were tested for the linear peptide. Multiple simulations were run from different initial random velocity distributions for each of the P:L ratios. The simulations were carried out in the presence and absence of counter ions, and using different electrostatic schemes.

Simulations parameters

The GROMACS software package (147) was used to perform all MD simulations. The GROMOS force-field 43a2 (148) was used to describe the peptide and peptide–solvent interactions. Simulations in water were also run using GROMOS force-field 53a6 (149). The force-field for DPPG lipids was optimized from DPPC (150) and POPG lipids (151), compatible with the GROMOS96 parameters. The choline head-groups were replaced by glycerol from the POPG force-field, and the tail parameters were taken from the DPPC force-field. The parameters were then optimized to achieve an area per lipid consistent with experiment (152). The equilibrated DPPG bilayer had a thickness of 3.54 ± 0.05 nm and an area per lipid of 0.69 ± 0.01 nm^2. All force-fields were parameterized for use with a group-based twin range cut-off scheme (using cutoffs of 1.0/1.4 nm and a pair-list update frequency of once per 10 steps), including a reaction field (153, 154) correction with a dielectric constant of 78 to account for the truncation of long-range electrostatic interactions. To test the effect of long-range electrostatic interactions, in some simulations the RF was replaced by the particle-mesh Ewald (PME) method. The water was modeled using the SPC model (155). A time step of 2 fs was used. Bond lengths were constrained using the LINCS algorithm (156). The simulations were performed in the $NP_|P_ZT$ ensemble using periodic boundary conditions. The temperature was weakly coupled (coupling time 0.1 ps) to T = 320 K using the Berendsen thermostat (157). The pressure was also weakly coupled (coupling time of 1.0 ps and compressibility of $4.5 \times 10\text{-}5$), using a semi isotropic coupling scheme in which the lateral ($P_|$) and perpendicular (P_Z) pressures were coupled independently at 1 bar, corresponding to a tension-free state of the membrane. The simulation setup is similar to that used in previous studies of peptide-membrane interactions (34, 35). For a general review on MD studies of peptide-membrane interactions see the work of Mátyus *et al.* (158).

Analysis

The secondary structure of the peptides was calculated with the DSSP code (159). For the cyclic peptide, the bonded N-terminus (K^1) and C-terminus (Q^{10}), present in the turn region, were neglected while calculating the secondary structure. The structural properties were then calculated from the average number of residues involved in each secondary structural feature along the simulation. The total "β-structure" is

reported as the sum of β-sheet and β-bridge (one hydrogen bond less than β-sheet) and the "non-structured", as the sum of coil, bend and turn.

To analyze the alignment of the lysine residues, the distance between the planes formed by the C_α, C_γ and N_ζ atoms of the spatially-symmetric lysine residues K^1-K^8, K^2-K^7 and K^4-K^5 were calculated.

Results

The cyclic peptide permeabilizes the membrane and has a preference for anionic lipids

The cyclic peptide BPC194 has a high antimicrobial activity (MIC values ranged from 3.1-12 μM) and low hemolytic activity (not exceeding 17% at 375 μM) (139). A calcein dequenching assay was performed to determine the membrane permeabilizing activity of the cyclic peptide, BPC194, two cyclic analogues (BPC294 with Tyr and BPC418 with Trp instead of Phe at position 6) and the corresponding linear analogues BPC193, BPC293, BPC417 (Table 1).

Table 1. Names and sequences of the peptides used in this study.

Cyclic		Linear	
Code	Sequence	Code	Sequence
BPC194	c(KKLKKFKKLQ)	BPC193	H-KKLKKFKKLQ-OH
BPC294	c(KKLKKYKKLQ)	BPC293	H-KKLKKYKKLQ-OH
BPC418	c(KKLKKWKKLQ)	BPC417	H-KKLKKWKKLQ-OH

Figure 1 summarizes the results obtained for the cyclic analog BPC194 and shows that it caused the leakage of calcein from vesicles comprising of anionic lipids. The leakage reached 100% in DOPG membranes though it did not exceed 5% in DOPC, even at high P:L ratios (Fig. 1A). Experiments with liposomes composed of mixtures of DOPG, DOPC and/or DOPE confirmed that the cyclic peptide (BPC194) has a preference for anionic lipids since the leakage increases with the content of DOPG lipids in the vesicles (Fig. 1B). Poration propensity of BPC194 in anionic lipids was independent of the vesicle size (Fig. 2)

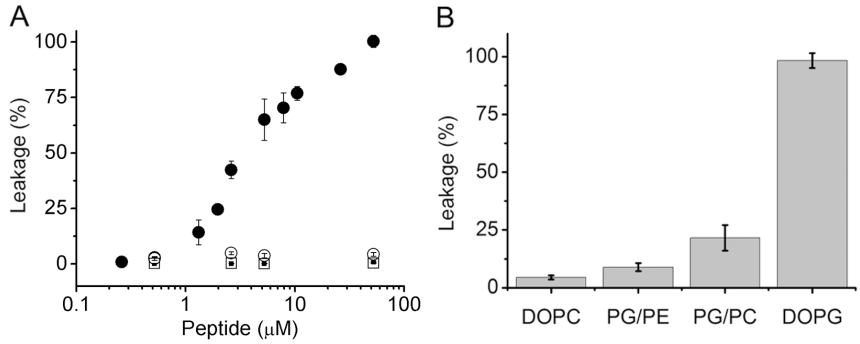

Figure 1. *Vesicle permeabilizing properties of peptides.* Leakage of calcein as a function of peptide concentration is shown. (A) Circles: the action of BPC194 on DOPG and DOPC vesicles (filled and hollow symbols, respectively). Squares: data obtained with BPC193 with DOPG and DOPC vesicles (small filled and big hollow symbols, respectively). (B) Calcein dequenching results for BPC194 using liposomes of different lipid composition: DOPC, DOPG/DOPE 1:1 (mol/mol) and DOPG/DOPC 1:1 (mol/mol) and DOPG. The end-points of leakage at a peptide concentration of 52 μM and a lipid concentration of 6.7 μM are shown. Error bars indicate deviation between individual experiments (n = 3).

All three cyclic analogues caused the leakage of calcein for anionic membranes (Fig. 3). These results are line with the *in vivo* data (139) and are consistent with the fact that bacterial membranes are generally more rich in negatively-charged lipids than the outer leaflet of the plasma membrane of higher eukaryotes, e.g. mammalian cells (40). The calcein leakage from vesicles was negligible for the linear analogues, irrespective of the lipid composition. The low antimicrobial activity of the linear peptide is consistent with the lack of membrane permeation in model membrane systems. Below, we focus on the interaction of the cyclic and linear analogues with anionic lipids to understand the remarkable differences in their membrane permeabilizing properties.

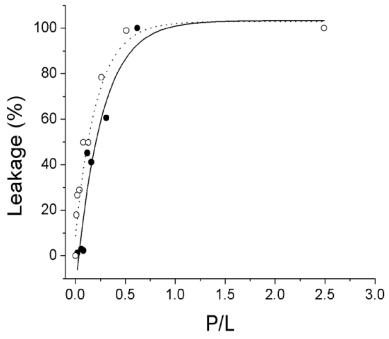

Figure 2. *Vesicle permeabilizing propensity of BPC194 with SUVs and LUVs*. The percentage of leakage of DOPG vesicles is represented as a function of P/L ratio (lipid concentration constant at 10.6 μM). BPC194 has similar poration propensity with small unilamellar vesicles, SUVs (80 nm in size; full circles) and 200 nm large unilamellar vesicles, LUVs (open circles).

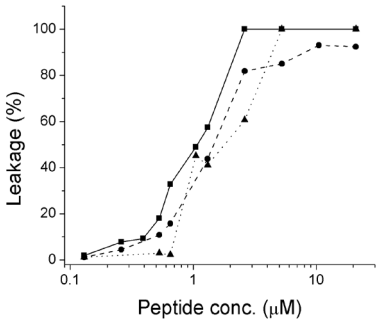

Figure 3. *Vesicle permeabilizing properties of the cyclic analogues BPC194, BPC294 and BPC418*. The percentage of leakage of calcein from DOPG liposomes is represented as a function of peptide concentration at a final lipid concentration of 10.6 μM. Triangles, dotted line represent data for BPC194; circles, dashed line: BPC294; and squares, solid line: BPC418. In all cases the cyclic peptides had similar membrane-permeabilizing properties.

Both the linear and cyclic peptides bind to PG membranes

To test whether the low activity of the linear peptides stems from their inability to bind to anionic membranes, we analyzed their membrane binding properties by MD simulations and fluorescence experiments. In the MD simulations, the peptides (BPC193 and BPC194) were placed in the water phase close to the surface of a DPPG bilayer at P:L ratios of 1:128, 4:128 and 9:128. Both peptides bound to the membrane rather fast and on similar (nanosecond) time scales (Figs. 4A and 4B). To validate the simulation data, the fluorescence of the tryptophan in BPC417 and BPC418 was used to monitor the interaction of the linear and cyclic peptides with the membranes. BPC417 and BPC418 bound to DOPG membranes albeit with different affinities (Fig. 4C). BPC418 bound to the membrane with a K_d, of 7 +/- 2 μM (under these conditions the overall P:L ratio = 0.84). BPC417 bound with a K_d for DOPG of 96 +/- 10 μM (P:L ratio = 0.0625). From the data presented in Fig. 4C, one can derive P:L ratios at which the amount of cyclic and linear peptide bound is equal and compare these conditions with those in Fig. 1A. Even at equal amounts of peptide interacting with the membrane, the cyclic peptide is orders of magnitude more effective in membrane permeabilization than the linear one. For instance, when the cyclic and the linear peptide are ~ 60% bound (P:L ratio of around 0.6 and 0.06, respectively) the cyclic peptide causes ~ 50% of dye leakage, while the linear analog is not active.

Both linear and cyclic peptides are structure-less in aqueous solution

To analyze the structure of the peptides in aqueous solution, atomistic MD simulations as well as CD measurements were performed. In the simulations, the cyclic and the linear peptide showed no defined secondary structure in aqueous solution and appeared mainly in a non-structured conformation (Figs. 5A and 5B). On average, only 13 and 16% β-structure was adopted by the cyclic and linear peptide, respectively (Table 2). Although we found that 50 ns of simulation were not sufficient for the peptides to completely sample their configurational space, the simulation data taken as a whole points to an unstructured conformation for both peptides in solution. The lack of secondary structure in the MD simulations was confirmed by CD measurements (Figs. 5I and 5J).

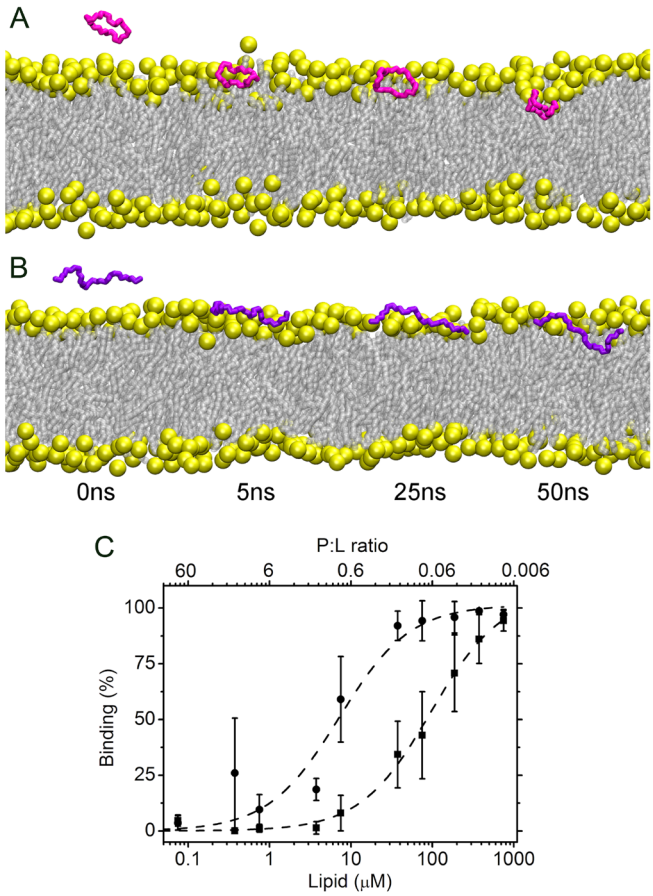

Figure 4. *Binding of cyclic and linear peptides to PG membranes*. (A) Time course of the simulation 1Ca of BPC194 (pink) interacting with DPPG membranes. (B) Time course of the simulation 1Lb of BPC193 (purple). In both A and B, the head-group phosphorus atoms are shown in yellow, the lipid tails in grey and side-chains have been removed for clarity. (C) Percentage binding of BPC418 (solid black circles) and BPC417 (solid black squares) at 6 μM concentration to DOPG membranes assessed by ultracentrifugation and employing the fluorescence of tryptophan. Error bars denote the deviation between individual experiments (n = 4); the top X-axis: P:L ratios corresponding to lipid concentrations indicated at the bottom axis. Dashed line: the fit of the data used to obtain the K_d.

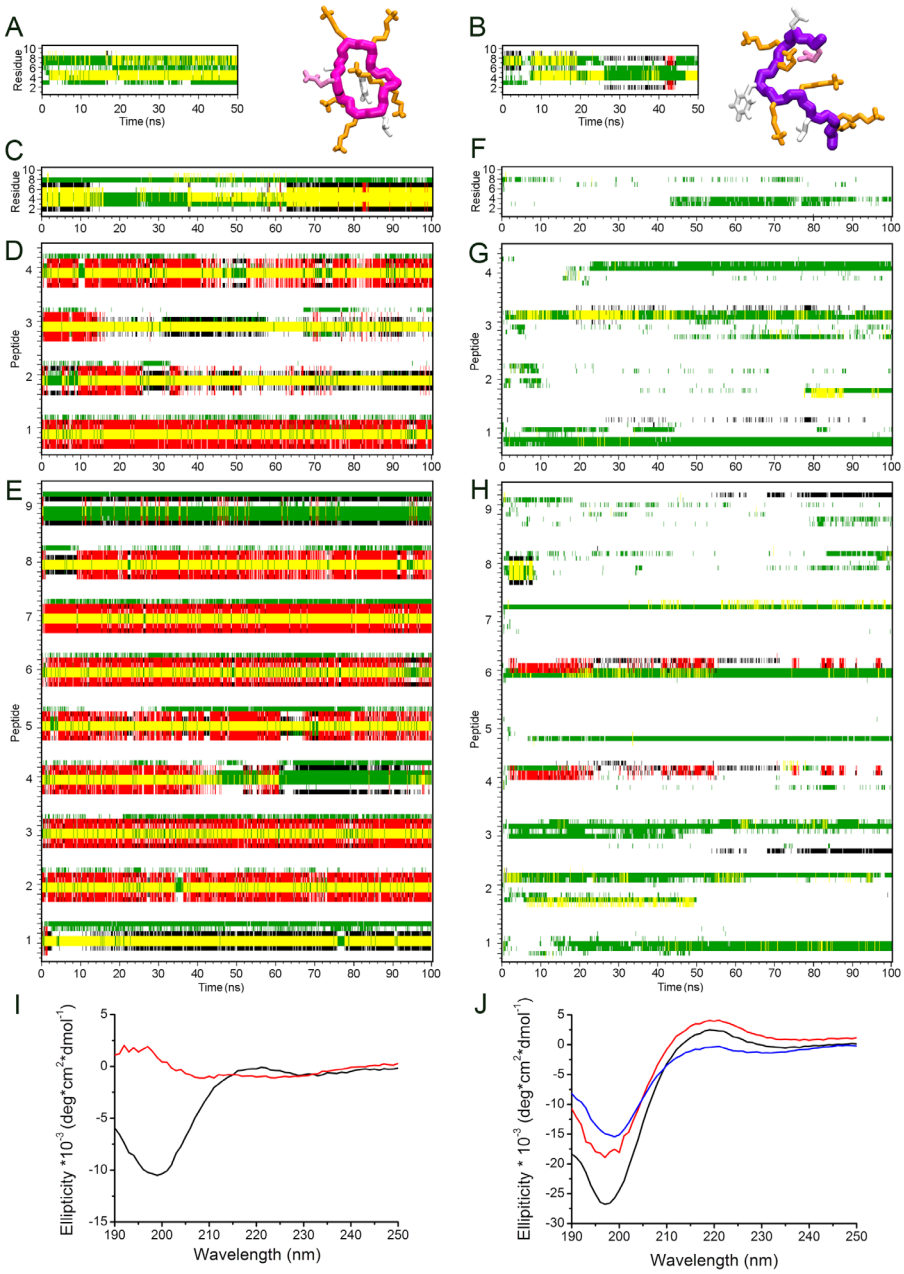

Figure 5. *Structure of peptides in water and upon membrane binding*. Secondary structure plot in water as determined by the DSSP code and representative snapshot of BPC194 (A) and BPC193 (B). The colors associated with the secondary structural elements are red (β-sheet), yellow (turn), green (bend), black (β-bridge) and white (coil). In both snapshots, Lys residues are shown in orange, Phe and Leu in white and Gln in light pink. (C-E) Cyclic peptide DSSP plots of the simulations at P:L ratios of 1:128, 4:128 and 9:128, respectively. (F-H) Linear peptide DSSP plot of representative simulations at P:L ratios 1:128, 4:128 and 9:128, respectively. (I) CD spectra of the cyclic BPC194 in aqueous buffer (black line) and in the presence of DOPG vesicles (red line) at a P:L ratio of 0.38. (J) CD spectra of the linear peptide BPC193 in buffer, in the presence of DOPG membranes (at P:L ratio 0.38) or a secondary structure inducer TFE (black, red and blue line, respectively). Peptides 0.15 mM, lipids 0.4 mM, TFE – 25% (vol/vol).

Table 2. Overview of secondary structure and binding characteristics in all simulations performed on the cyclic (BPC194) and linear (BPC193) peptides. Results are averaged over all peptides present in the system, and over all independent simulations. The average binding depth as well as the maximum binding depth observed for a particular peptide is given. The standard errors reported are calculated from the standard deviation, between all peptides in all simulations. [a]Center of mass of the peptide. [b]Center of mass of the phenyl ring of the phenylalanine residue.

Peptide	P:L ratio	Code	Nr. of Sim.	%Non-Structured	%β-Structure	Peptide Depth[a]		Phe Depth[b]	
						Av.	Max	Av.	Max
Cyclic	Water	Wa-Wc	3	87 ± 5	13 ± 5	-	-	-	-
	1:128	1Ca-1Cg	7	79 ± 3	21 ± 3	-0.34 ± 0.38	-1.16	-0.52 ± 0.65	-1.75
	4:128	4Ca-4Cc	3	67 ± 4	33 ± 4	-0.08 ± 0.23	-0.99	-0.03 ± 0.29	-0.86
	9:128	9Ca-9Cj	10	68 ± 2	32 ± 2	-0.24 ± 0.25	-1.2	-0.57 ± 0.20	-1.4
Linear	Water	Wd-Wk	8	84 ± 4	16 ± 4	-	-	-	-
	1:128	1La-1Lb	2	100 ± 0	0 ± 0	-0.18 ± 0.25	-0.78	-0.10 ± 0.41	-0.85
	2:60	2La-2Lb	2	-	-	-	-	-	-
	4:128	4La-4Lb	2	100 ± 0	0 ± 0	-0.10 ± 0.18	-0.75	0.50 ± 0.23	-0.46
	9:128	9La-9Lg	7	99 ± 0	1 ± 0	0.41 ± 0.19	-0.62	0.52 ± 0.19	-1.37

Cyclic peptide adopts β-structure upon binding to membranes

Upon interaction of BPC194 with the DPPG membrane surface, a secondary structure was induced within nanoseconds in the simulations (Fig. 5C-E). The average fraction of β-structure increased from 13% to 32% (Table 2). The increase in β-structure was most pronounced at the higher P:L ratios of 4:128 and 9:128. Visual inspection of the MD simulations of BPC194 showed that the β-structure formation gives rise to an amphipathic-like structure with a spatially-symmetric arrangement of two pairs of lysine residues: K^1-K^8 and K^2-K^7 on opposite strands. When the peptide adopted a β-structure, these lysine pairs aligned in a parallel manner and gave rise to a high charge density (Figs. 6A and 6B). When the intra-strand hydrogen bonds were weakened and the β-structure was lost, the lysine residues could point away from each other (Fig. 6C). On average, the distances between the lysine pairs at the membrane interface were reduced from 1 nm (in aqueous medium) to about 0.7 nm. Upon addition of DOPG membranes, a substantial change in ellipticity of BPC194 was observed (Fig 5I); similar behavior was seen for the tryptophan (BPC418) and tyrosine containing (BPC294) cyclic peptides but not for the linear analogues (Fig. 7). The CD spectra of the cyclic peptides in the presence of DOPG are reminiscent of β-sheet and β-turn structures reported for other (cyclic) peptides (160-162). However a quantitative deconvolution of the spectra is difficult as CD spectra simulators are designed for large proteins rather than cyclic small peptides. Unfortunately, it is not possible to perform solution-state NMR measurements on the membrane-associated states of the peptides, since the molecular mass of the vesicles to which the peptides are associated is so large that any NMR signal of the peptide would be broadened beyond detection.

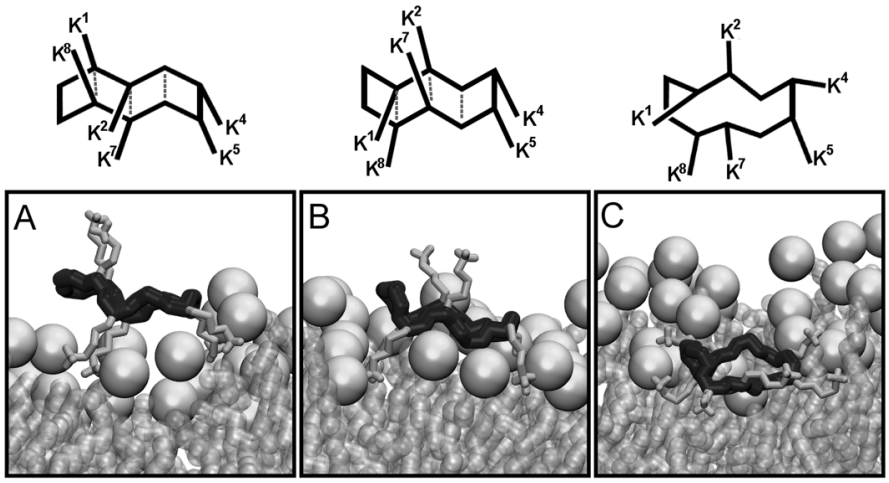

Figure 6. *Different binding modes of the cyclic peptide.* The lysine residues are depicted in grey, the head-group phosphorus atoms are represented as spheres and the acyl tails in grey. (A-B) In certain binding modes during the simulation, the lysine residues aligned with inter-strand hydrogen bonds (dashed grey). (C) In others, the lysines snorkelled out independently and the inter-strand distances increased.

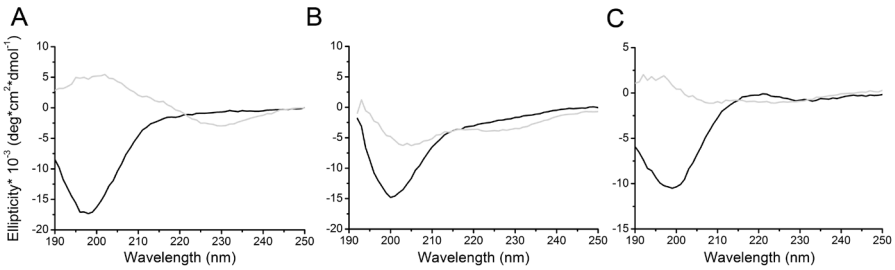

Figure 7. *Secondary structure of cyclic peptide analogues.* CD spectra of BPC294 (A), BPC418 (B) and BPC194 (C) in aqueous buffer (black line) and in the presence of DOPG liposomes (grey line) at P:L ratios of 1.5, 0.3 and 0.3, respectively. The peptide concentration was 0.15 mM, the lipid concentration 0.1 mM (A) and 0.4 mM (B and C). The spectra of BPC418 suffered from high scattering due to fusing vesicles and were acquired at lower lipid concentrations. The CD spectra of small cyclic peptides are difficult to deconvolute because of the contributions of different turns and aromatic residues, and the lack of experimental structural data such as X-ray and NMR. On the basis of our MD simulations and the fact that the recorded spectra are reminiscent of β-sheet and β-turn, we conclude that the peptides upon interaction with DOPG vesicles undergo folding.

The inactive linear peptide remains structure-less at the membrane surface

In contrast to the cyclic peptide, the linear analogue remained fully unstructured (Figs. 5F-H) with no intra-molecular hydrogen bonding at the DPPG membrane interface at P:L ratios of 1:128 and 4:128 (Table 2). At the highest P:L ratios (9:128) a few intermolecular interaction were observed, resulting in peptide clusters. This gave rise to some β-sheet characteristics on the interacting peptides, originating mainly from interactions of the peptide backbone and the glutamine side-chain. The CD measurements were entirely consistent with the MD simulations (Figs 5J).

The cyclic and linear peptides differ in membrane penetration

BPC194 was able to penetrate deeper into the phospholipid membrane than its linear counterpart. In the MD simulations, the distances between the phosphorus atoms of the outer leaflet and the centre of mass of the peptide were calculated and are plotted in Figs. 8A-D. The cyclic peptide BPC194 was able to insert below the level of the phosphorus atoms (see Table 2). Though a single peptide (P:L 1:128) appeared on average to bind deeper (-0.34 nm) compared to systems with P:L ratios of 4:128, 9:128 (-0.08 nm and -0.24 nm), the maximum insertion for individual peptides was at P:L ratio of 9:128 (-1.20 nm). Visual inspection of the trajectories showed that large values of insertion of the cyclic peptide were associated with high local perturbations, which led to poration of the membrane (163).The fluctuations in the outer leaflet, calculated as the deviation of the phosphorus atoms of the head-groups from their center of mass were ± 0.44 nm for the cyclic peptide. In contrast to the cyclic peptide, the linear analogue BPC193 did not embed very deep. The maximum insertion observed was -0.62 nm below the level of the phosphorus atoms and was not accompanied by large bilayer perturbations. Furthermore, low perturbations were seen in comparison to the cyclic peptide and the outer-leaflet fluctuations were ± 0.29 nm for the linear peptide.

Next, we examined the environment of the tryptophan from fluorescence emission spectra. The peptide that was initially in buffer was exposed to DOPG vesicles, which resulted in a blue-shift of the fluorescence emission peak (λ_{max}) of ~14 and ~10 nm for the cyclic and linear peptides, respectively (see Figs 8E and 8F; at these P:L ratios essentially all peptides are bound). The larger blue-shift for the cyclic peptide points to a more hydrophobic environment and thus to a deeper insertion into the membrane. Increasing the ionic strength resulted in a shift of the λ_{max} of the linear peptide back to what it was in the aqueous medium, which is indicative of reversible binding. The salt effect was not observed for the cyclic peptide, and even at the highest P:L ratio of 0.88 (where about 50% was bound (Fig. 4C) and the membranes were saturated with peptide), the backshift of λ_{max} was only marginal (Fig. 8G). Thus, the salt effects are also consistent with a deeper insertion of the cyclic peptide, BPC418, as compared to the linear one. It has been reported that certain peptides (*e.g* pep-1) (164) can translocate through the membrane without causing leakage/poration. We believe that the shallow and reversible membrane-embedding of BPC193 (incl. MD simulations and much less pronounced fluorescence blue-shift of the linear peptide as compared to the cyclic counterpart) argue against such possibility for the linear peptides.

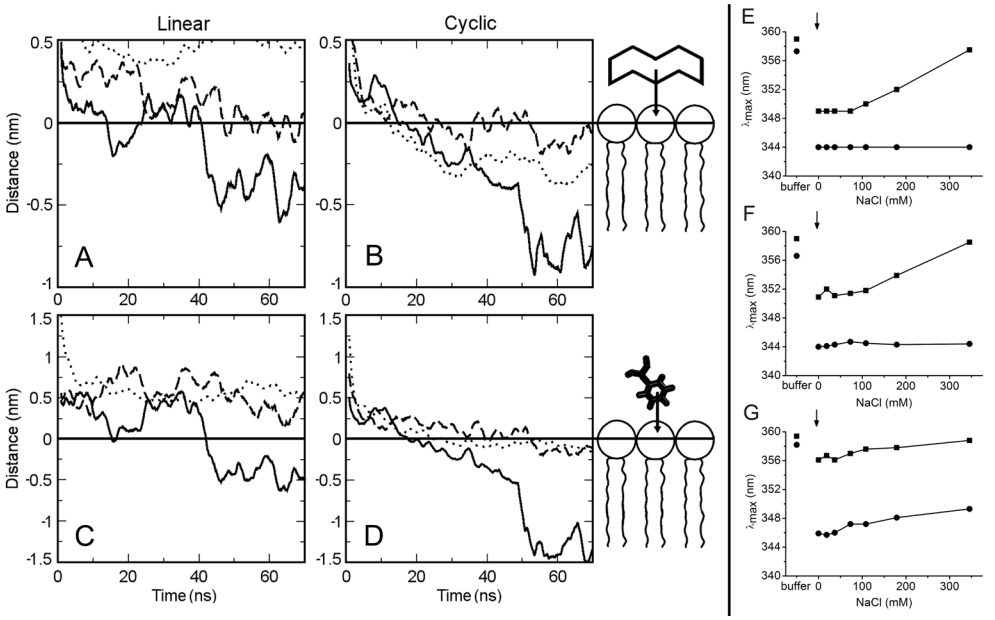

Figure 8. *Depth of insertion of cyclic and linear peptides to PG membranes and peptide environment changes.* (A-D) MD simulations of peptides. Distance between the centre of mass of the peptides BPC193 (A) and BPC194 (B) and the phosphorus atoms of the DPPG bilayer at different P:L ratios: 1:128 (solid line), 4:128 (dashed line) and 9:128 (dotted line). At higher P:L ratios, the distances plotted are the averages of all peptides in the system. (C-D) Distance between the phenylalanine residue and head-group phosphorus atoms. The zero value was taken as the interface boundary (horizontal solid line). (E-G) Peptide environment assessed by Trp fluorescence. Wavelengths of tryptophan fluorescence emission maxima (λ_{max}) of BPC418 (circles, solid line) and BPC417 (squares, dashed line) in buffer (first data point), upon addition of DOPG membranes (arrow), and following titration with NaCl up to 350 mM. The peptide concentration was 2 μM; DOPG was added at different concentrations, yielding (E) P:L = 0.0073, (F) P:L = 0.071 and (G) P:L = 0.88.

Discussion

Molecular mechanism of pore formation

Based on our results, we propose here a molecular-detailed model outlining the differences in mode of action of the cyclic and linear peptides (schematically presented in Fig. 9). Both peptides when present in the aqueous phase are mainly unstructured and have a propensity to bind to (anionic) membrane surfaces. From this point on, the behavior of the two peptides diverges. The cyclic peptide has a larger tendency to fold, enabling it to insert deeper into the membrane interface. Through cooperative interactions, some of these membrane-embedded and folded cyclic peptides cause large perturbations in the bilayer. The linear peptide assumes a more extended conformation and is unable to perturb the membrane substantially. Finally, the cyclic peptide is able to porate the vesicles and cause dye leakage while the linear is unable to do so. The model highlights the structural and partitioning differences of two related peptides with the same sequence but varying antimicrobial activity and thereby point to the critical features required for high antimicrobial activity. The mechanistic model proposed here resembles the one described for gramicidin S in the sense that the cyclic peptide interacts with the membrane, adsorbs to the bilayer surface, folds and gets inserted into the hydrophobic core of the membrane (165). However, for BPC194 the poration has been confirmed experimentally and evaluated

with molecular detail by MD simulations (163). The results of our study provide important clues for rational design of novel cyclic antimicrobial peptides (work in progress).

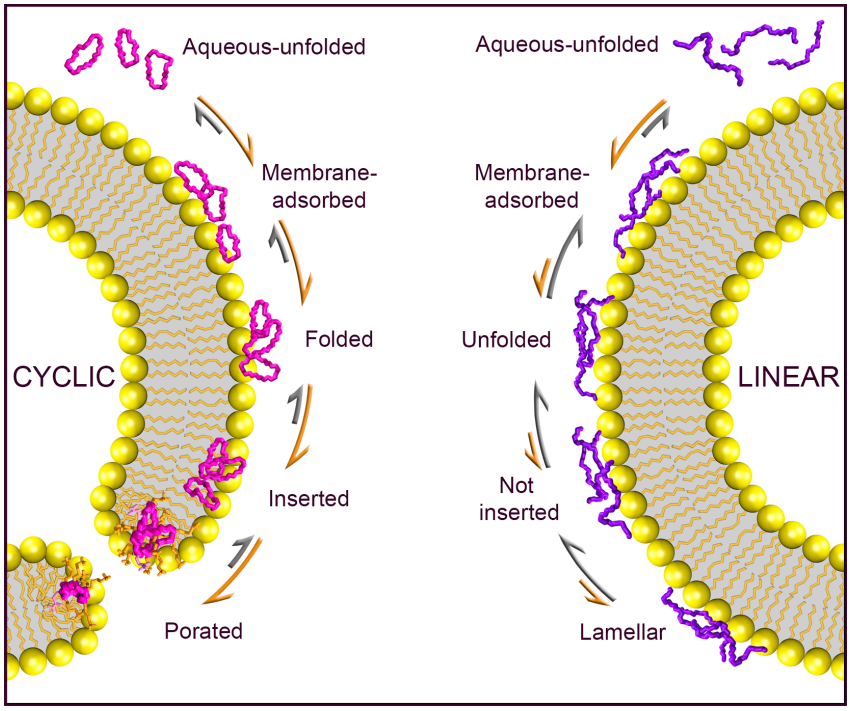

Figure 9. *A schematic view of the mechanism of action*. Left: The cyclic peptide BPC194 (pink); right: the linear analogue BPC193 (purple). The five possible thermodynamic states (stable or metastable) are: aqueous-unfolded, membrane-adsorbed, folded, inserted and porated. The equilibrium is shifted to the right for the cyclic peptide BPC194 and the porated state is the most favorable one. For the linear analogue BPC193, the membrane-adsorbed is the most favored state and the peptide remains unfolded at the surface of the membrane.

Folding and insertion of BPC194 at the membrane interface

The cyclization of the peptides that were studied is not linked to gain of structure in solution. However, upon membrane binding the cyclic peptide assumes a β-structure structure unlike the linear one. For BPC194, the β-structure gives rise to a spatially-symmetric arrangement of the lysine pairs, resulting in an amphipathic-like structure, a conformation that was seen also for gramicidin S (166). The linear peptide has larger conformational entropy, and folding of the backbone to a β-hairpin structure is less favorable than in the cyclic peptide. The structure formation and consequently a deeper insertion of the cyclic peptide was accompanied by local perturbations of the membrane-leaflet and could be linked to its higher charge density, compared to BPC193. The lower charge density of the linear peptide and the formation of peptide clusters may prevent the linear peptide from substantially perturbing or embedding into the membrane. A correlation between high charge density and poration has been previously seen for cyclic analogues of linear antimicrobial peptides (167).

Folding of BPC194 is reminiscent of folding in linear β-hairpin peptides

A very important aspect of this work is the prediction of the peptide folded states at the membrane interface by MD simulations and supported by CD studies. Predicting the correct folds and folding pathways of (poly)peptides, even short ones, remains a challenge. Folding of peptides into β-hairpins has been used as a paradigm for protein folding and a large number of pathways such as zip-in, zip-out and middle-out have been proposed (168-170). Multiple, long simulations and enhanced sampling methods have often been used to probe the folding events. In contrast, in the simulations presented here, folding at the membrane surface is sampled within nanoseconds after the peptide binds to the membrane. While kinetics at membrane interfaces is usually slow, the 'fast-folding' observed here is due to the limited phase-space of the cyclic peptide. For BPC194, only three hydrogen bonds are present in the folded state and due to cyclization, the backbone atoms involved in these hydrogen bonds are close together even in the unfolded state. In water, the peptide is non-structured because the thermal fluctuations are enough to break these three backbone hydrogen bonds that are then compensated by the neighboring water molecules. However, at the membrane interface the backbone atoms (that are always spatially close) form the three hydrogen bonds because of lack of other hydrogen-bond partners and the lower polarity of the membrane leading to the peptide adopting the folded state very fast. The folding is reminiscent of the zip-in model described for linear β-hairpins, whereby the ends first approach each other and then the hydrogen bonds are formed.

Conclusions

In conclusion, there is now compelling evidence that cyclization of certain sequences of membrane-active peptides enhances their antimicrobial performance. In this paper, we analyze the molecular basis for activity in a cyclic antimicrobial peptide, BPC194 by comparing the mechanism of action of the active and inactive analogues. We show that the molecular basis for the enhanced activity resides most likely in the restriction of the number of conformations in the cyclic peptide. We show that it can adopt a favorable orientation towards the membrane and acquire an ordered structure that allows a high charge density and amphipathic arrangement. The latter allows the cyclic peptide to locate itself deeper in the membrane as well as to perturb it more than its linear counterpart. Thus, the alignment of lysine residues on opposite strands leads to a high charge density and an amphipathic arrangement. We propose that these structural and partitioning behavior determined here are related to the difference in poration propensity and thus the antimicrobial activity.

Table 3. Summary of details of all the simulations performed on the cyclic (BPC194) and linear (BPC193) peptides together with secondary structure content during the simulation. The averages and standard errors are reported, standard errors are calculated from the standard deviation between all peptides in all simulations.

P:L Ratio	Code	Peptide	Structure	Force-field	Counter-ions	Electrostatic Regime	Time (ns)	%Non-structured	%β-structure
Water	Wa	Cyclic	Random	43a2	-	RF	50	85	15
	Wb	Cyclic	Random	43a2	6 Cl^-	PME	50	99	1
	Wc	Cyclic	Random	53a6	6 Cl^-	PME	100	77	23
	Average	Cyclic	-	-	-	-	-	87 ± 5	13 ± 5
	Wd	Linear	α-helix	43a2	-	RF	160	72	27
	We	Linear	α-helix	53a6	6 Cl^-	PME	30	96	4
	Wf	Linear	Bend	43a2	-	RF	54	90	10
	Wg	Linear	Bend	43a2	6 Cl^-	PME	50	92	8
	Wh	Linear	Bend	53a6	6 Cl^-	PME	100	94	6
	Wi	Linear	Extended	43a2	-	RF	55	90	10
	Wj	Linear	β-hairpin	53a6	6 Cl^-	RF	100	68	32
	Wk	Linear	β-hairpin	53a6	6 Cl^-	PME	100	66	33
	Average	Linear	-	-	-	-	-	84 ± 4	16 ± 4
1:128	1Ca	Cyclic	Random	43a2	-	RF	80	91	9
	1Cb	Cyclic	Random	43a2	-	RF	50	90	10
	1Cc	Cyclic	Random	43a2	-	RF	50	70	30
	1Cd	Cyclic	Random	43a2	-	RF	50	87	13
	1Ce	Cyclic	Chair	43a2	-	RF	50	76	24
	1Cf	Cyclic	Chair	43a2	-	RF	50	73	27
	1Cg	Cyclic	Chair	43a2	-	RF	50	69	31
	Average	Cyclic	-	-	-	-	-	79 ± 3	21 ± 3
	1La	Linear	Bend	43a2	-	RF	40	99	1
	1Lb	Linear	Extended	43a2	-	RF	100	100	1
	Average	Linear	-	-	-	-	-	100 ± 0	100 ± 0
2:60	2La	2 linear	α-Helix	43a2	-	RF	~200	70	30
	2Lb	2 linear	α-Helix	43a2	-	RF	~200	60	40
4:128	4Ca	Cyclic	Random	43a2	-	RF	100	69	30
	4Cb	Cyclic	Random	43a2	24 Cl^-	RF	100	63	37
	4Cc	Cyclic	Random	43a2	24 Cl^-	PME	40	68	32
	Average	Cyclic	-	-	-	-	-	67 ± 4	33 ± 4
	4La	Linear	Extended	43a2	24 Cl^-	RF	100	~100	~0
	4Lb	Linear	Extended	43a2	24 Cl^-	PME	40	100	0
	Average	Linear	-	-	-	-	-	100 ± 0	0 ± 0
9:128	9Ca	Cyclic	Random	43a2	-	RF	160	63	37
	9Cb	Cyclic	Random	43a2	-	RF	20	62	38
	9Cc	Cyclic	Random	43a2	-	RF	30	61	39
	9Cd	Cyclic	Random	43a2	-	RF	30	73	27
	9Ce	Cyclic	Random	43a2	54 Cl^-	RF	90	70	30
	9Cf	Cyclic	Random	43a2	54 Cl^-	RF	75	76	24
	9Cg	Cyclic	Random	43a2	54 Cl^-	RF	75	65	35
	9Ch	Cyclic	Random	43a2	54 Cl^-	PME	36	66	34
	9Ci	Cyclic	Random	43a2	54 Cl^-	PME	32	72	28
	9Cj	Cyclic	Random	43a2	54 Cl^-	PME	32	69	31
	Average	Cyclic	-	-	-	-	-	68 ± 2	32 ± 2
	9La	Linear	Extended	43a2	-	RF	142	~100	~0
	9Lb	Linear	Extended	43a2	-	RF	100	99	1
	9Lc	Linear	Extended	43a2	-	RF	41	100	0
	9Ld	Linear	Extended	43a2	-	RF	35	98	2
	9Le	Linear	Extended	43a2	54 Cl^-	RF	87	99	1
	9Lf	Linear	Extended	43a2	54 Cl^-	RF	85	98	2
	9Lg	Linear	Extended	43a2	54 Cl^-	PME	24	99	1
	Average	Linear	-	-	-	-	-	99 ± 0	1 ± 0

Acknowledgments

We acknowledge financial support from the Spanish MICINN (MAT2008-04834 to ADC) and MEC (BES-2006-11671 doctoral fellowship to ADC), Netherlands NWO (DS, SJM), SysMo via the BBSRC-funded KosmoBac programme (BP), NWO (Top-subsidy grant 700.56.302 to BP), the Zernike Institute for Advanced Materials (to support the appointment and research of GMC and JTM). We would also like to thank Dr. Gert N. Moll and Dr. Renske W. Hesselink for helpful discussions and assistance.

Chapter 3

The molecular basis for antimicrobial activity of pore-forming cyclic peptides

Anna D. Cirac, Gemma Moiset, Jacek T. Mika, Armağan Koçer, Pedro Salvador, Siewert J. Marrink, Bert Poolman and Durba Sengupta

Published in *Biophysical Journal* (2011) 100: 2422-2431

The mechanism of action of antimicrobial peptides is still poorly understood. To probe the biophysical characteristics that confer activity, we present here a molecular-dynamics and biophysical study of a cyclic antimicrobial peptide and its inactive linear analogue. In the simulations, the cyclic peptide caused large perturbations in the bilayer and cooperatively opened a disordered toroidal pore, 1-2 nm in diameter. Electrophysiology measurements confirm discrete poration events of size 1-2 nm by the cyclic peptide. We also show that lysine residues aligning parallel to each other in the cyclic but not linear peptide are crucial for function. By employing Dual-Color Fluorescence Burst Analysis (DCFBA), we show that both peptides are able to fuse/aggregate liposomes but only the cyclic peptide is able to porate them. The results provide detailed insight on the molecular basis of activity of cyclic antimicrobial peptides.

Introduction

How antimicrobial peptides (AMPs) kill bacteria by interacting with the cell membrane is not fully understood. These peptides, often small and cationic, are secreted into the aqueous phase, usually in an unfolded state and bind quickly to the target membrane, where secondary structure may be induced (24, 127, 130, 131, 171-174). At a certain threshold concentration antimicrobial peptides permeabilize the membrane, either by forming a discrete pore or by disrupting the bilayer structure (25, 28, 40, 127, 130, 132, 133, 167, 173, 175-179). For linear α-helical peptides the barrel-stave and toroidal-shaped model have been proposed as pore structures (29, 33, 73, 127, 167, 171, 180). In addition, a disordered toroidal pore has been proposed for linear antimicrobial peptides from molecular dynamics (MD) simulations (34, 35, 181).

Cyclic AMPs have emerged as good antimicrobial candidates due to their robust secondary structure and high activity (165, 182, 183). Gramicidin S, a cationic decapeptide, is one of the best studied cyclic AMPs (165, 182, 184-186) and has been shown to permeabilize bilayers but not to stabilize well-defined pores (187). MD simulations in DMSO solution (188) and with DMPC bilayers (189) have shown that gramicidin S has a relatively rigid backbone conformation, but no poration events were seen in the simulations. Arginine-rich cyclic peptides have been shown to assemble into nanotubes and extrude the bilayer in MD simulations (190). In general, the molecular details of the action of cyclic AMPs, such as whether these short peptides can open and stabilize pores, as well as the molecular basis for their increased activity is still unclear.

The focus of our work is a cyclic antimicrobial peptide, BPC194 that was chosen as the best candidate from a library of *de novo* synthesized cyclic peptides (139, 140). The cyclic peptide shows a high antimicrobial activity to different plant pathogenic bacteria (*Erwinia amylovora*, *Pseudomonas syringae* and *Xanthomonas vesicatoria*). Here, we present a combined MD and biophysical study of the cyclic peptide interacting with anionic lipid bilayers to understand its mechanism of action. The linear analogue BPC193, which is not active, has also been studied allowing us to reveal the functionally - important structural characteristics. We show that the only cyclic peptide is able to form pores in anionic membranes in line with its enhanced antimicrobial activity. The pore size was validated by three independent approaches - MD simulations, electrophysiology and DCFBA fluorescence imaging. We further extract the functionally - relevant structural properties and show the importance of charged residues in forming and stabilizing pores. Finally, an intermediate state was identified which is close to the real transition state during pore formation.

Materials and methods

Molecular Dynamics Simulations

System set-up. MD simulations were performed for systems containing 9 peptides (BPC194 c(KKLKKFKKLQ); BPC193 KKLKKFKKLQ) and a fully solvated DPPG (dipalmitoyl-phosphatidylglycerol; anionic lipid) bilayer. The simulations were carried out at a peptide:lipid (P:L) ratio of 9:128 for both cyclic and the linear analogues together with 6000~8000 water molecules and 128 K^+ as counter-ions for anionic lipids. The peptides were initially placed in the water phase at a distance of 1.5-2.3 nm from the membrane surface. The initial structure of the peptides was modeled using the leap module of AMBER 9 (146), as unstructured peptides with no intra-molecular hydrogen bonds. Multiple simulations were run from different initial random velocity distributions (Table 1).

Set-up for transition state simulations. A snapshot at 109 ns was taken from the simulation 9Ca (Table 1), as an example of the transition state. From this system, ten simulations were performed with different initial velocity distributions. The transition state was also modified to substitute the cyclic peptide for the linear analogue. This substitution was made by cutting the peptide bond between N-terminal residue and the C-terminal residue, as well as adding the corresponding missing atoms. The system was simulated as a linear peptide but with the initial conformation of the cyclic peptide (so called hairpin conformation). Further, a harmonic potential was applied to the linear peptide to pull the N-terminal from C-terminal to obtain a random-coil conformation in the transition state. For the modified systems, a minimization was carried out followed by an equilibration with constraints on phosphorus atom and water molecules to keep the position of the transition state. Ten simulations were run for the hairpin conformation and two of the random-coil conformation by changing the starting random velocities.

Analysis. The secondary structure of the peptides was calculated by using the DSSP code (159). For the cyclic peptide, the N-terminal residue K^1 and C-terminal residue Q^{10} that are present in the turn region, were neglected while calculating the secondary structure. The structural properties were then calculated from the average number of residues involved in each secondary structural feature along the simulation. The total β-structure is reported as the sum of β-sheet and β-bridge and the total non-structured as the sum of coil bend and turn. The persistence of structure over time was calculated as the percentage of time the β-structure was present.

Simulation parameters. All MD simulations were performed with the GROMACS software package (147). The peptide and peptide–solvent interactions were described by the GROMOS force-field 43a2 (148). The force-field for DPPG lipids was optimized from DPPC (150) and POPG lipids (151), compatible with the GROMOS96 parameters. The choline head-groups were replaced by glycerol from the POPG force-field, and the tail parameters were taken from the DPPC force-field. The parameters were then optimized to achieve an area per lipid consistent with experiment (152). The equilibrated DPPG bilayer had a thickness of 3.54 ± 0.05 nm and an area per lipid of 0.69 ± 0.01 nm^2. The force-fields have been parameterized for use with a group-based twin range cut-off scheme (using cutoffs of 1.0/1.4 nm and a pair-list update frequency of once per 10 steps), including a reaction field (RF, (154)) correction with a dielectric constant of 78 to account for the truncation of long-range electrostatic interactions. The water was modeled using the SPC model (155). The simulations were performed using periodic boundary conditions and a time step of 2 fs was used. The temperature was weakly coupled (coupling time 0.1 ps) to T = 320 K, using the Berendsen thermostat (157). The pressure was weakly coupled (coupling time of 1.0 ps and compressibility of 4.5×10^{-5}), using a semi-isotropic coupling scheme in which the lateral (P_l) and perpendicular (P_z) pressures are coupled independently at 1 bar, corresponding to a tension-free state of the membrane. The simulation setup is similar to that used in previous studies of peptide-membrane interactions (34, 35, 42). For a general review on MD studies of peptide-membrane interactions see the work of Mátyus *et al.* (158).

Biophysical Characterization

Electrophysiology measurements. A planar lipid bilayer setup was used as described below. The bilayer was formed by painting with 1 μl of a 20 mg/ml solution of DOPG lipid (1,2-dioleoyl-sn-glycero-3-phosphatidylglycerol, Avanti Polar Lipids) in n-decane (Aldrich) across the 250 μm opening of a Delrin cup that separates two solution-filled compartments, designated *cis* and *trans* (191-193). Both compartments were filled with a buffer solution consisting of 10 mM HEPES (2-(4-(2-hydroxyethyl)-

1-piperazinyl)-ethanesulfonic acid, (Roche Diagnostics GmbH), pH 7.0, containing 150 mM NaCl (Merck), further referred to as buffer A. The planar bilayers were stable at the voltages applied during the experiment. The transmembrane current (I_m) under different applied potentials (V) was monitored, using an integrating Bilayer Clamp Amplifier BC-535 (Warner Instruments). Currents were filtered through an 8-pole low-pass Bessel Filter LPF-8 (Warner Instruments) and digitized using Clampex 10.2 software (Axon Molecular Devices). Membrane conductance (G_m) events were identified as $G_m = I_m / V$ and analyzed with the Clampfit software (Axon Molecular Devices) (194). The peptides at 3 and 10 μM were added to the cis side of the planar lipid bilayer and stirred for 1 minute without applying voltage. In some cases a voltage of ± 40 mV was applied to pre-activate the peptide and decrease the time needed to observe activity. Subsequently, the conductance was recorded at different voltages ranging from 0 to ± 50 mV. A total of 10 traces were recorded each with freshly prepared DOPG membranes. The pore diameter was estimated by an extended version of the model proposed by Hille (66, 195) given by (196):

Eq. 1
$$d = \frac{\rho g}{\pi}\left(\frac{\pi}{2} + \sqrt{\frac{\pi^2}{4} + \frac{4\pi l}{\rho g}}\right)$$

where, d is the diameter of the pore, ρ is the resistivity of the buffer, g is the measured conductance and l is the length of the pore. The resistivity of the buffer A was assumed to be 80 Ωcm (66). The length of the pore equals the membrane thickness and was assumed to be 3.5 nm.

Dual-color fluorescence burst analysis. In the DCFBA experiment, liposomes were labeled with two, spectrally non-overlapping fluorescent probes (37). One probe was incorporated in the phospholipid bilayer, while the other filled the aqueous interior of the liposome. By using a dual-color laser-scanning microscope, we monitored membrane disrupting effects at the single liposome level. The results are presented in the DCFBA profiles as the population-distribution histogram of liposomes with a given internal marker concentration, C_i, given by:

Eq. 2
$$C_i = \frac{\int_{t_1}^{t_2} I_{SM}\,dt}{\left(\int_{t_1}^{t_2} I_L\,dt\right)^{\frac{3}{2}}}$$

where, I_L is the fluorescence of the lipid marker and I_{SM} is the fluorescence of the internal size marker in each fluorescence burst (38).

The average fluorophore population, P^{fluor}_{av}, is given by:

Eq. 3
$$P_{av}^{fluor} = \frac{\int_{t_1}^{t_2} \frac{I_{fluor}}{N_{peaks}}\,dt}{\int_{t_1}^{t_2} \frac{I^0_{fluor}}{N^0_{peaks}}\,dt}$$

where, I_{fluor} is the fluorescence intensity of each peak above a given threshold for every P:L ratio, I^0_{fluor} is I_{fluor} at P:L = 0, N_{peaks} is the number of peaks at every P:L ratio and N^0_{peaks} is N_{peaks} at P:L = 0. The relative population of the internal size marker, P^{SM}_{rel}, is given by:

Eq. 4

$$P_{rel}^{SM} = \frac{P_{av}^{SM}}{P_{av}^{membr}}$$

where, P^{SM}_{av} is the average internal marker population and P^{membr}_{av} is the average membrane fluorophore population.

DCFBA assay. Liposomes were prepared as described by van den Bogaart (37). Briefly, DiD (1,1'-dioctadecyl-3,3,3',3'-tetramethylindodicarbo-cyanine perchlorate; Invitrogen) labeled-liposomes were prepared by rehydration of a dried lipid film in the presence of glutathione (GSH)-labeled Alexa Fluor 488 (AF488, Invitrogen) as a aqueous phase marker in buffer A. The DiD/DOPG molar ratio was 1:12,000. Subsequently, the liposomes were extruded 11 times through a 200 nm polycarbonate filter (AVESTIN, Canada). The liposomes were separated from the non-encapsulated fluorophores by centrifugation (20 min, 270,000 × g, 20°C) and resuspended in buffer A to a final concentration of 5 mg/ml DOPG. Fluorescence burst analysis was carried out on a laser-scanning confocal microscope (197), as described by van den Bogaart (37, 133, 198). Different amounts of peptide were added to 64 μg/ml DOPG liposomal solutions, yielding final peptide-lipid ratios from 1/52 to 5/1. The samples were equilibrated for 10 minutes at room temperature after each addition of peptide. The fluorescence bursts were measured for 10 min. To estimate the size of the pore, a size marker was encapsulated inside the DiD-labeled vesicles, i.e., 10 kDa dextran labeled with fluorescein (Invitrogen).

Results and discussion

The cyclic peptide causes large perturbations in DPPG bilayers

To probe the poration propensity of BPC194, we performed simulations of the peptides interacting with a DPPG bilayer at a P:L ratio of 9:128. DPPG bilayers were chosen since the peptide is antimicrobial (characterized by anionic lipids) with low hemolytic activity (characterized by zwitterionic lipids). The time course of a particular simulation (Table 1, 9Ca) is depicted in Figure 1A, but similar behavior was observed in the remaining simulations (Table 1, 9Cb-Cg). The peptides were initially placed in the water layer close to the bilayer (0 ns) and subsequently bound fast (~5 ns) to the membrane interface. During the simulation, most of the peptides remained bound at the interface though, a few peptides were able to cooperatively perturb the outer leaflet and consequently insert deeper (Figure 1A, 16-60 ns). In the perturbed state, the positively-charged residues of the peptides interacted with the closest head-group moieties and pulled them, together with some water molecules, into the core of the membrane. The peptide-free inner leaflet was also affected by the action of the cyclic peptide bound on the outer leaflet. This behavior was seen repetitively during the simulation and was usually followed by a relaxation of both leaflets. Occasionally, a much larger perturbation occurred (109 ns), characterized by a decrease in the local lipid-chain order (Figure 2A). At this point, the perturbation was caused by a cooperative effect of three peptides, one of which adopted a transmembrane-orientation with its glutamine residue close to the centre of the hydrophobic core. In this position, the glutamine residue interacted with some head-group atoms of the inner leaflet. During this perturbation, a few water molecules were able to cross the membrane. However, the inner leaflet relaxed again and the orientation of the glutamine residue reverted back to the interface (Figure 1A, 115 ns). Only smaller perturbations of the membrane were observed in the remainder of the simulation.

Table 1. Overview of the MD simulations performed.

Code	System	Electrostatic Regime	Counter-ions	Time (ns)
9Ca	Cyclic	RF	-	160
9Cb	Cyclic	RF	-	20
9Cc	Cyclic	RF	-	30
9Cd	Cyclic	RF	-	30
9Ce	Cyclic	RF	54 Cl^-	90
9Cf	Cyclic	RF	54 Cl^-	75
9Cg	Cyclic	RF	54 Cl^-	75
9La	Linear	RF	-	140
9Lb	Linear	RF	-	100
9Lc	Linear	RF	-	40
9Ld	Linear	RF	-	35
9Le	Linear	RF	54 Cl^-	90
9Lf	Linear	RF	54 Cl^-	85

The cyclic peptide can form a disordered toroidal pore

In our previous simulations of AMP action (34, 35), the first event during pore formation was the bridging of the two leaflets by a peptide. Although such an orientation of the peptides was seen in simulation 9Ca (Figure 1A, 109 ns), it did not lead to a porated state. Nevertheless, we expect this highly perturbed state to be an intermediate, mimicking the transition state toward pore formation. To sample the conformational space around this so-called "transition state", ten simulations were set up; the velocities in the system were varied to provide a different direction on the potential energy surface that may lead to pore formation. Indeed, a pore was formed in six out of ten simulations; for details see Table 2 (C1-10). The mechanism of the pore formation is depicted in Figure 1B, using C9 as a representative of all simulations. The first time point (0 ns) was taken as the transition state from which the simulation was started (cf. Figure 1A, 109 ns). Water molecules readily inserted into the bilayer and finally after 1~2 ns, some water molecules crossed the bilayer to open a water channel. Head-group atoms of both leaflets moved inside the membrane core to line the water channel. From then on, the pore remained open and the lipid head-groups of both leaflets rearranged to form a disordered toroidal-shaped pore around 25 ns. The size of the water channel fluctuated both in time as well as along the direction of the pore axis, ranging between ~1 and 2 nm (see Figures 1B, 65 ns and Figure 2B-C). The pores formed in our simulations could be characterized as disordered toroidal pores with the peptides residing in different positions and orientations. In all cases, the pore was stabilized by three peptides; a dimer and a monomer, with the remaining peptides lying close to the pore. No peptide translocation was seen in the nanosecond time regime of the simulations.

Table 2. Overview of the ten simulations starting from the transition state with the cyclic peptide (C1-C10) and for the in-silico modified linear peptide (L1-L10) (DTP: disordered toroidal pore; HG: head-group atoms).

Code	Open Water Channel	Features	Remarks	Outer Leaflet Fluctuation	β-structure	No. of peptides in pore	Time (ns)
C1	2-3 ns	DTP	Stabilization HG 20 ns	± 0.50	29.9	3	40
C2	4 ns	DTP	Stabilization HG 12 ns	± 0.50	34.5	3	40
C3	4 ns	DTP	Stabilization HG 17 ns	± 0.52	36.7	3	40
C4	-	No pore	Perturbations afterwards	± 0.46	34.2	-	40
C5	1 ns	DTP	Stabilization HG 20 ns	± 0.54	34.2	3	40
C6	-	No pore	Perturbations afterwards	± 0.40	34.1	-	40
C7	-	No pore	Perturbations afterwards	± 0.48	32.8	-	40
C8	-	No pore	Perturbations afterwards	± 0.43	33.1	-	40
C9	1-2 ns	DTP	Stabilization HG 10 ns	± 0.59	33.4	3	125
C10	1-2 ns	DTP	Stabilization HG 10 ns	± 0.55	36.6	3	170
L1	25 ns	DTP	Stabilization HG 45 ns	± 0.47	33.2	1	50
L2	-	No pore	Relaxation	± 0.39	21.9	-	50
L3	-	No pore	Large Perturbations	± 0.48	16.1	1	50
L4	-	No pore	Relaxation	± 0.41	20.7	-	40
L5	-	No pore	Relaxation	± 0.38	19.8	-	40
L6	-	No pore	Relaxation	± 0.40	22.3	-	40
L7	20-30 ns	DTP	Stabilization HG 60 ns	± 0.54	22.2	1	150
L8	-	No pore	Relaxation	± 0.43	18.7	-	40
L9	-	No pore	Relaxation	± 0.45	26.7	-	60
L10	3-4	DTP	Stabilization HG 45 ns	± 0.48	17.0	1	150

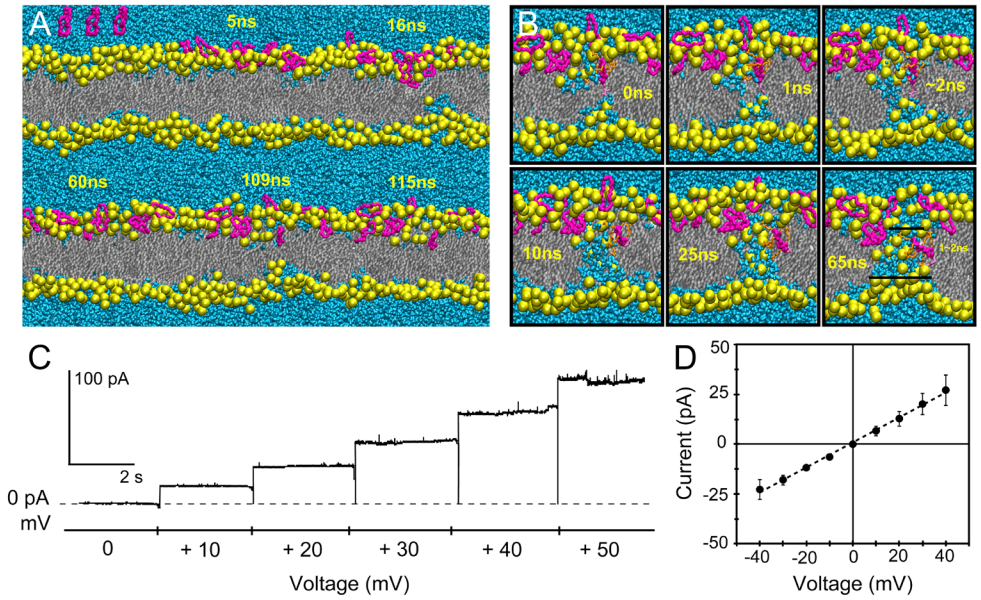

Figure 1. *The cyclic peptides cause large fluctuations in the membrane upon binding and can form a disordered toroidal pore.* (A) Time course of the simulation 9Ca. At 0 ns all peptides were placed close to the bilayer and they bound within 5 ns. The first perturbation of the inner leaflet was seen at 16 ns, when some lipids were pulled into the bilayer due to the action of the cyclic peptide. The highest perturbation was at 109 ns and involved three peptides, one of which adopts a transmembrane orientation. The inner leaflet relaxed at 115 ns. (B) The snapshot of the transition state (Fig. 1, 109ns) was taken as the starting structure (0 ns). An increase of the number of water molecules inserting into the bilayer was followed by the opening of a water channel (1-2 ns) and insertion of lipid head-groups further inside to form a toroidal-shaped pore (10-25 ns). A stable toroidal-shaped pore was seen at 65 ns. The head-groups are depicted in yellow spheres. The peptide backbone is shown in pink, lipid tails in grey and water molecules in cyan. To clarify the briding of the two leaflets from transition state and on, the lysine residues (orange) and the glutamine residue (light pink) are shown only for the peptide in a transmembrane orientation. (C) Current traces recorded after the addition of BPC194 peptide to DOPG membranes. (D) I-V curves plotted from seven independent current trace recordings of BPC194.

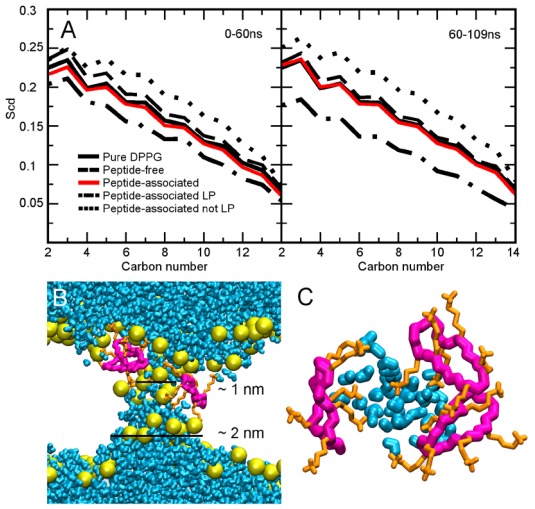

Figure 2. (A) *Lipids involved in the large perturbation show a decrease in their lipid-order parameter*. Lipid-tail order parameters of the Sn2 chain obtained from simulation C9a. The order parameters are plotted for pure DPPG (solid black line) as a reference, peptide-free leaflet (dashed line) and peptide-associated leaflet (solid red line), and the peptide-associated leaflets are divided between LP (Large Perturbation, dashed-dotted line) and not LP (not Large Perturbation, dotted line). The left plot shows the first simulation amongst 0-60 ns, where the peptides interacts and bind to membrane surface, and right plot the insertion till the largest perturbation occur (60-190 ns). (B-C) *Pore features.* (B) An example of the disordered toroidal pore (simulations C9). The peptides not directly involved in the pore are not shown for clarity. (C) The top view of the pore. The phosphorus atoms are colored in yellow spheres, the peptide backbone in pink and the lysine side-chain in orange. The water molecules that are present in the channel are depicted in cyan.

Electrophysiology revealed that pore formation is specific for cyclic peptides

To monitor the pore formation of BPC194 ion fluxes in a planar lipid bilayer setup were measured. An example of a current trace recorded upon addition of BPC194 to the *cis* compartment of the planar lipid bilayer setup is shown in Figure 1C. A voltage-dependent conductance was observed implying that a pore or channel was formed/opened. These conductance events were stable during the course of the recording, pointing towards the formation of discrete pores. The average I-V curve of all independent recordings is plotted in Figure 1D. The pore has an average unitary pore conductance of 0.61 ± 0.12 nS. Since the I-V curve is symmetric the pores formed by BPC194 are not ion selective. The diameter of the pore was estimated (see Eq. 1 from Materials and methods) to range between 1.5-1.9 nm. At higher peptide concentrations, we also observed higher overall conductance that was a multiple of the unitary conductance, reflecting the higher probability of pore formation. The same increase in probability of pore formation was observed on applying voltages higher than ± 50 mV. However, these extra poration events were transient with shorter dwell times.

The linear peptide does not perturb or porate DPPG bilayers substantially

Simulations of the linear analogue interacting with DPPG bilayers were performed under conditions identical to the cyclic peptide (Table 1, 9La-Lf). A typical time course of the simulation is depicted in Figure 3A. Upon binding, the linear peptides somewhat perturb the membrane, albeit much less than the cyclic ones. Larger perturbations leading to a transition state were not seen in any of the simulations with the linear peptide. Though the average thickness of the bilayer is similar for the two peptides (3.7 ± 0.1 nm for the linear and 3.6 ± 0.1 nm for the cyclic peptide), the perturbations in the outer leaflet are substantially higher when the cyclic peptide is attached. The fluctuations in the outer leaflet, calculated as the deviation of the phosphorus atoms of the head-groups from their center of mass are ± 0.44 nm for the cyclic peptide in comparison to ± 0.29 nm for the linear peptide. These results were supported by the electrophysiology measurements, in which the linear analogue did not show pore formation or ion flux through the membrane at the same voltage regime in which the cyclic peptide formed pores (Figure 3B).

Structure-Function relationship of the cyclic peptide

To investigate the relation between secondary structure and the ability of the peptides to stabilize a pore, we clustered the peptides depending on how far they lie from the pore and the role they play in stabilizing it (Figures 3A and 3B). Three classes of peptides were distinguished: those within the rim of the pore (distance 0.3 nm from the center of the pore, region 1), those lying at the mouth of the pore (within 0.3-1.5 nm, region 2) and those not involved in the pore (further away than 1.5 nm, region 3; Table 3). Peptides in region 1 adopt a stable secondary structure (40% β-structure) in all simulations where a pore is formed (six simulations). Although the number of residues involved in secondary structure varied between the three peptides, all three showed the longest persistence of β-structure over time (97%). The peptides belonging to region 2 also exhibited a high β-structure (39% for peptides of this region), but the percentage fluctuated over time and the persistence of β-structure was 89%. Finally, the peptides in region 3 exhibited multiple folds and adopted different conformations showing only 18% β-structure for the individual peptides.

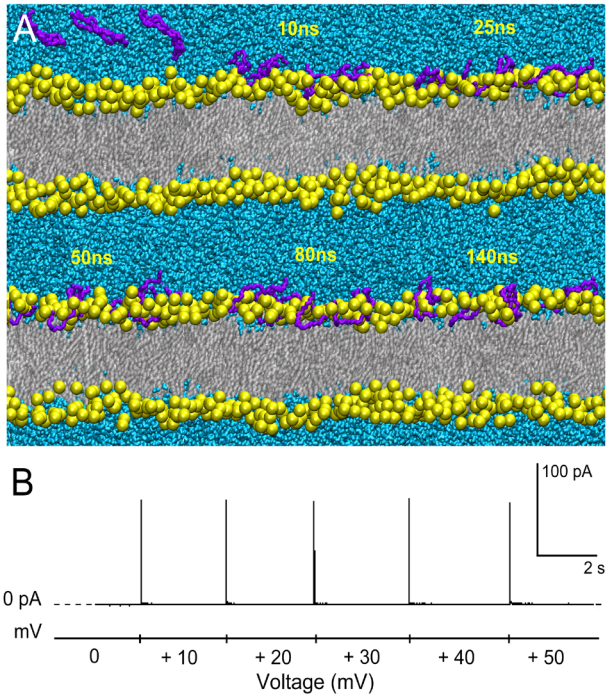

Figure 3. *The linear peptides do not induce fluctuations in the membrane.* (A) Time course of the simulation L9a. Initially (0 ns), all linear peptides were placed close to the outer leaflet. Within 10 ns all peptides bound and remained at the membrane interface. No large perturbations were seen along the simulation (25-140 ns). The head-groups of DPPG are depicted in yellow spheres, the peptide backbone in violet and lipid tails in grey. (B) Current traces recorded after the addition of BPC193 peptide to DOPG membranes.

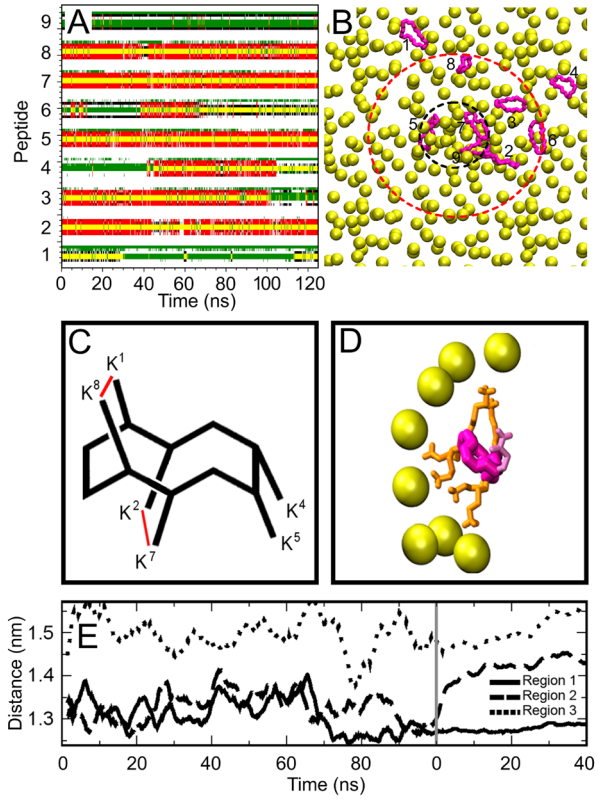

Figure 4. *Secondary structure related to the distance at the rim of the pore and its function.* (A) DSSP plot of the secondary structure of all peptides for simulation C9, taking the transition state as the 0 ns time point. (B) Top view of the pore showing the positions of the nine peptides. The phosphorus atoms of the outer leaflet are depicted as yellow spheres and the backbone is colored in pink. Region 1 peptides are those involved in the pore (within dashed black line). The peptides that remain at the rim of the pore (region 2) are delimited by the red dashed line. The peptides furthest from the pore (region 3) are outside the circles. (D) Parallel arrangement of lysine residues in the β-structure (D) An example of the aligned lysine residues stabilizing the lipid curvature in the porated state (side-view of the pore). (E) The average distance between lysine residues K^1-K^8 and K^2- K^7 (plotted as a sum) for peptides in regions 1, 2 and 3. The time scale to the left of the grey line refers to simulation 9Ca (before transition state formation 0-109 ns). The time frame to the right is an average for all simulations (C1-10) where a pore was formed with the starting time 0 ns being the putative transition state.

Table 3. *Secondary structure and distance from the centre of the pore for the peptides belonging to the three regions*. The values reported are an average calculated from all simulations where a pore was formed. The time of persistence of β-structure (see Materials and Methods) is also reported. The standard errors reported are calculated from the standard deviation, between all peptides in all simulations.

Region	Peptide	Distance (nm)	% Coil	% β-structure	% Bend	% Turn	% Time of β-structure
1	5	0.09 ± 0	20.7	45.7	10.3	23.4	94.8
	7	0.09 ± 0	19.6	47.9	8.4	24.1	98.4
	9	0.09 ± 0	25.2	26.2	45.4	3.4	97.7
	Average	0.09 ± 0	22 ± 1	40 ± 6	31 ± 11	17 ± 6	97 ± 1
2	2	0.30 ± 0.05	29.9	43.8	2.8	23.6	92
	3	0.78 ± 0.15	24.8	42.8	12.0	20.4	92.6
	6	1.10 ± 0.15	36.0	32.2	14.2	16.5	91.7
	8	1.50 ± 0.23	30.0	39.1	10.9	20.0	78.1
	Average	0.9 ± 0.2	30 ± 2	39 ± 2	10 ± 2	20 ± 1	89 ± 3
3	4	1.59 ± 0.30	38.5	28.1	15.3	18.2	62.5
	1	2.07 ± 0.25	45.4	8.6	30.9	15.1	33.6
	Average	1.8 ± 0.2	42 ± 2	18 ± 7	23 ± 6	17 ± 1	48 ± 10

The apparent importance of the β-structure for stabilization of the pore can be rationalized by considering the relative orientation of the lysine residues. As illustrated in Figure 4C, the β-structure gives rise to a parallel arrangement of the lysine pairs (K^1-K^8 and K^2-K^7) on the two strands that, presumably, facilitates the interaction of the lysines with the lipid head-groups in the curved geometry of the pore (Figure 4D). The distances between the lysine pairs K^1-K^8 and K^2-K^7 (plotted as a sum of the two values) for the three regions of the peptides is shown in Figure 4E. When the peptides are bound to the membrane (0-109 ns, till grey line), the value fluctuates for all three clusters of peptides. However, once the transition state is reached and later when a pore is opened (beyond grey line), the distance between the lysine pairs in the peptides in region 1 remained low, consistent with their high persistence of secondary structure. The value for the peptides in region 2 was also low at the transition state but increases as the pore relaxes. The peptides in region 3, which were not involved in the pore, showed the largest distance between the lysine pairs along the simulations.

Transition state alchemy: Why the linear peptide cannot stabilize pores

To test whether the β-strand conformation is indeed linked to activity, we repeated the simulations from the transition state with the linear peptide by in-silico alchemy, i.e. removing the peptide bond between the first and last residue. The results of these simulations are summarized in Table 2 (L1-10). In seven of the ten simulations, the bilayer relaxed and the linear peptide moved back to the interface. In the remaining three simulations, a water channel eventually opened. The time course of one of the poration events (L7) is depicted in Figure 5. Although we observed that the linear peptide is also able to stabilize a water pore (starting from the perturbations caused by the cyclic peptide), the pore differs from the pore formed in the presence of the cyclic peptides: i) Only one of the three peptides involved in the transition state remained embedded near the central pore region; and ii) The lipid head-groups did not line the pore as clearly as in the case of the cyclic peptide. In most of the simulations, the average percentage of β-structure dropped to a value around 20%, compared to > 30% for the cyclic peptide (cf. Table 2, C1-C10). In the simulations in which a pore was formed, the peptide in closest vicinity of the pore preserved a somewhat higher percentage of β-structure (~28%). Two additional unbiased transition state simulations of the linear peptide in its native random-coil conformation were

performed. We found that, in the extended conformation, the peptide could not stabilize even those head-groups that were already inserted into the membrane, and the bilayer recovered immediately from the large perturbations induced by the cyclic peptide. An overview of the poration features of the cyclic and linear peptide is presented in Table 4.

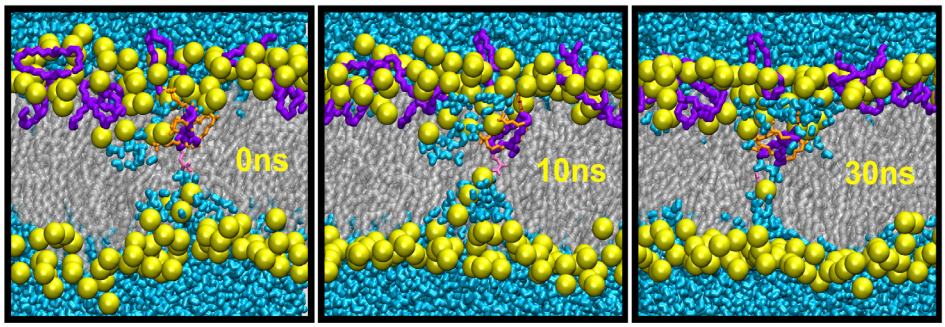

Figure 5. *The linear peptides cause large perturbations from the in-silico modified transition state*. Time course of a transient pore formed by a linear peptide (simulation L7). The time point 0 ns corresponds to the transition state taken from the simulation with the cyclic peptide. After 10-30 ns, large perturbations were seen and a few water molecules crossed the bilayer. Please note that in most simulations the bilayer relaxes and such large perturbations are not seen.

Table 4. Summary of pore features created by the cyclic peptide and the linear peptide.

Pore features	Cyclic peptide	Linear peptide
Pore propensity	High	Low
Pore diameter	1-2 nm	< 1 nm
Number of peptides inside	3	1
% β-structure	34 %	21 %
Outer leaflet deviation	± 0.55	± 0.48
Number of porated states	6/10	3/10
Number of lipid head-groups	8-11	6-10
Number of water molecules	100-123	76-84
Formation time	1-4 ns	3-30 ns

DCFBA reveals the mechanism of action on liposomes

Figure 6 shows the result of DCFBA experiments carried out with BPC194 and BPC193 in the presence of DiD-labeled DOPG vesicles filled with the internal marker, GSH-AF488. In such an experiment, poration of liposomes reduces the internal marker concentration and the DCFBA population histogram shifts to lower concentration values. In contrast, membrane fusion or aggregation results in a decrease in the number of detected liposomes, which is observed as a decrease in the area of the population histogram. For the cyclic analogue, at low P:L ratios (≤ 1), the number of liposomes decreased, which is indicative of fusion or aggregation (Figure 6A). The membrane fusion/aggregation activity was confirmed by confocal imaging of the liposomes and was accompanied by leakage of the internal marker (Figure 6A, panel β, P:L ratio of 0.3). Intriguingly, adding an excess of peptide (P:L ratios of 1-5) such that the vesicles are completely shielded by peptide preventing aggregation/fusion, the number of detected liposomes was restored and the concentration of molecules inside the liposomes dropped (Figure 6A, panel γ), which is indicative of pore formation. The linear peptide, BPC193 also caused membrane fusion or aggregation but at higher P:L ratios than its cyclic counterpart (Figure 6B). This was confirmed by confocal imaging at the highest concentration of the linear peptide (P:L ratio of 5) where large membrane aggregates were formed without loss of the internal marker, indicative of the lack of pore formation (Fig. 6A, panel δ).

To present the overall data comprehensively, the average membrane fluorescence per liposome and the relative concentration of the internal marker are plotted in Figures 5C and 5D (see Materials and Methods for more details). For BPC194, the average membrane fluorescence peaked at a P:L ratio of 0.5-1, while the relative concentration of the internal marker already dropped to zero at a P:L of 0.3. This behavior confirms the leaky fusion/aggregation action of the cyclic peptide. On the other hand, for BPC193, an increase in the membrane population and constant relative internal marker population was seen, thereby corroborating its non-leaky fusion/aggregation propensity.

Using the DCFBA technique and encapsulating bigger internal markers we could estimate the size of the pore. The smallest molecule that did not leak out was the 10 kDa Dextran-Fluorescein (Figure 7A) with a dimension of 2.1 nm (shortest axis measured assuming is a prolate ellipsoid), while GSH-AF488 leaked out with a diameter of ~1.7 nm (Figure 7B, measured by FCS). We conclude that the size of the pore is between 1.7 and 2.1 nm.

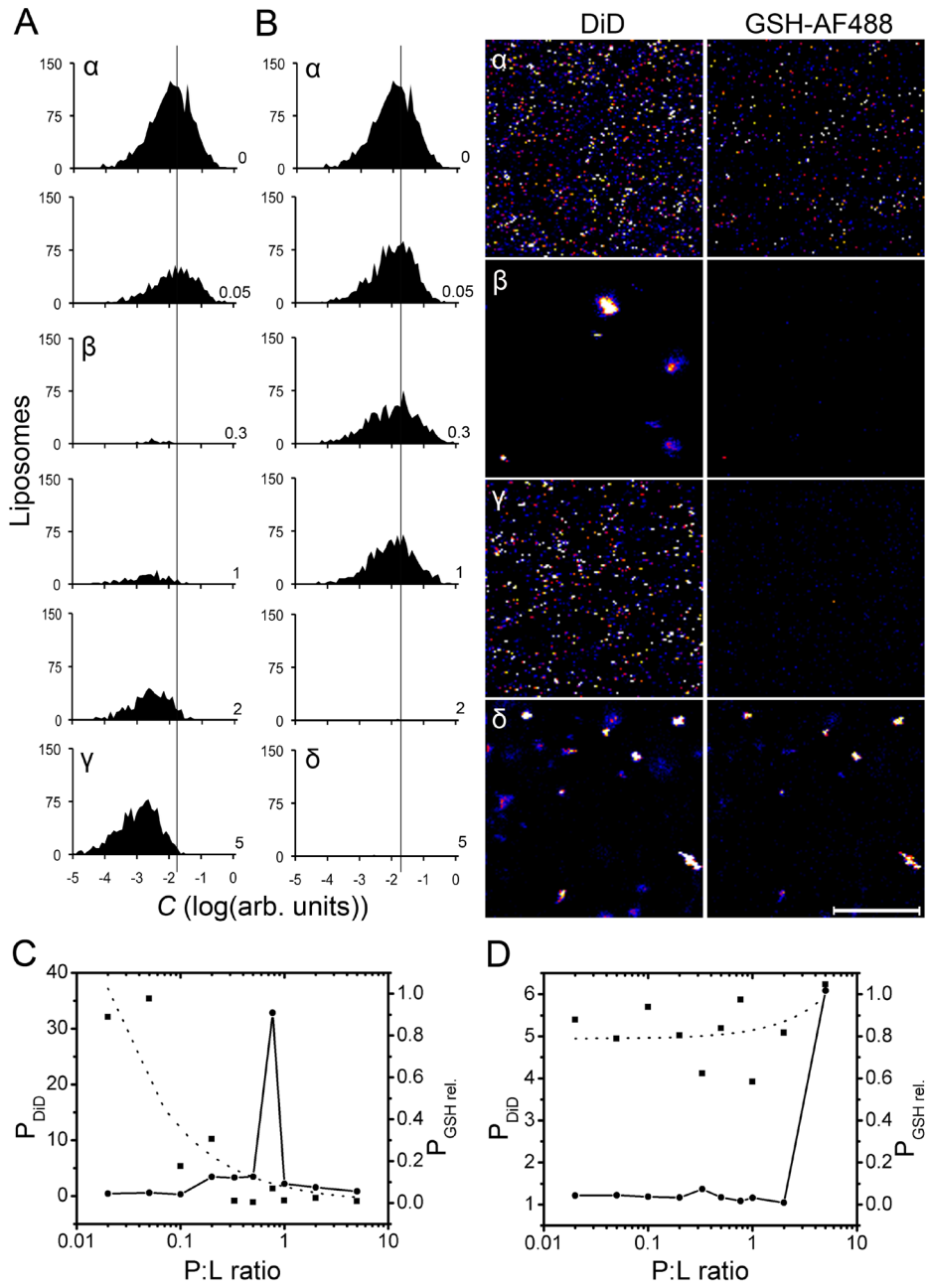

Figure 6. *Mechanism of action of peptides studied by DCFBA.* (A-B) DCFBA population histograms of BPC194 and BPC193, respectively. The numbers in the bottom right of the graphs refer to P:L ratios. The y-axis corresponds to the number of liposomes, the x-axis to the arbitrary marker concentration inside the liposomes. **Top right panels:** Confocal images of vesicles probed in the experiments shown in (A) and (B), indicated by Greek symbols (α-δ); left panels: membrane probe, DiD; right panels: internal marker probe, GSH-AF488. The scale bar is 20 μm. (C-D) Average DiD population (circles, solid line) and relative GSH population (squares, dotted line) for the cyclic and the linear peptide, respectively.

A

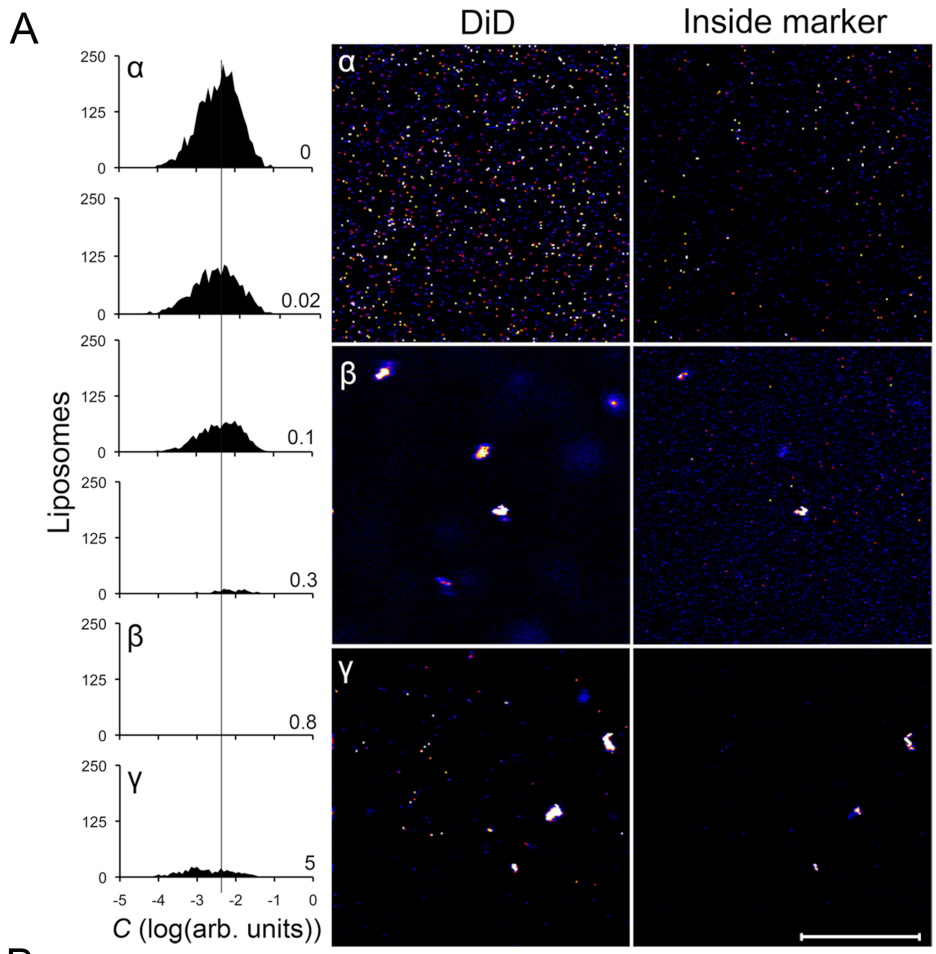

B

Molecule	Mw (Da)	Calculated Diameter[1] (nm)	Diameter measured by FCS[2] (nm)	Other estimated Dimension
GSH–AF488	1027	1.35	1.67 +/- 0.25	n.d.
10 kDa Dextran-Fluorescein	~ 10 000	2.86	5.35 +/- 0.8	2.12 x 8.48[3]

Figure 7. *Cyclic and linear peptides fuse or aggregate liposomes.* (A) DCFBA experiment of the peptide BPC194 with DiD-labeled vesicles and 10 kDa Dextran-Fluorescein as internal marker. Left: BPC194 induces liposome fusion/aggregation without leakage. Right: Confocal images of vesicles probed in the DCFBA experiments. Panel α represents the intact vesicles, panel β shows a P:L ratio where the peptide caused fusion/aggregation without leakage, and panel γ shows a P:L ratio where little fusion/aggregation was observed and the vesicles did not leak. The scale bar is 20 μm. (B) Data dimensions of internal size marker molecules. [1]Calculated on the basis of molecular weight, using the following equation:

$$r_s = \sqrt[3]{\frac{3Mw}{4\pi N_A \rho}}$$

where r_s is the Stokes radius of the molecule, M_w is the molecular weight, N_A the Avogadro constant and ϱ the density of the particle (calculated from composition, using the program Sednterp from http://jphilo.mailway.com/download.htm).

[2]The diffusion coefficient was determined in water at 20°C by fluorescence correlation spectroscopy (FCS), as described previously (199). The Stokes radius was calculated from the D values, using the Einstein-Stokes relationship:

$$D = \frac{k_B T}{6\pi r_s \gamma}$$

where, k_B is the Boltzman constant, T the temperature and γ the viscosity of the medium.[3] The dextran is assumed to be a prolate elipsoid with an axial ratio of 4 (for a 9.5 kDa Dextran, (200)). The semi-minor axis (α) and semi-major axis (β) are calculated using the r_s, measured in this work by FCS, from the dependence:

$$r = \left(\alpha\beta^2\right)^{1/3}$$

The dimensions of the dextran molecules should be taken with caution since they are not spherical and may lose their water shell while passing through the pore.

Discussion

Nature of the transition state. The simulations presented here elucidate the nature of the transition state of the poration process. One may assume that starting from a true transition state, the chance of arriving at either side of the transition state barrier is approximately equal (here the porated membrane versus the intact membrane). Although our statistics are necessarily limited, we observe 6 out of 11 simulations with the cyclic peptide to reach a porated state, starting from the state in which a large perturbation was observed in the original simulation (cf. Table 2, C1-10). In the remaining 5 out of 11 simulations, counting also the original trajectory, the system relaxed back to the intact membrane state. This intermediate or transition state is characterized by a single peptide bridging the two leaflets (cf. Figure 1B, 0 ns). The results are in line with kinetic models that suggest that such a state is important in pore formation (201).

Disordered toroidal pore. Using the transition state as seed for many independent trajectories, we were able to show that the deepest-embedded peptides may stabilize a toroidal-shaped pore of 1-2 nm diameter, which is in line with the electrophysiology and pore-sizing DCFBA experiments. Only two/three peptides actually lie in the pore while some of the remaining peptides line the mouth of the pore and stabilize the membrane curvature. The structure of the pore is reminiscent of pores seen in previous MD studies (34, 35, 181, 202) and has been termed the disordered toroidal pore.

Structure-function relationship. The simulations also highlight the importance of secondary structure in stabilizing the porated state. In the simulations, a constrained secondary structure rather than a high percentage of secondary structure was required to stabilize the pore. The importance of the secondary structure, induced on membrane binding and stabilized in the porated state, appears to be the alignment of the charged residues such that they fit the toroidal shape of the pore (cf. Figure 4D). This explains why the linear peptide is less active – for entropic reasons a folded structure is less favorable. This entropic penalty is 'prepaid' by the cyclic peptide. Thus, the linear peptide cannot open a pore but may stabilize it, if the starting structure is the transition state structure obtained with the cyclic peptide (cf. Figure 5).

Conductance, pore properties and fusion/aggregation. BPC194 forms stable and non-selective ion pores in planar lipid bilayer experiments, with a unitary conductance of 0.61 ± 0.12 nS, corresponding to a pore diameter of 1.5-1.9 nm. This is in contrast to other cyclic peptides such as gramicidin S that do not form stable pores (203). Stable

pores have however been seen for linear antimicrobial peptides such as alamethicin, magainins and defensins (204). Both the cyclic and linear peptides are fusogenic or cause aggregation, as indicated by DCFBA measurements, but only the cyclic peptide caused leakage as well. Similar to melittin (38), BPC194 causes leakage at the same concentration regime at which it fuses or aggregates DOPG membranes. However, further studies in this intriguing fusion/aggregation action are in progress.

Conclusions

There is now compelling evidence that cyclization of certain sequences of membrane-active peptides enhances their antimicrobial performance. In this paper, we analyze the molecular basis for the differences in activity of analogous cyclic and linear antimicrobial peptides. We show that the molecular basis for the enhanced activity resides most likely in the restriction of the number of conformations in the cyclic peptide. We show that it can adopt a favorable orientation towards the membrane and acquire an ordered structure that allows a high charge density and amphipathic arrangement. The latter allows the cyclic peptide to perturb the membrane substantially and to form discrete pores. Cyclization of the linear sequence locks the peptide in a poration-ready state, allowing it to perturb the bilayer and stabilize the curvature of a toroidal transmembrane pore. Without cyclization, entropy destabilizes the formation of a folded structure and consequently its amphipathic-like character and hence the linear peptide has a much lower propensity to induce pores. The work presented here provides detailed insight into the mode of action of cyclic peptides and will aid rational design of new antimicrobial molecules.

Acknowledgments

We thank LIPPSO group (University of Girona), for help with the synthesis of the peptides. We acknowledge financial support from the Spanish MICINN (MAT2008-04834 to ADC and PS) and MEC (BES-2006-11671 doctoral fellowship to ADC), the Netherlands NWO (DS, SJM), *SysMo via the BBSRC-funded KosmoBac programme (BP)*, NWO (Top-subsidy grant 700.56.302 to BP), NWO-Vidi (AK), ERC-Starting grant (AK) and the Zernike Institute for Advanced Materials to support the appointment and research of GMC and JTM.

Chapter 4

Dual action of BPC194: A membrane active peptide killing bacterial cells

Gemma Moiset*, Anna D. Cirac*, Marc C. A. Stuart, Siewert J. Marrink, Durba Sengupta and Bert Poolman

(*) Shared first authorship

Published in *PLoS ONE* (2013) 8: e61541

Membrane active peptides can perturb the lipid bilayer in several ways, such as poration and fusion of the target cell membrane, and thereby efficiently kill bacterial cells. We probe here the mechanistic basis of membrane poration and fusion caused by membrane-active, antimicrobial peptides. We show that the cyclic antimicrobial peptide, BPC194, inhibits growth of Gram-negative bacteria and ruptures the outer and inner membrane at the onset of killing, suggesting that not just poration is taking place at the cell envelope. To simplify the system and to better understand the mechanism of action, we performed Förster resonance energy transfer and cryogenic transmission electron microscopy studies in model membranes and show that the BPC194 causes fusion of vesicles. The fusogenic action is accompanied by leakage as probed by dual-color fluorescence burst analysis at a single liposome level. Atomistic molecular dynamics simulations reveal how the peptides are able to simultaneously perturb the membrane towards porated and fused states. We show that the cyclic antimicrobial peptides trigger both fusion and pore formation and that such large membrane perturbations have a similar mechanistic basis.

Introduction

Membrane active peptides (MAPs) represent a class of molecules that are able to interact with membranes, leading to fusion, poration and / or translocation. Depending on their mode of action, these peptides have been traditionally classified in three different categories: fusogenic peptides, antimicrobial peptides and cell-penetrating peptides (24, 205-207). More and more data suggest that this classification is too rigid as some peptides have multiple functionalities (43, 45, 208-215). For example, both fusogenic and antimicrobial peptides have been shown to induce leaky fusion in vesicles (43, 44, 216), and a cell-penetrating peptide has been shown to induce leaky fusion of liposomes (45). For antimicrobial peptides it has been speculated that this "multihit mechanism" increases their potency (27, 167). Despite much progress in the characterization of peptide-membrane interactions, the molecular details of the events leading to membrane fusion, poration, and peptide translocation are still poorly understood. A powerful tool to study peptide-membrane interactions at the molecular level is the molecular dynamics (MD) technique (158, 217-219).

Here, we combine MD simulations with a number of experimental techniques, including Dual-Color Fluorescence Burst Analysis (DCFBA), Förster Resonance Energy Transfer (FRET) and cryogenic Transmission Electron Microscopy (cryo-TEM), to explore the process by which peptides are able to act on a membrane in a dual way. Moreover, we relate our findings to cryo-TEM studies in *Escherichia coli* cells. The peptide investigated, BPC194: c(KKLKKFKKLQ), is a cyclic antimicrobial peptide that adopts a β-sheet structure upon interaction with the membrane (220). The peptide was selected from a library of de novo synthesized head-to-tail cyclic peptides (139, 140), which showed a high antimicrobial activity towards Gram-negative plant pathogenic bacteria like *Erwinia amylovora, Pseudomonas syringae* and *Xanthomonas vesicatoria*. We have previously probed the pore forming propensity of this peptide and showed that the β-conformation of the peptide is optimal for the stabilization of the curvature of the transmembrane pore (163).

We show here how BPC194 also induces membrane fusion, probing the process at an atomistic, molecular and ensemble level. Two seemingly unrelated processes: pore formation and membrane fusion are shown to occur simultaneously and influence the paths of both modes of action. Our in silico and in vitro observations correlate with in vivo data and provide a mechanistic framework for growth inhibition of bacterial cells by BPC194.

Materials and methods

Reagents and apparatus

The 2-(4-(2-hydroxyethyl)-1-piperazinyl)-ethanesulfonic (HEPES) was from Roche Diagnostics GmbH; 1,2-dioleoyl-sn-glycero-3-phosphatidylglycerol (DOPG) was from Avanti Polar Lipids; 1,1'-dioctadecyl-3,3,3',3'-tetramethylindodicarbo-cyanine perchlorate (DiD), 3kDa dextran-fluorescein, N-(7-nitrobenz-2-oxa-1,3-diazol-4-yl)-1,2-dihexadecanoyl-sn-glycero-3-phosphoethanolamine (NBD-PE) and Lissamine™ Rhodamine B 1,2-dihexadecanoyl-sn-glycero-3-phosphoethanolamine (Rh-DHPE) were from Invitrogen. For in vivo experiments, the medium used was Luria Broth (10 g/L Bacto Tryptone (Becton Dickinson), 5 g/L Yeast extract (Becton Dickinson) plus 10 g/L NaCl; Merck). The buffer used for cell imaging with the light microscope was 10 mM sodium phosphate, pH 7.5, containing 150 mM NaCl. For cryo-TEM assay with *E. coli* cells we used the buffer 120 mM potassium phosphate, pH 7.0, which has an osmolality equal to that of LB (measured by determination of the freezing point in an Osmomat 030, Gonotec) or sodium phosphate buffer (same for

light microscopy). In vitro solutions were prepared in 10 mM HEPES-NaOH, pH 7.2, containing 150 mM NaCl (the so-called physiologic ionic strength). The peptides BPC194, c(KKLKKFKKLQ), and its linear counterpart BPC193, H-KKLKKFKKLQ-OH, were synthesized as described previously (220) and purified by reverse-phase preparative HPLC (purities > 95%).

Strains, growth and cell imaging

Escherichia coli (*E. coli*) K-12 strain MC1061 (221) was grown from single colonies in LB at 37ºC under vigorous aeration until the culture reached an OD_{600} of 0.15 for light microscopy, 0.1 for peptide stability study and 0.6 for electron microscopy. Prior to the light microscopy, 1 mL of cells was washed twice with fresh LB medium and the pellet was finally resuspended in a 400 μL of LB to get an optimal cell density. Afterwards, 1.5% agarose solution in LB was pipetted onto a multispot microscope slide of 12 wells (Hendley-Essex). The coated slide was left to solidify at 4ºC for 15 min. A 1 μL drop of cell suspension mixed 1:1 (v/v) with buffer or peptide solution (final concentration range from 0.75 μM to 100 μM) was placed on each well and immediately covered with a coverslip. Cells were imaged for approximately 4 hours using Differential Interference Contrast (DIC) transmitted-light in an inverted microscope Observer Z1 (Carl Zeiss), equipped with a Zeiss LCI Plan-NeoFluar 63x objective (numerical aperture of 1.3) and a Cool-Snap HQ2 CCD camera (Photometrics). Cell growth rates were calculated from the increase in cell number over time; growth rates in liquid LB medium and LB-agarose were comparable. For electron microscopy, the cells were centrifuged (4 min; 10,000 x g; room temperature) and concentrated to a final OD_{600} of 100.

Peptide stability followed by High-Performance Liquid Chromatography (HPLC)

A 1 mL volume of *E. coli* cells, OD_{600} of 0.1, was pellet by centrifugation (4 min; 10,000 x *g*; room temperature) and resuspended in 1 mL 10 mM potassium phosphate, 150 mM NaCl, pH 7 (equiosmolar with LB medium) supplemented with 100 μM cyclic peptide, BPC194, or linear homologue, BPC193. Aliquots were taken after 5, 10, 30 and 60 min of incubation at r.t., and samples were centrifuged. Cell pellets and supernatants were kept at 4ºC until they were analyzed by HPLC. Reversed-phase HPLC with UV detection was performed on a Shimadzu system consisting of two LC-20AD pumps, SPD-M20A detector, a SIL-20AC HT auto-sampler and a CBM-20A system controller (Shimadzu, Kyoto, Japan). The peptides in the supernatant solutions were separated on a XTerra MS C18 column (3 × 150 mm) (Waters). The column temperature was set to 35ºC. Analyses were performed using a linear gradient of 5–95% eluent B (acetonitrile with 0.1% TFA; eluent A was water with 0.1% TFA) at a flow rate of 0.5 mL/min over 40 minutes. UV detection was carried out at 220 nm (PDA spectra 190–700 nm). The reversed-phase HPLC retention time of each peptide was determined when the peak was at its maximum height, and the area of the peak was used to determine the (relative) concentration of the peptides (using the appropriate standards and time zero samples). Since a fraction of the peptides is bound to cells, we treated cell pellets with 6M urea (final concentration) plus 1.5% (v/v) Triton X-100. After 30 min of extraction, the sample was centrifuged and the supernatant was analyzed by HPLC. In control experiments, standard samples of peptide were incubated with urea plus Triton X-100 in the same manner.

Preparation of lipid vesicles

Large unilamellar vesicles (LUVs) were prepared as described elsewhere(163). Briefly, rehydration of a dried DOPG lipid film was done in 10 mM HEPES-NaOH, 150 mM NaCl, pH 7.2. Vesicles were then subjected to five cycles of flash freezing in liquid nitrogen and rapid thawing at 37ºC. Subsequently, liposomes were extruded 11 times through a 200 nm polycarbonate filter (Avestin).

For the DCFBA experiments the lipid film was made by mixing the membrane dye DiD with DOPG lipids at a molar ratio of 1:12,000 (corresponding to ~15 molecules of DiD per liposome for vesicles with a diameter of 200 nm) and the rehydration was done in the presence of the lumen cargo molecule: 3 kDa dextran labeled with fluorescein (5 μM). Liposomes were separated from the non-encapsulated fluorophores by centrifugation (20 min; 270,000 x g; 20ºC) and resuspended in the buffer to a final lipid concentration of 80 μM.

For the FRET assays, the lipid film contained 1 mol% NBD-PE and/or 1 mol% Rh-DHPE, and the final lipid concentration was 125 and 250 μM DOPG.

For cryo-TEM, the liposomes were briefly sonicated before extrusion to increase the unilamellarity of the vesicles (5 pulses of 1 sec. at 75% amplitude with a Sonics Vibra Cell VCX 130 sonicator) and the final lipid concentration was 5 mM DOPG.

DCFBA

In the DCFBA experiment, liposomes were labeled with two, spectrally non-overlapping fluorescent probes (198). The DiD probe was incorporated in the phospholipid bilayer, while the fluorescein-labeled dextran filled the aqueous interior of the liposomes. By using a dual-color laser-scanning microscope, we monitored membrane-disrupting effects at the single liposome level. Different amounts of peptide (0 to 27 μM) were added to 80 μM DOPG liposomal solutions, yielding total peptide-to-lipid (P/L) ratio from 0 to 0.3. The samples were equilibrated for 10 minutes at room temperature after each addition of peptide. The fluorescence bursts, resulting from the diffusion of the liposomes through the detection volume, were measured for 10 min. The internal cargo concentration (C) of the i^{th} liposome (burst) is given by:

$$C_i = \frac{\int_{t_1}^{t_2} I_{IC}\, dt}{\left(\int_{t_1}^{t_2} I_L\, dt\right)}$$

where I_L is the fluorescence intensity of the lipid marker, *DiD*, above a certain threshold between t_1 and t_2. I_{IC} is the fluorescence of the internal cargo. The average concentration of internal cargo, C_{av}, over all the liposomes can be obtained from C_i:

$$C_{av} = \frac{1}{N}\sum_{i=1}^{N} C_i$$

where N corresponds to the number of liposomes (198). Samples were imaged on a commercial laser-scanning confocal microscope, LSM 710 (Carl Zeiss MicroImaging, Jena, Germany), using an objective C-Apochromat 40×/1.2NA, a blue argon ion laser (488 nm) and a red He-Ne laser (633 nm).

FRET

Fusion was monitored using the Förster resonance energy transfer (FRET)-based methodology described before by others, using a Cary Eclipse fluorescence spectrophotometer (Varian). Two different FRET assays were performed, i.e., positive- and negative-FRET. In positive-FRET, DOPG vesicles labeled with 1 mol% NBD-PE (donor) were mixed with DOPG vesicles labeled with 1 mol% Rh-DHPE (acceptor) at a molar ratio of 1:1. If fusion occurs, the lipids of the donor and acceptor vesicles will mix and the FRET efficiency, as monitored by an increase in the acceptor emission (intensity at λ_{em} = 590 nm, Rhodamine emission), will increase. On the other hand, in the negative-FRET assay, DOPG vesicles labeled with both 1 mol% NBD-PE and 1 mol% Rh-DHPE were mixed with unlabeled vesicles at a molar ratio of 1:3. In this case, as the vesicles fuse, the average distance between donor and acceptor increases. Thus, the FRET efficiency decreases proportionally and is monitored by an increase in the donor emission (intensity at λ_{em} = 530 nm, NBD emission). In both assays the peptide BPC194 was added to a final concentration in the range of 0 to 200 μM. The absorbance peaks of samples were kept <0.1, and various controls were done to minimize the inner filter effects (Fig. 1A-B). Quantification of fusion was calculated from the increase in NBD emission in the negative-FRET assay at two different lipid concentrations (125 and 250 μM). The 0% fusion was taken from the intensity of free-peptide vesicles. The other end of the fusion scale (100%) was calculated by adding $CaCl_2$ (194 mM) as a fusogenic agent to the vesicle suspension (222). Control experiments to correct the intensities for quenching of NBD and Rhodamine upon peptide and calcium addition were also performed (Fig. 1C-F).

Cryo-TEM

Samples for cryo-TEM were prepared by deposition of a few μL of vesicle solution (with buffer or peptide at a final P/L ratio of 0.01) or cell solutions (mixed 1:1 (v/v) with either buffer for the control or BPC194 to a final P/L ratio of 0.02 or 0.4) on holey carbon-coated grids (Quantifoil 3.5/1, Quantifoil Micro Tools). After blotting the excess liquid, the grids were vitrified in liquid ethane in a Vitrobot (FEI) and transferred to a Philips CM 120 cryo-electron microscope equipped with a Gatan model 626 cryo-stage, operating at 120 kV. Images were recorded under low-dose conditions with a slow-scan CCD camera. For the in vivo system, images were taken at two time points, one or 30 minutes after mixing with peptide. For the in vitro system, images were taken 10 minutes after mixing with peptide and a total of 98 cells were analyzed in the presence of peptide and 58 cells without peptide.

Simulations system set-up

The starting system consisted of two solvated DPPG (dipalmitoyl-phosphatidylglycerol; anionic lipid) bilayers in the fluid phase, comprising of 512 lipids each and placed at a distance of about 3 nm from each other. The DPPG lipids and their palmitoyl tails are well characterized in our group and have been used in our previous study on pore formation by BPC194 (163, 220). We emphasize that this lipid is in the fluid phase at conditions in the molecular dynamics simulations. BPC194 peptides were placed between the bilayers in the water phase at a P/L ratio of 1:15. The cyclic peptides were modeled based on a previous study (163, 220). The system consisted of about 32000 water molecules. K^+ ions were added as counter-ions for anionic lipids and Cl^- ions were added to neutralize the overall system. Five simulations were set up with different starting random velocities to obtain statistically significant results. A pure DPPG bilayer was also simulated for reference. Furthermore, a simulation where the inactive linear analog (BPC193) was tested at the same conditions as the active cyclic peptide was performed as a control. The linear peptide was modeled based on our

previous study with charged termini to best represent the experimental conditions (163, 220). For an overview of the simulations see Table 1.

Simulations parameters

The GROMACS software package (147) was used to perform all MD simulations. The GROMOS force-field 43a2 (148) was used to describe the peptide and peptide-solvent interactions. The force-field for DPPG lipids was taken from a previous study (163, 220). All force-fields were parameterized for use with a group-based twin range cut-off scheme (using cutoffs of 1.0/1.4 nm and a pair-list update frequency of once per 10 steps), including a reaction field (RF, (154)) correction with a dielectric constant of 78 to account for the truncation of long-range electrostatic interactions. The water was modeled using the SPC model (155). A time step of 2 fs was used. Bond lengths were constrained using the LINCS algorithm (156). The simulations were performed in the NP_lP_zT ensemble using periodic boundary conditions. The temperature was weakly coupled (coupling time 0.1 ps) to T = 320 K using the Berendsen thermostat (157). The pressure was also weakly coupled (coupling time of 1.0 ps and compressibility of 4.5×10^{-5}), using a semi isotropic coupling scheme in which the lateral (P_l) and perpendicular (P_z) pressures were coupled independently at 1 bar, corresponding to a tension-free state of the membrane. The simulation setup is similar to that used in previous studies of peptide-membrane interactions (34, 35, 42, 163, 220).

Characterization of lipid tilting and splaying

The tilt of the lipids was calculated by the angle between the vector of three atoms (P, C2A and C2P) and the *z*-axis as a reference. The values close to 0° mean no tilt whereas values close to 90° mean complete tilt. The splay of the lipids was calculated by the angle between the vectors of two atoms of one lipid tail (C2A, C2P) and the other lipid tail (C1A, C1P). The values close to 180° indicate the splay of the hydrocarbon tails.

Results

Cell growth inhibition and cell envelope defects by BPC194

To analyze the mechanism of action of BPC194, we monitored the aggregation, growth and morphology of *E. coli* cells by light microscopy and used the linear analog of BPC194, which lacks activity, as a control. Figure 2A summarizes the results of the cell growth over 4 hours of imaging (see also Movies S1-3 from doi:10.1371/journal.pone.0061541, (223)) The linear analog, BPC193, did not effect the cell growth up to a concentration of at least 100 μM. BPC194 already inhibited the growth at an order of magnitude lower concentration. The growth rate of *E. coli* as a function of peptide concentration is shown in Fig. 2C. Unlike the linear peptide, the cyclic peptide caused severe inhibition of growth and aggregation of the cells. This is a remarkable difference because both peptides have identical sequence and overall charge (+6 at physiological pH). To determine whether or not the different effects of BPC194 and BPC193 are caused by (partial) degradation of the peptides by *E. coli* cells, we tested their stability. The fate and concentration of the peptides was followed by reverse-HPLC. The results show that there is no observable degradation of the peptides after 1h of incubation with cells (or even cell lysates), that is, under conditions that BPC194 is completely inhibiting growth and BPC193 is having no effect (Fig. 3). To investigate further the effect of the cyclic peptide on the ultrastructure of the cells, we performed cryo-TEM (Fig. 2B). BPC194 caused disruption of the cell envelope (shown in black arrows) in all the cells analyzed, most notably the integrity of the inner and outer membrane (IM and OM) was disrupted. The cell envelope is no longer smooth (panel

B2) with the presence of contact sites between the IM and OM (panel B3) in about 30% of the cells, and in some regions the membrane was pinched off or budding off of vesicle-like structures was observed (panel B4). The results show that only the cyclic peptide is able to abolish cell division, which is preceded by cell aggregation. The positive charge of the peptide is not sufficient for cell aggregation and subsequent disruption of the cell envelope, as the linear analog does not show similar effects. The locked cyclic conformation of BPC194 might be the key factor in the initial interaction with the cell envelope, causing large physical stress and damage, what leads to inhibition of cell division and ultimately to cell death.

Table 1. Overview and statistics of the MD simulations.

Simulation	Time (ns)	Nr. Pores	Time scale Pore (ns)	Tilt > 85°	Splay > 170°
Pure DPPG	100	-	-	0	2
F1	360	2	40 / 58	24	9
F2	210	-	-	18	8
F3	590	1	150	28	12
F4	160	2	10 / 70	10	6
F5	230	-	-	16	10
Average	-	-	-	19.2 ± 3.1	8.9 ± 1.1

The percentage of lipids in the contacting monolayers which, during the simulation, tilt by more than > 85° or splay by more than > 170° is indicated. The standard error of the average is obtained from the standard deviation between all five simulations. The simulation length and formation of pores is also indicated.

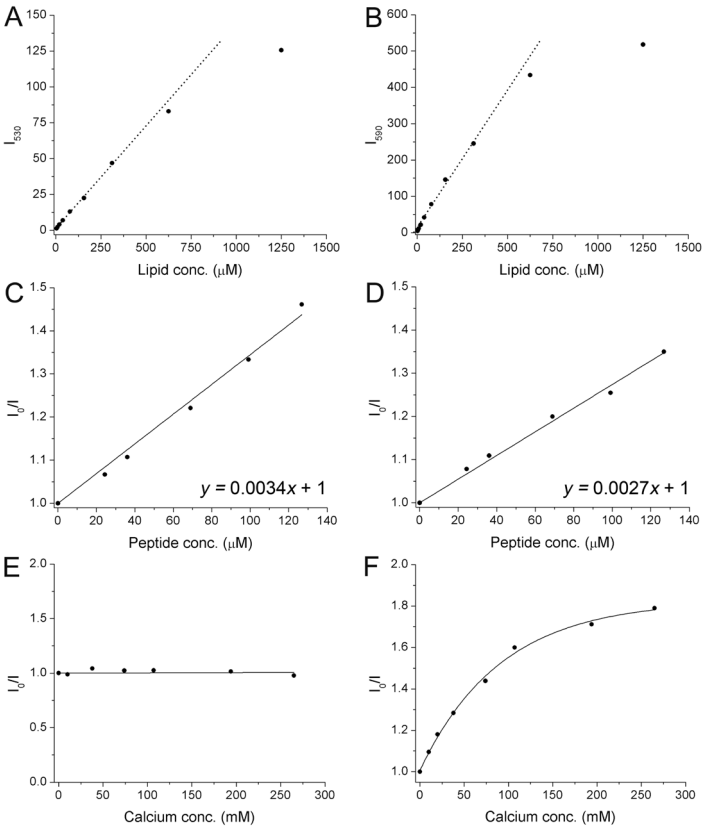

Figure. 1. *Controls for inner filter effect and quenching of fluorophores by peptide and calcium.* (A-B) NBD and Rhodamine fluorescence as a function of lipid concentration. The dotted lines show the linear regime where inner filter effects are not present. (C-D) NBD and Rhodamine fluorescence as a function of peptide concentration. The dependence of I_0/I on peptide concentration (see equation) was used to correct for the quenching. (E-F) NBD and Rhodamine fluorescence as function of calcium concentration. Calcium does not quench NBD emission intensity but does quench the Rhodamine fluorescence.

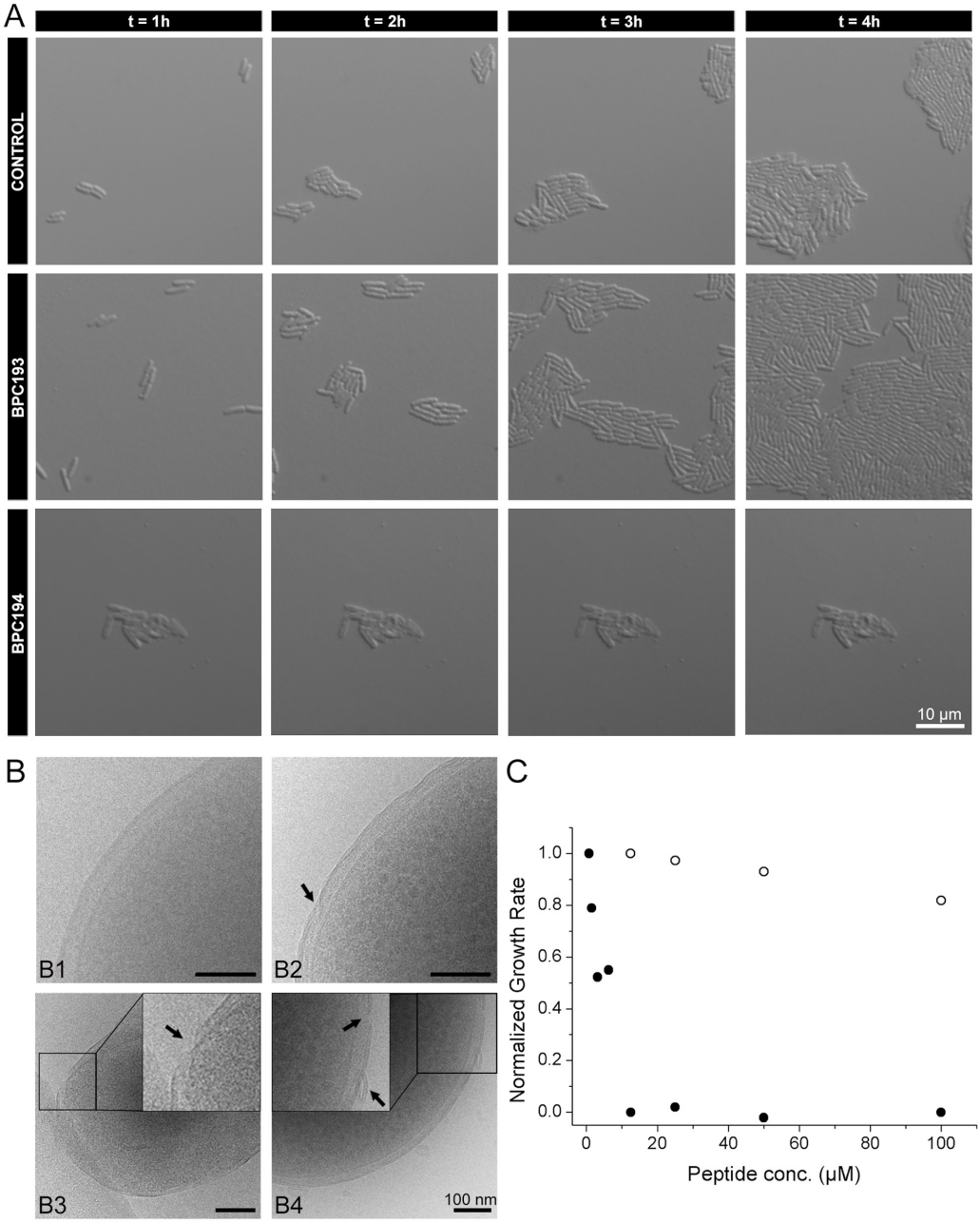

Figure 2. *Growth inhibition and cell envelope defects by BPC194.* (A) Cell growth imaging of *E. coli* without peptide (control) and with 12.5 μM of BPC193 or BPC194 during four hours. Note that the first image was taken after 1h. and one or two cell divisions had already taken place in the control and BPC193 samples. (B) Cryo-TEM micrographs of *E. coli* cells without (B1) and with BPC194 (B2-B4). Black arrows point out severe disruption of the cell envelope: membrane irregularities (B2); putative contact sites between IM and OM (B3); rupture of the cell envelope and budding off of vesicle-like structures (B4). Scale bars represent 100 nm. (C) Cell growth rates of *E. coli* in the presence of different concentrations of BPC194 (full circles) and its linear analog, BPC193 (empty circles). The values are normalized to the growth rate in the absence of peptide, which corresponded to 1.15 h^{-1}.

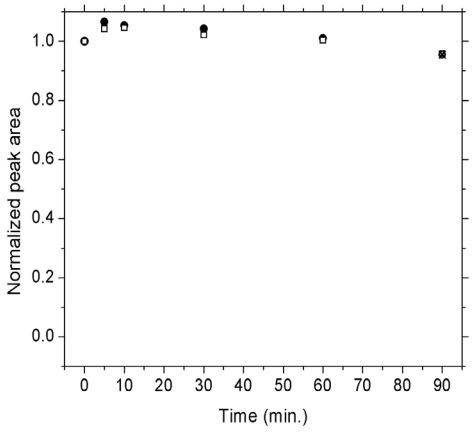

Figure 3. *Stability of peptides.* Normalized peak area of BPC194 (full circles) and BPC193 (empty squares) after incubation with *E. coli* cells for different periods of time. The data points at 90 min. (depicted with a crossed-circle or –square for BPC194 or BPC193, respectively) represent the aliquots incubated for 60 min with cells and subsequently another 30 more min in the presence of 6M urea plus 1.5% (v/v) Triton X-100. Peptides not exposed to cells but incubated with urea plus Triton X-100 did not show any decrease in the peak area (data not shown). The retention times were 20.0 min for BPC193 and 23.4 min for BPC194. As is evident from the data, we did not observe significant breakdown of either BPC193 or BPC194 upon incubation with *E. coli* cells up to a period of at least 1h.

Simultaneous pore formation and fusion action of BPC194

The use of model systems is required to get fundamental chemical understanding of the mode of action of membrane-active compounds as whole cells are simply too complicated for such an analysis. We used DOPG vesicles albeit that, similar observations have been made in membranes composed of mixtures of zwitterionic and anionic lipids (220). However, the higher the fraction of anionic lipids, the stronger the binding and poration of BPC194. We used solely negatively charged lipids as in this system the pores are stable for long periods of time (on the time scale of minutes) as inferred from electrophysiology studies (163). DCFBA, FRET and cryo-TEM techniques were used to probe the peptide-membrane interactions of BPC194, using BPC193 as negative control. First, DCFBA experiments were performed upon addition of different amounts of peptide to the DiD-labeled vesicles, filled with the internal cargo 3 kDa dextran-fluorescein (198). The average concentration of internal cargo and the normalized intensity of membrane-associated DiD per liposome as a function of peptide-to-lipid ratio are summarized in Fig. 4A. As the P/L ratio increases the amount of dextran inside the vesicles, C_{av}, decreases, which is indicative of the poration activity of the peptide (full circles). In parallel with the cargo leakage, we observed that the amount of DiD per vesicle increased, which points towards vesicle fusion or aggregation (empty squares). The DCFBA data (Fig. 4A) in conjunction with the confocal images (Fig. 4B) confirm the two concurrent events, poration and fusion/aggregation. In panel γ, mesoscopic aggregates can be observed in the DiD channel, whereas the corresponding signal of internal cargo has disappeared due to leakage.

To distinguish between fusogenic action (lipid mixing of vesicles) and aggregation, we performed both positive-FRET (Fig. 4C) and negative-FRET (Fig. 4D) (222). The fusogenic action of the cyclic peptide BPC194 was confirmed by both assays, thus classifying the observations of Fig. 4B γ as fusion of vesicles. Using the emission intensity of the FRET donor, NBD-PE, after correcting for peptide quenching, we quantified the percentage of fusion at each P/L ratio with two different lipid concentrations (Fig. 4E). The percentage of fusion increased with the peptide addition until a P/L of roughly 0.3, at which the fusion of vesicles as probed by FRET was maximal. At this particular P/L ratio, the cargo of the vesicles had already completely leaked out (Fig. 4A and 4B). As a control, we analyzed the inactive linear analog of BPC194, that is BPC193, at the same peptide concentrations and there was no change in the FRET efficiency (Fig. 4C; inset).

Cryo-TEM also revealed the fusogenic behavior of BPC194 and the most representative images of vesicles without peptide, with BPC194 and BPC193 are shown in Fig. 4F. Vesicles without peptide were on average about 200 nm. BPC194 yielded larger vesicles, consistent with membrane fusion, whereas the linear BPC193 brought the vesicles close together but vesicle fusion was not observed (Fig. 4F). The linear BPC193 peptide was previously shown to be inactive and vesicles aggregates were already seen by confocal microscopy (163, 220).

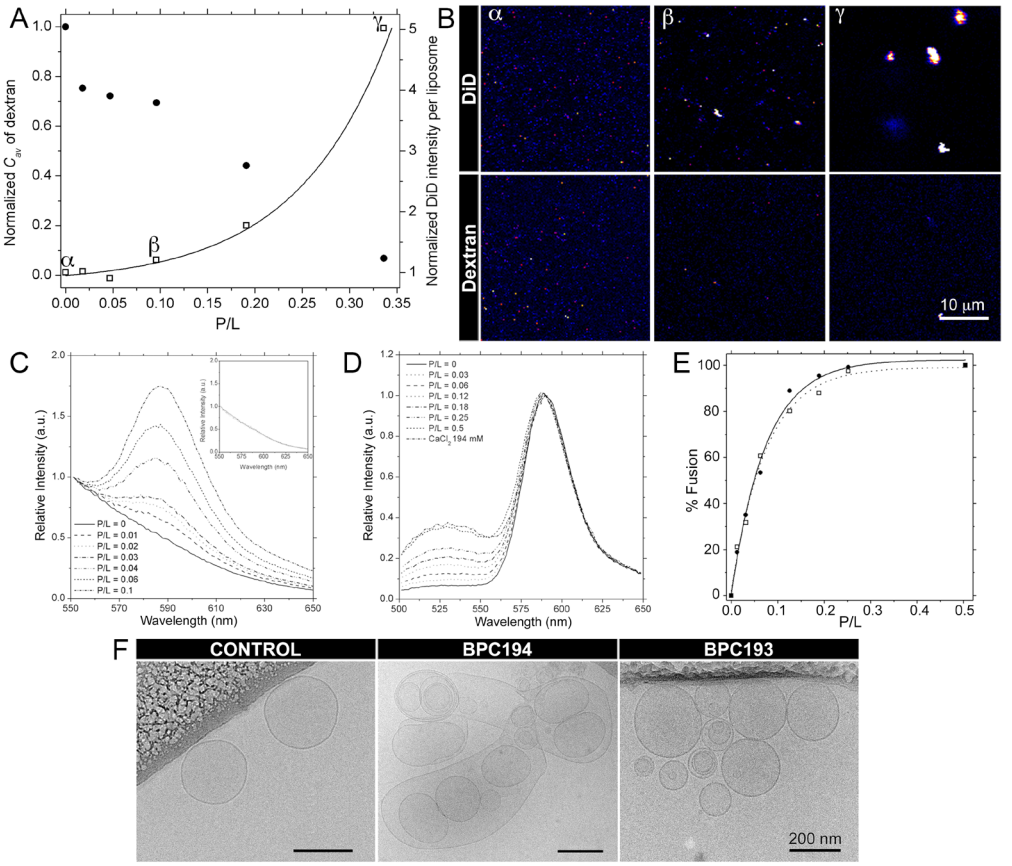

Figure 4. *Simultaneous pore formation and fusion activity of BPC194.* (A) The normalized concentration of dextran inside the liposomes, C_{av}, (filled circles) and the normalized intensity of membrane-associated DiD per liposome (empty squares) at different P/L ratios. (B) Confocal images of the lipid vesicles in the DiD and dextran detection channel at three different P/L ratios; α, P/L=0; β, P/L=0.1; and γ, P/L=0.3. (C) Positive-FRET upon peptide addition. The emission of Rhodamine increases due to vesicle fusion. Inset: Controls done with the ‚inactive' linear analog of BPC194, that is, BPC193 at the same peptide concentrations. (D) Negative-FRET upon peptide addition. The emission of NBD increases due to a decrease in FRET efficiency as a result of vesicle fusion. (E) Quantification of fusion at different P/L ratios and at two different lipid compositions, 125 μM (full circles) and 250 μM (empty squares). (F) Representative cryo-TEM micrographs of DOPG vesicles without peptide (control) and with BPC194 or the linear analog BPC193.

We note that complete fusion occurs at a bound peptide-to-lipid ratio of around 0.15. It has been shown by Melo and coworkers that the bound peptide concentrations at the MIC value are comparable to those of the thresholds effects (pore formation) in model membranes (40, 175, 224). The apparent difference between the in vivo and in vitro numbers arises from the fact that in a standard MIC assay, the number of cells is very low and the lipid concentrations are in the nanomolar range. When all

these factors are taken into account, the corresponding P/L ratio in the bacterial cell is around 0.1 and thus very similar to what we find in the membrane model system. In accordance, substantial fusion and leakage were observed at similar P/L ratios in the in vivo and in vitro assays. The overall data indicate that the fusogenic and poration activity of the cyclic peptide occur simultaneously and points to a "multi-hit" mechanism of action.

Molecular basis for concurrent fusion and leakage by MD simulations

To study the fusion and leakage events at an atomistic level, MD simulations of two DPPG bilayers were set up with multiple copies of the peptide placed between them (Fig. 5A). We note that in the simulations DPPG is in the fluid, liquid-disordered state. The P/L ratio was set to 1/15, i.e. at intermediate values for fusion and poration as observed experimentally. A control simulation was performed with the linear analog, BPC193, at the same P/L ratio. The linear counterpart of BPC194 is not able to form pores, as shown previously (163) or fuse the two apposed bilayers (Fig. 6). Five independent simulations were performed with the cyclic peptide, exploring a total time scale of more than 1 microsecond (Table 1). Representative snapshots showing the sequence of events in a particular simulation (F1, cf. Table 1) is depicted in Fig. 5B-D and the whole trajectory is shown in Movie S4 (from doi:10.1371/journal.pone.0061541, (223)). The other four simulations showed qualitatively similar behavior. The following steps were observed: i) peptide binding leading to membrane contact, ii) lipid perturbations leading to membrane bridge formation, and iii) peptide penetration resulting in pore formation.

Initial Membrane Contact: An initial fast binding of the peptides was observed with most peptides binding to one of the proximal monolayers, typically within 10 ns, (Fig. 5B). The binding is facilitated by multiple electrostatic interactions of the positively charged lysine residues with the negatively charged head-group moieties of the PG lipids. Importantly, a few of the peptides were able to interact simultaneously with both membranes. As a result, these peptides formed a bridge between the apposing membranes. A close-up of a few of these bridging peptides is presented in Fig. 5E.

Membrane Bridge formation: Due to the effect of the bridging peptides, some of the lipids were perturbed locally and protruded out of the membrane and interacted with the apposing membrane, creating a membrane bridge (Fig. 5C). We refer to this state as a membrane bridge since full contact between the hydrophobic tails of lipids from the contacting leaflets did not occur, which is characteristic of membrane stalks. The membrane bridge remained stable during the length of the simulation. Formation of the membrane bridge takes place on a time scale of 10-20 ns, i.e., the time required for the bridging peptides to extract the lipid tails from the contacting monolayers. The membrane bridge showed high saddle spray curvature and can be considered an intermediate towards complete stalk formation during the process of fusion.

Pore formation: Subsequent to the formation of the membrane bridge, spontaneous pore formation was observed (Fig. 5D). In MD simulations, pores are distinguished by a disruption of the lamellar phase and water molecules are seen to traverse the bilayer freely via the pore. Pore formation was triggered by a few of the peptides, not involved in stabilizing the membrane bridge, that insert deeper into the bilayer. We would like to point out that the pores formed in the simulations are not fusion pores, rather they are formed adjacent to the membrane bridge and mimic the stalk/pore complex described elsewhere (225, 226). Whether or not pores are actually formed appeared to be a stochastic process, with three out of five simulations showing pore formation (Table 1). In two of the simulations even two pores were formed. In each case, the pores formed adjacent to the membrane bridge, on a time scale ranging between 10 to 150 ns. A close-up of the membrane bridge and pore complex is shown

in Fig. 5F. The pores formed are reminiscent of the disordered toroidal type as shown in previous simulation studies for this peptide (163) and other antimicrobial peptides (34, 35).

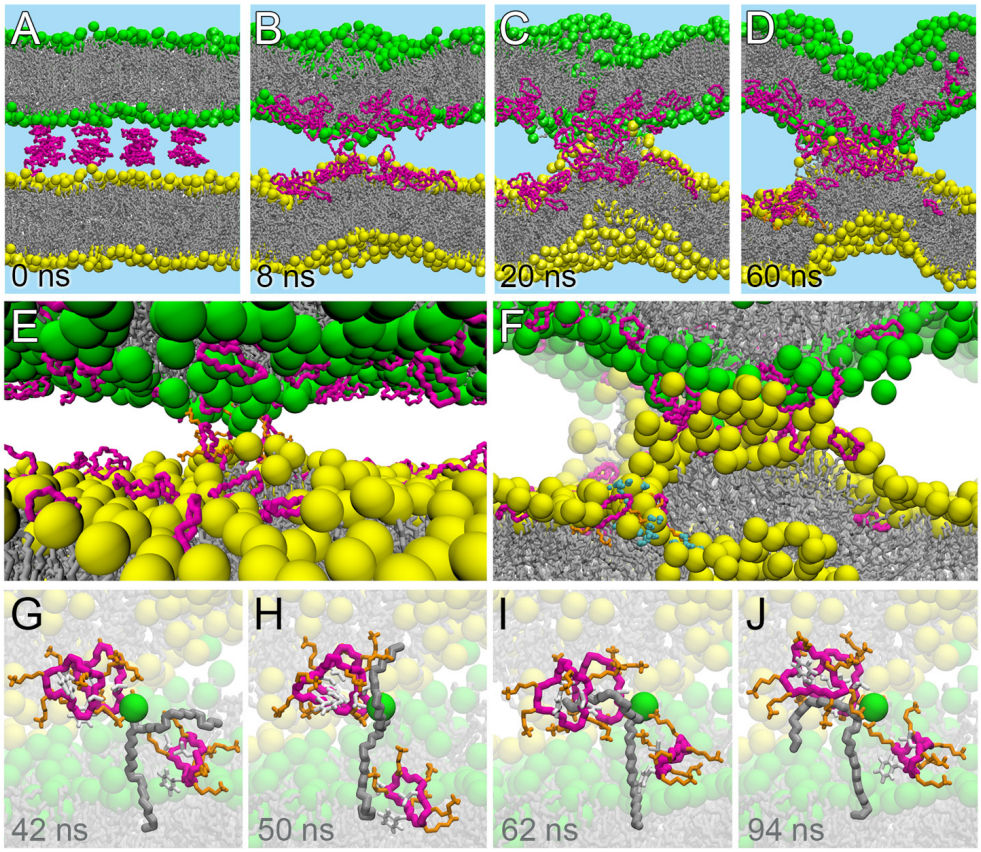

Figure 5. Molecular view of the sequence of events of the leaky fusogenic action of cyclic peptides. (A) Initial simulation setup with peptides placed between two bilayers. (B) Bridging of proximal leaflets of the two bilayers by BPC194. (C) Lipid bulging caused by the action of peptides associated with the bilayers. (D) Pre-stalk intermediate accompanied by disordered toroidal pore. (E) Close-up of the bridging peptides. (F) Close-up of the stalk-pore complex. (G-J) Splaying of a lipid during the course of a simulation. The peptides are depicted in pink, the phosphorous atoms in yellow and green respectively and the lipid chains in grey. The water is not shown for clarity. In panel F, the water molecules within the pore in one of the bilayers are shown in blue. The other pore cannot be seen in the zoom-in but is visible in panel D.

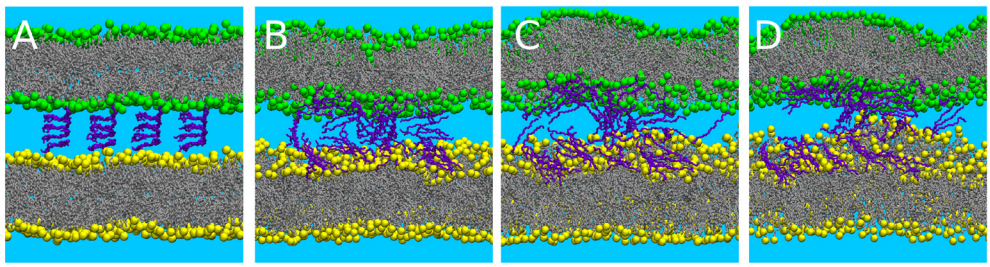

Figure 6. *MD simulation of the inactive linear peptide in contact with a membrane.* (A) Initial simulation setup of the linear analogue (BPC193), which is the same as for the cyclic peptide BP194 (0 ns). (B-D) From 8 to 70 ns of the simulation, the linear peptides are not able to perturb the membranes and induce fusion. Poration or pre-stalk events are not observed.

To further characterize the perturbing effect of the peptides on the lipids, we quantified the splaying and tilting of the lipid tails (see methodology for details). The results are given in Table 1. In each of the five simulations, the tilting is quite substantial compared to a pure bilayer. For example, in simulation-F3, 28% of the lipids of the proximal leaflet tilted more than 85° from their initial position at least once during the simulation. In a reference simulation of a pure DPPG bilayer, no such extensive tilting is observed. In addition, several lipids were also significantly splayed to values larger than 170°, implying a full opening of the lipid tails. Not surprisingly, the lipids that are most perturbed are the lipids in direct contact with the peptides, and especially the lipids involved in the formation of the membrane bridge, and later the pore. An example is presented in Fig. 5G-J, showing how a single lipid is splayed by interacting with a few neighboring peptides (see Movie S5 from doi:10.1371/journal.pone.0061541, (223)). In this particular example, the splayed lipid tail remains stable over 50 ns. The stabilizing contacts between the peptides and the lipids are formed between the lysine residues and the charged head-groups, and the apolar phenylalanine and leucine residues shielding the hydrophobic tails of the lipids from the water.

Discussion

On the basis of the in vivo and in vitro experimental data as well as the molecular dynamics simulations, we show how a synthetic cyclic antimicrobial peptide, BPC194, operates by dual action. Two seemingly different mechanisms are shown to occur concurrently, namely membrane poration and fusion. The mechanism is similar to the leaky fusion mechanism but follows a different pathway since complete leakage of vesicular content is seen and pore formation is independent of fusion. Despite the differences and higher complexity of the whole cell system as compared to the membrane model system, aggregation phenomena were observed concomitant with the inhibition of growth while membrane rupture was demonstrated by cryo-TEM. Although we did not observe genuine fusion intermediates between the IM and OM in our cryo-TEM studies of *E. coli* cells, we note that in Gram-negative bacteria those membranes are in close contact (5-20 nm apart) (227) and both were obstructed or brought close to each other at the point where BPC194 inhibited growth. BPC194 will not fuse bacteria together but the ability to fuse membranes may increase the potency of the peptide in cell membrane permeation of Gram-negative bacteria, i.e. when the IM and OM are in close contact.

Based on our atomistic molecular dynamics simulations and biophysical characterization, we propose a mechanism by which the peptides perform their dual action. Firstly, the peptides bind to the membrane/water interface. Both electrostatic interactions between the lysine residues and the lipid head groups and the partitioning of the hydrophobic side chains into the lipid bilayer stabilize this binding mode. In our previous work, we showed that the cyclic peptide, binds stronger compared to its linear analog, due to its pre-folded amphipathic conformation (220). When two membranes are present in close proximity as in our current simulation setup, the peptides are actually able to bridge the two membranes. Being able to keep two liposomes at close distance is likely a necessary condition for fusion, but not sufficient, as the linear analog can induce aggregation but not fusion (Fig. 4C, Fig. 4F and Fig. 6A-D). By adsorbing at the interface the peptides exert considerable stress on the outer, contacting monolayers, which can be rationalized in terms of their wedge-like shape (228). The stress induced causes a strong disordering of the lipids in the vicinity of the peptides, leading to lipid splaying, tilting, and protrusions as evidenced by our MD simulations. Eventually, a membrane bridge is formed, in which multiple (bridging) peptides and lipids form a large protrusion connecting the two apposing monolayers. The membrane bridge (also referred to as the pre-

stalk in literature (229, 230)) has been suggested to be an important intermediate in the stalk-mediated pathway to fusion. In particular, recent MD studies show that at least under conditions of low hydration, early membrane fusion kinetics is not determined by the stalk energy but by the energy of pre-stalk transition states involving solvent-exposed lipid tails (229, 230). Likewise, in MD studies of vesicle fusion mediated by either lung surfactant protein SP-B (231) or by SNARE complexes (232), the proteins are observed to trigger spontaneous fusion events by anchoring two vesicles and facilitating the formation of a lipid bridge between the proximal leaflets. Also of interest is a coarse-grained simulation study of another small antimicrobial cyclic peptide, RRKWLWLW (190). At high enough concentrations, coating of the membrane caused extrusion of lipids from the exposed bilayer leaflet, leading ultimately to a release of phospholipid micellar aggregates (in this study no apposing membrane was present). Thus, destabilization of lipids by membrane active peptides appears to be a generic feature.

Interestingly, concurrent with the formation of the membrane bridge, our MD simulations show that a pore is induced in the lipid membrane, pointing to a dual role of the BPC194. Pore formation is generally viewed as the main mode of action of antimicrobial peptides leading to cell content leakage or even complete lysis of the cell membrane. However, we speculate that under conditions where membranes are in close proximity, both stalks and pores can be formed as another way to relieve the lipid stress caused due to asymmetric peptide binding. A system with both fusion stalks and adjacent pores (distinct from the fusion pores) has been termed a stalk/pore complex and has recently been shown to represent a key intermediate in a possible fusion pathway (225). Although apposing membranes are pre-established in our simulation studies, they also occur in our in vitro studies in which liposomes are found to aggregate, possibly as a result of the bridging peptides. The stalk/pore pathway is distinct from the traditional pathway of fusion, which proceeds via the formation of a stalk that expands in a radial way forming a hemifusion diaphragm (225, 233-236). Fusion is completed when the hemifusion diaphragm ruptures (via a fusion pore). In the stalk/pore pathway, one or more pores appear in the vicinity of the stalk, allowing propagation of the stalk along the edge of the pore. Upon closure, the HD state is reached, or, in the case when two pores have formed, full fusion is accomplished. Such a pathway has been predicted to be energetically favorable based on mean field calculations (237). In fact, in MD simulations, the stalk/pore complex is stabilized by fusion peptides, and the peptides and lipids form an inverted cubic phase consisting of a network of stalk/pore complexes (238, 239). The pores seen in our simulations in the proximity of the membrane bridge is reminiscent of such a pathway and may be considered an intermediate prior to a stalk/pore complex. Thus, we believe that BPC194 can lower the energy barrier towards fusion by stabilizing the stalk/pore complex. The experimental work also suggests that AMPs can stabilize non-lamellar phases, and particularly inverted cubic phases (240). The ability of AMPs to induce saddle-splay curvature has furthermore been linked to the lipid composition of the membrane, and has been implicated to be a generic mechanism for formation of pores, blebs, buds, and tubes(241). These results point to a stabilization of saddle-splay (Gaussian) curvature by membrane adsorbed peptides. In this respect, BPC194, a synthetic cyclic antimicrobial peptide may act similar to fusion peptides.

Conclusions

In conclusion, by using *in vivo, in vitro* and *in silico* methods, we have established that fusion and poration are correlated in the case of BPC194, a synthetic antimicrobial peptide. This dual action is most likely functionally relevant and may contribute to the high potency towards bacterial killing. As probed by DCFBA and optical imaging, poration and fusion occur simultaneously at the same concentration regimes. In fact, in the DCFBA profiles, an increase of leakage coincides qualitatively with an increase in membrane fusion. Cryo-TEM corroborates the fusogenic action of the peptide. The MD simulations furthermore show that pores and stalk-like membrane bridges are formed simultaneously. We believe that the interaction of the cyclic antimicrobial peptide BPC194 with bilayers promotes saddle-splay curvature that is required for both stalks and pores. In case of isolated membranes, pores are formed, but in case membranes are in close proximity the peptides are able to bridge them. This, in turn, leads to the formation of a stalk/pore complex, which is an on-pathway intermediate for membrane fusion. Together, these results explain the dual action of cyclic peptides causing both fusion and leakage. The results are consistent with the whole cell studies, which correlate membrane reorganization with bacteriostasis. Based on our current work and recent studies in other groups (226, 231, 232, 238, 239), we believe that the stalk/pore pathway could be a common mode of action of membrane active peptides.

Acknowlegments

The authors thank M. Planas and L. Feliu from the LIPPSO group (University of Girona) for the support on the peptide synthesis, M. Melo for the fruitful discussions and the technical assistance with movie rendering and J.W. Veening for providing us with the multispot microscope slides.

Chapter 5

Modulation of a synthetic channel by DNA scaffold

Gemma Moiset*, Lorina Gjonaj*, Gerard Roelfes and Bert Poolman

(*) These authors contributed equally to this work

Manuscript in preparation

We show how DNA is a suitable and simple scaffold to assemble and control the aggregation behavior of an analog of the pore-forming peptide, Alamethicin, to modulate the poration state. Two strategies were used: DNA-templated peptide oligomerization via base pairing, resulting in a dimer, and via G-quadruplex motif, resulting in a tetrameric arrangement.

Introduction

Membrane permeability is regulated through complex transmembrane proteins that serve as transporters or channels. Generally, transporters pump ions or solutes against their concentration gradient, using either ATP or electrochemical gradients. Channels facilitate the movement of molecules down their concentration gradient and operate orders of magnitude faster than transporters. The high flux of ions (or neutral solutes) through channels allows for various applications. They have been used for their high charge or size selectivity in sensing devices, or switches have been incorporated to control their assembly or activity (242). Ion channels based on protein or peptides have been engineered to sense external stimuli such as pH, light, small molecules, temperature or ions (67, 142). One of the most investigated and engineered membrane protein is the staphylococcal α-haemolysin (αHL). The pore formed by the wild-type protein contains seven subunits assembled around a central axis, resembling a mushroom, with a well-defined β-barrel hydrophilic pore lumen (243). Bayley and co-workers developed several mutants of αHL that undergo stochastic sensing at the single molecule level. They have been engineered to sense compounds such as metal ions (244, 245), organic molecules, incl. amino acids (246, 247) and proteins (248). αHL has also been used for single molecule DNA sequencing with direct identification of individual nucleotides molecules by the pore (249, 250). Besides αHL-based pores, there have been several attempts to successfully sequence DNA using synthetic nanopores (251). Recently, a synthetic membrane channel constructed entirely from DNA and anchored to the lipid membrane via cholesterol has been reported. This synthetic DNA nanopore serves as a single molecule biosensor and discriminates analyte molecules on the basis of geometry and size (87).

Small peptides have also been engineered to control their aggregation and pore formation. Alamethicin is an antimicrobial peptide from the family of peptaibols, produced by *Trichoderma viride* and active against Gram-positive bacteria and fungi. It consists of 20 amino acids and is acetylated at the N-terminus and has a phenylalaniol moiety at the C-terminus. Owing to the high content of aminoisobutyric acid (Aib), the peptide has a typical α-helical conformation(30, 252). The amphiphilic monomers self-assemble into a bundle of helices forming a so-called 'barrel-stave' pore, as shown by molecular modeling (70), electrophysiology studies (71, 72) and recently by X-ray diffraction (73), solid-state NMR (74) and electrochemical scanning tunneling microscopy (EC-STM) (75). The bundle of helices traverses the membrane and gives rise to a voltage-dependent ion channel, with the hydrophilic face of the helices forming the pore of the channel (253). The oligomerization of the alamethicin peptides does not occur with a fixed stoichiometry. Once inserted into the membrane, the monomers associate and dissociate leading to different sub-conductance states, which relate to different pore sizes (254). It is thought that pores are formed from 3-4 to 10-12 peptides but direct evidence is limited (71, 255-258).

Various alamethicin analogues have been synthesized to obtain more insight in the process of ion-selectivity, pH gating, temperature dependence of the oligomerization and structure of the different conducting states. Covalent anchoring of the peptides has been shown to stabilize specific conductance state as shown by their increased life time. Linking the monomers together reduces their freedom of movement, and the defined helical bundles give information on the conductance and oligomeric state. In 1 M KCl the trimer, tetramer, pentamer or hexamer showed conductances ranging from 0.1 nS to 1.5 nS. However, single mutations in the alamethicin channels or the strategy used to covalently tether the monomers had a great influence in the conductance state (76).

Different scaffolds such as flexible linkers, fullerenes, cyclic templates or simple disulfide bonds have been used to link the alamethicin peptides together. Alamethicin conjugated C-terminally to fullerene or lipid moieties led to increased life times and stabilization of 4 different defined oligomer assemblies (259). The synthesis of two different covalent dimers attached by flexible linkers resulted in three particular conductance states stabilized with life times, depending on the linker, 50- to 170-fold longer than observed with alamethicin monomers. The lowest state was attributed to the tetramer (two dimers), the second state to the odd number of five monomers and the third state to the hexamer; the latter having a conductance of approximately 1 nS in 1M KCl (260). Similar conductance levels were observed upon dimerization of two alamethicin monomers via a disulfide bond between N-terminal linkers. Channels had 100 times longer life times, and two main conductance levels were stabilized (261). Okazaki and co-workers assigned the lowest conductance state to be the tetramer (and the next one the hexamer), in agreement with You and Jaikaran but opposite to what Hanke and Boheim presumed earlier (260, 262). Tetrameric alamethicin was also obtained by chemically linking the monomers via the side chains of four lysines present in a octameric peptide with the C-terminus of the alamethicin monomers, which resulted in channels with a conductance of 60 pS in 1M KCl (263). In another strategy, a porphyrin moiety was used as scaffold for tetramerization. Single-channel recordings of the porphyrin-templated peptide showed much smaller but more uniform conductance channels than produced by the monomeric peptide. Long-lived channels were observed in 1M HCl but not in KCl (264). The cyclodextrin-scaffolded alamethicin produced long-lived channels with only one conductance state (77).

There is also great potential for non-covalent linking of alamethicin analogues, as this allows reversible switching of ion conductance. To control the peptide assembly, an extramembrane leucine zipper segment was attached to the alamethicin, and the resulting channel was stabilized in a single open state. The conductance of the channel was 0.12 nS in 1M KCl (78). The stabilization of alamethicin channel has also been achieved via metal ions such as Zn^{2+}, Ni^{2+} and Co^{2+}, bearing and extra histidine at the N-terminus (82). By adding a chelator, the channel can in principle be destabilized. Also, it has been possible to fully reduce the ion conductivity of alamethicin channels by binding of carbonic anhydrase II (CA II) to a benzenesulfonamide group present at the C-terminus of the peptide. The ion transport is restored upon addition of excess competitor group to the solution, which released CA II (80). Another example to dramatically reduce the channel current is via C-terminal tagging of alamethicin with biotin and introducing streptavidin to the system. Further addition of biotin hydrazide recovered the channel activity (81).

DNA has been used as a template to control several processes such as chemical reactions by modulating the effective molarity of highly dilute reactants (83), to perform DNA-based asymmetric catalysis (84, 85) or to control protein activity (86). Here, we report the use of DNA to modulate the alamethicin assembly and thus the size of the channel. Scheme 1 shows the dimerization strategy, using two DNA-peptide hybrids, Alm dUL-C-3'DNA and Alm dUL-C-5'DNA. The complementary DNA strands are covalently attached to the peptides through a linker. The gathering of two peptides is based on the base-pairing concept by anchoring each monomer to a complementary DNA sequence, resulting in the hybrid duplex. We use electrophysiology measurements and dual-color burst analysis (DCFBA) to characterize the channels formed. We also use a G-quadruplex motif to tether four peptides together (see Appendix). This report demonstrates the potential of extramembranous DNA coupling to design new and controllable channels that could find a future application in the field of nano-switches and biosensors.

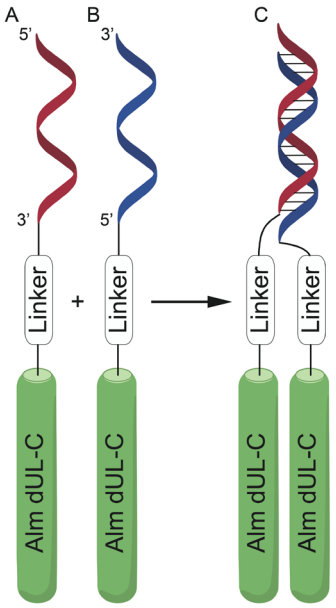

Scheme 1. *Schematic representation of the dimerization of DNA-peptide hybrids.* (A) Alm dUL-C-3′DNA. (B) Alm dUL-C-5′DNA. (C) Hybrid duplex. Cilinders, Alm dUL-C peptide helices; the complementary DNA strands are presented in red and blue.

Materials and methods

Reagents and apparatus

Alm dUL-C: Ac-LPLALAQLVLGLLPVLLEQFC-NH_2 was purchased from Cambridge Peptides Ltd (Birmingham, UK). 3-Maleimidopropionic and 6-maleimidohexanoic acid N-hydroxysuccinimide esters were acquired from TCI Europe. Synthetic 11-mer oligonucleotides Oligo 1 ($^{5'}$ACCATGCTTAA$^{3'}$-$(CH_2)_6$-NH_2) and Oligo 2 (H_2N-$(CH_2)_6$-$^{5'}$TTAAGCATGGT$^{3'}$) were purchased from BioTez (Berlin Buch). Oligonucleotide concentrations were determined using the Nanodrop ND-100 (Thermo Fisher Scientific). Column chromatography was performed on silica gel. Reversed phase-HPLC (RP-HPLC) analysis were performed on a Shimadzu LC-10AD VP, Waters Xterra MS C18 column (3.0 x 150 mm, particle size 3.5 μm) using generally the gradient A (for DNA samples) of CH_3CN/Triethylammonium acetate (TEAA) buffer 50 mM pH = 7.0. Gradient A: 05/95 from 0 to 10 min, to 35/65 at 60 min, to 70/30 at 65 min, to 05/95 at 70 min for 20 min; flow of 0.5 mL/min. For purification purposes of the DNA-peptide hybrid compounds, a Waters Xterra Prep MS C18 column (7.8 x 150 mm, particle size 10 μm) was used in combination with solvent gradient B. Gradient B: 20/80 from 0 to 10 min, to 100/0 at 55 min for 15 min, to 20/80 at 80 min for 10 min; flow of 1.0 mL/min. MALDI-TOF measurements were done on a Voyager-DE Pro apparatus (Matrix: 20 μL of a solution of 2, 4, 6-Trihydroxyacetophenone 0.5 M in EtOH + 10 μL of a solution of ammonium citrate dibasic 0.1 M in double distillated (dd) H_2O + 2 μL sample solution in dd H_2O). Phospholipids 1-palmitoyl-2-oleoyl-sn-glycero-3-phosphatidylcholine (POPC) and 1,2-dioleoyl-sn- glycero-3-phosphatidyl-ethanolamine (DOPE) were from Avanti Polar Lipids (Alabaster, AL). The *n*-decane was from Sigma-Aldrich (St. Louis, MO).

Synthesis of the maleimide-functionalized DNA

300 μL of amino-modified oligonucleotide, Oligo 1 (3′DNA) or Oligo 2 (5′DNA), solubilized in dd H_2O at 200 μM was mixed with 200 μL of 200 mM sodium phosphate pH 7.2 and 100 μL of the maleimido N-hydroxysuccinimide ester solution (compound

1 or **2**, 20 mg/mL in DMF), yielding maleimide(1 or 2)-3′DNA and maleimide(1 or 2)-5′DNA. The reaction was vortexed at room temperature for 4h. The functionalized DNA was purified by size exclusion chromatography (Sephadex G-15, eluting with 50 mM TEAA buffer, pH 7.0) and characterized by RP-HPLC and MALDI-TOF.

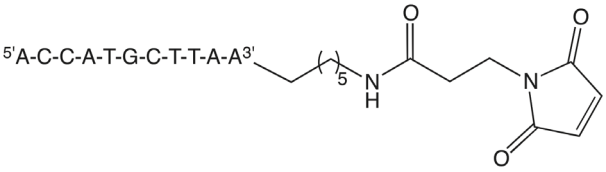

Maleimide(1)-3′DNA
RP-HPLC rt = 40 min
MALDI-TOF (m/z) = 3648 $[M+Na]^+$
(calculated 3652)

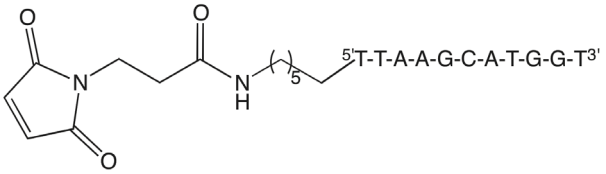

Maleimide(1)-5′DNA
RP-HPLC rt = 35 min
MALDI-TOF (m/z) = 3722 $[M+Na]^+$
(calculated 3722)

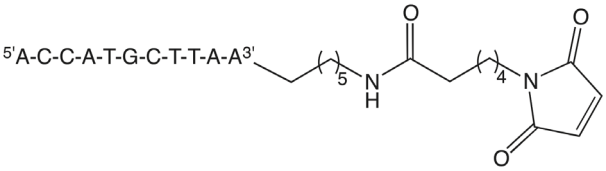

Maleimide(2)-3′DNA
RP-HPLC rt = 40 min.
MALDI-TOF (m/z) = 3672 (calculated 3671)

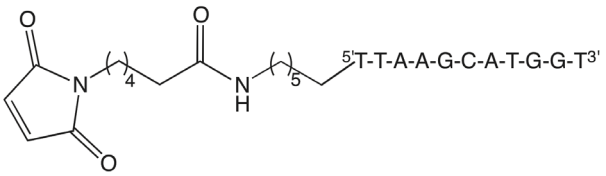

Maleimide(2)-5′DNA
RP-HPLC rt = 36 min
MALDI-TOF (m/z) = 3741 (calculated 3742)

Synthesis of the DNA-peptide hybrids

100 μL of maleimide(2)-3′DNA or maleimide(2)-5′DNA at 100 μM, solubilized in 50 mM TEAA buffer pH 7.0, was added to 300 μL Alm dUL-C of a freshly made solution of peptide in DMF (2.0 mg/mL). The solutions of DNA and peptide were flushed under nitrogen atmosphere before and during the overnight stirred reaction. The crude mixture was centrifuged and the supernatant was purified by RP-HPLC, using gradient B. The products, Alm dUL-C-3′DNA hybrid and Alm dUL-C-5′DNA hybrid, were analyzed by RP-HPLC and MALDI-TOF.

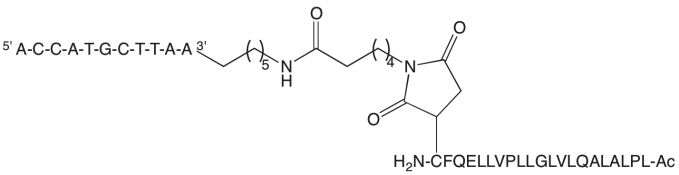

Alm dUL-C-3′DNA hybrid
RP-HPLC rt = 42 min
MALDI-TOF (m/z) = 5974
(calculated 5976)

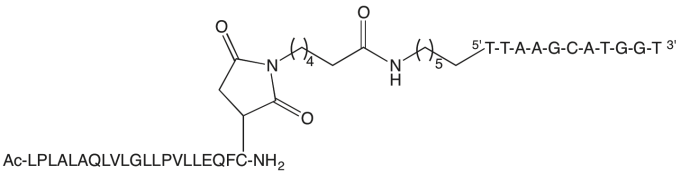

Alm dUL-C-5′DNA hybrid
RP-HPLC rt = 42 min
MALDI-TOF (m/z) = 6051
(calculated 6045)

Electrophysiology measurements

A planar lipid bilayer setup (or black lipid membrane – BLM) was used as described below. The bilayer was formed by painting with 1 μl of a 20 mg/ml solution of POPC/DOPE (3/7) lipid in *n*-decane across the 250 μm opening of a Delrin cup that separates two solution-filled compartments, designated *cis* and *trans* (191-193). Both compartments were filled with a buffer solution consisting of 1 M KCl. The transmembrane current (I_m) at different clamping potentials (V) was monitored, using an integrating Bilayer Clamp Amplifier BC-535 (Warner Instruments). Currents were filtered through an 8-pole low-pass Bessel Filter LPF-8 (Warner Instruments) and digitized using Clampex 10.2 software (Axon Molecular Devices). Membrane conductance (g) events were identified as $g = I_m/V$ and analyzed with the Clampfit software (Axon Molecular Devices) (163). Before adding the peptide, the membranes were checked for stability by applying the same range of voltage as in the presence of compound. The compounds were added to the *cis* side of the planar lipid bilayer and stirred for 1 minute without applying voltage. Three traces per compound were recorded with freshly prepared membrane. The pore diameter was estimated by an extended version of the model proposed by Hille (66, 265), given by Cruickshank *et al.* (196):

Eq. 1
$$d = \frac{\rho g}{\pi}\left(\frac{\pi}{2} + \sqrt{\frac{\pi^2}{4} + \frac{4\pi l}{\rho g}}\right)$$

where d is the diameter of the pore, r is the resistivity of the buffer, g is the measured conductance, and l is the length of the pore. The unitary pore conductance, g, was estimated from all recordings. The resistivity of the buffer, 1M KCl, was assumed to be 0.1 Ωm (266). The length of the pore equals the membrane thickness and was assumed to be 3.5 nm.

DCFBA

Liposomes were prepared as described by van den Bogaart (37). Briefly, 1,1′-dioctadecyl-3,3,3′,3′-tetramethylindodicarbo-cyanine perchlorate (DiD; Invitrogen, Carlsbad, CA) labeled-liposomes were prepared by rehydration of a DOPC/DOPE (3:7) dried lipid film in the presence of glutathione (GSH)-labeled Alexa Fluor 488 (AF488), 3 kDa dextran labeled with fluorescein (Invitrogen) or 10 kDa dextran labeled with fluorescein (all from Invitrogen) as aqueous phase markers in 10 mM 2-(4-(2-hydroxyethyl)-1-piperazinyl)-ethanesulfonic acid (HEPES; Roche Diagnostics, Mannheim, Germany), pH 7.0, containing 150 mM NaCl (Merck, Whitehouse Station, NJ). The DiD/lipid molar ratio was 1:40,000. Subsequently, the liposomes were extruded 11 times through a 200 nm polycarbonate filter (AVESTIN, Ottawa, Ontario, Canada). The liposomes were separated from the non-encapsulated fluorophores by centrifugation (20 min, 270,000 g, 20˚C) and resuspended in the same buffer to a final lipid concentration of 625 μM. Fluorescence burst analysis was carried out on a laser-scanning confocal microscope, LSM 710 (Carl Zeiss MicroImaging, Jena, Germany), using an objective C-Apochromat 406/1.2 NA, a blue argon ion laser (488 nm) and a red He-Ne laser (633 nm). Different compounds were added to the liposomes to a final concentration of 5, 10 or 20 μM. The samples were equilibrated for 10 min at room temperature after each addition. The fluorescence bursts of single liposomes were measured for 5 min. The results are presented in the DCFBA profiles as the population-distribution histogram of liposomes with a given internal marker concentration, *Ci*, given by:

Eq. 2

$$C_i = \frac{\int_{t_1}^{t_2} I_{SM}\,dt}{\left(\int_{t_1}^{t_2} I_L\,dt\right)^{\frac{3}{2}}}$$

where I_L is the fluorescence of the lipid marker and I_{SM} is the fluorescence of the internal size marker in each fluorescence burst (38). The amount of vesicles was taken as the total number of lipid bursts.

Results

Synthesis of the DNA-peptide hybrids and the dimer hybrid duplex

The non-natural amino acid Aib of alamethicin complicates the synthesis of the peptide. Therefore, we use the analogue Alm dUL, firstly synthesized by Molle *et al.* (267), in which the Aib residues and the C-terminal phenylalaniol (Pheol) are replaced by leucine (Leu) and an amidated phenylalanine (Phe), respectively. The acetylated N-terminus was maintained. This analogue showed a behavior consistent with the 'barrel-stave' model with conductance ratios of the sub-levels very similar to those of wild-type alamethicin. However, the life times of the channels were about one order of magnitude shorter (267, 268). An extra cysteine (Cys) on the C-terminus was added to couple the peptide to the maleimide functionality introduced into the DNA.

Synthesis of maleimide(2)-3'DNA and maleimide(2)-5'DNA

The DNA-peptide hybrids, Alm dUL-C-3'DNA and Alm dUL-C-5'DNA, were synthesized from two different starting oligonucleotides, Oligo 1 and Oligo 2. Oligo 1 (modified at the 3'-terminus) and Oligo 2 (modified at the 5'-terminus) bearing a hexyl amino linker were reacted with the 3-maleimidopropionic acid N-hydroxysuccinimide ester **1** (Scheme 2A, shows the reaction for Oligo1). The maleimide moiety of the modified DNA proved to be instable during the reaction conditions of the conjugation to the peptide (Scheme 2).

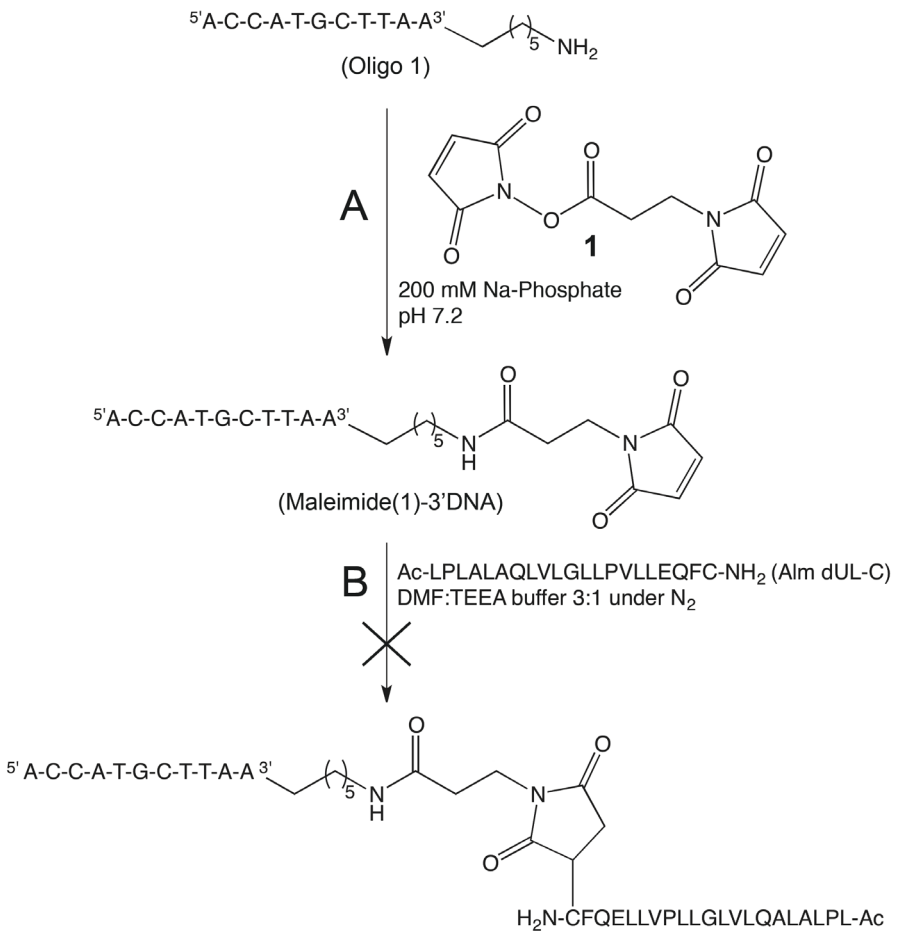

Scheme 2. Synthesis of the DNA-peptide hybrid from Oligo 1 with ester 1.

We thus decided to couple the DNA to a longer maleimide linker, ester **2.** (Scheme 3). An excess of maleimide ester **2** was added to the solution of the amino-modified DNA, Oligo 1 and Oligo 2, in 200 mM sodium phosphate, pH 7.2 (Scheme 3A). The reactions were followed by HPLC and purified by size-exclusion chromatography resulting in yields between 78-88 %. Analytical HPLC traces of the two resulting compounds maleimide(2)-3'DNA and maleimide(2)-5'DNA are shown in Figure 1A and 1B.

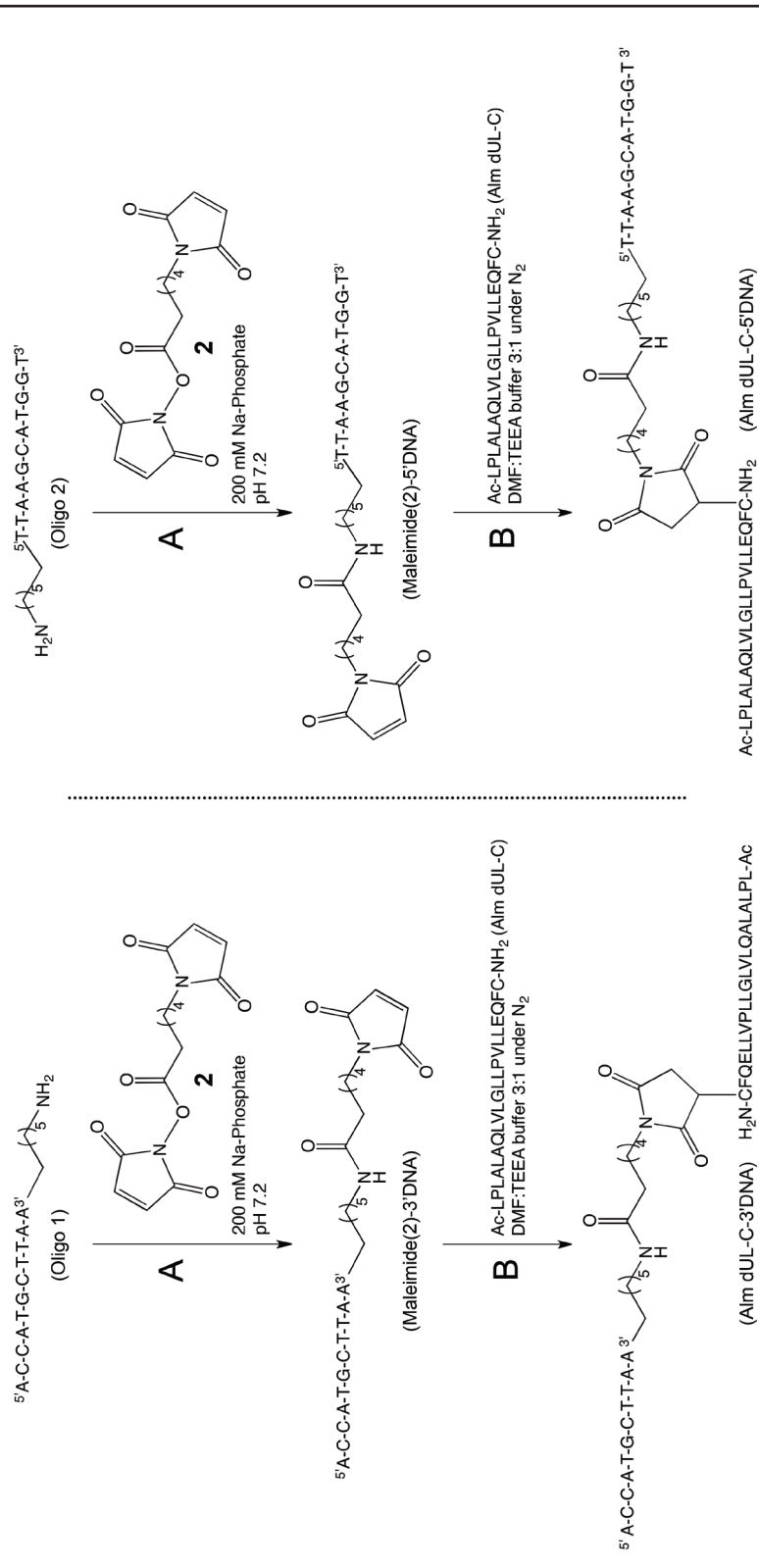

Scheme 3. *Synthesis of the DNA-peptide hybrids with ester* 2. Left panel, reaction with Oligo 1; right panel, reaction with Oligo 2. (A) Yields of 78-88 %. (B) Yields of 13-15 %.

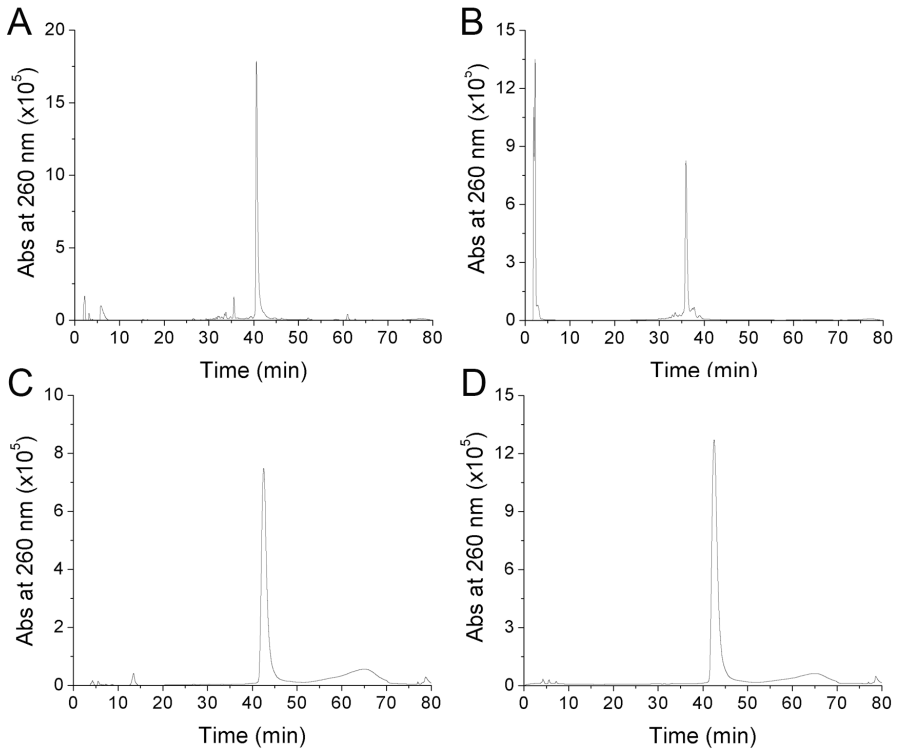

Figure 1. *RP-HPLC traces of maleimide-functionalized DNA and DNA-peptide hybrids*. (A) Maleimide(2)-3′DNA. (B) Maleimide(2)-5′DNA. (C) Alm dUL-C-3′DNA. (D) Alm dUL-C-5′DNA.

Synthesis of the Alm dUL-C-3′DNA and Alm dUL-C-5′DNA

The synthetic peptide was highly insoluble in water, making the coupling procedure more challenging than expected. Different solvents in mixture with water were tested to solubilize the peptide, but always some precipitation of the peptide was observed. The optimum reaction conditions were found with the peptide solubilized in a polar solvent like DMF and the functionalized DNA in TEAA buffer (50 mM, pH =7.0), using DMF:TEAA ratio of 3:1 for the conjugation (Scheme 3B). An undesired product was obtained during the reaction, which was identified with MALDI-TOF. The peptide reacted with 6-maleimidohexanoic acid of which there were still trace amounts present in the functionalized DNA obtained after purification by size-exclusion chromatography. Excess of the Alm dUL-C was used (10-30 equivalent) to bring the reaction to completion. The reaction was conducted under nitrogen atmosphere to minimize disulfide bond formation between cysteine residues of two monomers. The hybrids, Alm dUL-C-3′DNA and Alm dUL-C-5′DNA, were purified by RP-HPLC (Figure 1C and 1D) with a final yield of 10-13% over two steps and characterized by MALDI-TOF (Figure 2).

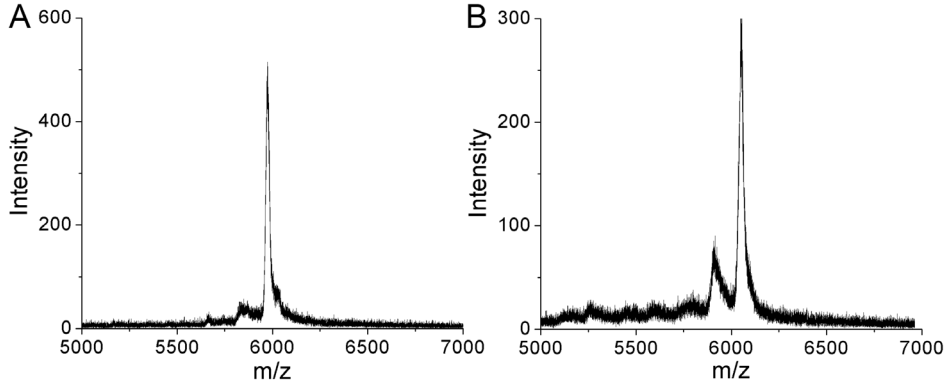

Figure 2. *MALDI-TOF spectra of the DNA peptide hybrids.* (A) Alm dUL-C-3'DNA, m/z = 5974. (B) Alm dUL-C-5'DNA, m/z = 6051.

Hybridization

The hybridization was carried out by mixing equal volumes of 300 μM DNA-peptide hybrid solution. The mixture was then heated to 90˚C and subsequently cooled down to room temperature. The dimeric hybrid duplex solution had a concentration of 150 μM, assuming hybridization. Unfortunately, neither RP-HPLC nor MALDI-TOF characterization could be performed since dissociation of the duplex occurred under the conditions of analysis.

DNA hybridization stabilizes Alm-formed pores

To evaluate the electrical behavior of the DNA-peptide hybrids and the dimeric hybrid duplex, the planar lipid bilayer setup was used. Figure 3 shows the recorded single-channel traces. Alm dUL-C peptide without DNA showed short-lived events and conductance states of 0.2 nS, 0.6 nS and 1 nS; the first one being the most populated (Fig 3A). These results are in agreement with those obtained with Alm dUL (conductance of 0.12, 0.56 and 1 nS), showing that the monomers have the freedom to assemble together with different oligomeric states. These three difference conductance levels are thought to represent tetrameric, pentameric and hexameric channels (267). The two DNA-peptide hybrids, Alm dUL-C-3'DNA and Alm dUL-C-5'DNA also gave very short-lived channel openings but with smaller conductance than observed with Alm dUL-C, which might be at attributed to the presence of the 11-mer oligonucleotide. The process of self-assembly of the hybrid duplex resulted in a major conductance ~0.75 nS or multiples thereof (Fig. 3D). The other conductance states are all of uniform size, implying that channels of similar conductance are opening simultaneously. Using Eq. 1 we estimate the pore size of the hybrid duplex to be about 0.6 nm in diameter. We tentatively assign the 0.75 nS level to a hexameric channel (three dimers). The hybrid duplex also shows two lowly populated conductance states of around 1 and 1.9 nS. These could represent higher oligomeric states but we did not characterize them further. Molle *et al*. assigned a 1.9 nS channel to the octameric state. However, the membrane lipid composition was different from ours and the datasets cannot be compared directly (267). The channel life times of the hybrid duplex also appeared longer, around 4 ms on average, compared to the ones of Alm dUL-C and the two hybrids Alm dUL-C-3'DNA and Alm dUL-C-5'DNA, around 0.3 ms on average. All modified Alm channels tested allowed the flux of both positive and negative ions (data not shown).

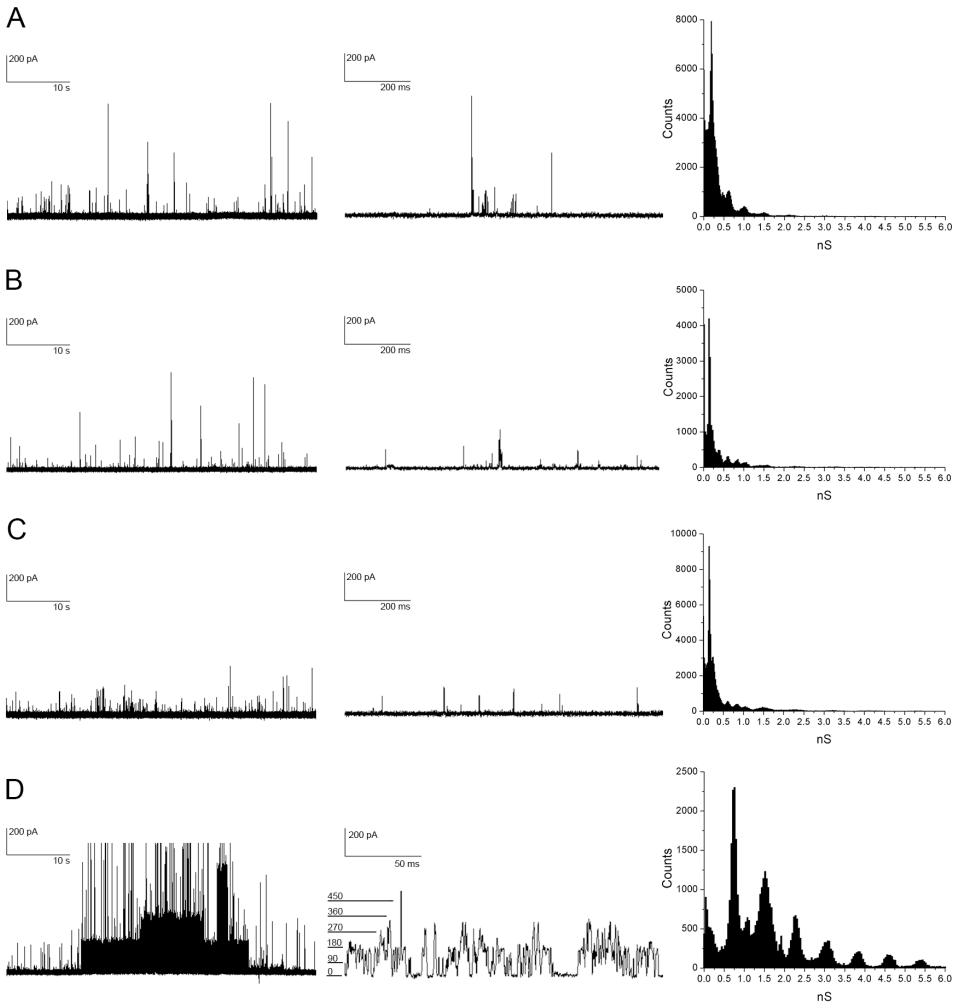

Figure 3. *Single-channel recordings*. Left and middle panels show two different magnifications of the traces, and the right panels show the population of the conductance levels. (A) Alm dUL-C, 7.5 nM. (B) Alm dUL-C-3'DNA, 7.5 nM. (C) Alm dUL-C-5'DNA, 7.5 nM. (D) Hybrid duplex, 0.75 nM. Numbers in the middle panel represent the current values of the multiple levels in pA.

The DNA stabilized state is not concentration dependent

Next, we determined whether or not the occurrence of the conductance state of 0.75 nS is peptide concentration dependent by analyzing the concentration range of 0.075-3.5 nM (Figure 4). Our data show in all cases multiples of the 0.75 nS conductance and there was no correlation between the number of channels and the concentration peptide added to the buffer reservoir of the black-lipid membrane set up. This might mean that the local concentration at the membrane surface is similar in all the cases.

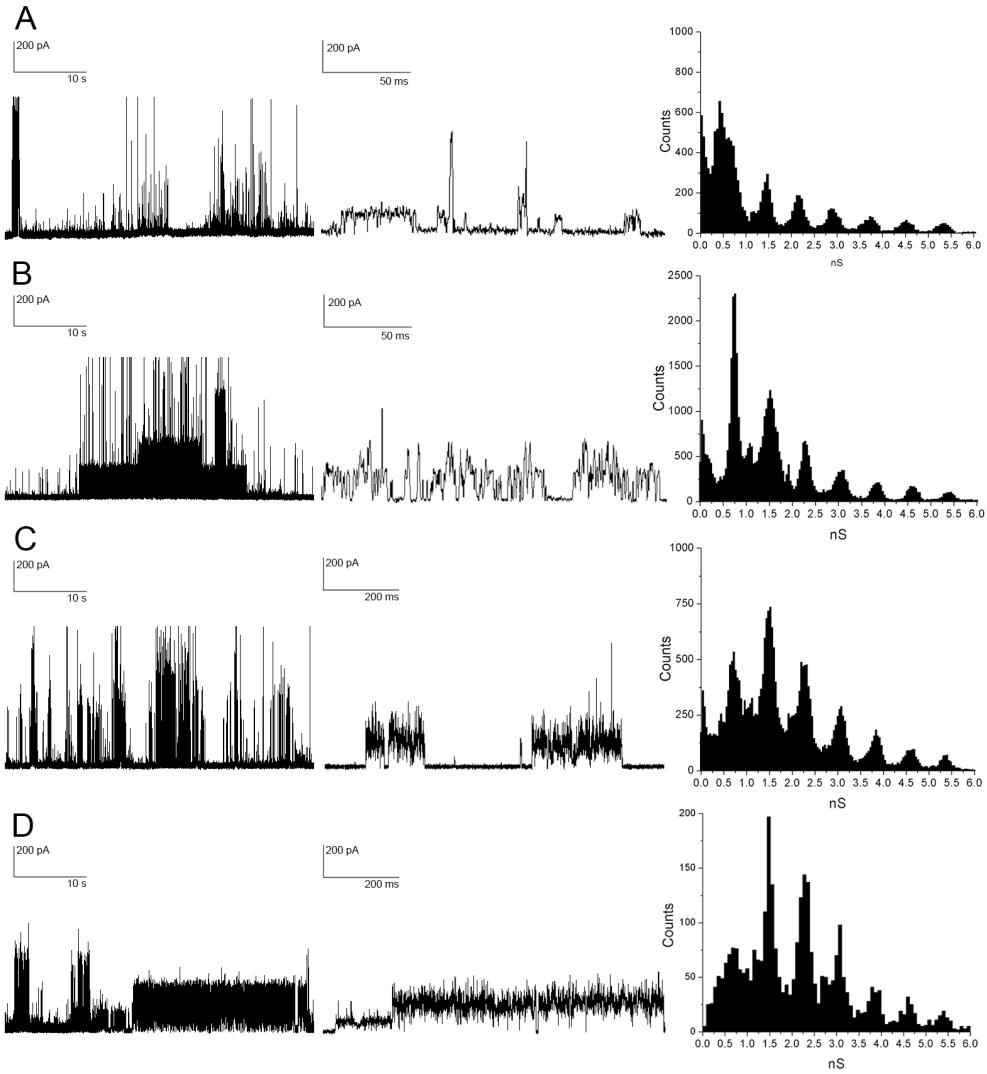

Figure 4. *Single-channel recordings of hybrid duplex at different concentrations.* Left and middle panels show two different magnifications of the traces, and the right panels show the population of conductance levels. (A) 3.5 nM. (B) 0.75 nM. (C) 0.15 nM. (D) 0.075 nM.

As a control, we analyzed the mixture of the two hybrids, Alm dUL-C-3′DNA and Alm dUL-C-5′DNA, prior to DNA hybridization (Fig. 5A). The results are similar to those of Alm dUL-C and the two hybrid peptides analyzed separately (Fig. 3A-C), indicating that the monomers assemble dynamically resulting in several oligomeric states. Importantly, these data demonstrate that in case of hybrid duplex (Fig. 3D), the two DNA-modified peptides indeed hybridized and this resulted in a preferred channel assembly. In another control the Alm dUL-C-3′DNA monomer was hybridized with Oligo 2 (Alm dUL-C-3′DNA/Oligo2) without bearing peptide (Fig. 5B), and so only monomers with double stranded DNA could be formed. As expected, the conductance states are very similar to those obtained by the Alm dUL-C-3′DNA monomer (Fig. 3B). The probability of various conductance states differed somewhat and some additional conductance levels were obtained with Alm dUL-C-3′DNA/Oligo2. This could be due to the hindrance caused by the two DNA strands

per monomer instead of one.

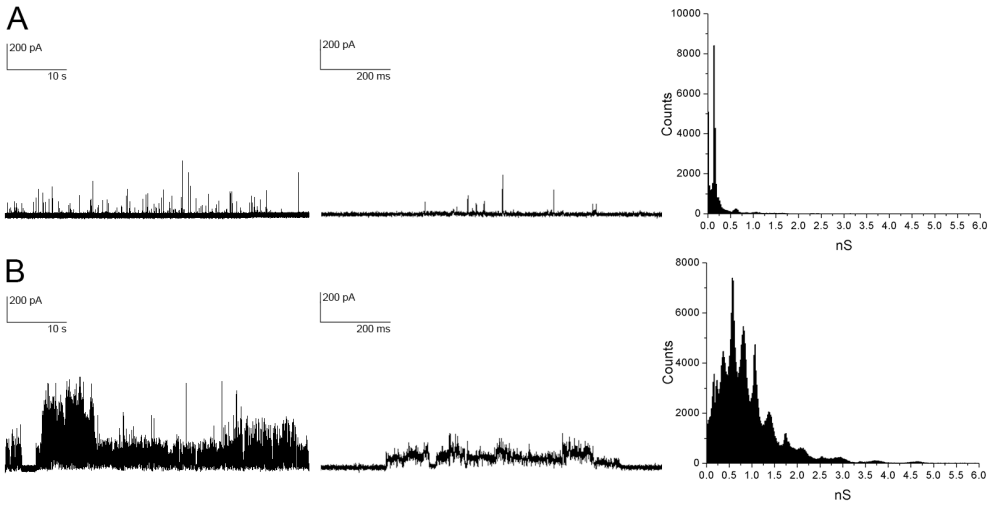

Figure 5. *Single-channel recordings of control samples.* Left and middle panels show two different magnifications of the traces, and the right panels show the population of conductance levels. (A) Mixture of Alm dUL-C-3'DNA + AlmdUL-C-5'DNA without hybridization, 3.75 nM. (B) Alm dUL-C-3'DNA/Oligo2, 3.75 nM.

DCFBA to probe the dimensions of the Alm-DNA channels

To estimate the minimal pore diameter of the channels, we performed DCFBA with different size markers encapsulated inside the vesicles. We used GSH-AF488 (Fig. 6A), 3KDa dextran-fluorescein (Fig. 6B) and 10 KDa dextran-fluorescein (Fig. 6C). We observed leakage of GSH-AF488 with Alm dUL-C-5'DNA and Alm dUL-C, as seen in fig. 6A (blue and black dashed line, respectively) by a left-shift towards lower vesicle concentrations. This indicates that the minimal pore diameter is at least 1.35 nm (hydrodynamic radius of GSH-AF488).(163) The peptide without DNA showed greater leakage (Fig. 6A, black dashed and blue lines), indicating that the DNA has some influence on the conformation or dynamics of the pore. In the case of Alm dUL-C-5'DNA we also observed substantial release of 3 KDa dextran and some of 10 KDa dextran (Fig 6B and 6C blue line). That would correspond to a pore size around 2 nm by the dimensions of the 10 KDa dextran (shortest axis measured assuming the shape of a prolate ellipsoid).(163) Surprisingly, Alm dUL-C-3'DNA and the hybrid duplex did not leak any of the size markers even though these channels facilitated the flux of ions with conductances from 0.2-1.5 for Alm dUL-C-5'DNA and a main stabilized conductance of 0.75 nS for the hybrid duplex. These data clearly show that the structure of the DNA (hybrid duplex *versus* single-stranded, and 5' *versus* 3'linked) has major impact on the channel functioning.

Figure 6D shows that the parental peptide, Alm dUL-C and the two DNA-peptide hybrids, Alm dUL-C-3'DNA and Alm dUL-C-5'DNA, resulted in a decreased number of vesicles detected, which either means that vesicles are fusing or aggregating in the presence of the DNA-peptide hybrids. When vesicle fusion or aggregation occurs, the diffusion of those slows down and less vesicles diffuse through the detected focal volume. Another reason for the decreased amount of vesicles could be vesicle disruption, although this can not be the case here as the background fluorescence in the DCFBA traces was similar in all cases.

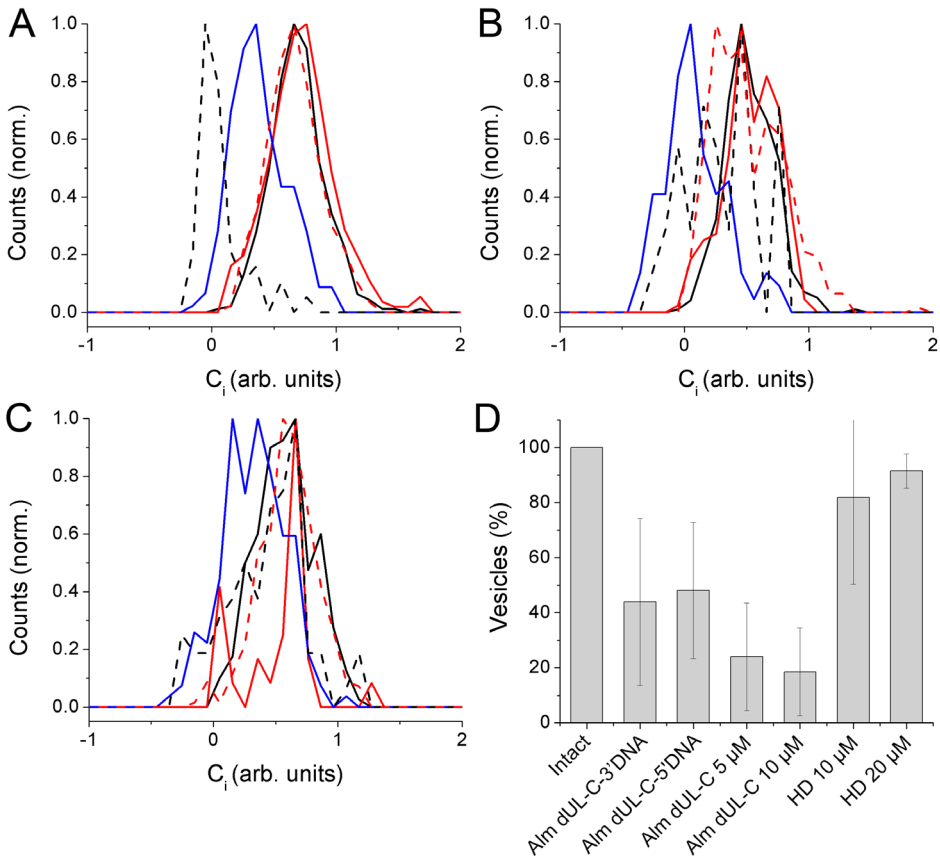

Figure 6. *Contents leakage via DNA-peptide hybrids and hybrid duplex by DCFBA analysis and using markers of different size.* (A) GSH-AF488. (B) 3 KDa dextran-fluorescein (C) 10 KDa dextran-fluorescein. Black lines: intact vesicles, without peptide; red line: Alm dUL-C-3′DNA at 10 μM; blue line: Alm dUL-C-5′DNA at 10 μM; dashed black line: Alm dUL-C at 10 μM; dashed red line: hybrid duplex at 20 μM. (D) The relative number of vesicles is given as percentage; error bars represent standard deviation of the mean (n = 3).

Conclusions

We synthesized two complementary DNA-peptide hybrids, Alm dUL-C-3'DNA and Alm dUL-C-5'DNA, and by hybridization we formed the dimeric, hybrid duplex. All the compounds inserted into the POPC/DOPE (7:3) membranes as shown by the electrical recordings and observation of single-channel conductances. The non-duplexed hybrids showed similar channel behavior as the parental Alm dUL-C peptide with conductance states in 1 M KCl of about 0.2, 0.6 and 1 nS, which by comparison with literature (267), could correspond to tetrameric, pentameric and hexameric channels. In contrast, the hybrid duplex gave a main conductance state of about 0.75 nS, which would be equivalent to a pore diameter of about 0.6 nm. Considering the hindering effects of the DNA strands, we assign this conductance state to the hexameric assembly. Tetrameric assemblies of alamethicin gave lower conductance levels (0.1-0.2 nS) (78). A pore size estimated from electrophysiology of about 0.6 nm is in agreement with the DCFBA experiments as none of the marker molecules leaked out of the vesicles when the hybrid duplex was used. The smallest marker, GSH-AF488, has an approximate diameter of 1.35 nm measured by its hydrodynamic radius) (163). Because GSH-AF488, the 3KDa-dextran and the 10 KDa-dextran are released from one of the DNA hybrids, Alm dUL-C-5'DNA, the pore diameter must be at least 2 nm. The size is in agreement the highest conductance analyzed by this compound, 5.25 nS, corresponding to a pore diameter of 1.8 nm. The parental peptide Alm dUL-C only allowed the leakage of GSH-AF488, what corresponds to a pore size of at least 1.35 nm, also in agreement with the maximum conductance observed of 4 nS equivalent to a pore diameter of 1.55 nm.

In summary, the DNA-driven dimerization of Alm dUL-C stabilizes the channel and may be a means to control the gating by further functionalization of the DNA moiety. Disassembly of the dimers with competing DNA or other strategies could lead to release of molecules with a diameter up to about 1.35 nm.

APPENDIX: The use of G-quadruplex DNA as a scaffold for Alm dUL-C channels

We used the G-quadruplex DNA motif as a scaffold to build a tetrameric peptide-based channel (Scheme 4). G-rich synthetic nucleotides can have a unique structure that have found applications in biotechnology and nanotechnology (269). G-quadruplexes have also been investigated as building blocks for creating and mimicking ion channels. Different G-quadruplex structures have been reported depending on the orientation of the strands. Here, we use the Oligo G (GGGTT) that forms a parallel G-quadruple in the presence of potassium ions as depicted in scheme 4.

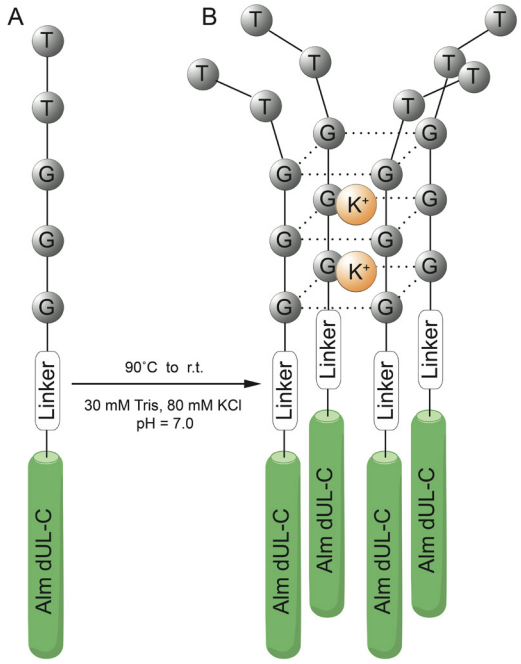

Scheme 4. Schematic representation of G-quadruplex DNA based peptide formation. (A) Alm dUL-C-G hybrid. (B) G-quadruplex-peptide, GQ.

Materials and methods

Reagents. Oligo G (H_2N-$(CH_2)_6$-$^{5'}$GGGTT$^{3'}$) and Oligo N (H_2N-$(CH_2)_6$-$^{5'}$GTATT$^{3'}$) were purchased from BioTez (Berlin Buch).

Synthesis of the maleimide-funcionalized DNA. Same procedure as for the maleimide(2)-3′DNA and maleimide(2)-5′DNA (see previous materials and methods)

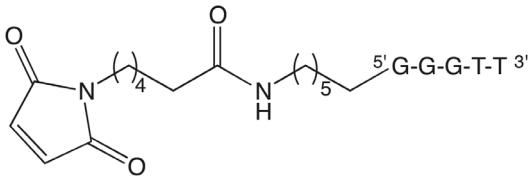

Maleimide(2)-G
RP-HPLC retention time = 30 min
MALDI-TOF (m/z) = 1905 (calculated 1904)

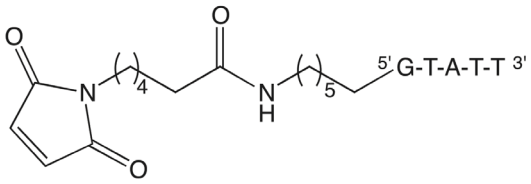

Maleimide(2)-Gnegative
RP-HPLC retention time = 39 min
MALDI-TOF (m/z) = 1865 (calculated 1863)

Synthesis of the DNA-peptide hybrids. Same procedure as for Alm dUL-C-3′DNA and Alm dUL-C-5′DNA (see previous materials and methods)

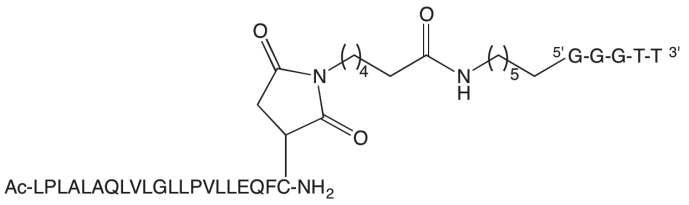

Alm dUL-C-G hybrid
RP-HPLC rt = 70 min
MALDI-TOF (m/z) = $[M+2K–H^-]^+$ 4289 (calculated 4288)

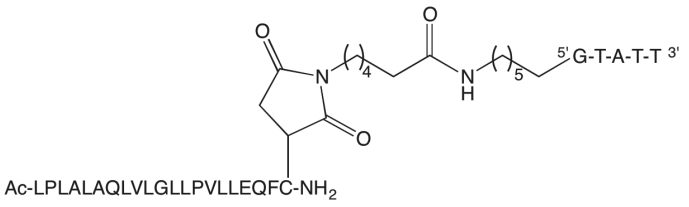

Alm dUL-C-Gnegative hybrid
RP-HPLC rt = 43 min
MALDI-TOF (m/z) = 4172 (calculated 4170)

Results

Synthesis of the DNA-peptide hybrids and the G-quadruplex

The Alm dUL-C-G hybrid was obtained via the complementary DNA strands (see previous section). Scheme 5 shows the two reactions carried out. The amino modified Oligo G reacted with ester 2, resulting in the maleimide conjugate of the oligo, Maleimide(2)-G (Scheme 5A). The compound was then purified by size-exclusion chromatography. The final hybrid was obtained by mixing the maleimide (2)-G in TEAA with the Alm-dUL-C in DMF under nitrogen atmosphere overnight (Scheme 5B). Purification of the conjugates was performed by RP-HPLC and can be seen in figure 7.

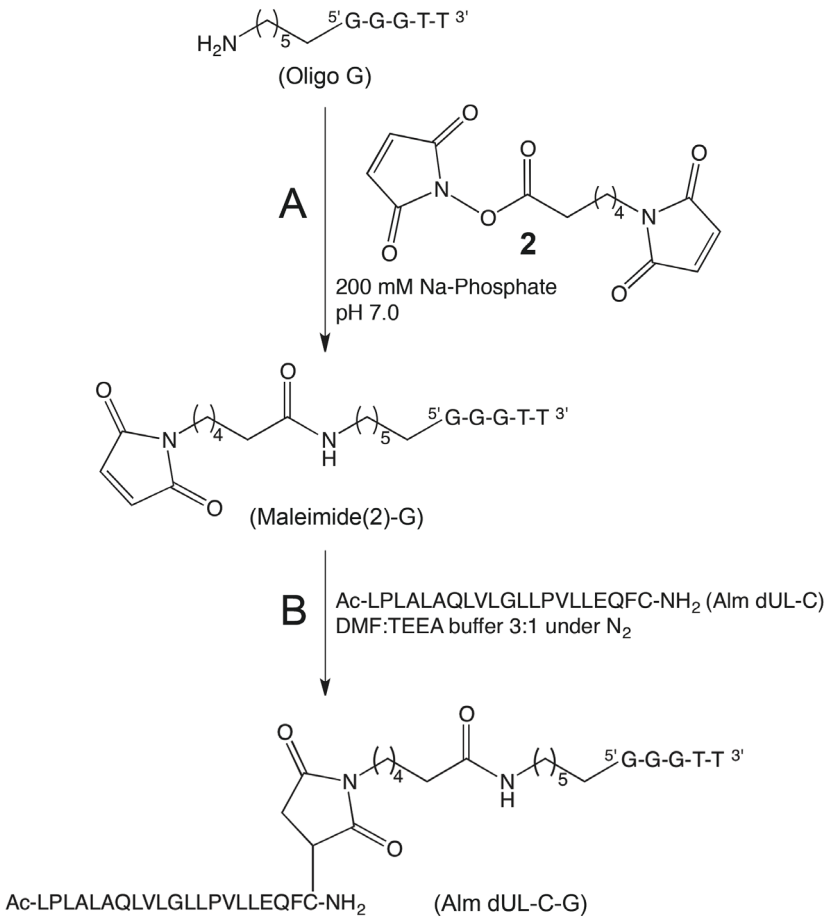

Scheme 5. *Synthesis of the DNA-peptide hybrids from Oligo G with ester* 2. (A) Yield of 85 %. (B) Yield of 20 %. Total yield of 17 %.

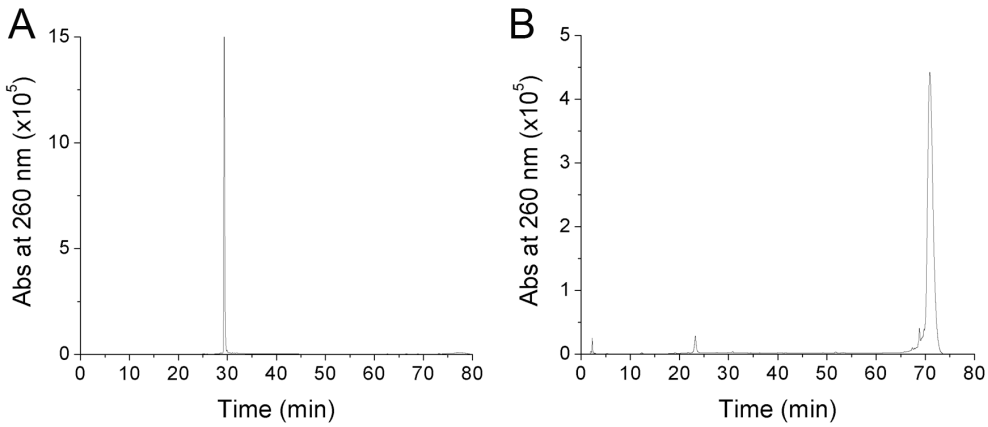

Figure 7. *RP-HPLC traces of maleimide-functionalized DNA and DNA-peptide hybrids*. (A) Maleimide(2)-G. (B) Alm dUL-C-G hybrid.

As a control we synthesized another DNA-peptide conjugate with the Oligo N (GTATT), that is not able to form G-quadruplexes. This hybrid, Alm dUL-C-Gnegative, remains monomeric and serves as a control for the tetrameric assembly of the GQ. Alm dUL-C-Gnegative was obtained by reacting the amino modified Oligo with the maleimide ester 2 (same reactions than in scheme 5) with a yield of 87 %. Then, by reaction with the Alm dUL-C, the hybrid was obtained with a yield of 23 % and final yield of 20 % over the two steps. Figure 8 shows the MALDI-TOF spectra of the two hybrids synthesized, Alm dUL-C-G hybrid and Alm dUL-C-Gnegative hybrid.

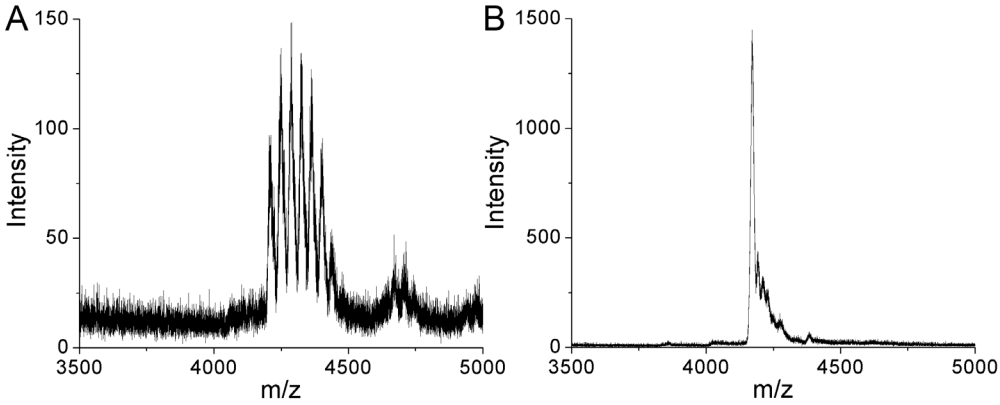

Figure 8. *MALDI-TOF spectra of the DNA-peptide hybrids*. (A) Alm dUL-C-G, m/z = 4289. The different peaks are the result of positive ions trapped in the quadruplex structure (e.g. Na^+ and K^+). (B) Alm dUL-C-Gnegative, m/z = 4172.

The oligo G-peptide should fold and form a G-quadruplex motif in the presence of potassium ions. One of the techniques commonly used to identify and characterize the G-quadruplex formation is circular dichroism (CD) spectroscopy (270). Figure 9 shows the CD spectra of the two DNA-peptide hybrids. The Alm dUL-C forms a α-helix peptide and yields a different CD spectrum than parallel G-quadruplex or β-DNA structures. The single strands of DNA are expected to be orientated 5'-3' folding into a parallel G-quadruplex structure, with a positive band at ~260 nm and a negative band at ~240 nm. As anticipated, in the case of Alm dUL-C-Gnegative hybrid no G-quadruplex structure was obtained.

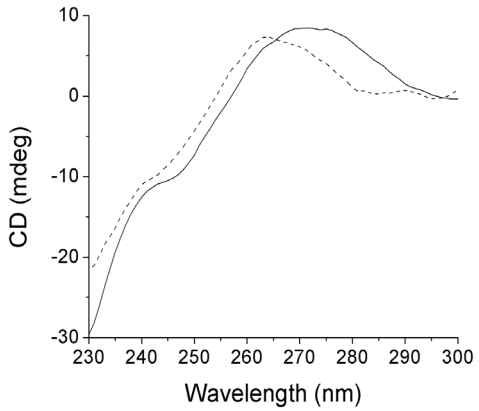

Figure 9. *CD spectra of the DNA-peptide hybrids*. Dashed black line represents the Alm dUL-C-G forming the GQ. Full black line represents the Alm dUL-C-Gnegative hybrid.

GQ forms a channel with a main conductance state of 1 nS

The channel behavior of the G-quadruplex forming hybrid, Alm dUL-C-G, and the negative control, Alm dUL-C-Gnegative, was studied by electrophysiology measurements (see previous materials and methods). In this case, a voltage of 180 mV was applied for a few minutes to decrease the time needed to observe activity. All the recordings were subsequently conducted at 60 mV. Figure 10 shows the single-channel recordings. As expected, the Alm dUL-C-Gnegative yielded different conductance states, corresponding to a different number of monomers assembling together; the first observed level was populated the most and corresponded to a conductance of around 0.2 nS (Figure 10A), which is similar to the behavior of Alm dUL-C, Alm dUL-C-3'DNA and Alm dUL-C-5'DNA (see above). The negative control was not able to form a stable preferred assembly but instead aggregates in a dynamic fashion. In contrast, the GQ mainly stabilizes one preferred conductance state of about 1 nS with relatively long-lived events (Fig. 10B), corresponding to a pore diameter of 0.7 nm by using Eq. 1. The other conductance levels represent multiples of 1 nS, corresponding to more than one channel opened simultaneously. Thus, the G-quartet motif dictates the aggregation of the peptides resulting in a tetrameric synthetic channel.

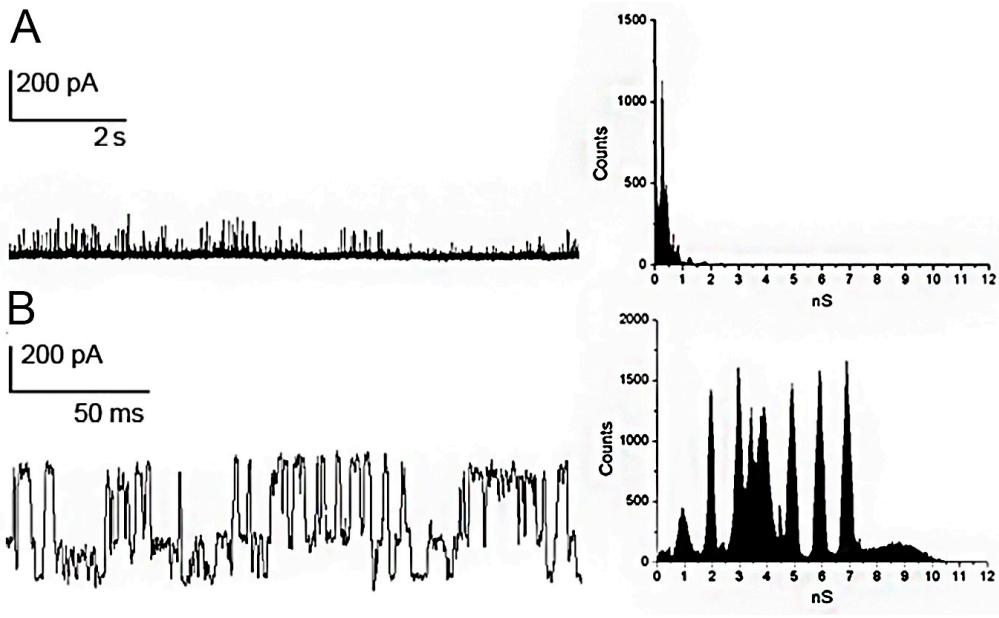

Figure 10. *Single-channel recordings of the DNA-peptide hybrids.* Left and middle panels show two different magnifications of the traces, and the right panels show the population of conductance levels. (A) Negative control, Alm dUL-C-Gnegative hybrid, 3.5 nM (B) GQ, 3.5 nM.

DCFBA shows no leakage of any size marker analyzed

The DCFBA analysis with the three different size markers of tetrameric G-quadruplex, GQ and the negative monomeric Alm dUL-C-Gnegative hybrid are shown in figure 11. The results show no leakage of any size marker analyzed, not even the smallest i.e. GSH-AF488 which is 1.35 nm in diameter (Fig. 11A-C; dashed black lines). Surprisingly, the negative control, Alm dUL-C-Gnegative gave similar results, even though the monomers have the freedom to associated and dissociate. DNA repulsions of the single strands may influence the number of monomers associating and thus the pore size.

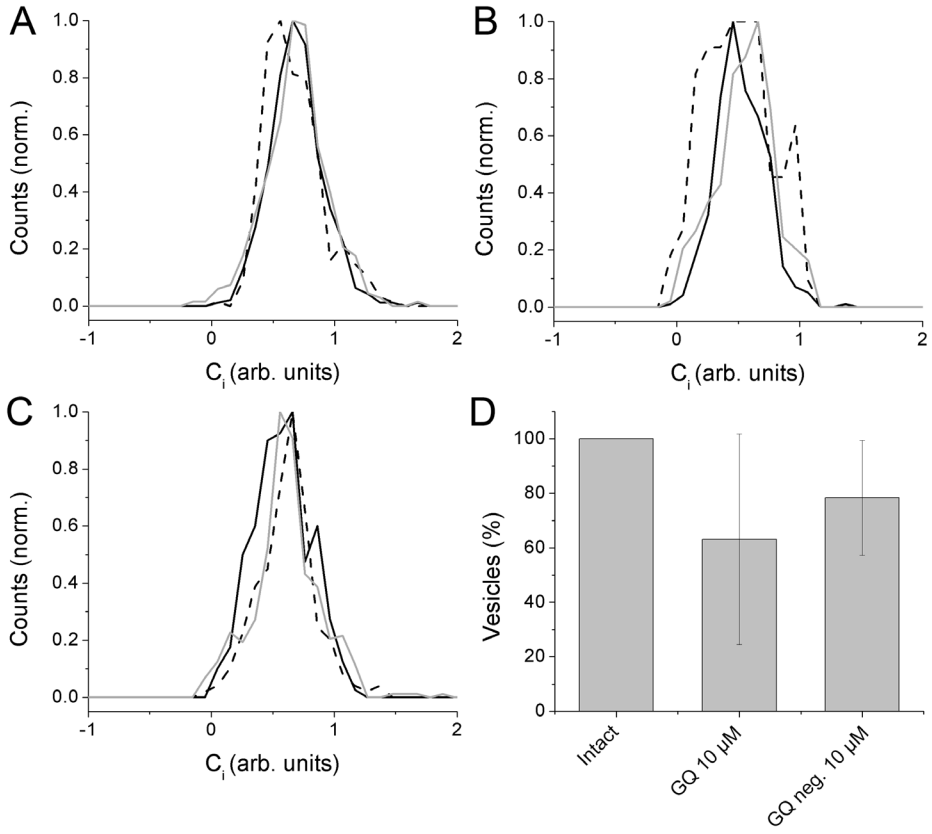

Figure 11. *Pore leakage by DCFBA analysis using different size markers.* (A) GSH-AF488. (B) 3 KDa dextran-fluorescein (C) 10 KDa dextran-fluorescein. Black lines: intact vesicles, without peptide; dashed black line: GQ at 10 μM; grey line: Alm dUL-C-Gnegative at 10 μM. (D) Relative amount of vesicles indicated as %; error bars represent the standard deviation of the mean (n = 3).

Conclusions

The synthesis of a tetrameric alamethicin-based synthetic channel was achieved by the hybridization of Alm dUL-C peptide with a 5-mer oligonucleotide that forms a G-quadruplex in the presence of potassium ions. The channel had a conductance of about 1 nS, which could correspond to a pore diameter of 0.7 nm. This pore size is consistent with the absence of contents release from vesicles shown by DCFBA.

Chapter 6

Membrane domain disruption by disaccharides

Gemma Moiset*, César A. López*, E. Rijpkema, L. Syga, R. Bartelds, Abhishek Cukkemane, Marc Baldus, Bert Poolman and Siewert J. Marrink

(*) These authors contributed equally to this work.

Manuscript in preparation

Disaccharides are well known for their membrane protective ability by coating the lipid headgroups. Interaction between sugars and multi-component membranes, however, remains largely unexplored. Here we combine molecular dynamics simulations and fluorescence microscopy to study the effect of mono- and disaccharides on model membranes that phase separate into L_o and L_d domains. Remarkably, we find that non-reducing disaccharides strongly destabilize the L_o phase leading to uniformly mixed membranes. Monosaccharides, on the other hand, do not have a noticeable effect on the phase behavior, even when the concentration is increased to a matching level of sugar rings. To unveil the driving force for this process, additional simulations were performed in which the sugar linkage was artificially modified. These data point to an incommensurate nature of the disaccharide geometry and the lipid cholesterol packing in the L_o phase. Together, our results show that non-reducing disaccharides can have a strong impact on lateral membrane organization. The mechanism by which disaccharides disturb the L_o domain might prove to be a more generic way by which surface bound agents could affect membranes.

Introduction

One of the most intriguing phenomena in biology is the occurrence of anhydrobiosis in the life cycle of several organisms from all kingdoms of life such as yeasts, tardigrades, nematodes, bacteria and plants. In the anhydrobiotic state, the amount of liquid water in the organism is reduced to a level where the metabolism is completely (but reversibly) stopped (47, 48, 271). A common physiological response to anhydrobiosis is the synthesis of cryo-protective sugars, such as the disaccharides sucrose and trehalose, which are accumulated intracellularly also during temperature drifting, osmotic shifting and oxidative stress (272-274).

The direct interaction between lipid and sugar molecules have been demonstrated by a diversity of experimental techniques, including infrared spectroscopy, differential scanning calorimetry, nuclear magnetic resonance (NMR), and X-ray diffraction (61, 275-279). Sugars have proven to be effective in protecting membrane by lowering the gel-fluid phase transition upon dehydration. This phenomenon has been observed for the monosaccharide glucose and disaccharides sucrose and trehalose (49, 50, 52-55). The effect can be explained by a direct replacement of the water molecules by the sugars, preventing the increase in the packing of the lipid acyl chains in the dry state. This effect is called the "water replacement" hypothesis (52, 55, 56, 60). Other explanations for the protection ability of sugars during dehydration are the "vitrification", the "water-entrapment" and the "hydration repulsion" hypotheses, which indicate that sugars protect biomolecules by the formation of amorphous glasses, by concentrating water molecules close to the membrane or by being excluded from the surface (57-60). The latter would reduce the compressive stress of the membrane upon dehydration. Even though different hypotheses have been put forward, several studies have indicated that different mechanisms of protection may act simultaneously (60).

In fully hydrated membranes the sugar-lipid interactions have been classified in the "interaction" and "exclusion" hypotheses. In the first one the sugars interact directly with the lipid membranes as seen by an expansion of the phospholipid monolayers when sucrose or trehalose are added (49, 62, 280, 281). The increased membrane area is caused by the sugars intercalating between the lipid headgroups. On the contrary, the "exclusion" hypothesis, describes a partial depletion of sugar in the hydration zone of the lipid bilayer (55, 59, 61, 62). Andersen and coworkers demonstrated that the two opposing views on lipid-sugar interactions might both be true and take place simultaneously. At low sugar concentration the attractive contribution between sugar and lipid by hydrogen bonding dominates, resulting in a lateral expansion of the membrane due to the intercalation of the sugars in between the lipid headgroups. At higher concentrations the kosmotropic contribution dominates, which causes a general depletion of sugars from aqueous interfaces (62).

So far, studies have been mostly directed at simplified model membranes. Real membranes, however, consist of a complex mixture of hundreds of different lipid types and proteins. The current view describes biomembranes as a heterogeneous material in which preferential association of certain lipids, sterols, and proteins can lead to the formation of nanodomains, so-called "lipid rafts". Such rafts, enriched in cholesterol and saturated lipids, display physicochemical properties different from those of their disordered fluid surroundings, and are believed to play an important role in the self-assembly of membrane proteins into functional platforms (1, 18, 282). Thus, a complete overview of the mechanism of action of different sugars should be undoubtedly analyzed and compared in terms of membranous lateral heterogeneity.

In this work we have used molecular dynamics (MD) simulations together with fluorescence confocal microscopy to study the effects of sugars on membranes with coexisting L_o and L_d domains. We found that the lateral organization of the membrane is drastically affected by the interaction with small sugars. Single monosaccharides (glucose and fructose) and reducing disaccharides (including palatinose, maltose and gentiobiose) do not modify the L_o/L_d equilibrium, while non-reducing disaccharides (e.g. trehalose and sucrose) disrupt the domains and promote lipid re-mixing. The effect is observed at relatively low amounts of sugar and apparently inherent to the disaccharides structure.

Materials and methods

Molecular dynamics simulations

All simulations were carried out with the Gromacs MD package, version 4.0.5. The MARTINI coarse grained (CG) force field (283, 284) was used to describe the interactions. Molecules considered in this study are the saturated lipids dipalmitoyl-phosphatidylcholine (diC(16:0)PC, DPPC), the unsaturated lipid dilinoleoyl-PC (diC(18:2)PC, DLiPC), cholesterol, and the sugars glucose (GLC), trehalose (TRH), and sucrose (SUC) at 60 mM, 200 mM, and 600 mM concentrations. An equilibrated L_o/L_d lipid bilayer (285) was used as initial conformation for our simulations. The system is composed of 769 DPPC, 507 DLiPC, and 538 cholesterol molecules (4:3:3 molar ratio). Additional simulations of L_o and L_d mimetic membranes were used to probe the structural effects of sugar binding. The L_o membrane consists of 328 DPPC and 164 cholesterols (2:1 ratio), the L_d membrane of 448 DLiPC and 44 cholesterols (10:1 ratio). Temperature in each case was maintained by coupling to a heat bath at 288 K.

GUVs preparation

GUVs were prepared by electroformation (286, 287). Briefly, a lipid mixture of N-stearoyl-D-*erythro*-sphingosylphosphorylcholine (SM), 1,2-dioleoyl-*sn*-glycero-3-phosphocholine (DOPC) and cholesterol was prepared from the lipid stock solution in chloroform/methanol (9:1) with a molar ratio of 4:3:3 (lipids were purchased from Avanti Polar Lipids). The fluorescent lipid marker DiI-C_{18} (1,1′-dioctadecyl-3,3,3′,3′-tetramethylindodicarbocyanine perchlorate, Molecular Probes, Invitrogen) dissolved in chloroform, and the ovine brain ganglioside GM1 (GM1, Avanti Polar Lipids) dissolved in methanol were added to the lipid mixture at the amount of 0.1 mol%. The lipid mixture was applied to indium-tin oxide-coated glasses, solvents were evaporated and glasses were pre-warmed at 50ºC before placing them in the electroformation chamber of Nanion Vesicle Prep Pro (Nanion Technologies GmbH, Munich, Germany). The chamber was filled with buffer (10 mM KPi, pH 7,2) or buffer containing different concentrations of saccharides, pre-warmed at 50ºC. An alternating current was applied across the cell unit with 1.1 V, 10 kHz of frequency and 50ºC for 1 hour. Sugar solutions osmolarities were checked on OSMOMAT 030 (Genotec). GUVs had a diameter of 5–15 μm. As a control we repeated some of the experiments with DPPC instead of SM similar as in the MD simulations (data shown in Fig. 8 and Table 3).

GM1 labeling with AF-488

Labeling was done according to an established protocol with minor modification (288). Briefly, GM1 was kept on ice for 30 min with oxidizing reagent (sodium meta-periodate). After the oxidation of GM1, sodium sulfite was used to quench excess of sodium meta-periodate instead of using ultrafiltration (289). Subsequently, Alexa Fluor 488 hydrazide was added. The reaction was conducted at room temperature for 2 hours, after which GM1 was separated from free AF488 by size-exclusion chromatography (GE Healthcare NAP5 Sephadex G-25 column).

Confocal fluorescence microscopy and data analysis

GUVs were incubated for 10 minutes with the Alexa Fluor 488 conjugate of cholera toxin B subunit (AF-CTB, Molecular Probes, Invitrogen), for which GM1 is the natural receptor; the complex GM1-CTB was detected only in areas from which DiI-C_{18} was strongly excluded (290). Thus, AF-CTB reports SM-enriched (L_o) domains and DiI-C_{18} reports DOPC-enriched domains. After incubation, GUVs were immobilized with the hydrogel Articyt (Nano-FM), previously adjusted to the desired saccharide concentration to avoid osmotic stress. Samples were imaged on a commercial laser-scanning confocal microscope, LSM 710 (Carl Zeiss MicroImaging, Jena, Germany), using an objective C-Apochromat 40×/1.2NA, a blue argon ion laser (488 nm) and a red He-Ne laser (633 nm) at 20ºC or 40ºC. The pixel dwell time for the laser-scanning was 2,55 μs with a pixel step of 0.2 μm. Images were collected from two independent lipid preparations (biological replicates) for each sugar concentration and each preparation was analyzed three times (technical replicates), from which technical errors were subtracted. A total of 500 GUVs were analyzed from randomly chosen images of each sugar concentration. GUVs were classified in four categories: Mixed (where the probes of the liquid-ordered and disordered phases co-localize), Separated (where the two probes are localized in different domains), Red (vesicles stained with DiI-C_{18} and reporting the liquid-disordered phase) or Green (vesicles stained with AF-CTB and reporting the liquid-ordered phase). The purely red and green vesicles are likely due to the heterogeneity in the GUV formation, i.e. not all the vesicles constitute a ternary mixture of SM, DOPC and Cholesterol. We cannot rule out that in the red and green vesicles the complementary domains are present with dimensions below the optical resolution but consider heterogeneity in the vesicle by electroformation more likely. For each concentration, weighted averages and standard deviations were calculated (considering the number of GUVs per image) for the technical replicates and for the biological replicates.

Solid state NMR

All ssNMR experiments were conducted using 3.2 mm triple-resonance (^{1}H,^{13}C,^{15}N) probe heads at static magnetic fields of 18.8 T corresponding to 800 MHz, ^{1}H resonance frequency. The maltose solution and lipid based samples were spun at magic angle spinning (MAS) rates of 3 kHz and 12 kHz, respectively, at 25˚C. The natural abundance ^{13}C detected 1D experiments included cross polarization (CP) and direct excitation-based measurements (291). CP duration of 1 ms was employed according to the n=-2 Hartmann-Hahn matching condition with rf field strengths of 83 kHz (^{1}H) and 50 kHz (^{13}C) with SPINAL64 ^{1}H decoupling at 83 kHz during detection periods (292). All data were processed using a Brüker Topspin 2.1, Patch Level 6, and the 2D spectra were analyzed using SPARKY (293). Chemical shifts of the molecules were annotated on the basis of reported assignments for lipids (294, 295) and maltose (296, 297).

Results

Liquid-ordered domains dissolve when coated with disaccharides in computer simulations

To probe the effect of sugars on phase-separated membranes, we modeled a ternary membrane system composed of DPPC, DLiPC and cholesterol (4:3:3 molar ratio), which is laterally partitioned into two coexisting fluid domains: a L_o domain rich in saturated lipids (DPPC) and cholesterol, and a L_d domain containing a high amount of the polyunsaturated lipid (DLiPC) and a reduced level of cholesterol. We performed MD simulations of this system at a coarse-grained (CG) level of resolution, using the Martini force field (298).

Figure 1A shows the CG topology for the different lipid and sugar molecules simulated, together with the starting structure of the system. In the absence of sugars, the domain separation is stable, in line with the experimental phase diagram for similar ternary mixtures (299). However, after the addition of 200 mM of sucrose, we observe a clear destabilization of the L_o and L_d domains as illustrated in the graphical snapshots from the simulation (Figure 1B). To quantify the mixing of the lipid constituents, the fraction of contacts between the saturated and unsaturated lipids was calculated (Figure 1C). The number of contacts steadily increases during the simulation, pointing to a destabilizing effect of sucrose on the domains. Towards the end of the simulation, after 2 μs, an almost homogeneously mixed membrane is observed. The mixing process seems to occur very fast, with nearly 75% of the final fraction of contacts established within 0.5 μs. We obtain similar results when we replace sucrose by another disaccharide, trehalose (Figure 1C). While the disturbing effect is observed with both disaccharides, the lateral distribution is more strongly affected by the addition of sucrose. At high sugar concentrations, 600 mM, the effect of trehalose is smaller than that of sucrose and even smaller than that of 200 mM trehalose.

Remarkably, performing the simulations with the monosaccharide glucose, the domains appear perfectly stable (Figure 1C). To make sure this difference does not arise solely from the amount of sugar rings, we compared different concentrations monosaccharide and disaccharides containing the same moles of rings, e.g. 400 mM glucose compared to 200 mM trehalose. The results indicate that even when the same number of rings is present only trehalose and sucrose are affecting the membrane organization.

AF-CTB is the most suitable L_o marker

Three different ways of labeling the liquid-ordered phase were studied as shown in Figure 2. Head-labeled GM1 with AF488 is localized in both, L_o and L_d, phases (Fig. 2A) albeit with a preference for Lo. Tail-labeled GM1 with BODIPY mislocalizes in the L_d phase, as seen by the co-localization with the L_d marker DiI-C_{18} (Fig. 2B). This is most likely due to the presence of the fluorophore in the lipid tail, which adds a degree of disorder. Free GM1 in the presence of AF-CTB is predominantly localized in the L_o phase and excluded from the L_d marker DiI-C_{18} (Fig. 2C). The toxin clusters the ganglioside by binding to different subunits. Those clusters have a stronger preference for the L_o phase than monomeric GM1. This method proved most suitable for discriminating L_o and L_d phases and mixing of lipid phases upon addition of saccharides.

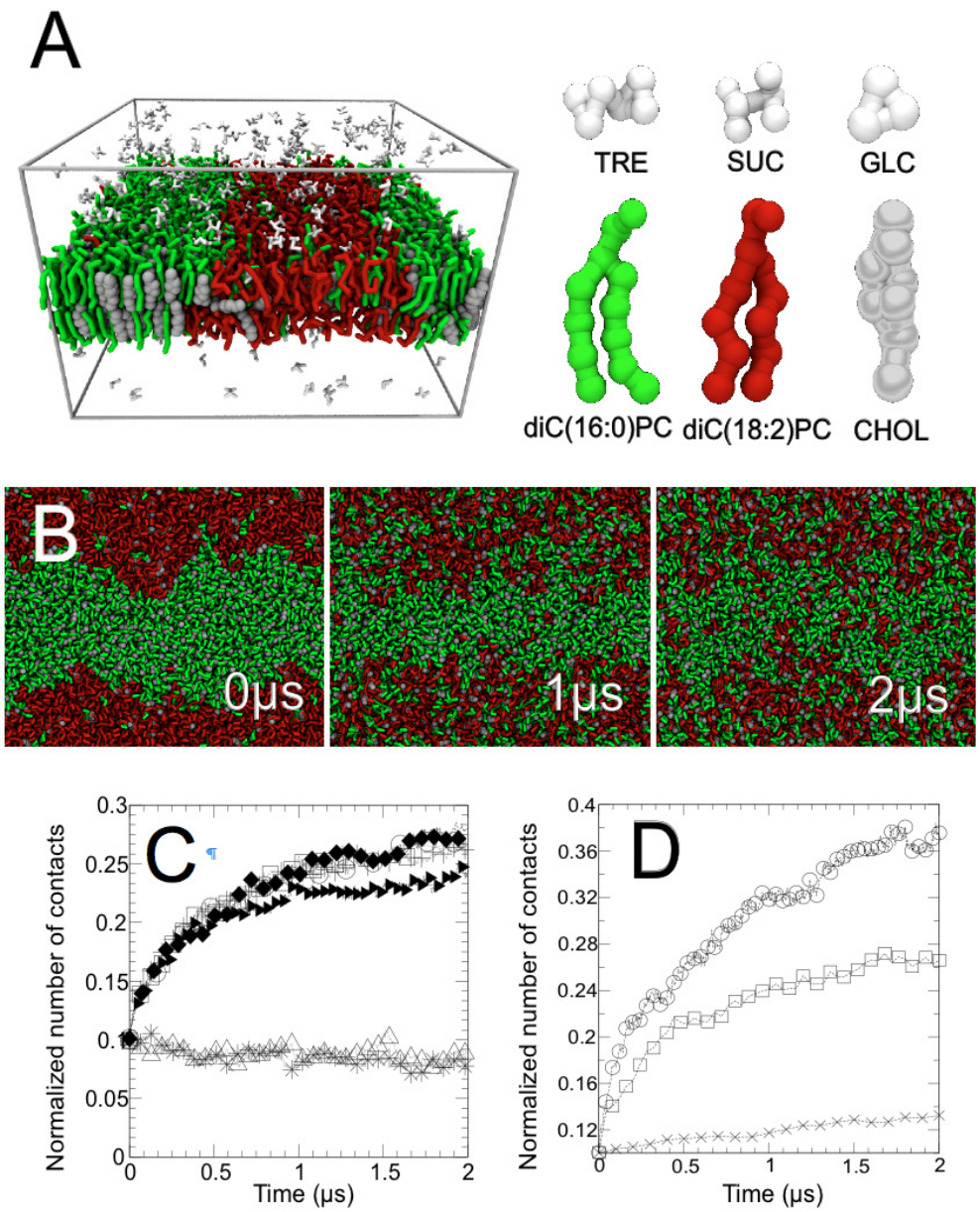

Figure 1. *Domain mixing induced by disaccharides.* (A) Starting configuration, membrane phase separated into L_o and L_d domains enriched in saturated (green) and unsaturated (red) lipids, respectively. Cholesterol (grey) and sugars (white) are also depicted. Water is not shown. (B) Time series of lipid mixing after the addition of 200 mM sucrose. (C) Normalized number of contacts between saturated and unsaturated lipids after the addition of 100 mM sucrose (crosses), 200 mM sucrose (open circles), 600 mM sucrose (filled squares), 200 mM trehalose (open squares), 600 mM trehalose (filled triangles), 200 mM glucose (open triangles), and 400 mM glucose (stars). (D) Normalized number of contacts between saturated and unsaturated lipids after the addition of 200 mM sucrose using either longer bonds (crosses) or flexible rotation points (open circles) between the two independent sugar rings. The profile for normal sucrose at 200 mM is shown as reference (open squares).

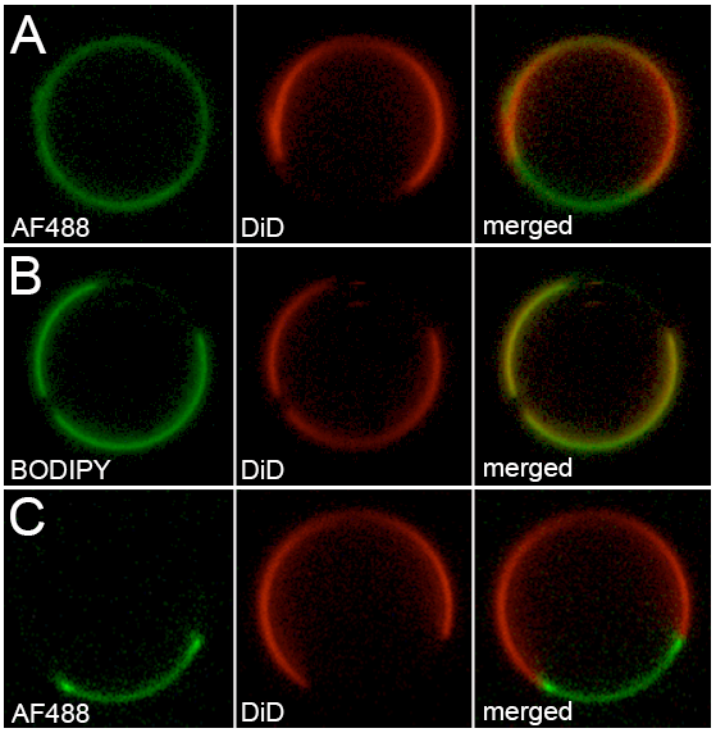

Figure 2. *Images of GUVs with different L_o labeling strategies.* (A) Head-labeled AF488-GM1. (B) Tail-labeled BODIPY-GM1. (C) AF-CTB bound to GM1.

Confocal imaging confirms the potent effect of non-reducing disaccharides on membrane organization

To test the in silico predictions, we analyzed the lipid organization of GUVs by confocal fluorescence microscopy at 20ºC. GUVs composed of SM:DOPC:Cholesterol (4:3:3) were formed in the presence of different saccharides (Figure 3 for structures of all compounds used in this study). We quantified the disruption of the membrane organization by calculating the percentage of vesicles that showed lipid mixing, i.e. fluorescence co-localization of L_o and L_d domains in the presence of sugars. In all the experiments, we used the pair DiI-C_{18} and AF-CTB bound to the GM1 as L_d and L_o marker, respectively (Kahya JBC 2003), proven to be the best L_o/L_d labeling pair compared to DiI-C18 with either head- or tail-labeled GM1 (Fig. 2).

Figures 4A and 4B show and example of a vesicle with L_o and L_d domain mixing and no mixing, respectively. The quantification of the lipid mixing in the presence of different concentrations of glucose, sucrose and trehalose is shown in Figure 4C. The two disaccharides, sucrose and trehalose, increased the mixing of the lipid domains more than the monosaccharide glucose did. However, at the highest concentration of trehalose, 800 mM, the mixing effect seems to decrease. In line with the simulations, at high concentrations trehalose has a less disruptive effect on the membrane organization than sucrose (Fig.1C), and in fact the trehalose gets expelled more from the bilayer. Overall, the MD simulations and experimental data are in agreement with each other.

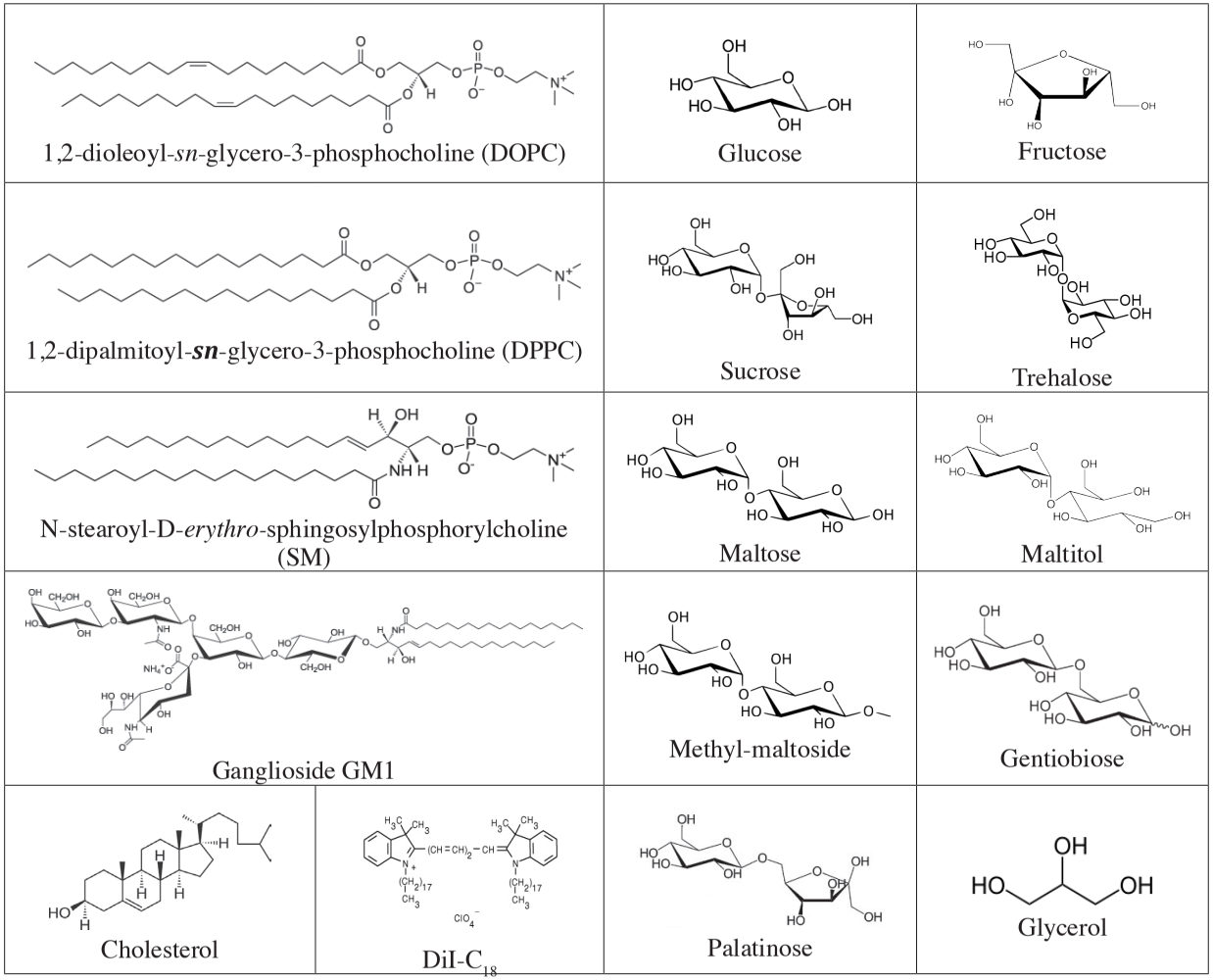

Figure 3. *Structure and names of the compounds used in this study.*

The percentage of GUVs showing lipid mixing with the highest concentrations of disaccharides is not particularly high. This is most likely due to heterogeneity in the GUVs, i.e. not all the vesicles constitute a ternary mixture of SM, DOPC and Cholesterol. In all the samples we also observed a substantial amount of vesicles with only L_o or L_d staining, and seemingly formed by only one or two types of lipid (Table 1). However, there is a clear difference between the effects of the two disaccharides, sucrose and trehalose, and the monosaccharide glucose on the membrane organization.

Table 1. Results of all saccharides used in this study.

	Concentration [mM]	Osmolarity [Osm/kg]	Mixed GUVs [%]	Separated GUVs [%]	Green GUVs [%]	Red GUVs [%]
KPi	0	0	0 ± 0	83.5 ± 5.7	13.9 ± 5.1	2.6 ± 0.6
Glucose	50	0.052	0 ± 0	73.9 ± 6.8	18.8 ± 3.8	7.3 ± 2.9
	100	0.113	0 ± 0	62.2 ± 5.5	22.4 ± 2.7	15.4 ± 2.8
	300	0.325	0.2 ± 0.3	57.8 ± 1.7	36.5 ± 1.0	5.5 ± 1.0
	400	0.439	0.5 ± 0.2	68.2 ± 6.7	27.2 ± 4.5	4.1 ± 2.1
	600	0.616	0.8 ± 0.3	70.5 ± 4.2	23.5 ± 4.7	5.2 ± 0.1
	800	0.817	1.3 ± 0.5	71.7 ± 1.5	24.5 ± 3.1	2.5 ± 1.0
Sucrose	50	0.040	0.4 ± 0.01	67.5 ± 0.2	22.6 ± 1.9	9.5 ± 1.7
	200	0.214	1.3 ± 0.005	59.8 ± 0.5	35.7 ± 0.9	3.2 ± 0.4
	300	0.299	4.3 ± 0.9	64.5 ± 0.1	26.0 ± 0.8	5.2 ± 0.3
	400	0.405	8.5 ± 1.0	63.8 ± 12.5	23.5 ± 9.0	4.2 ± 2.9
	600	0.604	14.6 ± 0.9	56.5 ± 8.1	22.8 ± 6.6	6.1 ± 2.5
	800	-	16.3 ± 0.04	54.9 ± 0.8	22.6 ± 0.3	6.2 ± 0.5
Trehalose	100	0.118	2.0 ± 0.5	69.9 ± 1.6	22.2 ± 1.2	5.9 ± 0.1
	400	-	4.9 ± 1.9	42.2 ± 7.7	23.1 ± 5.6	29.8 ± 12.8
	600	0.584	11.8 ± 1.5	51.9 ± 12.7	19.1 ± 3.9	17.2 ± 6.8
	800	-	8.0 ± 2.6	41.5 ± 3.7	32.1 ± 13.8	18.3 ± 11.1
Fructose + Glucose	300	-	0.8 ± 0.02	60.0 ± 6.9	26.8 ± 6.5	12.6 ± 13.4
Palatinose	400	0.399	1.3 ± 0.5	68.2 ± 5.0	25.1 ± 5.1	5.4 ± 0.3
Gentiobiose	400	0.395	1.6 ± 0.1	70.6 ± 1.5	21.6 ± 0.8	6.2 ± 0.6
Maltose	300	0.284	0.7 ± 0.08	73.4 ± 1.8	20.6 ± 1.4	5.3 ± 0.5
	400	0.420	0.7 ± 0.4	73.3 ± 0.3	17.4 ± 7	8.6 ± 7.1
Maltitol	400	0.402	1.4 ± 0.3	75.4 ± 3.4	21.6 ± 4.3	1.6 ± 1.1
Methyl-Maltoside	400	-	7.3 ± 0.3	67.7 ± 3.0	19.0 ± 2.6	5.9 ± 0.7
Glycerol	600	0.570	0 ± 0	72.5 ± 9.9	25.6 ± 5.1	1.9 ± 0.7

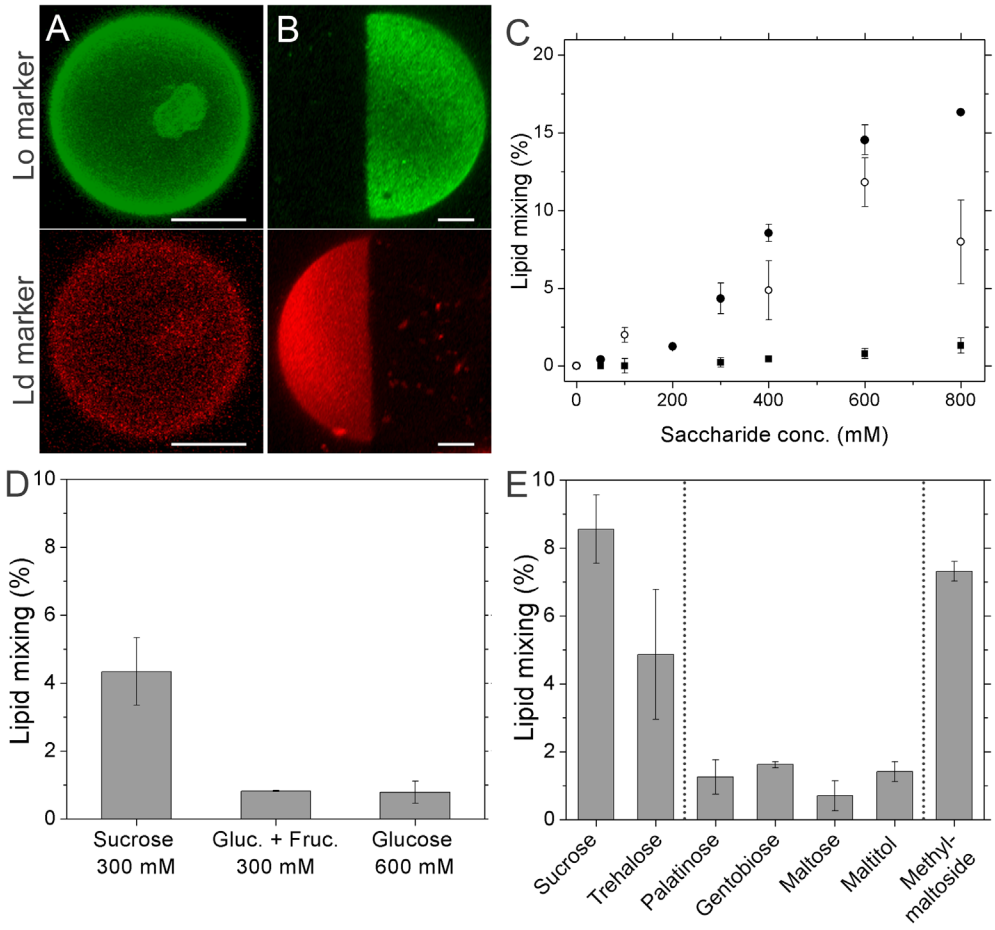

Figure 4. *Domain mixing induced by saccharides in GUVs.* (A) 3D projection of a GUV showing lipid mixing with the L_o and L_d domains co-localized. (B) 3D projection of a GUV with no lipid mixing, the L_o and L_d domains are segregated. Scale bars represent 2 μm. (C) Percentage of lipid mixing upon addition of glucose (empty squares), sucrose (full circles) and trehalose (empty circles) to SM:DOPC:Cholesterol (4:3:3) GUVs. (D) Percentage of lipid mixing upon addition of 300 mM sucrose, 300 mM mixture of glucose and fructose and 600 mM glucose. (E) Lipid mixing with the non-reducing sugars sucrose and trehalose, several reducing sugars e.g. palatinose, gentobiose and maltose; and two analogues of maltose, maltitol and methyl-maltoside; each at a concentration of 400 mM. Errors represent standard deviations of the biological replicates.

The number of sugar rings cannot explain the remarkable effect of the disaccharides; doubling the concentration of monosaccharides would yield the same effect and it clearly does not as shown in Figure 4D. The lipid mixing by 600 mM glucose is almost negligible (0.8 ± 0.3%) and lower than the 4.3 ± 0.9% mixing of 300 mM sucrose. Furthermore, if we compare 300 mM sucrose with a mixture of the two monosaccharides that constitute sucrose i.e. glucose and fructose, at the same concentration the lipid mixing is again much lower by the mixture of two monosaccharides (0.8 ± 0.02%). These results, together with the MD data of Fig. 1D, indicate that the linkage between the two rings of the sucrose is crucial for the effect on the membrane organization of this non-reducing disaccharide.

Saccharides directly interact with lipid headgroups in a concentration dependent manner

We have shown that disaccharides are able to modify the lateral organization of lipids in model bilayers, whereas monosaccharides do not. Moreover, the strength of the effect depends on the amount of carbohydrates in solution. A direct interaction between the sugars and lipids seems required to explain these effects. We therefore investigated the binding affinity of the sugars by analyzing the electron density profiles across the membrane, obtained from additional simulations of L_o and L_d membrane mimetics. The resulting profiles are shown in Figure 5A. In general, we see that sugars are able to bind to the membrane up to the level of the glycerol linkage, both for L_o and L_d mimicking membranes. At low sugar concentrations (60 mM), the sugars are enriched at the interface. This preferential binding mode of the sugars to the membrane/water interface is more pronounced for the disaccharides. On the contrary, at higher osmotic conditions (600 mM), a partial depletion of sugars away from the bilayer interface is observed with a concomitant increased tendency towards clustering of the carbohydrates in the aqueous subphase. Our results are consistent with the experimental data reported by Andersen and coworkers (62). Based on neutron scattering data combined with thermodynamic measurements, they show strong binding of sugars to membranes at low concentration and gradual repelling at concentrations exceeding ~200 mM. Interestingly, sucrose and trehalose show a peak in electron density right at the membrane/water interface. Such a peak is not observed in case of glucose, suggesting a stronger interfacial-binding mode for the disaccharides. Comparing the effects of the sugars on L_o and L_d membranes, we observe very similar behavior. Anderson *et al.* also noted little difference between binding of sugars to either fluid or gel phase membranes. A close up of the binding mode of glucose and sucrose to both L_o and L_d membranes, at 200 mM, is shown in Figure 5C. The presence of both a membrane-bound and membrane-depleted population at this concentration is clearly visible. Noticeable is also the stronger embedding of the disaccharide at the membrane/water interface, with individual sugar molecules intercalating between the phospholipid and cholesterol headgroups. The embedding of the interfacially bound sugars is very similar to that observed in all-atom MD simulations (300, 301).

Taken together, our results indicate that sugars are able to destabilize the lateral heterogeneity of bilayers through direct contact with the phospholipid headgroups, and that this interaction is strongly affected by the amount of carbohydrates in solution. However, although the binding of disaccharides is somewhat stronger than monosaccharides, the difference is rather small and cannot account for the dramatic effect of disaccharides on the domain stability.

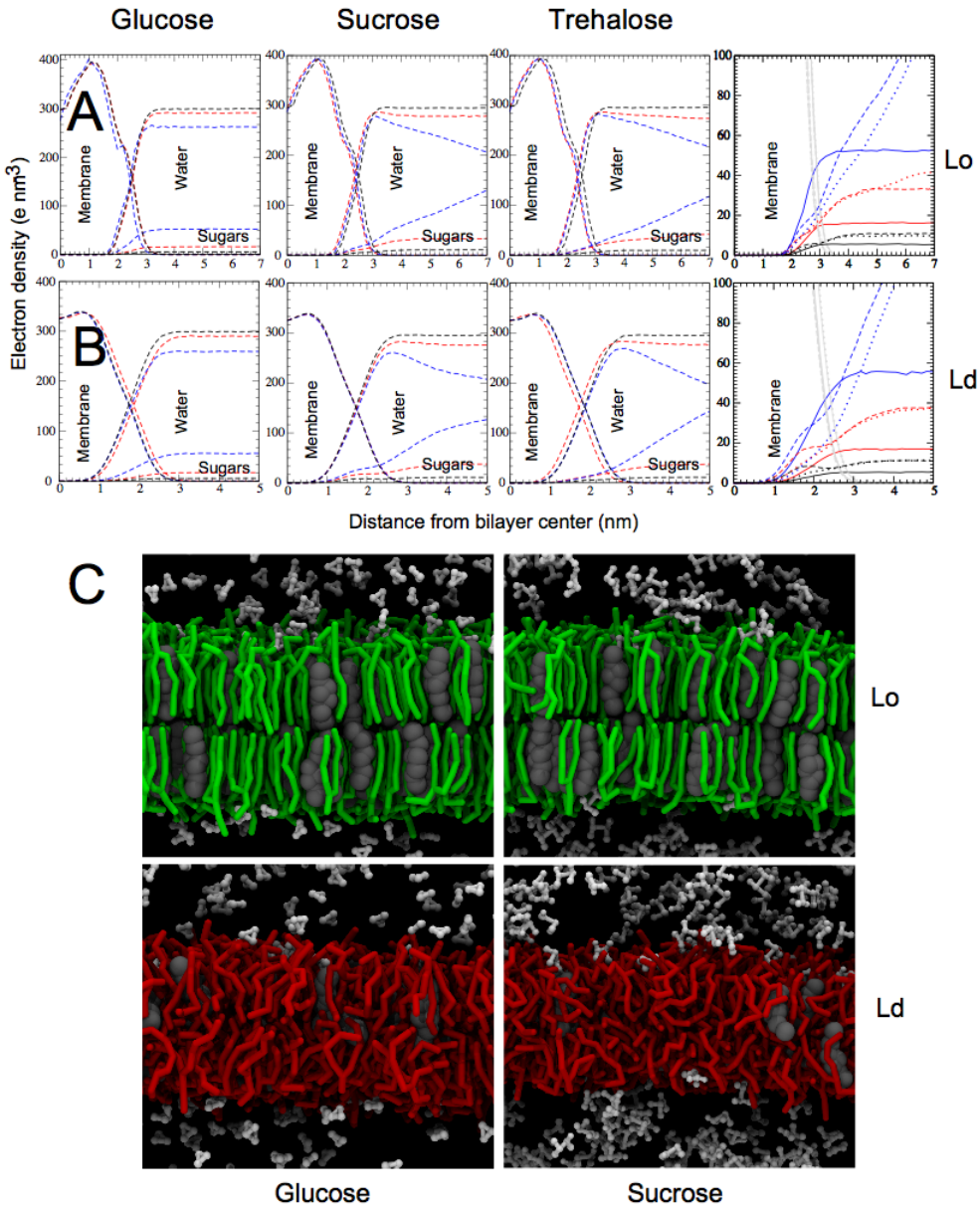

Figure 5. *Interaction of L_o and L_d domains with sugars.* Electron density profiles for glucose, sucrose, and trehalose interacting with L_o (A) or L_d (B) membranes. In addition, right most insets show a close up of the interaction between the sugars and the membrane (full line glucose, broken line sucrose and dotted line trehalose) at different concentrations (black 60 mM, red 200 mM and blue 600 mM). (C) Snapshots of the sugar distribution across the lipid-water interface for glucose (left) and sucrose (right) interacting with L_o (top) and L_d (bottom) membranes at 200 mM sugar.

Constrained geometry of disaccharides perturbs tight packing of L_o phase

The only remaining candidate for explaining the different behavior of mono- versus disaccharides, is the sugar linkage. To test the effect of the glycosidic linkage, we performed additional MD simulations in which the linker was either made longer (an increase in size from 0.429 nm to 1.0 nm), or made completely flexible (i.e. all the dihedral terms corresponding to the plane-plane orientation were excluded). The results in case of sucrose are shown in Figure 1D, in terms of a plot of the contact fraction between saturated and unsaturated contact lipids over time. Remarkably, sucrose in which the two monomers are linked at a larger distance is unable to disperse the domains. Keeping the linkage at the natural distance but increasing its flexibility, on the other hand, results in fast mixing of the lipids. The speed of the domain disruption is even larger compared to normal sucrose. We conclude that the close proximity of two sugar rings, a distinguishing feature of disaccharides, causes the destabilization of L_o/L_d coexistence.

Membrane organization is exclusively altered by non-reducing sugars

We showed that sucrose and trehalose affect the lipid organization of the membranes, whereas glucose does not. Our *in silico* data suggest that the presence of two sugar rings linked closely together is a prerequisite for this effect. To further prove that we need disaccharides to disrupt the membrane organization, we checked other disaccharides with our experimental setup. Surprisingly, none of the disaccharides tested (palatinose, gentiobiose and maltose) have an actual effect on mixing the lipid domains at 400 mM (Figure 4E). As opposed to sucrose and trehalose, these disaccharides are reducing sugars. In solution, reducing sugars can have the second monosaccharide ring open containing an aldehyde group, which is in equilibrium with the hemiacetal (when the pyranose ring is formed). In order to verify whether the lack of lipid mixing of the reducing sugars is due to the opening of the hemihacetal to aldehyde, we analyzed two analogues of maltose, maltitol and methyl-maltoside (see structures in Fig. 3). Maltitol is a hydrogenated maltose and does not possess an aldehyde in its open form, so the reaction back to the hemiacetal (closed pyranose) is not possible, giving rise to a fully open ring. In contrast to maltitol, methyl-maltoside has an extra methyl group in the hydroxyl of the hemiacetal, eliminating the equilibrium towards the aldehyde and locking the saccharide in its closed form. As shown in Figure 4E, maltitol acts similarly to the regular maltose, having a low effect on lipid mixing. On the contrary, methyl-maltoside, has a vast increase in the percentage of lipid mixing. These results show that only disaccharides containing two closed rings, either the two non-reducing (sucrose and trehalose) or the synthetic maltose analogue methyl-maltoside, are able to disrupt the lipid organization. This difference on lipid mixing by non-reducing sugars against reducing sugars or monosaccharides is even more pronounced when performing the experiments at 40ºC instead of 20ºC (Figure 6 and Table 2). The results show an increased lipid mixing of nearly 25% with 400 mM sucrose compared to 8% at lower temperature. In the case of 400 mM glucose or maltose, there is no lipid mixing at higher temperatures.

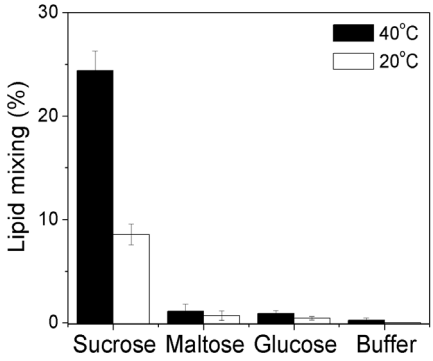

Figure 6. *Domain mixing induced by sugars at low and high temperature*. The percentage of vesicles with lipid mixing upon addition of the non-reducing sugar sucrose, the reducing sugar maltose, the monosaccharide glucose and buffer to SM:DOPC:Cholesterol (4:3:3) GUVs at 20˚C (empty bars) and 40˚C (full bars). The concentration of all sugars was 400 mM.

Table 2. Percentage of GUVs at 40°C.

	Concentration [mM]	Osmolarity [Osm/kg]	Mixed GUVs [%]	Separated GUVs [%]	Green GUVs [%]	Red GUVs [%]
KPi	0	0	0.3 ± 0.2	57.1 ± 0.6	33.5 ± 3.9	9.1 ± 3.0
Glucose	400	0.439	0.9 ± 0.3	70.2 ± 3.4	23.9 ± 3.7	5.0 ± 0.03
Sucrose	400	0.405	24.4 ± 1.8	54.4 ± 3.5	14.8 ± 5.9	6.4 ± 0.5
Maltose	400	0.420	1.1 ± 0.6	69.5 ± 3.5	19.6 ± 1.9	9.8 ± 2.1

To test whether the opening of the second ring of the reducing saccharides is favored upon binding to the lipid bilayer, we performed solid state NMR (ssNMR) of maltose in solution and in the presence of the SM:DOPC:Cholesterol (4:3:3) bilayer. The ^{13}C results are shown in Figure 7. When compering the maltose in solution, depicted in green, and the maltose in the presence of membranes, in blue, there are two main chemical shift changes. Those changes are illustrated in the top panel of Figure 7, highlighted with circles. There is an extra peak appearing around 82 ppm that could correspond to a chemical shift of maltitol, hydrogenated maltose with the second ring open. The discrimination between maltose and maltitol with ssNMR is not straightforward since they have almost all the ^{13}C chemical shifts identical. The only exceptions are the carbon-4 of the second glucose unit that is ~82 ppm and for maltitol it is ~77 ppm, and the anomeric carbon that is ~92 and ~96 ppm for α and β of maltose, respectively, and ~63 ppm for the same carbon in maltitol (see chemical shifts of both molecules in http://sdbs.riodb.aist.go.jp; National Institute of Advanced Industrial Science and Technology). These extra peaks appearing for maltose in the presence of membranes could represent the open form of the second ring. The other noticeable difference is that the chemical shifts of the anomeric carbon of maltose are slightly shifted towards higher values (three peaks in the range of 95-105 ppm) and the peaks are broader. This might be an effect of the hydrogen bonding with the membrane. When comparing the rigid fraction of maltose (Fig. 7 red line) with the rigid + mobile fraction (Fig. 7 blue line) of maltose, we conclude that maltose is peripherally associated with membranes.

Overall, the NMR measurements provide qualitative evidence that there is a change in the maltose structure in the presence of membranes. We speculate that a significant fraction of maltose has the second ring in an open form, which might be the reason that maltose is not able to disrupt the membrane organization. Our work thus indicates that not all disaccharides are able to disturb the membrane organization. The closed conformation of the second monosaccharide ring is a key factor in the lipid mixing. Amongst all saccharides found in nature, non-reducing sugars sucrose and trehalose are the only two capable of reorganizing the lipids of the membranes.

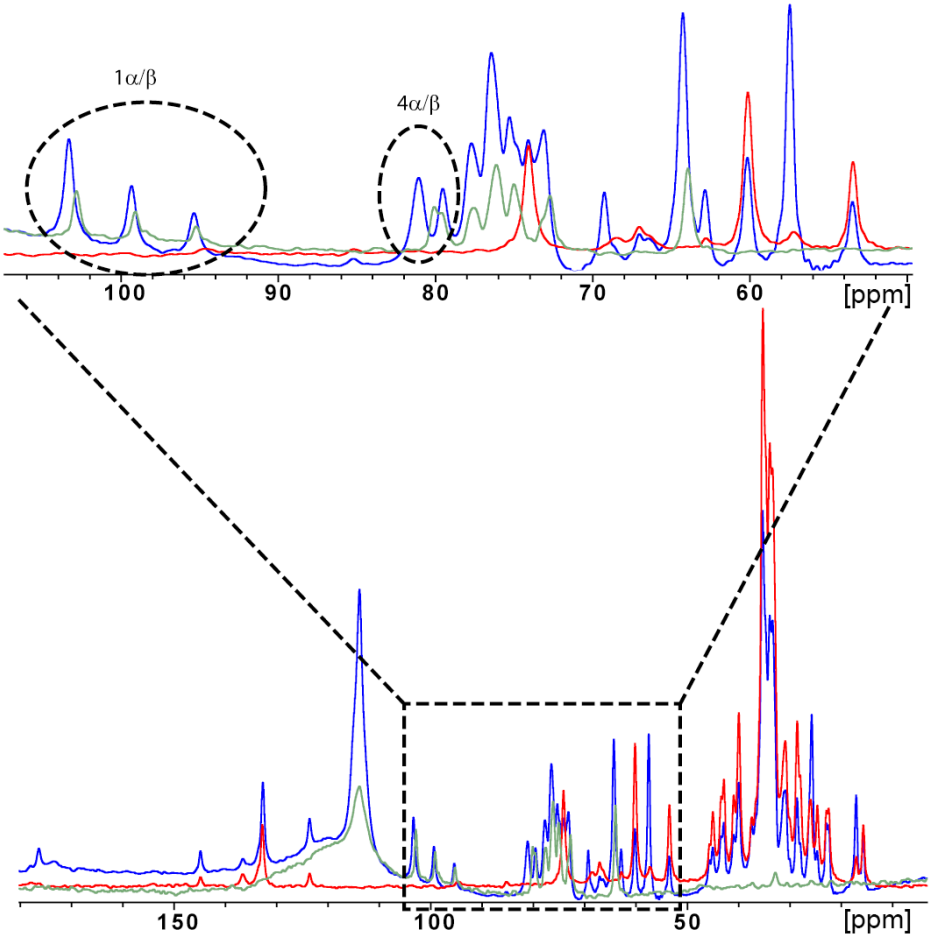

Figure 7. *^{13}C chemical shifts of maltose and membranes.* Bottom panel highlights the entire spectra and the boxed region and top panel illustrates the specific signals for maltose and the chemical shift changes in presence of lipids. Maltose in solution (green), maltose in the presence of SM:DOPC:Cholesterol (4:3:3) membranes (rigid components in red and rigid + mobile components in blue).

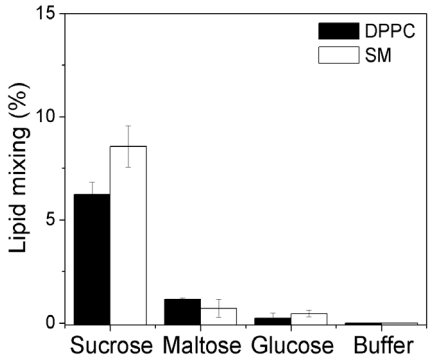

Figure 8. *Domain mixing in GUVs with different lipid composition.* The percentage of vesicles with lipid mixing upon addition of the non-reducing sugar sucrose, the reducing sugar maltose, the monosaccharide glucose and buffer to SM:DOPC:Cholesterol (4:3:3) GUVs (empty bars) and DPPC:DOPC:Cholesterol (4:3:3) GUVs (full bars). The concentration of all sugars was 400 mM.

Table 3. Percentage of GUVs with a membrane composition of DPPC:DOPC:Cholesterol at 4:3:3, molar ratio.

	Concentration [mM]	Osmolarity [Osm/kg]	Mixed GUVs [%]	Separated GUVs [%]	Green GUVs [%]	Red GUVs [%]
KPi	0	0	0 ± 0	86.1 ± 9.6	11.2 ± 4.9	2.7 ± 1.8
Glucose	400	0.439	0.2 ± 0.2	78.1 ± 4.7	19.3 ± 3.6	2.4 ± 0.8
Sucrose	400	0.405	6.2 ± 0.6	79.6 ± 0.5	10.6 ± 1.1	3.6 ± 0.9
Maltose	400	0.420	1.2 ± 0.1	87.4 ± 1.05	8.1 ± 1.0	3.3 ± 2.0

Discussion

The picture emerging from our combined computational and experimental approach is the following. Mono- and disaccharides interact with lipid membrane by direct interactions of the carbohydrates with the phospholipid headgroups as shown by the MD simulations. These interactions affect the organization of lipid domains present in membranes formed by saturated lipids, unsaturated lipids and cholesterol. The extent of lipid mixing is directly related to the amount of sugar present in solution. However, the disruption properties are exclusive to non-reducing disaccharides such as sucrose and trehalose, which insert quite deeply at the membrane/water interface when compared to glucose. A possible explanation could be that monosaccharides are small enough to fit in between the lipid polar groups without destabilizing them. On the contrary, non-reducing disaccharides, sucrose and trehalose, are composed of two pyranoses without a free hemiacetal. Those disaccharides are much bulkier, so once they are bound to the lipids in specific positions they might spread them to some extent. Thus, preventing tight interactions between the lipid headgroups and the lipid tails. In other words, non-reducing disaccharides stabilize a disordered phase. As a consequence lipids comprising the L_o phase become loosely packed, causing mixing of the domains and resulting in a homogeneous lateral organization of the bilayer. Reducing sugars, once they are bound to the lipids, might be stabilized in the open form where only the first pyranose ring is present. This conformation might not be bulky enough to spread the lipids sufficiently to cause mixing. Reducing sugars change their structure in water almost without any energy loss, so opening the second ring does not require a lot of energy. There is no quantitative data available about the opening and closing of reducing sugars in the presence of membranes, but the observations of maltose and maltitol opposed to those of methyl-maltoside in the lipid mixing together with the structural observations by ssNMR support this hypothesis. The MD simulations and the experimental observations are in perfect

agreement, even though in the initial experiments the L_o phase was composed of a different type of saturated lipid. The MD simulations were performed with DPPC, whereas in the experiments SM was used. A control experiment showed the same behavior on lipid mixing by sucrose, maltose and glucose with membranes composed of DPPC instead of SM (Figure 8 and Table 3).

Importantly, the non-reducing sugars sucrose and trehalose are the only two saccharides accumulated in large amounts by numerous organisms under conditions of complete dehydration; these sugars are also synthesized or taken up under conditions of osmotic stress (partial dehydration). It is well accepted that these sugars may replace the water molecules around the polar residues of membranes and proteins. This stabilizes the membranes by avoiding the shrinkage, lateral stress and the increase in the phase transition temperature when water is removed in the process of drying (272). Besides substituting the water molecules, sucrose and trehalose expand the membrane. Upon binding to lipid monolayers, the area per molecule increases. The expansion occurs at low and high temperatures, which is different from the effect of glycerol that only expands the membrane at temperatures above the phase transition temperature of DPPC monolayers. In our experimental set up with GUVs, glycerol had no effect on the lipid organization (Table 1). The efficiency of expanding the monolayer films is directly related to the ability to stabilize the membrane structure and function at low water contents (49). If sugars have similar effects on the structure of native membranes, then the synthesis or accumulation of non-reducing disaccharides might dissolve the nanoscale assemblies present in the plasma membrane of eukaryotic, which may impact the functioning of several membrane proteins.

Acknowledgements

This work was supported by the Netherlands Organisation for Scientific Research (NWO): ECHO.08. BM.041 and ChemThem “Out-of-Equilibrium Self-Assembly” 728.011.202). The authors thank Manuel Jäger for kindly providing us with the methyl-maltoside.

Chapter 7

Localization and dynamics of proteins in the plasma membrane of *Saccharomyces cerevisiae*

Gemma Moiset*, Frans Bianchi*, Paul Schavemaker, Michiel Punter, Antoine van Oijen, Andrew Robinson and Bert Poolman

(*) These authors contributed equally to this work.

Manuscript in preparation

The Plasma Membrane (PM) of *S. cerevisiae* is described as a polarized environment in which proteins are segregated between: eisosomes, rafts and endocytic sites. The ensemble behaviour of proteins in the PM has been studied using conventional fluorescence microscopy such as Fluorescence Recovery After Photobleaching (FRAP), showing that the slow diffusion of polytopic membrane proteins allows for its polarization. In this study, we will analyse whether the origin of the slow diffusion and polarized localization is due to membrane confinement and/or oligomerization of the proteins. As a model system we use Lyp1p and Can1p basic amino-acid transporters from the yeast PM, of which Can1p is reported to reside within, and outside of, eisosomes. We have probed the ensemble diffusion behaviour of these proteins using FRAP, as well as Single Particle Tracking (SPT) to study the behaviour at a single molecule level. FRAP and SPT analyses confirm the slow diffusion of the proteins, $5\text{-}10*10^{-4}$ $\mu m^2/s$, which is in the same order as found for Pma1p. Super-resolution imaging by PALM confirms that Can1p and Lyp1p have a polarized distribution at the PM, however none of the proteins appeared to be confined by SPT analysis. Clustering or oligomeric state effects were probed by counting the number of fluorophores from single diffraction-limited fluorescent spots showing that the majority of can1p and lyp1p is monomeric and that the polarized distribution arises because of the low copy number of these proteins in the PM.

Introduction

The lateral organization and compartmentation of cellular functions is a key step in the evolution of eukaryotic cells. Within lipid membranes, specific domains can exist due to phase separation of lipids and embedded proteins. *Saccharomyces cerevisiae* is an excellent model system to study membrane domain formation and is often used comparatively with mammalian cell systems. A clear example is the presence of 'lipid rafts' as segregated lipid-protein entities rich, which are rich in sphingolipids and sterols. In the yeast plasma membrane there are the so-called MCC/eisosome and MCP domains, occupied by and named after the H^+/Arginine symporter Can1p and the plasma membrane H^+-ATPase Pma1p, respectively (98, 101-104). The former is thought to be enriched in ergosterol, whereas MCPs are rich in sphingolipids (302, 303). Thus, even though both domains are thought to contain sterol (i.e. ergosterol) and sphingholipid (the dominant lipid in yeast PM), the relative abundance differs. Owing to the patch-like organization of MCC/eisosomes and the accommodation of several proteins they are frequently denominated lipid rafts (98, 101, 106, 107, 302), but their properties seem different from those in mammalian cells (100) or membrane model systems such as GUVs (Chapter 6). The yeast PM division into two defined and stable compartments seems to be too strict. Can1p has been shown to localize in the patch-like MCC/eisosome domain, excluded from the MCPs (101, 106, 107). However, other measurements indicate that 70% of the Can1p is localized outside of MCCs (113). By counting the number of MCC/eisosomes per cell and assuming dimensions of 300 x 50 nm, the domains make up about 5 % of the PM surface and thus Can1p would be accumulated in the MCC/eisosomes several fold. A recent study has revealed uneven distributions of all PM proteins suggesting that numerous domains coexist, partially overlapping, in the yeast plasma membrane (114). Thus, questioning whether MCC is the solely patch-like domain in the yeast PM.

The segregation of proteins in the PM of yeast has also been associated with the extremely slow diffusion of proteins and lipids in the membranes and may lead to polarization in the cell. The way cells can maintain this membrane polarization is by keeping a balance between the lateral diffusion, the directed transport to the PM and endocytosis (115, 124, 304). By studying the dynamics at the single molecule level we analyze whether Can1p is strictly confined in the MCC domains and compare the observations to that of another basic amino acid permease, Lyp1p. The localization and dynamics of this H^+/Lysine symporter have not been studied before.

Many membrane proteins function as multimers and oligomerization of these proteins has been associated with slowed diffusion rates in mammalian cells (305). For instance, the lateral diffusion of E-cadherin is reduced by 10 to 40 upon oligomerization in the plasma membrane of mammalian cells. However, this result is inconsistent with the general understanding of the physicochemical basis of translational diffusion in lipid bilayers, where the mobility of proteins within the two-dimensional space of the membrane is rather insensitive to changes in the size of the diffusing unit (64, 306). In fact, for proteins with radii (R) up to 5 nm it has been shown that the lateral diffusion coefficient scales with $ln(1/R)$. The slowed diffusion rates in mammalian cells upon oligomerization have been explained by the trapping of the molecules in the membrane skeleton. In case of AAP transporters, the family to which Lyp1p and Can1p belong, there is virtually no information on their oligomeric state in the PM or internal membranes. From genetic screens there is some evidence that the general amino acid permease Gap1p might form oligomers (307) and for other transporters there is evidence that they need to oligomerize for proper trafficking through the early secretory pathway (308). The crystal structure of a bacterial homologue of the yeast amino acid transporters, the arginine/agmatine exchanger AdiC (309, 310), points to a homodimeric structure, which is supported by

glutaraldehyde crosslinking studies. Another two examples are the dimeric H^+/Na^+ antiporter, Nha1p, and the tetrameric glycerol channel, Fps1p (311, 312). We use those two proteins to compare the differences on the diffusion rates with Can1p and Lyp1p.

In this study, we analyze the diffusion, polarized localization and oligomerization of plasma membrane proteins by ensemble and single molecule measurements. We correlate the phenomena to understand the basis for the slow diffusion and localization pattern in the yeast PM.

Materials and methods

Plasmids and strains

All strains are based on *S. cerevisiae* strain BY4742 bearing the *ura3* selection marker (Table 1). All plasmids were generated using uracil excision-based cloning (313). Genomic DNA isolation of *S. cerevisiae* BY4742 was carried out according to Sherman *et al.* (314) For the amplification of DNA with uracil containing primers polymerase chain reactions (PCR) were performed with PfuX7 (315). Amplified fragments were assembled into full plasmids (Table 2) by treatment with DNA glycosidase and DNA glycosylase-lyase endo VIII, commercially available as USER, following the manufacturer's instruction (New England Biolabs, Ipswich, Ma, USA). Ligation products were transformed into chemically competent *E. coli* MC1061 cells (316). All constructs assembled from PCR fragments were verified by DNA sequencing. Genomic tagging and deletion of genes were done with standard PCR-based homologous recombination, using the primers listed in Table 3. Transformation of plasmids and linear constructs into *S. cerevisiae* was performed as described by Drew *et al.* (317)

Plasmid generation

The sequences of oligonucleotide primers used in this study are listed in Table 3. The plasmid pRS426GAL1-lyp1-Ypet-his was constructed by a four PCR fragment ligation, in which the backbone of the pRS426GAL1-GFP vector was amplified with primer pairs Pr1/Pr2 and Pr3/Pr4 in two fragments that excluded the GFP coding region. The fragment coding for the *ypet* gene was amplified from a synthetically generated coding sequence ordered from (GeneArt, Regensburg, Germany), using primer pair Pr5/Pr6. The *lyp1* gene was amplified from *S. cerevisiae* BY4742 chromosomal DNA with primer pair: Pr9/Pr10. Ligation of the four PCR amplified fragments using USER enzyme resulted in a fusion of *lyp1* and *ypet,* separated by a sequence for tobacco etch virus (TEV) protease cleavage site and followed by sequence for a His_8 tag (i.e. *lyp1-TEV-YPet-his*$_8$).

To construct pRS426GAL1-lyp1-Ypet-Ypet-his the *ypet* gene was amplified twice, using primer pairs Pr5-Pr8 and Pr6-Pr7. Annealing of the five fragments and USER ligation resulted in a plasmid carrying a *lyp1*-TEV-*Ypet-Ypet-his*$_8$ fusion gene. Similar plasmids were constructed for *can1*, *nha1* or *fps1* in place of *lyp1*, using primer pairs Pr11/Pr12, Pr13/Pr14 and Pr15/Pr16, respectively. For all constructs, plasmids were isolated from the *E. coli* host and the sequences of the fusion genes were verified. Each plasmid was then transformed into a *S. cerevisiae* By4742 knockout strains that lack the chromosomal copy of the corresponding gene.

The plasmid Pug72-mEos3.1 was constructed from 3 PCR fragments, using the uracil excision based cloning method. The backbone and the *ura3* marker were both separately amplified from the Pug72 plasmid using primer pairs Pr17/Pr20 and

Pr18/Pr19, respectively. *mEos3.1* was amplified using primer pair Pr21/Pr22 from a synthetically generated coding sequence, ordered from (GeneArt, Regensburg, Germany). The fragments were treated with USER and transformed into *E. coli* MC1061 as described previously.

For the construction of the *S. cerevisiae* BY4742 Δ*art1*/Δ*art2* strain we made use of the *ura3* selection marker and the ability for its counter selection on 5 fluoro-orotic acid (5FOA) as described by Alani *et al.* (318). The *ura3* cassette was amplified from the Pug72 plasmid with primer pairs Pr23/24 and Pr25/Pr26 for the disruption of *art2* and *art1*, respectively. Primers were designed in a similar way as described by Akada *et al.* (319). A region of 50-90 bp downstream of the targeted gene was included in the upstream primer, creating two homologous flanking regions to the *ura3* selection marker. The amplified *art1* disruption cassette was transformed into *S. cerevisiae* BY4742 and the cells were recovered on a uracil-depleted medium to select for recombinants. In a second round of selection, double-crossover recombinants lacking the *ura3* marker were isolated by growth on a medium containing 5FOA. The *art2* gene was disrupted by repeating the procedure on the Δ*art1* strain.

For genomic replacement of *lyp1* and *can1* with *lyp1-meos3.1* and *can1-meos3.1*, we amplified the *meos3.1-ura3* cassette from the Pug72-mEos3.1 plasmid using PCR. For the tagging of *lyp1* and *can1* we used primer pairs Pr27/28 and Pr29/30 respectively. Integration and counter selection of the *meos3.1-ura3* cassette was performed as during construction of the Δ*art1* strain.

Table 1. Yeast strains used in this study.

Strains	Characteristics	Reference
S. cerevisiae BY4742	*Matα his3Δ1 leu2Δ0 lys2Δ0 ura3Δ0*	Invitrogen
E. coli MC1061	–	Casadaban *et al.*1980
S. cerevisiae BY4742 *Δlyp1*	*Matα his3Δ1 leu2Δ0 lys2Δ0 ura3Δ0 Δlyp1 kanMx*	Giaever *et al.* 2002
S. cerevisiae BY4742 *Δcan1*	*Matα his3Δ1 leu2Δ0 lys2Δ0 ura3Δ0 Δcan1 kanMx*	Giaever *et al.* 2002
S. cerevisiae BY4742 *Δnha1*	*Matα his3Δ1 leu2Δ0 lys2Δ0 ura3Δ0 Δnha1 kanMx*	Giaever *et al.* 2002
S. cerevisiae BY4742 *Δfps1*	*Matα his3Δ1 leu2Δ0 lys2Δ0 ura3Δ0 Δfps1 kanMx*	Giaever *et al.* 2002
S. cerevisiae BY4742 *ΔArt1 ΔArt2 lyp1-mEos3.1*	*Matα his3Δ1 leu2Δ0 lys2Δ0 Art1Δ0 Art2Δ0 lyp1-mEos3.1 ura3*	This study
S. cerevisiae BY4742 *can-mEos3.1*	*Matα his3Δ1 leu2Δ0 lys2Δ0 Art1Δ0 Art2Δ0 can1-mEos3.1 ura3*	This study
S. cerevisiae BY4742 *lyp1-mEos3.1*	*Matα his3Δ1 leu2Δ0 lys2Δ0 lyp1-mEos3.1 ura3*	This study

Table 2. Yeast plasmids used in this study

Plasmids	Characteristics	Reference
pRS426GAL1-GFP	pRS426 with *gal* promoter and GFP-His fusion cassette with *ura3* selection marker	Newstead *et al.* 2007
pRS426GAL1-lyp1-Ypet-his	pRS426GAL1-GFP derivative with *lyp1* fused to *ypet*	This study
pRS426GAL1-lyp1-Ypet-Ypet-his	pRS426GAL1-GFP derivative with *lyp1* fused to *ypet-ypet*	This study
pRS426GAL1-can1-Ypet-his	pRS426GAL1-GFP derivative with *can1* fused to *ypet*	This study
pRS426GAL1-can1-Ypet-Ypet-his	pRS426GAL1-GFP derivative with *can1* fused to *ypet-ypet*	This study
pRS426GAL1-nha1-Ypet-his	pRS426GAL1-GFP derivative with *nha1* fused to *ypet*	This study
pRS426GAL1-fps1-Ypet-his	pRS426GAL1-GFP derivative with *fps1* fused to *ypet*	This study
Pug72	Amp^R, *Ura3* chromosomal integration cassette	Güldener *et al.* 2002
Pug72 *mEos3.1*	Pug 72 with *ura3* flanking homologous regions and reverse *mEos3.1* fusion gene	This Study

Growth conditions

Yeast cells were grown at 30˚C in synthetic dropout media lacking uracil (320). Cells were initially grown in medium containing 2% [w/v] glucose to an optical density at 600 nm (OD_{600}) of 0.2–0.4. For single particle tracking and oligomeric state analysis, the cells were centrifuged (1600 x g, at room temperature for 2 min), resuspended to OD_{600} ~0.2-0.4 in medium containing 2% [w/v] raffinose in place of glucose and grown one more hour. At this stage, most cells contained < 10 fluorescent protein foci when imaged on a single-molecule fluorescence microscope (see below). For PALM experiments, cells grown in glucose medium were concentrated by centrifugation to OD_{600} ~10 prior to imaging. For time-lapse PALM measurements, the cells were grown at 30˚C to an OD_{600} of 0.2–0.4 in glucose media that contained either standard concentrations of lysine and arginine (76 mg/L each), or 10 times lower levels (7.6 mg/L each). For FRAP experiments, cells grown in glucose medium were transferred to medium containing both raffinose (2% [w/v]) and glucose (0.1% [w/v]) and sustained at mid-exponential growth phase over 36 hours (OD_{600} of 0.2-0.5). Then, the cells were induced with 0.2 % [w/v] galactose for 2.5 hours prior to the FRAP measurement. For Can1p- and Lyp1p-labelled cells, lysine, arginine and methionine were omitted from the raffinose/glucose medium.

Table 3. *Primers used in this study* (italics represent identical regions introduced for metabolic excision marker after genomic integration of the Pug72 *mEos3.1* cassette)

Primer name	Sequence	Purpose
Pr1 4158	ACCACCACCAUCATCATCATCATTAACTGCAGGAATTC	Rev primer for amplification of pRS426GAL1-GFP vector annealing at histag for swaping c terminal fusion protein.
Pr2 3631	AGCACTACCCUTTAGCTGTTCTATATGCTGCC	Fw primer for amplification of pRS426GAL1-GFP
Pr3 4158	ACCACCACCAUCATCATCATCATTAACTGCAGGAATTC	Fw primer for amplification of pRS426GAL1-GFP vector starting at histag for swaping c terminal fusion protein
Pr4 4171	ATTTTGGGAUCCACTAGTTCTAGAATCCGGGG	Rev primer for pRS426GAL1-GFP backbone amplification anneals behind *gal* promoter.
Pr5 4159	AGGGGAAAAUTTATATTTTCAAGGTTCTAAAGGTGAAGAATTATTCACTGG	Fw primer for amplification of *ypet gene* and insertion into pRS426GAL1-GFP.
Pr6 4160	ATGGTGGTGGUGGAGCTCTTTGTACAATTCATTCATACC	Rev primer for amplification of *ypet gene* and insertion into pRS426GAL1-GFP.
Pr7 4566	ACAAAGAGCUCGGAGGAGGATCTAAAGGTGAAGAATTATTCACTGG	Fw primer for amplification of *ypet gene* for construction of double ypet fusion.
Pr8 4565	AGCTCTTTGUACAATTCATTCATACCCTCGG	Rev primer for amplification of *ypet gene* for construction of double ypet fusion including a linker.
Pr9 4165	ATCCCAAAAUGGGCAGGTTTAGTAACATAATAACGTCC	Fw primer for amplification of *S. cerevisiae lyp1* gene for insertion into pRS426GAL1-GFP.
Pr10 4166	ATTTTCCCCUCCTGCAACAGCAGCCCAGAATTTCTC	Rev primer for amplification of *S. cerevisiae lyp1* gene for insertion into pRS426GAL1-GFP.
Pr11 4164	ATTTTCCCCUCCTGCTACAACATTCCAAAATTTGTCCC	Fw primer for amplification of *S. cerevisiae can1* gene for insertion into pRS426GAL1-GFP.
Pr12 4163	ATCCCAAAAUGGGAACAAATTCAAAAGAAGACGCCGACATAG	Rev primer for amplification of *S. cerevisiae can1* gene for insertion into pRS426GAL1-GFP.
Pr13 4402	ATCCCAAAAUGGCTATCTGGGAGCAACTAGAAG	Fw primer for amplification of *S. cerevisiae nha1* gene for insertion into pRS426GAL1-GFP.
Pr14 4403	ATTTTCCCCUCCCTTATTGAGACCAAGCGTTTTTGATAGCG	Rev primer for amplification of *S. cerevisiae nha1* gene for insertion into pRS426GAL1-GFP.
Pr15 4508	ATTTTCCCCUCCTGTTACCTTCTTAGCATTACC	Fw primer for amplification of *S. cerevisiae fps1* gene for insertion into pRS426GAL1-GFP.
Pr16 4507	ATCCCAAAAUGGGCAGTAATCCTCAAAAAGCTCTAAAC	Rev primer for amplification of *S. cerevisiae fps1* gene for insertion into pRS426GAL1-GFP.
Pr17 4309	AGTCCGACCU*GGGCGCGCGCGAATTAGCCGCGGCGTGGCCTTCCCAAATTT GGGTAGGGC*GTCTAGAGATCCCAATACAACAGATCAC	Primer for construction of the Pug72 *mEos3.1* fusion cassette, containing upstream homologous region flanking *Ura3*, for excision of the *Ura3* marker after genomical integration.
Pr18 4310	ACTAACCCGU*GGGCGCGCGCGAATTAGCCGCGGCGTGGCCTTCCC AAATTTGGGTAGGGC*CTCGAGAACCCTTAATATAACTTCGT	Primer for construction of the Pug72 *mEos3.1* fusion cassette, containing downstream homologous region flanking *Ura3*, for excision of the *Ura3* marker after genomical integration.
Pr19 3756	ACGGGAACGUCGTACGAAGCTTCAGCTGGC	Rev primer for amplification of Pug72 backbone for insertion of fluorescent protein in Pug72 vector..
Pr20 4101	ACGGGTTAGUAGCTCGTTTTATTTAGGTTCTATCGAGG	*Rev primer for amplification of Ura* marker for Pug72 *mEos3.1* cassette.
Pr21 4105	ACGTTCCCGUATGAGTGCGATTAAGCCAGACA	Fw primer for Amplification of *mEos3.1* for Pug72 *mEos3.1* fusion cassette
Pr22 4106	AGGTCGGACUTTATCGTCTGGCATTGTCAGGC	Rev primer for Amplification of *mEos3.1* for Pug72 *mEos3.1* fusion cassette
Pr23 4686	TCATTCTTCATCACTCATCAAAGGCACTATTTCGTCATAA CGCGGAGGCTGTCTAGAGATCCCAATACAACAGATCAC	Fw primer for amplification of *art2* specific knockout cassette from Pug72 vector.
Pr24 4685	CTCTTTTAAATAGAGAAGAACAAGCAAGATTTTTCCCTAC CCCTATTGGGCGAATTATTCTACGATAATTATATATATAG AGCCACTGCATGAGCTCGTTTTATTTAGGTTCTATCGAG	Rev primer for amplification of *art2* specific knockout cassette from Pug72 vector.
Pr25 4684	CTACTGGGTTATTCTATTGGAATCTAGAAAATCGGAAAAGTTT TGTATTCTGATATCGTCTAGAGATCCCAATACAACAGATCAC	Fw primer for amplification *art1* specific knockout cassette from Pug72 vector.
Pr26 4683	CTGATTTTTACTCCTACTTAGTATACATTTCACTAAACAATACGTTTTACCCG TTAAAGGTATTTACCATATATTTTTATCTTAG ATACCTAGCTCGTTTTATTTAGGTTCTATCGAGG	Rev primer for amplification of *art*1 specific knockout cassette from Pug72 vector.
Pr27 3537	GCGAAATGGCGTGGAAATGTGATCAAAGGTAA TAAAACGTCATATCTGATATCACCTAATAACTTCG	Fw primer for amplification of *can1* specific *meos3.1* fusion cassette from Pug72 *mEos3.1.*
Pr28 3543	CTATTTTTTTATTTTTTTCTATTTTGAAGGCATGCAA GAGGTTCTGTGACTGATATCACCTAATAACTTCG	Fw primer for amplification of *lyp1* specific *meos3.1* fusion cassette from Pug72 *mEos3.1.*
Pr29 4191	GAAGACGACGAGCCTAAGAATTTATGGGAGAAATT CTGGGCTGCTGTTGCAATGAGTGCGATTAAGCCAGAC	Rev primer for amplification of *lyp1* specific *meos3.1* fusion cassette from Pug72 *mEos3.1.*
Pr30 4194	GAAGATCATGAACCAAAGACTTTTTGGGACAAAT TTTGGAATGTTGTAGCAATGAGTGCGATTAAGCCAGAC	Rev primer for amplification of *can1* specific *meos3.1* fusion cassette from Pug72 *mEos3.1.*

Microscopy equipment

For single particle tracking, oligomeric state analysis and PALM measurements, a fully automated home-built Olympus IX-81 inverted microscope with a high numerical aperture objective (100 X, NA = 1.49, oil immersion, Olympus, UApo) was used, as shown schematically in Scheme 1. Solid-state lasers were from Coherent (Santa Clara, USA): 405 nm (cube, 100 mW), 514 nm (Sapphire, 150 mW) and 568 nm (Sapphire, 150 mW). Laser pulses were automatically generated using computer-controlled shutters, and neutral-density filter wheels were used to attenuate the laser power. Laser beams were collimated with lenses and combined using dichroic mirrors. Imaging was performed in epi-fluorescence mode and emitted light was collected on a 512x512 pixels Electron Multiplying Charge Coupled Device (EM-CCD) camera (C9100-13, Hamamatsu, Japan).

For FRAP measurements a commercial laser-scanning confocal microscope, LSM 710 (Carl Zeiss MicroImaging, Jena, Germany) was used. The microscope was equipped with a C-Apochromat 40x/1.2 NA objective and a blue argon ion laser (488 nm).

FRAP measurements

Cells were immobilized in between two microscope slides and the focal plane positioned to the mid-section of the cells. Subsequently, an area at the each of the cell, corresponding to the PM, with a radius of 0.5-1.0 μm was photo-bleached with a short (26 μs) focused high power light pulse. Immediately afterwards several images of the fluorescence recovery were collected every 20 s over a total time period of 2400 s, using 1 % of the laser output power. During the entire experiment, the stage was heated to 30°C using a Pecon climate chamber. Data analysis was carried out in imageJ (321). Images were corrected for x-y drift using cross correlation fitting. The fluorescence intensity over time of the PM was corrected for photo-bleaching effects by fitting the decay to a single exponential. The bleaching area was selected and the recovery was fitted to a single exponential to find the half time of recovery. The diffusion coefficient (D) was estimated according to equation 1, derived from Axelrod *et al.* (322):

Eq. 1 $$D = \gamma \frac{w^2}{4t_{0.5}}$$

where D is the diffusion coefficient, w the radius of the bleaching spot, $t_{0.5}$ the half time of recovery and γ a correction factor which is 0.88 for circular beams. The radius of the bleaching spot was 1.0 μm ± 0.1 μm as determined by Meinema *et al.* (121).

Single-particle tracking

Cells were embedded and immobilized in 0.5 % (w/v) agarose and placed in between two microscope slides. Fluorescent microspheres (TransFluoSpheres, d=0.04 μm, ex/em=488/560 nm, Invitrogen) were premixed with the cells and, post data collection, their position used to correct for x-y drift. The experimental setup permitted cell growth (which was slow relative to the time span of the experiments) and provides a low fluorescence background necessary for single molecule imaging. The focal plane was placed at the mid-section cells. Time-lapse movies were recorded once every 34 ms, 100 ms, 300 ms, 1 s, 10 s, 11 s or 30 s. Typically, 100 - 200 frames were collected per measurement. All movies were recorded using 34 ms exposure times per frame. Application of excitation light (λ=514 nm at 50 W/cm^2) was synchronized with the camera exposures. Throughout the experiment, the microscope stage was heated to 30°C. ImageJ was used to correct the drift at sub-pixel level, and to fit and track the

peaks. The diffusion coefficient (*D*) of the particles was calculated in two different ways: (i) from the linear time dependence of the mean square displacement (*MSD*) using Eq. 2 and assuming a 1D diffusion along the plasma membrane (PM) and (ii) by fitting step-size distributions with the 1D diffusion Eq. 3.

Eq. 2 $$MSD = d^2 = 2nDt + c$$

where *n* is the dimensionality, *D* is the lateral diffusion coefficient, *t* is time, *d* is displaced distance and c is an offset arising from localization uncertainty.

Eq. 3 $$p(d) = \frac{A}{\sqrt{4\pi Dt}} e^{-\frac{d^2}{4Dt}}$$

where *p(d)* represents the probability of a particle displaced at a distance *d*, *A* is the proportionality constant, *D* is the diffusion coefficient and *t* is frame time (323).

In both cases, only trajectories corresponding to the PM and having a minimum length of 8 steps were selected (for 30 s-sampling measurements, a minimum of 5 steps was taken). Plots of MSD *versus* time were produced by averaging data from several trajectories. The distribution of step sizes of the experiments performed at different rates was plotted and fitted using a 1D diffusion model (Eq. 3).

Oligomeric state analysis

Sample preparation and data acquisition was the same as described under single-particle tracking. The first frame of each recording, before photo-bleaching takes place, was used to analyze the fluorescence intensity of each diffraction limited focus. Frames towards the end of each movie captured single YPet molecules as they spontaneously returned from a dark state to the fluorescent state. These observations were used to determine the fluorescence of a single YPet molecule. The intensities of unbleached foci were divided by the average intensity of a single molecule to reveal the number of molecules per focus.

Photo-Activated Localization Microscopy (PALM)

A single layer of cells was placed in between two microscope slides, which would sufficiently immobilize them for the time period of the experiment (typically 3 min). For mEos3.1 and mEos3.2 imaging excitation light (λ=568 nm) was introduced at 180 W/cm^2 for all the samples except the chromosomal Lyp1p-mEos3.1 in the Δ*art1*/Δ*art2* deletion strain, in which case the laser power was set to 450 W/cm^2 to increase the signal-to-noise ratio. A second laser (λ=405 nm) was used to induce individual mEos3.1 molecules to switch from the green fluorescent state to the red fluorescent state. The laser power was adjusted to activate only a small sub-set of molecules at a time and was kept the same for all the experiments. Typically, 5000 frames were collected per measurement, with the microscope at room temperature (~23˚C). PALM reconstructions were generated by processing the acquired data with home-written PALM software. Foci originating from individual molecules were identified and their point spread functions fit with a 2D Gaussian function allowing their position determined with a resolution of ~30 nm.

FRAP simulations

The program Smoldyn™ was used to perform all the simulations (http://www.smoldyn.org/index.html) and data were analyzed using Mathematica. A yeast cell was represented as a sphere with a diameter of 5 μm. 4000 particles were randomly positioned over the surface of the cell except for the bleaching spot. The bleaching spot was a square with sides of 2 μm long. The center of the bleaching spot was positioned at the center of the focal plane. The particles were allowed to move over the surface by Brownian diffusion with a diffusion coefficient of 0.03 μm²/s. The simulation time step was 1 ms and the total simulated time 100 s. The positions of all particles were extracted every 2 s. The number of molecules in an area of 1 μm high and as wide as the bleaching spot (2 μm at t=0) was monitored and fit with equation 4.

Eq. 4 $$f(t) = A(1 - e^{-\tau t})$$

where A is the number of particles in the region at equilibrium, t is the time and τ the recovery time constant. The calculated τ from Eq. 4 was used to calculate the diffusion coefficient with equation 5.

Eq. 5 $$D = \frac{0.88\omega^2}{4\left(\frac{ln(0.5)}{-\tau}\right)}$$

where D is the diffusion coefficient, ω is the width of the bleached region and τ the recovery time constant.

SPT simulations

Again, Smoldyn was used to perform the simulations and the data were analyzed in Mathematica. Twelve simulations were performed with the following diffusion coefficients: 0.0001, 0.00015, 0.00025, 0.0005, 0.001, 0.0015, 0.0025, 0.005, 0.01, 0.015, 0.025 and 0.05 μm²/s. The displacement of particles within the focal plane (represented with a band) in the middle of the cell was used for the analysis; the band thickness in the z-direction was 1 μm. The localization noise was included in each simulation by taking as noise the experimental displacement data from the fastest sampling time, 34 ms. We assumed that due to the extremely slow diffusion of the analyzed proteins the apparent displacement originates primarily from localization uncertainty. The diffusion coefficients obtained in the simulations were compared against the input values and their relationship was used to correct the experimental data. Each simulation was started with a 1000 particles randomly positioned on the membrane band at the middle of the cell. The particles were allowed to move over the surface by Brownian motion. The simulation time step was 0.1 ms and the total simulated time was 90 s. The positions of all particles were extracted every 10 s. All the step sizes (displacements) on this 10 s time step were put in a distribution. Only those particles that remained within the band during the entire simulation were used, and the distributions were fitted with Eq. 3.

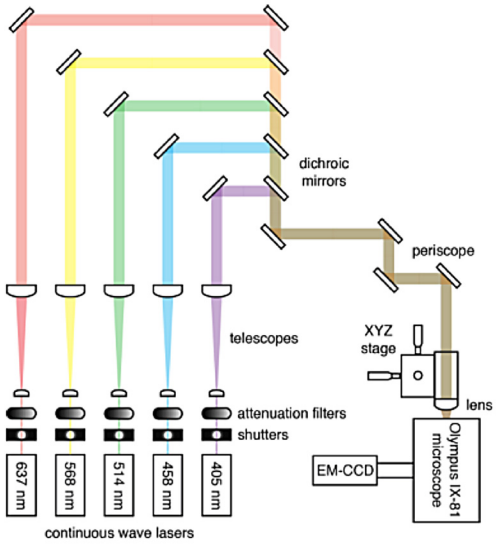

Scheme 1. *Scheme of live cell imaging single molecule fluorescence microscopy set up.* Optical scheme composed of various continuous wave lasers, computer-controlled shutters, neutral-density attenuation filters and dichroic mirrors. Inverted Olympus IX-81 microscope with a fully automated XYZ stage and coupled to an EM-CCD camera.

Results

Lateral diffusion of polytopic membrane proteins in the PM of yeast is extremely slow

We probed the lateral diffusion of polytopic membrane proteins localized at the plasma membrane using Fluorescence recovery after photo-bleaching (FRAP). We expressed Ypet fusions of the lysine-H^+ symporter Lyp1p, the arginine-H^+ symporter Can1p, the sodium/H^+ antiporter Nha1p and the glycerol channel Fps1p. Despite differences in structure and PM domain partitioning of the proteins, the lateral diffusion of Lyp1p, Can1p and Nha1p is very similar, as shown in Figure 1. The recovery profiles could be fitted to a single exponential function, indicating that there is one mobile fraction. These curves yielded very similar diffusing coefficients of 0.00045 ±0.00009, 0.00065 ±0.00011 and 0.00050 ±0.00012 $\mu m^2/s$, for Lyp1p, Can1p and Nha1p, respectively. For Fps1p the recovery curve is a function of two mobile fractions; one showing faster diffusion (D = 0.0035 $\mu m^2/s$) than the other proteins and one showing slower diffusion (D = 0.00006 $\mu m^2/s$). Despite the small variation in lateral diffusion rates between Lyp1p, Can1p and Nha1p they differ in normalized recovery; for Lyp1p and Nha1p, the values are 64 % and 53 %, respectively. In case of Can1p we observed a relatively large variation in fluorescence recovery between cells, with ranges from 60 % to 100 %. The differences in Can1p recovery might be attributed to residence of a fraction of the molecules in MCCs/eisosomes.

In order to validate our analysis technique, we analyzed simulated diffusion data (Figure 2) Molecules were allowed to diffuse freely with a diffusion coefficient of 0.03 $\mu m^2/s$. The region representing the focal plane analyzed with the confocal microscope (see previous section) was taken with a thickness of 1 μm. The recovery of the particles in the photo-bleached region was followed and fitted the same way as the experimental data. The diffusion coefficient obtained, 0.032 $\mu m^2/s$, was very similar to the theoretical one, 0.03 $\mu m^2/s$, validating the analysis strategy. Overall, the diffusion rates of proteins in the *S. cerevisiae* PM are 1–3 orders of magnitude slower than proteins of similar size in the vacuolar membrane (Valdez-Taubas *et al.* (115); our own measurements on Vba1p yield D = 0.07 $\mu m^2/s$, data not shown).

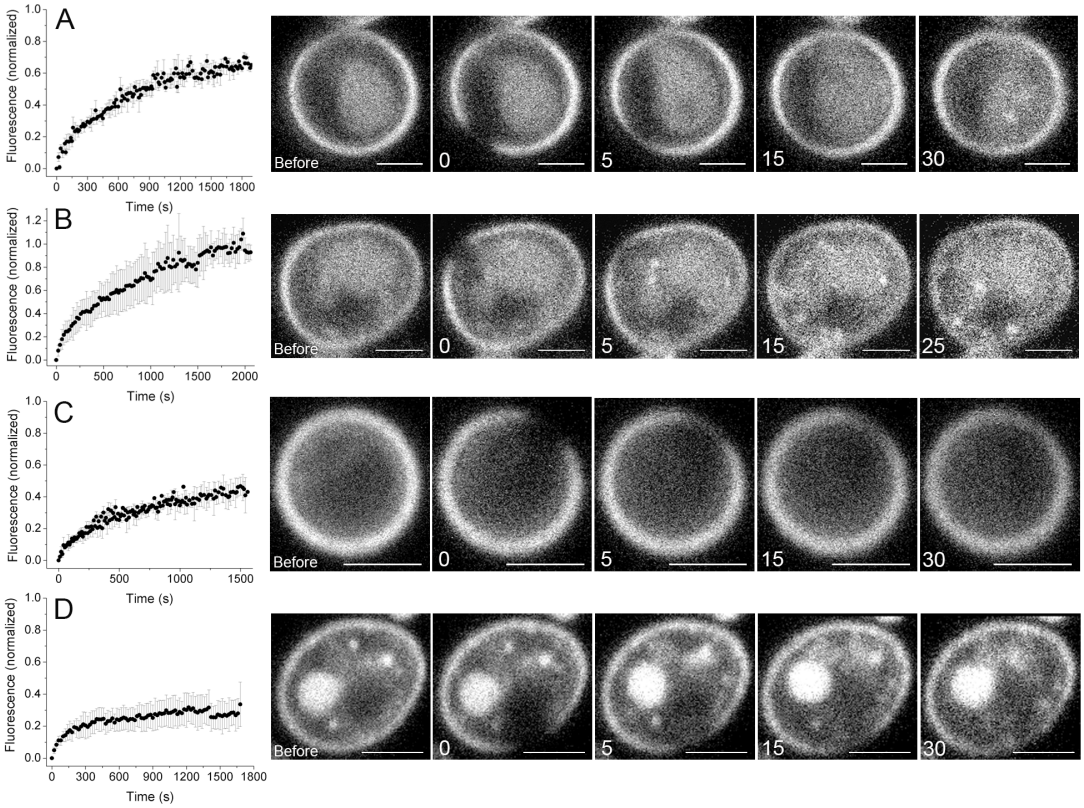

E

Protein	*D* (μm²/s)	SD of *D* (μm²/s)	Normalized Recovery	SD of normalized Recovery
Lyp1p-Ypet	0.00045	0.00009	0.639	0.032
Can1p-Ypet	0.00065	0.00011	0.815	0.120
Nha1p-Ypet	0.00050	0.00012	0.528	0.023
Fps1p-Ypet	0.003[1] / 0.00006[2]	0.001[1] / 0.00005[2]	0.313	0.039

Figure 1. *FRAP measurements of plasma membrane proteins of yea*st. Normalized fluorescence recovery of Lyp1p (A), Can1p (B), Nha1p (C) and Fps1p (D). Confocal images of before and different time points after photo-bleaching are shown in the right panels. Scale bars represent 2 μm. (E) Diffusion coefficient values and normalized recoveries with the respective standard deviations of each protein. [1]Fast fraction and [2]slow fraction of Fps1p.

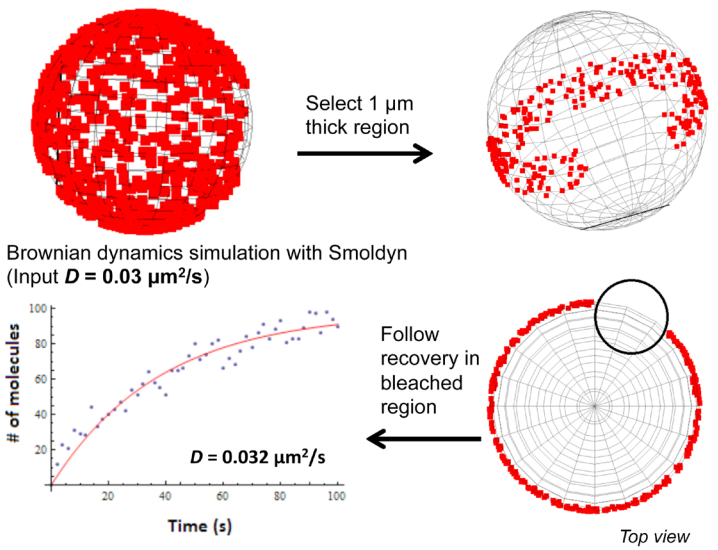

Figure 2. *FRAP simulation.* Simulation of Brownian diffusion in a cell with 4000 particles. Photo-bleached region of 2 μm width and 1 μm thick. Recovery of the particles in the bleached region (blue dots) and exponential fitting of the data (red line).

Single-particle tracking confirms slow diffusion of Lyp1p and Can1p

The ensemble-averaged behavior of Lyp1p, Can1p, Nha1p and Fps1p show that the lateral diffusion of these PM molecules is extremely slow, irrespective of their assumed location in the membrane (see Introduction on MCC, MCP and possible other domains). However, conventional methods such us FRAP probe only long-range diffusion of molecules. If molecules are confined in specific membrane domains, diffusion within these compartments may go unnoticed when probed by FRAP. We thus performed single-particle tracking of the two homologous proteins present in the PM of yeast (see Scheme 2 for sequence alignment): Can1p, thought to accumulate in MCC domains, and Lyp1p, which is not known to partition in a specific membrane domain. We carried out the step size analysis to determine whether or not the microscopic diffusion (SPT) of the molecules is as slow as the macroscopic diffusion (FRAP). To probe possible physical confinement of the proteins or interaction with other components of the cell, we determined the relationship between the mean squared displacement (MSD) and time. Figures 3 and 4 show the step size distributions (A-G) and the estimated diffusion coefficients at different frame times (H). The apparent rates of diffusion decrease with longer sampling times until reaching a plateau. The distributions indicate slow diffusion. At fast sampling rates, the proteins produce very small displacements between frames and the measured step-size distributions are dominated by localization uncertainty. Only once the delay between images is sufficiently long, we can resolve protein displacements from the localization noise. The data obtained in those longer experiments (3, 10 and 30 s sampling) were used to calculate the averaged diffusion rates. By SPT we measure diffusion coefficients of 0.00041 $\pm$ 0.00018 $\mu m^2/s$ and 0.00038 $\pm$ 0.00027 $\mu m^2/s$, for Lyp1p and Can1 respectively, consistent with the values measured by FRAP (0.00045 and 0.00065 $\mu m^2/s$).

Scheme 2. *Sequence alignment of Lyp1p and Can1p proteins.*

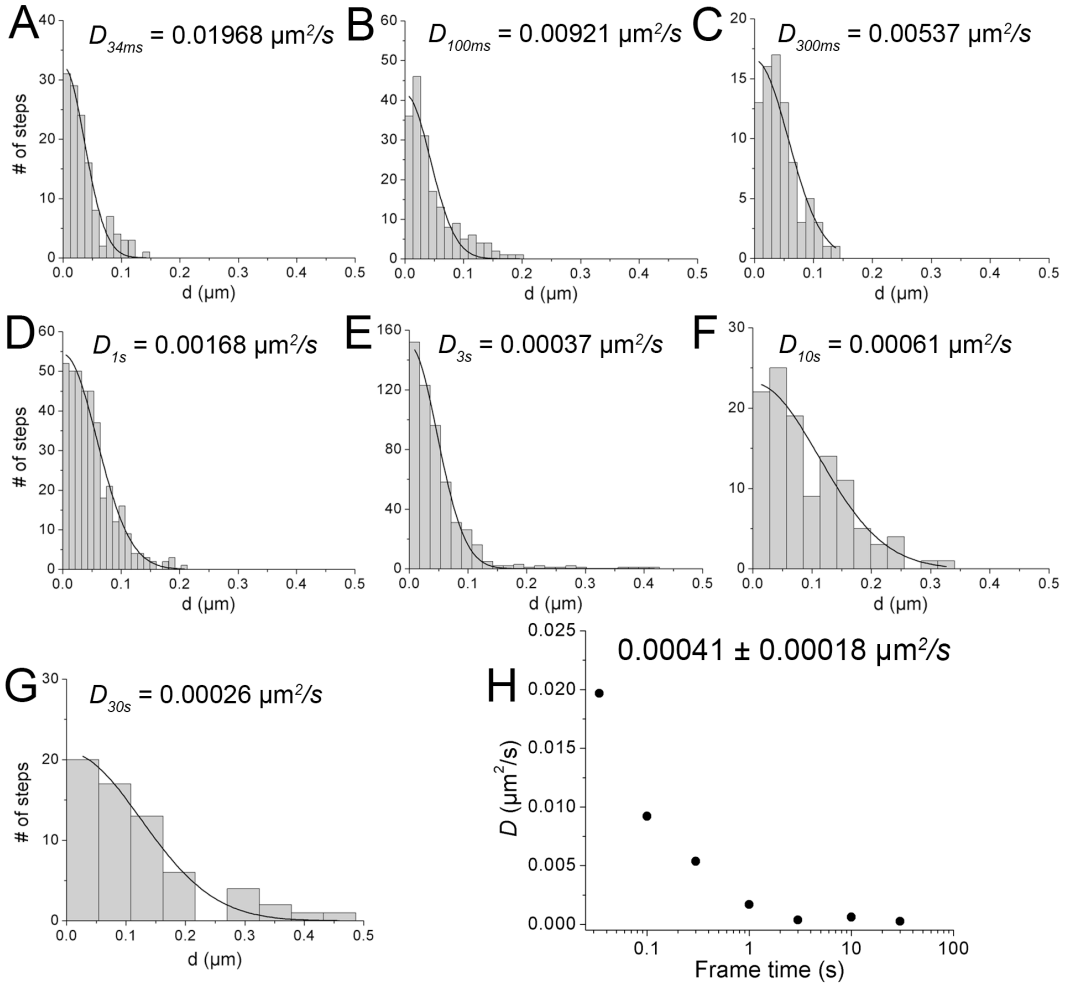

Figure 3. *Step size analysis of Lyp1p-YPet diffusion at different frame times.* (A-G) Step size (displacement, *d*) distribution of experiments performed at frame times of 34 ms, 100 ms, 300 ms, 1 s, 3 s, 10 s and 30 s. The diffusion coefficients obtained by 1D diffusion fit are shown. (H) Diffusion coefficients plotted as a function of the frame time. Averaged diffusion and standard deviation of the last three frame times (E-G) are shown.

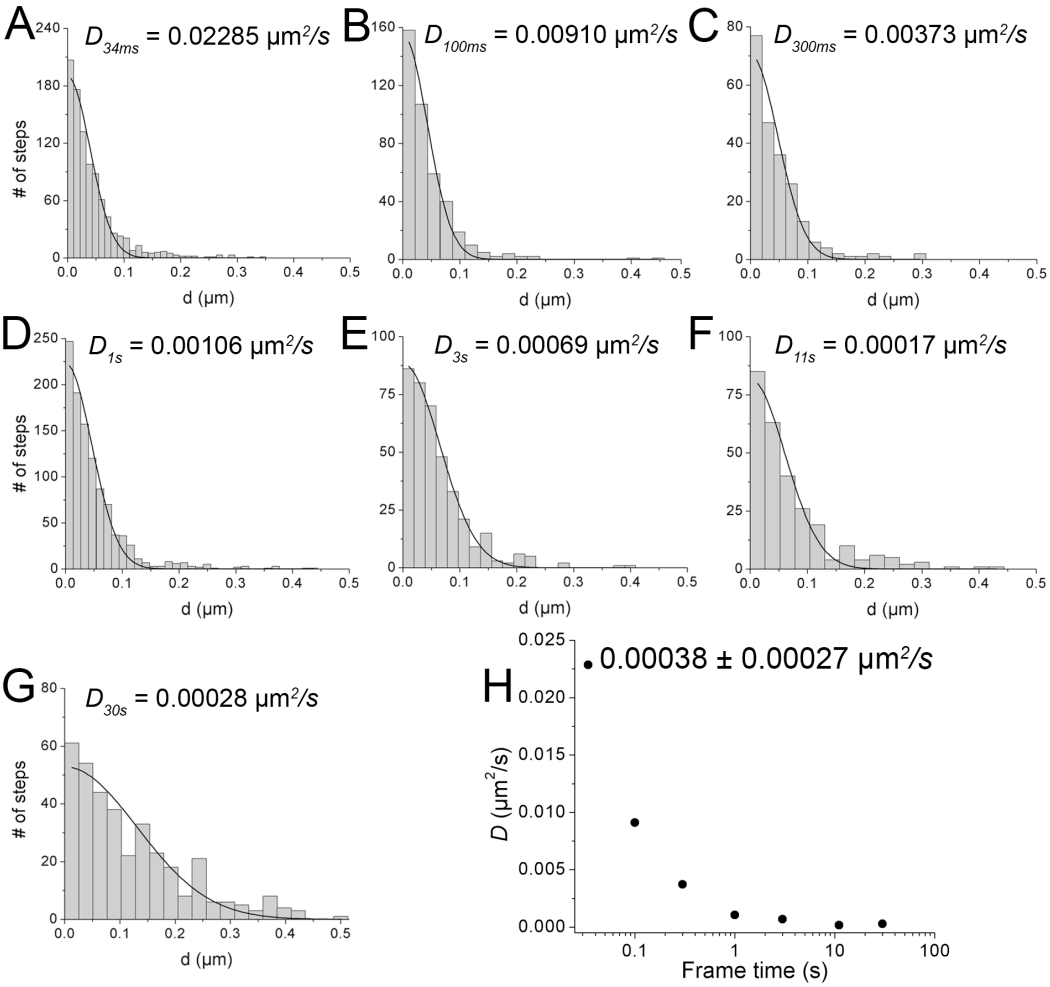

Figure 4. *Step size analysis of Can1p-YPet protein at different frame times.* (A-G) Step size (displacement, *d*) distribution of experiments performed at frame times of 34 ms, 100 ms, 300 ms, 1 s, 3 s, 11 s and 30 s. The diffusion coefficients obtained by 1D diffusion fit are shown. (H) Diffusion coefficients plotted as a function of the frame time. Averaged diffusion and standard deviation of the last three frame times (E-G) are shown.

SPT simulations show how the diffusion coefficients obtained experimentally are somewhat underestimated

In order to verify the step size analysis we performed simulations of the single particle tracking data. Figure 5A shows an example of a step size distribution obtained by simulating the data with an input diffusion coefficient of 0.025 μm²/s. The localization noise was taken from the displacement obtained with the fastest frame time, 34 ms. From the acquisition speed up to 3 s/frame the displacement is constant, which corresponds to the localization noise. The displacement of the proteins is greater than the localization noise from 3 s/frame, where an increase is seen with higher frame times (Figure 6). The distribution of displacements was fitted with a 1D diffusion model (Eq. 3) to calculate the observed diffusion coefficient. Figure 5B depicts the relation between the obtained coefficients (D_{obs}) and the ones introduced before running the simulation (D_{in}). Across a range of input diffusion rates there is a discrepancy between the input and measured diffusion coefficients (Fig 5B). This discrepancy arises due to the difference in the geometry of yeast and the simulated cell, which was not taken into account in our analysis. The corrected diffusion coefficients for Lyp1p and Can1p were taken from the relationship between D_{in} and D_{obs} data resulting in 0.0011 and 0.0009 $\mu m^2/s$, respectively.

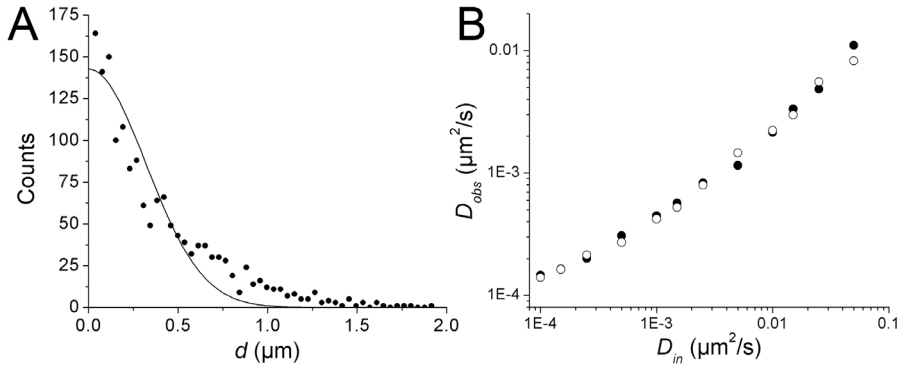

Figure 5. *SPT simulation.* (A) Step size distribution of a spherical cell 5 μm in diameter. The band where the particles were analyzed was 1 μm thick and the input D was 0.025 μm²/s. Displacements, d, obtained from the simulation are depicted in black circles and the 1D fit as a line. (B) Relationship between the D_{obs} and D_{in} considering the localization noise in the data. D obtained from displacements along the x-axis depicted in full circles and the y-axis in empty circles.

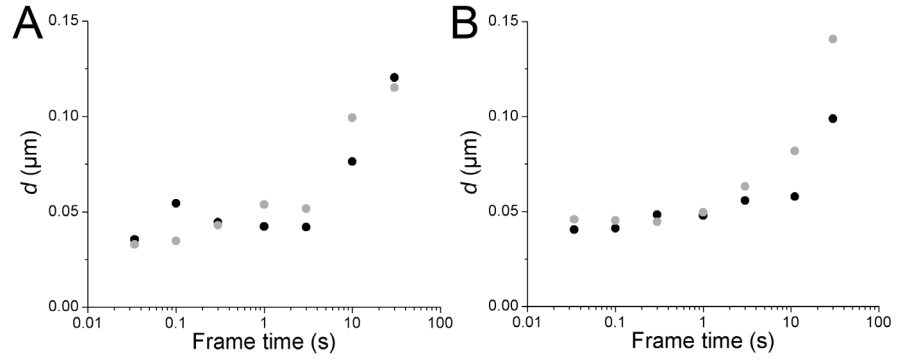

Figure 6. *Mean displacements of Lyp1p and Can1p at different frame times.* (A) Lyp1p displacements in the x-axis (grey) and y-axis (black). (B) Similar data for Can1p.

No evidence for confinement

The step size analysis shows that the microscopic diffusion of both proteins, Lyp1p and Can1p, is very similar to the ensemble diffusion coefficients obtained with FRAP. This slow diffusion could be due to anomalous diffusion produced by confinement or interaction with other proteins. In order to probe for these effects, we analyzed the relationship between the MSD and the step time interval. If protein diffusion follows a random unhindered random walk, the MSD will be linear with time. However, if the diffusion is hindered or restricted the MSD-time plot will be irregular, and with protein confinement the MSD will plateau and not exceed the diameter of the confined area. Figures 7 and 8 (A-G) show MSD plots for Lyp1p and Can1p imaged with different sampling times. While the trajectories are relatively short due to photobleaching and diffusion out of the focal plane, all plots are well fit by a linear function. Each line intercepts the Y-axis at a value greater than zero. This is a known effect of localization uncertainty in the measurements (324). The gradients of the fit lines are similar across all measurements and yield diffusion coefficients consistent with those calculated from step-size distributions and FRAP, $0.00049 \pm 0.00005\ \mu m^2/s$ and $0.00069 \pm 0.00005\ \mu m^2/s$, for Lyp1p and Can1 respectively. Since we did not account for the cell shape during the analysis, there are likely to be minor discrepancies with the real values.

The data are not consistent with confined diffusion. By averaging all the MSD-time plots we assume that all proteins reside in the same environment and undergo the same type of diffusion. We also produced MSD-time plots for each individual trajectory. In each case there is no convincing evidence of a plateau that would indicate confinement. This stands in contrast with the observation that Can1p accumulates in the MCC domains with dimensions of 50-300nm and suggests that Can1p diffuses freely in the yeast PM. There remains the possibility that the compartments or confined areas in yeast are too small to be probed given the spatial resolution of our technique (~50 nm) and that our observations are of slower movements between compartments, as shown for mammalian cells (325, 326). If this is true, the compartments must have an average area less than ~$0.005\ \mu m^2$ (the localization uncertainty) and molecules must reside in these compartments for only tens of milliseconds. Alternatively, it is possible that Can1p is not kinetically trapped in MCCs and diffuses in and out freely, and that the partitioning is due to a different membrane lipid composition (106).

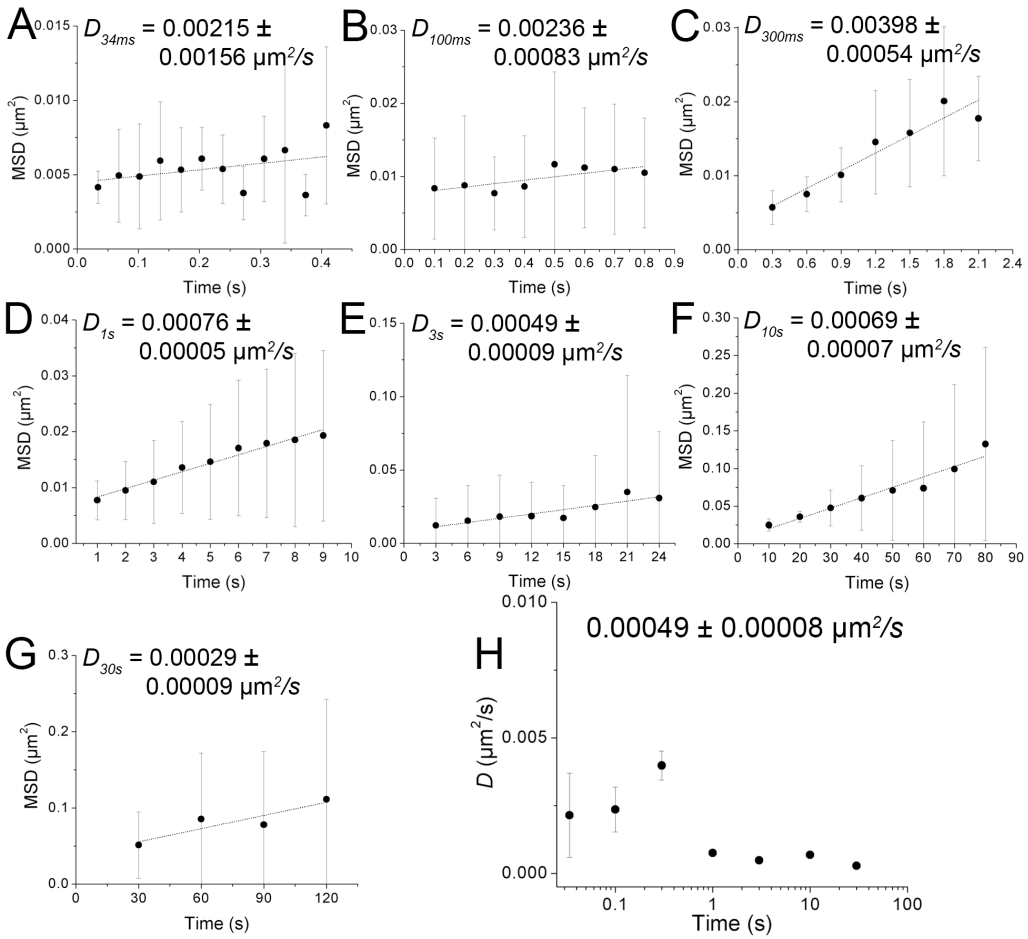

Figure 7. *MSD of Lyp1p protein at different frame times*. (A-G) MSD-time plots of experiments performed at the frame times of 34 ms (n = 6), 100 ms (n = 8), 300 ms (n = 4), 1 s (n = 16), 3 s (n = 21), 10 s (n = 6) and 30 s (n = 7). The diffusion coefficient was obtained from the slope of each graph. Errors represent averaged standard deviation. (H) Diffusion coefficients plotted as a function of the frame time. Averaged diffusion and standard deviation of the last three frame times (E-G) are shown.

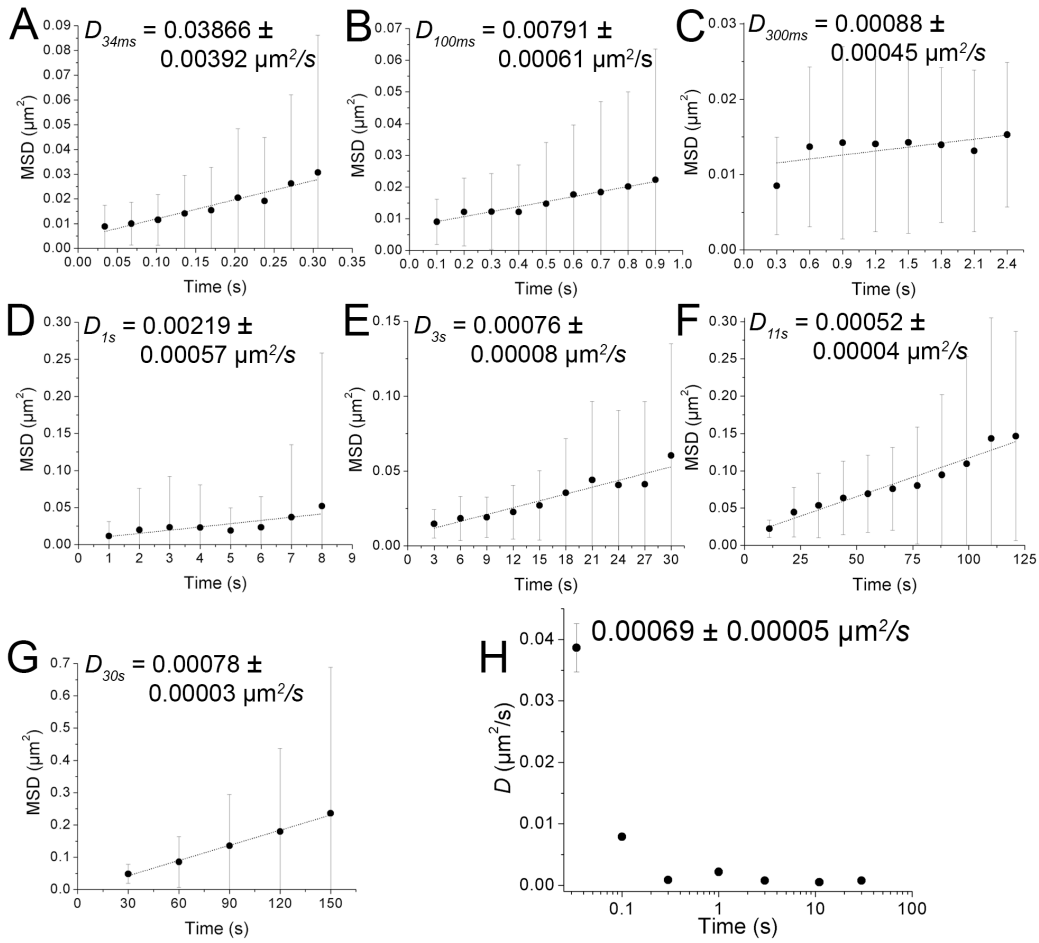

Figure 8. *MSD of Can1p protein at different frame times*. (A-G) MSD-time plots of experiments performed at frame times of 34 ms (n = 42), 100 ms (n = 17), 300 ms (n = 9), 1 s (n = 36), 3 s (n = 16), 11 s (n = 10) and 30 s (n = 34). The diffusion coefficient was obtained from the slope of each graph. Errors represent averaged standard deviation. (H) Diffusion coefficients plotted as a function of the frame time. Averaged diffusion and standard deviation of the last three frame times (E-G) are shown.

Lyp1p and Can1p are monomeric

We set out to determine the oligomeric state of Lyp1p and Can1p within the yeast PM. There are many methods to determine the oligomeric state of membrane proteins in the detergent-solubilized state (327). However, to determine the quaternary structure without disrupting the membrane environment is difficult. Single molecule analysis is arguably the method of choice to discriminate between monomeric, dimeric, trimeric and tetrameric species (328); for higher oligomeric states the method becomes tedious, however large complexes have been described by fluorophore counting (329). To determine the oligomeric state of Lyp1p and Can1p, we quantified the YPet fluorescence of individual proteins recorded during our single-particle tracking experiments. For each protein we analyzed both single-tagged (e.g. Lyp1p-YPet) and double-tagged (e.g. Lyp1p-YPet-YPet) constructs (bleaching steps of single- and double-tagged Lyp1p are shown in Figures 9C and 9D). In these experiments, as in the single particle tracking analysis, the expression levels were very low, in order to minimize spatial overlap between foci. In the case of Lyp1p-YPet, a relatively broad distribution is observed and is centered at 1 molecule per focus (Fig 9A). The distribution is likely broad because of noise. However, we assume that some of the brighter foci contain spatially overlapping molecules. For Lyp1p-YPet-YPet, a similar distribution is observed, but this time it is centered at 2 molecules per focus (Fig. 9A). Can1p-YPet-YPet produces a similar distribution, centered at two molecules per focus (Fig. 9B). These observations indicate that both Lyp1p and Can1p are predominantly in monomeric form in the yeast PM.

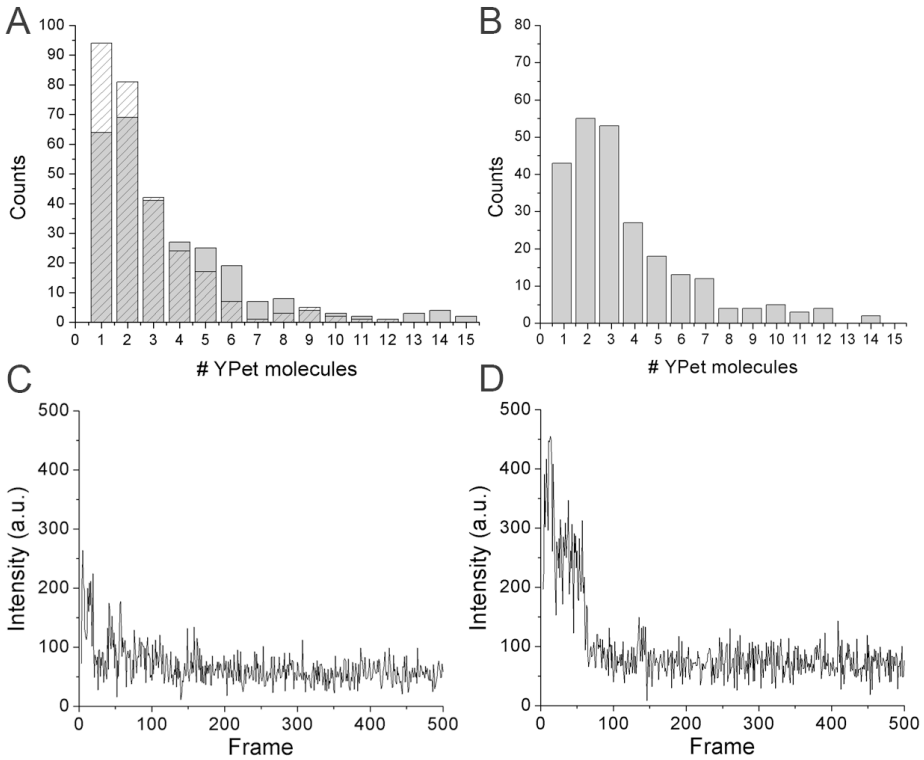

Figure 9. *Oligomeric state of Lyp1p and Can1p*. Number of YPet photo-bleaching steps molecules per diffraction-limited spot for fusions with Lyp1p (A) and Can1p (B). The proteins are expressed at low level in the plasma membrane of yeast. Striped bars represent the proteins labelled with one YPet and the full bars with two (tandem) YPet molecules. (C) Single YPet bleaching step along 500 frames. (D) Double YPet bleaching steps along 500 frames.

Heterogenous distribution of membrane proteins due to low expression levels

We here apply a high resolution imaging technique with fluorophore-tagged proteins, PALM, to study the organization of the plasma membrane of yeast. We studied Lyp1p and Can1p, each fused to the photo-switchable protein mEos3.1. Both fusion proteins were expressed at endogenous levels from their native chromosomal positions. Figure 10 shows the reconstructed images of Lyp1p-mEos3.1 (A) and Can1p-mEos3.1 (B), together with the bright-field image of the cells. The localization precision is 30.8 nm and 29.7 nm for Lyp1p and Can1p, respectively (C and E). Both proteins have a mean mEos3.1 fluorescence intensity of around 2000 in arbitrary units. Our results show that Can1p has a patchy organization at the plasma membrane, as would be expected of proteins associated with MCC domains (98, 101). Surprisingly, however, Lyp1p, which is not known to be present in these domains, also shows a patchy distribution on the PM. The number of patches is on average lower for Can1p (9.5 patches per cell, n = 20) than Lyp1p (16.4 patches per cell, n = 20). Inspection of intensity fluctuations within the original movies suggests that these patches each contain one or two molecules that are repeatedly localized (Fig. 11). This suggests that the endogenous levels of those proteins in the PM are very low, in fact they are similar to the levels we induced for our single-particle tracking measurements. Putting MCCs and MCPs to the side, the low endogenous levels of these proteins suggest a simpler explanation for their heterogeneous distribution in the PM: there are simply not enough molecules to form a smooth distribution!

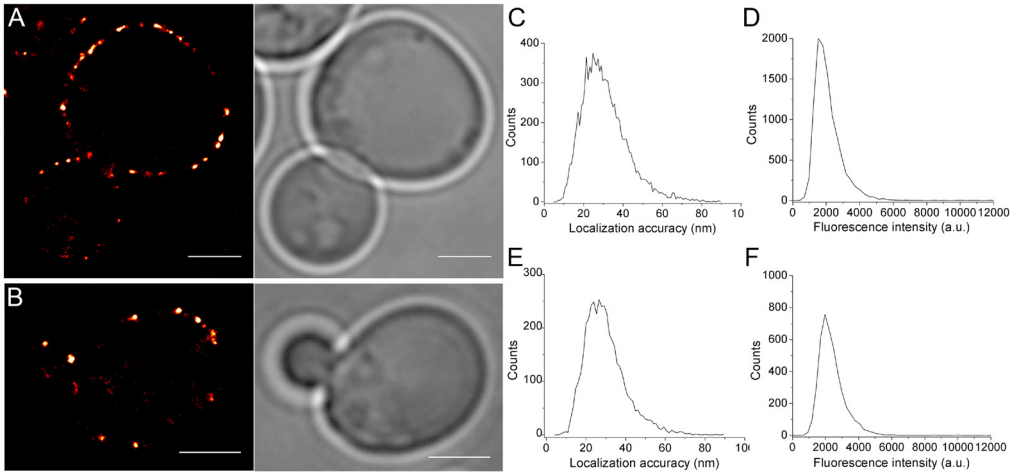

Figure 10. *Localization of Lyp1p and Can1p.* PALM reconstructions of Lyp1p-mEos3.1 (A) and Can1p-mEos3.1 (B); both transporter genes were chromosomally tagged with mEos3.1. Localization accuracy of mEos3.1 (C and E). Fluorescence intensity of mEos3.1 (D and F). Scale bars represent 2 μm.

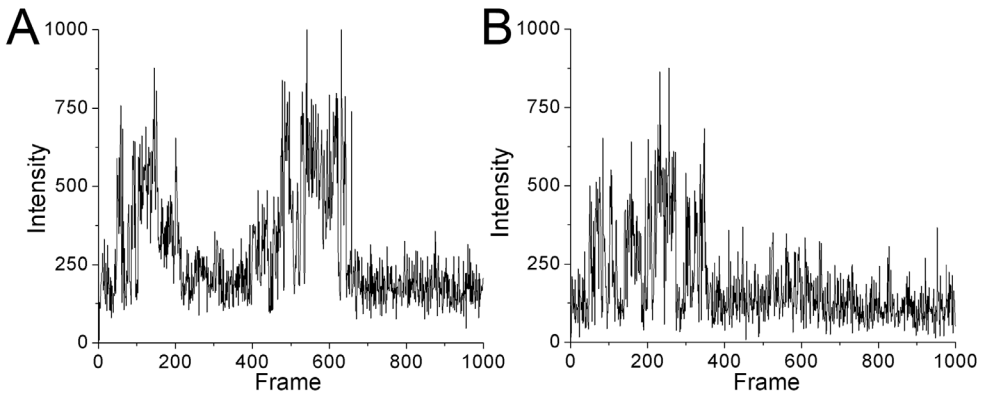

Figure 11. *Fluorescence intensity of a single molecule along the movie.* (A) Lyp1p (B) Can1p.

The amount of Lyp1p at the PM increases when the lysine/arginine concentration is reduced

We analyzed whether the protein levels increase when their substrate levels (lysine and arginine) are decreased, and if so, whether this causes a change in the localization pattern. Figure 12 shows the reconstructed images of a cell grown with normal levels of substrate, 76 mg/L (Fig. 12A) and 10 times lower, 7.6 mg/L (Fig. 12B). The number of patches increases on average from 16.4 (n = 20) to 21.2 (n = 14) as can be seen in Fig. 12A and 12B, respectively. By looking at the fluorescence intensity profile along the PM when the substrate levels are lower, the gaps in between each patch are smaller in size but the localization is not fully homogeneous (Fig. 12C and 12D, start and end point of the profile are illustrated by the arrows in the PALM reconstructions). As shown in Figure 12E, by lowering the concentration of lysine and arginine 10 times, the total number of Lyp1p-mEos3.1 localizations per cell increased 2-fold (Fig. 12E). Levels of other PM transporters in yeast, such as Gap1, have been shown to increase in response to decreasing substrate concentrations, suggesting that the substrate concentration controls the level of protein at the plasma membrane (307). As before, each of the patches we observe appears to contain one or two molecules, thus even under low-substrate conditions the levels of Lyp1p in the PM remain relatively low.

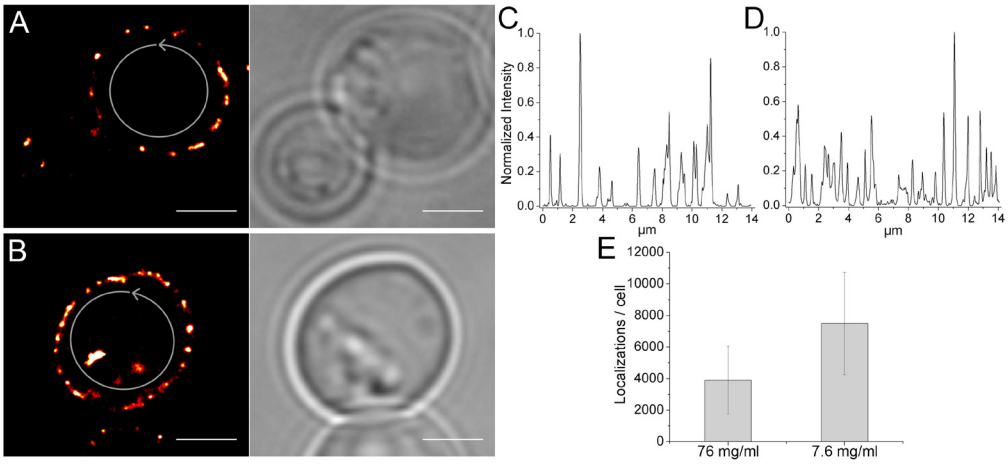

Figure 12. *Localization of Lyp1p in cells incubated with different amounts of substrate, lysine and arginine.* (A) Localization of Lyp1p in standard medium containing 76 mg/L of lysine and arginine and (B) medium containing 10 times less lysine and arginine, 7.6 mg/L. The bright-field images are depicted in the right panel. Arrows define the direction along the PM used to calculate the fluorescence intensity profile of Lyp1p in standard medium (C) and low substrate medium (D). Number of localizations per cell in different media with different concentrations of lysine and arginine (E). Errors represent standard deviation from the mean of 16 cells. Scale bars represent 2 μm.

Deletion of art1 and art2 decreases the internalization of Lyp1p

To investigate the effect of Lyp1p turnover on the organization of the protein in the PM, we performed PALM imaging in Art1 and Art2 null strains. It is known for yeast that Art1 and Art2 play a direct role in the down regulation of Lyp1p at the PM. Art1 and Art2 are members of the ART family (arrestin-related trafficking adaptors) and target Lyp1p for ubiquitination by Rsp5 and subsequent internalization to the multi vesicular endosome (MVE). Lyp1p internalization is triggered by two distinct pathways, one involves a high concentration of lysine in the medium and the other involves stresses such as the addition of cycloheximide, conditions known to trigger endocytosis of polytopic PM proteins (e.g. Can1p) (330). Art1 is required for the lysine-induced Lyp1p endocytosis, whereas Art2 is required for the stressed-induced internalization of the transporter (331). Figure 13A shows that Lyp1p in the double-knock out strain is spread more evenly over the PM as compared to the wild-type strain. The gaps between the localized proteins are less frequent and smaller as shown by the fluorescence intensity profile along the PM (Fig. 13B). We conclude that the residence time of Lyp1p at the PM is increased in the Art1/2 null strain, and that higher levels of protein accumulate. These experiments reinforce the conclusion that the dynamics of Lyp1p regulation at the PM is mostly at the level of (biogenesis and) endocytosis.

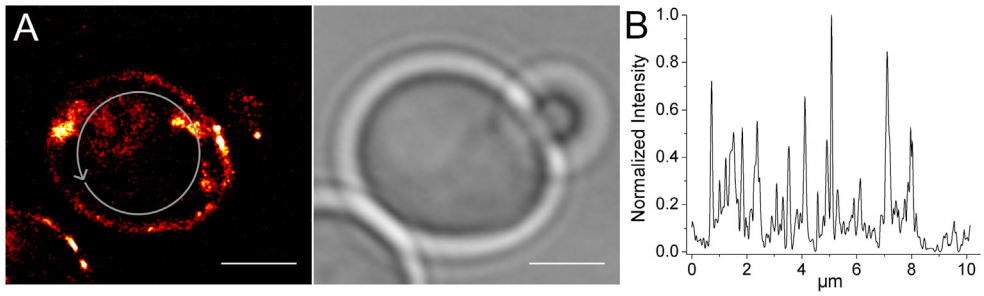

Figure 13. *Localization of Lyp1p in Art1/2 null strain*. (A) Localization of Lyp1p (left panel) and the bright-field image (right panel). The arrow defines the direction along the PM used to calculate the fluorescence intensity profile of Lyp1p (B). Scale bars represent 2 μm.

Discussion

In this study we analyzed the diffusion of membrane proteins by ensemble-averaged FRAP measurements and single-molecule SPT. The results indicate similar diffusion speeds for Nha1p, Lyp1p and Can1p within a range of 0.00045-0.00065 $\mu m^2/s$. The values are very similar to the ones obtained for the plasma membrane ATPase Pma1p and Gap1p with diffusion coefficients of 0.0004 to 0.0007 $\mu m^2/s$ (116, 119). These proteins contain 10-13 transmembrane (TM) helices. On the contrary Fps1p, with 6 TM helices, showed two distinct mobile fractions, a fast one with a diffusion coefficient of 0.003 $\mu m^2/s$ and a slow one of 0.00006 $\mu m^2/s$. The results of a previous study suggest Fps1p to be a tetramer in the PM of yeast. We consider it unlikely that the slower diffusing population corresponds to the tetramer, whereas the fast population relates to the monomeric state. The immobile fractions of all the membrane proteins tested by FRAP could be explained by clustering or ER/vesicle trapping prior to PM delivery due to high protein levels.

The diffusion coefficients of Lyp1p and Can1p obtained by SPT are in perfect agreement with those of the FRAP measurements. As shown here and by others (115, 117), the diffusion of plasma membrane proteins in yeast is at least two orders of magnitude slower than in mammalian cells. This slow diffusion of integral membrane proteins and lipids seems to be a general feature of the plasma membrane proteins of *S. cerevisiae*. The specific lipid composition of yeast might be an important factor in the slow diffusion of PM proteins. It is already known that the number of sphingolipids and ergosterol increases along the secretory pathway, and the PM being the organelle with the higher amounts and thus tighter membrane packing (2). Moreover, the dominant sphingolipid in yeast is the inositol-P-ceramide (IPC), which has a hydroxylated C_{26} acyl chain (90). This very long chain fatty acid differs from the chains of sphingomyelin in mammalian cells and is predicted to increase the lipid packing of the membrane. Intriguingly, the diffusion coefficient of similar size membrane proteins in the endoplasmic reticulum (ER) and vacuolar membrane of yeast are 2-3 orders of magnitude faster than in the PM (115, 120, 121). There is only a 4-fold difference between the lateral diffusion of lipid anchored proteins in the vacuole and the PM (119). In our analysis the diffusion of palmitoylated fluorescent reporters, anchored to the inner leaflet of the PM solely via the acyl chain, is relatively slow ($D = 0.02 \mu m^2/s$) albeit much faster than that of the integral membrane proteins. This suggests that the outer leaflet of the membrane or unknown interactions contributes enormously to the slow diffusion of polytopic membrane proteins.

The stoichiometry of a complex is usually well regulated and often linked to the function of the protein (327). For instance, Nha1p has been shown to function as

antiporter only when dimers are formed (311). Can1p and Lyp1p are shown to be monomeric, at least when expressed endogenous protein levels. This analysis rules out the formation of big protein aggregates as the cause for the slow diffusion.

PALM imaging shows how Can1p and Lyp1p distribute laterally in distinct areas, i.e. in a few patches along the PM. In general, cells have very few of those patches, around 10 seen when imaging the cross-section of the cell. By analyzing the intensity profile along the movies, we find that the patches accommodate only one or two proteins. This, together with the oligomeric state analysis, indicating that Lyp1p and Can1p are monomeric, shows that low amounts of the proteins are present in the PM. Our data agree with a recent study by Spira and co-workers, who showed that none of the proteins analyzed are co-localizing in the yeast PM (114). They interpret the data as the coexistence of various protein domains that only partially overlap. Their observations can be easily explained by the low number of proteins in the PM of yeast. The number of Lyp1p patches is increased when the substrate levels are low or when the proteins responsible of the Lyp1p recycling are deleted. This suggests that not only the low amounts but also protein endocytosis is influencing the polarization of the PM. This was already suggested on the basis of theoretical considerations and some experimental data for other proteins in the yeast PM (115, 124, 304).

Our SPT analysis shows the absence of any protein confinement. Therefore, the polarized patch-like distribution of Lyp1p and Can1p at the PM is not due to physical barriers hindering the proteins to diffuse further. There is still the remote possibility that compartments are present with sizes below our spatial resolution, approximately 0.005 μm^2 in area. The lack of confinement does not necessarily contradict the observations made by others where Can1p is shown to reside in a domain of 300 nm in diameter (98, 101, 102, 302). Can1p may partition in MCCs/eisosomes but the diffusion in or out of the domains may be fast and the diffusion in- and outside the MCCs may be similar. Thus, Can1p may not be kinetically trapped but thermodynamically favor the MCC domain. This would also be in accordance with the observation made by Brach and co-workers that 70% of Can1p resides outside of MCC/eisosome compartments and that endocytosis of Can1p takes place outside the MCC (113). In fact, Strádalová *et al.* demonstrated that the endocytosis is excluded from the cortical ER and the MCC/eisosomes (126). This is supported by observations made by Grossmann and co-workers, who showed that protonophores or deletion of genes specifying MCC proteins increased protein endocytosis (106).

We propose a simple model to explain the heterogeneous distribution of Lyp1p and Can1p in the yeast PM. The levels of these proteins in the PM are kept low through a combination of slow synthesis/PM delivery and Art1/2-dependent internalization. Once in the PM, membrane proteins diffuse slowly. Because of this, individual molecules appear as foci or small patches when imaged in the milliseconds to seconds time-regime, which is standard practice in the field. Moreover, if two proteins are delivered by the same vesicle to a given position at the PM, it will take long before they segregate. And this may explain why we observe either one or two proteins per focus. The slow diffusion we observe is not caused by the formation of large aggregates and is unlikely due to confinement within micro-compartments. If there are no physical barriers, the yeast lipid composition (highly rich in sphingolipids and ergosterol) and/or the crowding might be responsible for the extremely slow diffusion. To confirm this hypothesis, diffusion studies *in vitro* using model membranes (giant unilamellar vesicles) composed of yeast PM lipids with reconstituted proteins are required. It is also possible that the diffusion of integral membrane proteins is hindered through their interaction with cell wall components or ER anchors. Dual-color PALM measurements could be used to probe for co-localization and coordinated motion of membrane proteins, which would provide valuable insight into the environment in which the proteins function in the yeast PM.

Chapter 8

General discussion and future perspectives

Interaction of small molecules with membranes: Amphipathic pore-forming peptides

Antimicrobial peptides appear potentially effective in inhibiting or killing microbial cells without much negative effect on host cells, which makes them important targets for therapeutic applications. In this thesis, we describe the molecular basis for the antimicrobial activity of a cyclic peptide compared to its linear inactive analogue. The secondary structure acquired upon peptide binding, caused the right arrangement of the hydrophilic/positively charged and hydrophobic residues allowing pores to be formed. An amphipathic arrangement is a very common feature of antimicrobial peptides and facilitates the insertion of the peptide into the hydrophobic core of the membranes. However, the overall structure of the amphipathic cyclic peptide is unique and different from f.i. amphipathic helices that also form pores. Some antimicrobial peptides can also translocate the cell membranes and interact directly with intracellular processes or targets. The combination of multiple modes of action is currently being investigated and related to the low resistance that microbial cells present to these compounds. The multi-modes of action described *in vitro* are not easy to correlate to mechanistic processes that occur *in vivo*. The cyclic peptide studied here also showed a dual-mode mode of action by causing membrane poration and fusion. This tandem mechanism has been also observed by the G13A mutant of the influenza hemagglutinin, which possesses a leaky fusion phenotype (43). The lack of microbial resistance together with the wide range of cell targets makes antimicrobial peptides attractive for the discovery and development of novel anti-infective agents. The rational design of new agents will require further understanding of the molecular basis of their selective activity with low cytotoxicity and more detailed structure-activity relationships. The combination of molecular modeling with experimental approaches is the key to this understanding and will amplify the antimicrobial effectiveness of conventional antibiotics.

Interaction of small molecules with membranes: reducing *versus* non-reducing sugars

The survival of many organism to extreme conditions such as high or low temperatures, desiccation, high salt concentration, and lack of oxygen, have intrigued scientists for centuries. Anhydrobiosis, the best known form of cryptobiosis, is derived from the Greek and means "life without water" (274). In this state the organisms may stay alive for years or even centuries with their metabolism dropped to a minimum; cells are activated upon rehydration (273).

Non-reducing sugars like sucrose and trehalose have been shown to stabilize membranes and proteins upon dehydration, and many organisms are able to synthesize these compounds in high amounts, allowing them to survive desiccation. We have shown that these sugars are able to affect the membrane organization by disrupting the tight packing of the liquid-ordered lipid phases. Sugars spread the lipids by intercalating in between the head groups, increasing the lipid area and expanding the membrane. The increased degree of disorder in those lipid domains results eventually in a homogeneous distribution of lipid phases in model membranes. The relatively short linkage in between the two sugar rings and the non-reducing nature of sucrose and trehalose are crucial for the lipid domain mixing. Eukaryotic cell membranes have been shown to compartmentalize lipids and proteins in nanoscale domains, lipid rafts (see introduction), where vital processes take place. Non-reducing saccharides could also perturb the confinement of those proteins affecting their function and at the same time stabilizing them during anhydrobiosis. The change in the membrane lipid environment could affect the function and stability

of proteins, which is likely to be critical during anhydrobiosis.

Design of novel membrane pores: Applications in synthetic biology

Natural membrane channels have been widely used as inspiration for the development of new ion pores in synthetic biology. They have appealing applications as antibiotics, drug delivery vehicles, catalysts, detectors and sensors. In this thesis we have used the natural antimicrobial peptide, alamethicin, as the membrane channel in combination with the versatile DNA chemistry to modulate the channel behavior. The use of complementary DNA strands or G-quadruplex motifs has resulted in the stabilization of a preferred oligomeric state of the channel units, leading to pores with a stable unitary conductance. The approach of combining pore-forming properties of peptides with functionalization by DNA has potential application in the drug delivery field. However, further improvements in the design are needed, which could include the development of synthetic channels with controlled disassembly of the DNA scaffolds and thus freeing the peptide monomers eliminating the size restriction that they initially possessed. In such a design, the delivery of large macromolecules could take place in a controlled fashion. The *in vivo* application of these systems would require the injection of complementary DNA strands or alternatives to potassium ions to stabilize the G-quadruplex motif. They could also be tested and used as antimicrobial agents due to the self-insertion propensity of those peptide-DNA hybrids. The drug delivery field is still in need of future progress in mechanistic and structural studies to maximize the efforts towards the design and synthesis of effective compounds "beyond the simple hole".

Protein dynamics in the plasma membrane of *Saccharomyces cerevisiae*

Eukaryotic cell membranes have proven to be highly organized with the capability to sub-compartmentalize, which impacts the intracellular membrane trafficking and signaling. One of the well-established membrane organizations is the formation of membrane 'rafts', which are described as dynamic nanoscale sterol, sphingolipid-enriched, ordered assemblies of specific proteins (1). *Saccharomyces cerevisiae* serves as a model system for mammalian cells to study several processes, including the membrane organization. The yeast plasma membrane has found to be organized in the MCC/eisosome, MCP and MCT domains. However, recent studies also suggested that the plasma membrane of yeast accommodates several protein domains that partially overlap with each other (114). In this thesis, we have shown that the amino acid transporter Can1p, thought to be component of the MCC domain, is not confined to a specific domain when expressed at endogenous levels (chromosomal expression). The lateral diffusion of the protein in the plasma membrane (PM) is extremely slow and similar to that of other polytopic membrane proteins tested such as Lyp1p, Nha1p and Fps1p. Our super-resolution imaging experiments have shown that the polarized distribution of these proteins along the PM might be the result of low expression levels under normal conditions. This localization pattern is also influenced by the slow mobility of the proteins as proteins inserted into the PM do not readily diffuse away from each other. The high contents of sterols and sphingolipids in the PM increase the ordering and stiffness of the membranes, which is likely the basis for the slow diffusion of the proteins. Our results favor the hypothesis that plasma membrane polarity is reached by the resultant of slow protein diffusion, high membrane viscosity and low protein levels. The next question that needs to be answered is whether the described microdomains in the PM of yeast are real or whether overexpression has contributed to apparent heterogeneities.

Dual-color PALM will allow us to analyze the co-localization of PM transporters with well-known protein components at high resolution and resolve issues on membrane domains in the PM of yeast. Such experiments together with studies of the dynamics of proteins in model membranes prepared from yeast PM lipids should allow us delineate the basis for slow diffusion and domain formation.

References

1. Simons K, Sampaio JL (2011) Membrane organization and lipid rafts. *Cold Spring Harbor perspectives in biology* 3:a004697.
2. Van Meer G, Voelker DR, Feigenson GW (2008) Membrane lipids: where they are and how they behave. *Nat Rev Mol Cell Biol* 9:112–124.
3. Sharpe HJ, Stevens TJ, Munro S (2010) A comprehensive comparison of transmembrane domains reveals organelle-specific properties. *Cell* 142:158–169.
4. Klemm RW et al. (2009) Segregation of sphingolipids and sterols during formation of secretory vesicles at the trans-Golgi network. *J Cell Biol* 185:601–612.
5. Singer SJ, Nicolson GL (1972) The fluid mosaic model of the structure of cell membranes. *Science* 175:720–731.
6. Simons K, Ikonen E (1997) Functional rafts in cell membranes. *Nature* 387:569–572.
7. Karnovsky MJ, Kleinfeld AM, Hoover RL, Klausner RD (1982) The concept of lipid domains in membranes. *J Cell Biol* 94:1–6.
8. Kahya N, Scherfeld D, Bacia K, Poolman B, Schwille P (2003) Probing lipid mobility of raft-exhibiting model membranes by fluorescence correlation spectroscopy. *J Biol Chem* 278:28109–28115.
9. Baumgart T, Hess ST, Webb WW (2003) Imaging coexisting fluid domains in biomembrane models coupling curvature and line tension. *Nature* 425:821–824.
10. Bacia K, Schwille P, Kurzchalia T (2005) Sterol structure determines the separation of phases and the curvature of the liquid-ordered phase in model membranes. *Proc Natl Acad Sci USA* 102:3272–3277.
11. Kahya N, Scherfeld D, Bacia K, Schwille P (2004) Lipid domain formation and dynamics in giant unilamellar vesicles explored by fluorescence correlation spectroscopy. *J Struct Biol* 147:77–89.
12. Baumgart T et al. (2007) Large-scale fluid/fluid phase separation of proteins and lipids in giant plasma membrane vesicles. *Proc Natl Acad Sci USA* 104:3165–3170.
13. Levental I et al. (2009) Cholesterol-dependent phase separation in cell-derived giant plasma-membrane vesicles. *Biochem J* 424:163–167.
14. Lingwood D, Ries J, Schwille P, Simons K (2008) Plasma membranes are poised for activation of raft phase coalescence at physiological temperature. *Proc Natl Acad Sci USA* 105:10005–10010.
15. Lichtenberg D, Goñi FM, Heerklotz H (2005) Detergent-resistant membranes should not be identified with membrane rafts. *Trends Biochem Sci* 30:430–436.
16. Shaw AS (2006) Lipid rafts: now you see them, now you don't. *Nature immunology* 7:1139–1142.
17. Munro S (2003) Lipid rafts: elusive or illusive? *Cell* 115:377–388.
18. Eggeling C et al. (2009) Direct observation of the nanoscale dynamics of membrane lipids in a living cell. *Nature* 457:1159–1162.
19. Simons K, Gerl MJ (2010) Revitalizing membrane rafts: new tools and insights. *Nat Rev Mol Cell Biol* 11:688–699.
20. Veatch SL, Soubias O, Keller SL, Gawrisch K (2007) Critical fluctuations in domain-forming lipid mixtures. *Proc Natl Acad Sci USA* 104:17650–17655.
21. Schäfer LV et al. (2011) Lipid packing drives the segregation of transmembrane helices into disordered lipid domains in model membranes. *Proc Natl Acad Sci USA* 108:1343–1348.
22. van Duyl BY, Rijkers DTS, de Kruijff B, Killian JA (2002) Influence of hydrophobic mismatch and palmitoylation on the association of transmembrane alpha-helical peptides with detergent-resistant membranes. *FEBS Lett* 523:79–84.

23. Levental I, Lingwood D, Grzybek M, Coskun U, Simons K (2010) Palmitoylation regulates raft affinity for the majority of integral raft proteins. *Proc Natl Acad Sci USA* 107:22050–22054.

24. Brogden KA (2005) Antimicrobial peptides: pore formers or metabolic inhibitors in bacteria? *Nat Rev Microbiol* 3:238–250.

25. Epand RM, Vogel HJ (1999) Diversity of antimicrobial peptides and their mechanisms of action. *Biochim Biophys Acta* 1462:11–28.

26. Boman HG (1991) Antibacterial peptides: key components needed in immunity. *Cell* 65:205–207.

27. Shai Y (2002) From innate immunity to de-novo designed antimicrobial peptides. *Curr Pharm Des* 8:715–725.

28. Hancock REW (1997) Peptide antibiotics. *The Lancet* 349:418–422.

29. Yeaman MR, Yount NY (2003) Mechanisms of antimicrobial peptide action and resistance. *Pharmacol Rev* 55:27–55.

30. Fox RO, Richards FM (1982) A voltage-gated ion channel model inferred from the crystal structure of alamethicin at 1.5-Å resolution. *Nature* 300:325–330.

31. Baumann G, Mueller P (1974) A molecular model of membrane excitability. *J Supramol Struct* 2:538–557.

32. Pouny Y, Rapaport D, Mor A, Nicolas P, Shai Y (1992) Interaction of antimicrobial dermaseptin and its fluorescently labeled analogues with phospholipid membranes. *Biochemistry* 31:12416–12423.

33. Ludtke SJ et al. (1996) Membrane pores induced by magainin. *Biochemistry* 35:13723–13728.

34. Leontiadou H, Mark AE, Marrink SJ (2006) Antimicrobial peptides in action. *J Am Chem Soc* 128:12156–12161.

35. Sengupta D, Leontiadou H, Mark AE, Marrink SJ (2008) Toroidal pores formed by antimicrobial peptides show significant disorder. *Biochim Biophys Acta* 1778:2308–2317.

36. Henriques ST, Melo MN, Castanho MARB (2007) How to address CPP and AMP translocation? Methods to detect and quantify peptide internalization in vitro and in vivo (Review). *Mol Membr Biol* 24:173–184.

37. Van Den Bogaart G, Krasnikov V, Poolman B (2007) Dual-color fluorescence-burst analysis to probe protein efflux through the mechanosensitive channel MscL. *Biophys J* 92:1233–1240.

38. Van Den Bogaart G, Mika JT, Krasnikov V, Poolman B (2007) The lipid dependence of melittin action investigated by dual-color fluorescence burst analysis. *Biophys J* 93:154–163.

39. Sochacki KA, Barns KJ, Bucki R, Weisshaar JC (2011) Real-time attack on single Escherichia coli cells by the human antimicrobial peptide LL-37. *Proc Natl Acad Sci USA* 108:E77–81.

40. Melo MN, Ferre R, Castanho MARB (2009) Antimicrobial peptides: linking partition, activity and high membrane-bound concentrations. *Nat Rev Microbiol* 7:245–250.

41. Hsu JCY, Yip CM (2007) Molecular dynamics simulations of indolicidin association with model lipid bilayers. *Biophys J* 92:L100–2.

42. Yesylevskyy S, Marrink SJ, Mark AE (2009) Alternative mechanisms for the interaction of the cell-penetrating peptides penetratin and the TAT peptide with lipid bilayers. *Biophys J* 97:40–49.

43. Lai AL, Tamm LK (2010) Shallow boomerang-shaped influenza hemagglutinin G13A mutant structure promotes leaky membrane fusion. *Journal of Biological Chemistry* 285:37467–37475.

44. Cummings JE, Vanderlick TK (2007) Aggregation and hemi-fusion of anionic vesicles induced by the antimicrobial peptide cryptdin-4. *Biochim Biophys Acta* 1768:1796–1804.

45. Yang S-T, Zaitseva E, Chernomordik LV, Melikov K (2010) Cell-penetrating peptide induces leaky fusion of liposomes containing late endosome-specific anionic lipid. *Biophys J* 99:2525–2533.

46. Luque-Ortega JR, van't Hof W, Veerman ECI, Saugar JM, Rivas L (2008) Human antimicrobial peptide histatin 5 is a cell-penetrating peptide targeting mitochondrial ATP synthesis in Leishmania. *FASEB J* 22:1817–1828.

47. Crowe JH, Crowe LM, Carpenter JF, Aurell Wistrom C (1987) Stabilization of dry phospholipid bilayers and proteins by sugars. *Biochem J* 242:1–10.

48. Crowe LM (2002) Lessons from nature: the role of sugars in anhydrobiosis. *Comp Biochem Physiol A* 131:505–513.

49. Crowe JH, Whittam MA, Chapman D, Crowe LM (1984) Interactions of phospholipid monolayers with carbohydrates. *Biochim Biophys Acta* 769:151–159.

50. Crowe JH, Crowe LM, Chapman D (1984) Preservation of membranes in anhydrobiotic organisms: The role of trehalose. *Science* 223:701–703.

51. Crowe JH, Crowe LM (1988) Factors affecting the stability of dry liposomes. *Biochim Biophys Acta* 939:327–334.

52. Crowe JH et al. (1988) Interactions of sugars with membranes. *Biochim Biophys Acta* 947:367–384.

53. Crowe JH et al. (2005) Stabilization of dry Mammalian cells: lessons from nature. *Integr Comp Biol* 45:810–820.

54. Nakagaki M, Nagase H, Ueda H (1992) Stabilization of the lamellar structure of phosphatidylcholine by complex formation with trehalose. *Journal of Membrane Science* 73:173–180.

55. Lenné T, Bryant G, Holcomb R, Koster KL (2007) How much solute is needed to inhibit the fluid to gel membrane phase transition at low hydration? *Biochim Biophys Acta* 1768:1019–1022.

56. Crowe JH, Hoekstra FA, Crowe LM (1992) Anhydrobiosis. *Annu Rev Physiol* 54:579–599.

57. Green JL, Angell CA (1989) Phase relations and vitrification in saccharide-water solutions and the trehalose anomaly. *J Phys Chem* 93:2880–2882.

58. Massari AM et al. (2005) The influence of aqueous versus glassy solvents on protein dynamics: Vibrational echo experiments and molecular dynamics simulations. *J Am Chem Soc* 127:14279–14289.

59. Westh P (2008) Glucose, sucrose and trehalose are partially excluded from the interface of hydrated DMPC bilayers. *Phys Chem Chem Phys* 10:4110–4112.

60. Horta BAC, Perić-Hassler L, Hünenberger PH (2010) Interaction of the disaccharides trehalose and gentiobiose with lipid bilayers: A comparative molecular dynamics study. *J Mol Graphics Modell* 29:331–346.

61. Lenné T, Garvey CJ, Koster KL, Bryant G (2009) Effects of sugars on lipid bilayers during dehydration--SAXS/WAXS measurements and quantitative model. *J Phys Chem B* 113:2486–2491.

62. Andersen HD, Wang C, Arleth L, Peters GH, Westh P (2011) Reconciliation of opposing views on membrane-sugar interactions. *Proc Natl Acad Sci USA* 108:1874–1878.

63. Veatch SL et al. (2008) Critical fluctuations in plasma membrane vesicles. *ACS Chem Biol* 3:287–293.

64. Ramadurai S et al. (2009) Lateral diffusion of membrane proteins. *J Am Chem Soc* 131:12650–12656.

65. Gouaux E, Mackinnon R (2005) Principles of selective ion transport in channels and pumps. *Science* 310:1461–1465.

66. Hille B (2001) *Ion channels of excitable membranes* (Sinauer Sunderland, MA). 3rd Ed.

67. Sisson AL, Shah MR, Bhosale S, Matile S (2006) Synthetic ion channels and pores (2004-2005). *Chem Soc Rev* 35:1269–1286.

68. Bayley H, Jayasinghe L (2004) Functional engineered channels and pores (Review). *Mol Membr Biol* 21:209–220.

69. Futaki S (1998) Peptide ion channels: design and creation of function. *Biopolymers* 47:75–81.

70. Sansom MS, Kerr ID, Mellor IR (1991) Ion channels formed by amphipathic helical peptides. A molecular modelling study. *Eur Biophys J* 20:229–240.

71. Boheim G (1974) Statistical analysis of alamethicin channels in black lipid membranes. *J Membr Biol* 19:277–303.

72. Cafiso DS (1994) Alamethicin: a peptide model for voltage gating and protein-membrane interactions. *Annu Rev Biophys Biomol Struct* 23:141–165.

73. Qian S, Wang W, Yang L, Huang HW (2008) Structure of the alamethicin pore reconstructed by x-ray diffraction analysis. *Biophys J* 94:3512–3522.

74. Bertelsen K, Dorosz J, Hansen SK, Nielsen NC, Vosegaard T (2012) Mechanisms of peptide-induced pore formation in lipid bilayers investigated by oriented 31P solid-state NMR spectroscopy. *PLoS ONE* 7:e47745.

75. Pieta P, Mirza J, Lipkowski J (2012) Direct visualization of the alamethicin pore formed in a planar phospholipid matrix. *Proc Natl Acad Sci USA* 109:21223–21227.

76. Woolley GA (2007) Channel-forming activity of alamethicin: effects of covalent tethering. *Chem Biodivers* 4:1323–1337.

77. Hjørringgaard CU et al. (2012) Cyclodextrin-scaffolded alamethicin with remarkably efficient membrane permeabilizing properties and membrane current conductance. *J Phys Chem B* 116:7652–7659.

78. Futaki S et al. (2001) Alamethicin-leucine zipper hybrid peptide: a prototype for the design of artificial receptors and ion channels. *J Am Chem Soc* 123:12127–12134.

79. Futaki S, Asami K (2007) Ligand-induced extramembrane conformation switch controlling alamethicin assembly and the channel current. *Chem Biodivers* 4:1313–1322.

80. Mayer M, Semetey V, Gitlin I, Yang J, Whitesides GM (2008) Using ion channel-forming peptides to quantify protein-ligand interactions. *J Am Chem Soc* 130:1453–1465.

81. Zhang Y, Futaki S, Kiwada T, Sugiura Y (2002) Detection of protein-ligand interaction on the membranes using C-terminus biotin-tagged alamethicin. *Bioorg Med Chem* 10:2635–2639.

82. Noshiro D, Asami K, Futaki S (2010) Metal-assisted channel stabilization: disposition of a single histidine on the N-terminus of alamethicin yields channels with extraordinarily long lifetimes. *Biophys J* 98:1801–1808.

83. Li X, Liu DR (2004) DNA-templated organic synthesis: nature's strategy for controlling chemical reactivity applied to synthetic molecules. *Angew Chem Int Ed Engl* 43:4848–4870.

84. Roelfes G, Ben L Feringa (2005) DNA-based asymmetric catalysis. *Angew Chem Int Ed Engl* 44:3230–3232.

85. Roelfes G, Boersma AJ, Ben L Feringa (2006) Highly enantioselective DNA-based catalysis. *Chemical Communications*:635–637.

86. Oltra NS, Bos J, Roelfes G (2010) Control over enzymatic activity by DNA-directed split enzyme reassembly. *Chembiochem* 11:2255–2258.

87. Langecker M et al. (2012) Synthetic lipid membrane channels formed by designed DNA nanostructures. *Science* 338:932–936.

88. Stevens TJ, Arkin IT (2000) Do more complex organisms have a greater proportion of membrane proteins in their genomes? *Proteins* 39:417–420.

89. van der Rest ME et al. (1995) The plasma membrane of Saccharomyces cerevisiae: structure, function, and biogenesis. *Microbiol Rev* 59:304–322.

90. Patton JL, Lester RL (1991) The phosphoinositol sphingolipids of Saccharomyces cerevisiae are highly localized in the plasma membrane. *J Bacteriol* 173:3101–3108.

91. Bagnat M, Keränen S, Shevchenko A, Shevchenko A, Simons K (2000) Lipid rafts function in biosynthetic delivery of proteins to the cell surface in yeast. *Proc Natl Acad Sci USA* 97:3254–3259.

92. Lauwers E, André B (2006) Association of yeast transporters with detergent-resistant membranes correlates with their cell-surface location. *Traffic* 7:1045–1059.

93. Serrano R, Kielland-Brandt MC, Fink GR (1986) Yeast plasma membrane ATPase is essential for growth and has homology with (Na+ + K+), K+- and Ca2+-ATPases. *Nature* 319:689–693.

94. Umebayashi K (2003) Ergosterol is required for targeting of tryptophan permease to the yeast plasma membrane. *J Cell Biol* 161:1117–1131.

95. Dupré S, Haguenauer-Tsapis R (2003) Raft partitioning of the yeast uracil permease during trafficking along the endocytic pathway. *Traffic* 4:83–96.

96. Hearn JD, Lester RL, Dickson RC (2003) The uracil transporter Fur4p associates with lipid rafts. *J Biol Chem* 278:3679–3686.

97. Lee MCS, Hamamoto S, Schekman R (2002) Ceramide biosynthesis is required for the formation of the oligomeric H+-ATPase Pma1p in the yeast endoplasmic reticulum. *J Biol Chem* 277:22395–22401.

98. Malinska K, Malinsky J, Opekarová M, Tanner W (2003) Visualization of protein compartmentation within the plasma membrane of living yeast cells. *Mol Biol Cell* 14:4427–4436.

99. Daicho K et al. (2007) The ergosterol biosynthesis inhibitor zaragozic acid promotes vacuolar degradation of the tryptophan permease Tat2p in yeast. *Biochim Biophys Acta* 1768:1681–1690.

100. Malinsky J, Opekarová M, Grossmann G, Tanner W (2013) Membrane microdomains, rafts, and detergent-resistant membranes in plants and fungi. *Annu Rev Plant Biol* 64:501–529.

101. Malinska K, Malinsky J, Opekarová M, Tanner W (2004) Distribution of Can1p into stable domains reflects lateral protein segregation within the plasma membrane of living S. cerevisiae cells. *J Cell Sci* 117:6031–6041.

102. Strádalová V et al. (2009) Furrow-like invaginations of the yeast plasma membrane correspond to membrane compartment of Can1. *J Cell Sci* 122:2887–2894.

103. Berchtold D, Walther TC (2009) TORC2 plasma membrane localization is essential for cell viability and restricted to a distinct domain. *Mol Biol Cell* 20:1565–1575.

104. Douglas LM, Wang HX, Li L, Konopka JB (2011) Membrane Compartment Occupied by Can1 (MCC) and Eisosome Subdomains of the Fungal Plasma Membrane. *Membranes (Basel)* 1:394–411.

105. Young ME et al. (2002) The Sur7p family defines novel cortical domains in Saccharomyces cerevisiae, affects sphingolipid metabolism, and is involved in sporulation. *Mol Cell Biol* 22:927–934.

106. Grossmann G et al. (2008) Plasma membrane microdomains regulate turnover of transport proteins in yeast. *J Cell Biol* 183:1075–1088.

107. Grossmann G, Opekarová M, Malinsky J, Weig-Meckl I, Tanner W (2007) Membrane potential governs lateral segregation of plasma membrane proteins and lipids in yeast. *EMBO J* 26:1–8.

108. Harris TJC, Ravandi A, Awrey DE, Siu C-H (2003) Cytoskeleton interactions involved in the assembly and function of glycoprotein-80 adhesion complexes in dictyostelium. *J Biol Chem* 278:2614–2623.

109. Lauwers E, Grossmann G, André B (2007) Evidence for coupled biogenesis of yeast Gap1 permease and sphingolipids: essential role in transport activity and normal control by ubiquitination. *Mol Biol Cell* 18:3068–3080.

110. Walther TC et al. (2006) Eisosomes mark static sites of endocytosis. *Nature* 439:998–1003.

111. Ziółkowska NE, Karotki L, Rehman M, Huiskonen JT, Walther TC (2011) Eisosome-driven plasma membrane organization is mediated by BAR domains. *Nat Struct Mol Biol* 18:854–856.

112. Walther TC et al. (2007) Pkh-kinases control eisosome assembly and organization. *EMBO J* 26:4946–4955.

113. Brach T, Specht T, Kaksonen M (2011) Reassessment of the role of plasma membrane domains in the regulation of vesicular traffic in yeast. *J Cell Sci* 124:328–337.

114. Spira F et al. (2012) Patchwork organization of the yeast plasma membrane into numerous coexisting domains. *Nat Cell Biol* 14:640–648.

115. Valdez-Taubas J, Pelham HRB (2003) Slow diffusion of proteins in the yeast plasma membrane allows polarity to be maintained by endocytic cycling. *Current Biology* 13:1636–1640.

116. Ries J, Klose C, Walch-Solimena C, Schwille P (2008) How to measure slow diffusion in yeast cell membranes. *Proceedings of SPIE* 6991:69910W–1.

117. Greenberg ML, Axelrod D (1993) Anomalously slow mobility of fluorescent lipid probes in the plasma membrane of the yeast Saccharomyces cerevisiae. *J Membr Biol* 131:115–127.

118. Ganguly S, Singh P, Manoharlal R, Prasad R, Chattopadhyay A (2009) Differential dynamics of membrane proteins in yeast. *Biochem Bioph Res Co* 387:661–665.

119. Vinnakota KC, Mitchell DA, Deschenes RJ, Wakatsuki T, Beard DA (2010) Analysis of the diffusion of Ras2 in Saccharomyces cerevisiae using fluorescence recovery after photobleaching. *Phys Biol* 7:026011.

120. Meinema AC et al. (2011) Long unfolded linkers facilitate membrane protein import through the nuclear pore complex. *Science* 333:90–93.

121. Meinema AC, Poolman B, Veenhoff LM (2013) Quantitative analysis of membrane protein transport across the nuclear pore complex. *Traffic* 14:487–501.

122. Pruyne D, Bretscher A (2000) Polarization of cell growth in yeast. *J Cell Sci* 113 (Pt 4):571–585.

123. Pruyne D, Bretscher A (2000) Polarization of cell growth in yeast. I. Establishment and maintenance of polarity states. *J Cell Sci* 113 (Pt 3):365–375.

124. Marco E, Wedlich-Söldner R, Li R, Altschuler SJ, Wu LF (2007) Endocytosis optimizes the dynamic localization of membrane proteins that regulate cortical polarity. *Cell* 129:411–422.

125. Kukulski W et al. (2011) Correlated fluorescence and 3D electron microscopy with high sensitivity and spatial precision. *J Cell Biol* 192:111–119.

126. Strádalová V et al. (2012) Distribution of cortical endoplasmic reticulum determines positioning of endocytic events in yeast plasma membrane. *PLoS ONE* 7:e35132.

127. Brogden KA, Ackermann M, McCray PB, Tack BF (2003) Antimicrobial peptides in animals and their role in host defences. *Int J Antimicrob Agents* 22:465–478.

128. Lehrer RI, Ganz T (1999) Antimicrobial peptides in mammalian and insect host defence. *Curr Opin Immunol* 11:23–27.

129. Dathe M, Nikolenko H, Klose J, Bienert M (2004) Cyclization increases the antimicrobial activity and selectivity of arginine- and tryptophan-containing hexapeptides. *Biochemistry* 43:9140–9150.

130. Jenssen H, Hamill P, Hancock REW (2006) Peptide antimicrobial agents. *Clin Microbiol Rev* 19:491–.

131. Zasloff M (2002) Antimicrobial peptides of multicellular organisms. *Nature* 415:389–395.

132. Huang HW (2000) Action of antimicrobial peptides: two-state model. *Biochemistry* 39:8347–8352.

133. Van Den Bogaart G, Guzman JV, Mika JT, Poolman B (2008) On the mechanism of pore formation by melittin. *J Biol Chem* 283:33854–33857.

134. Houston ME et al. (1998) Influence of preformed alpha-helix and alpha-helix induction on the activity of cationic antimicrobial peptides. *J Pept Res* 52:81–88.

135. Davies JS (2003) The cyclization of peptides and depsipeptides. *J Pept Sci* 9:471–501.

136. Ganz T (2003) Defensins: antimicrobial peptides of innate immunity. *Nat Rev Immunol* 3:710–720.

137. Kato T, Izumiya N (1977) Conformations of di-N-methylleucine gramicidin S and N-methylleucine gramicidin S compatible with the sidedness hypothesis. *Biochim Biophys Acta* 493:235–238.

138. Toke O (2005) Antimicrobial peptides: new candidates in the fight against bacterial infections. *Biopolymers* 80:717–735.

139. Monroc S et al. (2006) Improvement of cyclic decapeptides against plant pathogenic bacteria using a combinatorial chemistry approach. *Peptides* 27:2575–2584.

140. Monroc S et al. (2006) De novo designed cyclic cationic peptides as inhibitors of plant pathogenic bacteria. *Peptides* 27:2567–2574.

141. Kates SA et al. (1993) A novel, convenient, three-dimensional orthogonal strategy for solid-phase synthesis of cyclic peptides. *Tetrahedron Lett* 34:1549–1552.

142. Kocer A, Walko M, Meijberg W, Ben L Feringa (2005) A light-actuated nanovalve derived from a channel protein. *Science* 309:755–758.

143. Clark EH, East JM, Lee AG (2003) The role of tryptophan residues in an integral membrane protein: diacylglycerol kinase. *Biochemistry* 42:11065–11073.

144. Matos C, Lima JLC, Reis S, Lopes A, Bastos M (2004) Interaction of antiinflammatory drugs with EPC liposomes: calorimetric study in a broad concentration range. *Biophys J* 86:946–954.

145. Melo MN, Castanho MARB (2007) Omiganan interaction with bacterial membranes and cell wall models. Assigning a biological role to saturation. *Biochim Biophys Acta* 1768:1277–1290.

146. Case DA, Darden TA, Cheatham TE III et al. (2006) AMBER 9. *University of California*.

147. Van Der Spoel D et al. (2005) GROMACS: fast, flexible, and free. *J Comput Chem* 26:1701–1718.

148. van Gunsteren WF et al. (1996) *Biomolecular Simulation: The {GROMOS96} manual and user guide* (vdf Hochschul- verlag AG an der ETH Zürich and BIOMOS b.v., Zürich, Switzerland.).

149. Oostenbrink C, Soares TA, van der Vegt NFA, van Gunsteren WF (2005) Validation of the 53A6 GROMOS force field. *Eur Biophys J* 34:273–284.

150. Anézo C, de Vries AH, Höltje H-D, Tieleman DP, Marrink SJ (2003) Methodological issues in lipid bilayer simulations. *J Phys Chem B* 107:9424–9433.

151. Zhao W, Róg T, Gurtovenko AA, Vattulainen I, Karttunen M (2007) Atomic-scale structure and electrostatics of anionic palmitoyloleoylphosphatidylglycerol lipid bilayers with Na+ counterions. *Biophys J* 92:1114–1124.

152. Pabst G, Danner S, Karmakar S, Deutsch G, Raghunathan VA (2007) On the propensity of phosphatidylglycerols to form interdigitated phases. *Biophys J* 93:513–525.

153. Babakhani A, Gorfe AA, Gullingsrud J, Kim JE, Andrew McCammon J (2007) Peptide insertion, positioning, and stabilization in a membrane: insight from an all-atom molecular dynamics simulation. *Biopolymers* 85:490–497.

154. Tironi IG, Sperb R, Smith PE, van Gunsteren WF (1995) A generalized reaction field method for molecular dynamics simulations. *J Chem Phys* 102:5451.

155. Berendsen HJC, Postma J, Van Gunsteren W, Hermans J (1981) Interaction models for water in relation to protein hydration. *Intermolecular forces* 331:331–338.

156. Hess B, Bekker H, Berendsen HJC, Fraaije JGEM (1997) LINCS: a linear constraint solver for molecular simulations. *J Comput Chem* 18:1463–1472.

157. Berendsen HJC, Postma JPM, van Gunsteren WF, DiNola A, Haak J (1984) Molecular dynamics with coupling to an external bath. *J Chem Phys* 81:3684.

158. Matyus E, Kandt C, Tieleman DP (2007) Computer Simulation of Antimicrobial Peptides. *Curr Med Chem* 14:2789–2798.

159. Kabsch W, Sander C (1983) Dictionary of protein secondary structure: pattern recognition of hydrogen-bonded and geometrical features. *Biopolymers* 22:2577–2637.

160. Wu M, Hancock RE (1999) Interaction of the cyclic antimicrobial cationic peptide bactenecin with the outer and cytoplasmic membrane. *J Biol Chem* 274:29–35.

161. Manning MC, Illangasekare M, Woody RW (1988) Circular dichroism studies of distorted alpha-helices, twisted beta-sheets, and beta turns. *Biophys Chem* 31:77–86.

162. Bush CA, Sarkar SK, Kopple KD (1978) Circular dichroism of β turns in peptides and proteins. *Biochemistry* 17:4951–4954.

163. Cirac AD et al. (2011) The molecular basis for antimicrobial activity of pore-forming cyclic peptides. *Biophys J* 100:2422–2431.

164. Henriques ST, Quintas A, Bagatolli LA, Homblé F, Castanho MARB (2007) Energy-independent translocation of cell-penetrating peptides occurs without formation of pores. A biophysical study with pep-1. *Mol Membr Biol* 24:282–293.

165. Jelokhani-Niaraki M, Hodges RS, Meissner JE, Hassenstein UE, Wheaton L (2008) Interaction of gramicidin S and its aromatic amino-acid analog with phospholipid membranes. *Biophys J* 95:3306–3321.

166. Kondejewski LH et al. (1996) Modulation of structure and antibacterial and hemolytic activity by ring size in cyclic gramicidin S analogs. *J Biol Chem* 271:25261–25268.

167. Shai Y (2002) Mode of action of membrane active antimicrobial peptides. *Biopolymers* 66:236–248.

168. Chen C, Xiao Y (2008) Observation of multiple folding pathways of beta-hairpin trpzip2 from independent continuous folding trajectories. *Bioinformatics* 24:659–665.

169. Dinner AR, Lazaridis T, Karplus M (1999) Understanding beta-hairpin formation. *Proc Natl Acad Sci USA* 96:9068–9073.

170. Muñoz V, Henry ER, Hofrichter J, Eaton WA (1998) A statistical mechanical model for beta-hairpin kinetics. *Proc Natl Acad Sci USA* 95:5872–5879.

171. Hancock REW, Rozek A (2002) Role of membranes in the activities of antimicrobial cationic peptides. *Fems Microbiol Lett* 206:143–149.

172. Seelig J (2004) Thermodynamics of lipid-peptide interactions. *Biochim Biophys Acta* 1666:40–50.

173. Shai Y (1999) Mechanism of the binding, insertion and destabilization of phospholipid bilayer membranes by alpha-helical antimicrobial and cell non-selective membrane-lytic peptides. *Biochim Biophys Acta* 1462:55–70.

174. White SH, Wimley WC (1999) Membrane protein folding and stability: physical principles. *Annu Rev Biophys Biomol Struct* 28:319–365.

175. Ferre R et al. (2009) Synergistic effects of the membrane actions of cecropin-melittin antimicrobial hybrid peptide BP100. *Biophys J* 96:1815–1827.

176. Huang HW, Chen F-Y, Lee M-T (2004) Molecular mechanism of Peptide-induced pores in membranes. *Phys Rev Lett* 92:198304.

177. Huang HW (2006) Molecular mechanism of antimicrobial peptides: the origin of cooperativity. *Biochim Biophys Acta* 1758:1292–1302.

178. Tossi A, Sandri L, Giangaspero A (2000) Amphipathic, alpha-helical antimicrobial peptides. *Biopolymers* 55:4–30.

179. Yang L, Harroun TA, Weiss TM, Ding L, Huang HW (2001) Barrel-stave model or toroidal model? A case study on melittin pores. *Biophys J* 81:1475–1485.

180. Subbalakshmi C, Sitaram N (1998) Mechanism of antimicrobial action of indolicidin. *Fems Microbiol Lett* 160:91–96.

181. Jean-François F, Elezgaray J, Berson P, Vacher P, Dufourc EJ (2008) Pore formation induced by an antimicrobial peptide: electrostatic effects. *Biophys J* 95:5748–5756.

182. Jelokhani-Niaraki M, Prenner E, Kay C, McElhaney RN, Hodges R (2002) Conformation and interaction of the cyclic cationic antimicrobial peptides in lipid bilayers. *J Pept Res* 60:23–36.

183. Matsuzaki K (2009) Control of cell selectivity of antimicrobial peptides. *Biochim Biophys Acta* 1788:1687–1692.

184. Gibbs AC et al. (1998) Unusual beta-sheet periodicity in small cyclic peptides. *Nat Struct Biol* 5:284–288.

185. Lee DL, Hodges RS (2003) Structure-activity relationships of de novo designed cyclic antimicrobial peptides based on gramicidin S. *Biopolymers* 71:28–48.

186. Prenner EJ, Lewis RN, McElhaney RN (1999) The interaction of the antimicrobial peptide gramicidin S with lipid bilayer model and biological membranes. *Biochim Biophys Acta* 1462:201–221.

187. Mak DO, Webb WW (1995) Two classes of alamethicin transmembrane channels: molecular models from single-channel properties. *Biophys J* 69:2323–2336.

188. Mihailescu D, Smith JC (1999) Molecular dynamics simulation of the cyclic decapeptide antibiotic, gramicidin S, in dimethyl sulfoxide solution. *J Phys Chem B* 103:1586–1594.

189. Mihailescu D, Smith JC (2000) Atomic detail peptide-membrane interactions: molecular dynamics simulation of gramicidin S in a DMPC bilayer. *Biophys J* 79:1718–1730.

190. Khalfa A, Tarek M (2010) On the antibacterial action of cyclic peptides: insights from coarse-grained MD simulations. *J Phys Chem B* 114:2676–2684.

191. Mueller P, Rudin DO, Tien HT, Wescott WC (1962) Reconstitution of cell membrane structure in vitro and its transformation into an excitable system. *Nature* 194:979–980.

192. Mueller P, Rudin DO, Tien HT, Wescott WC (1962) Reconstitution of excitable cell membrane structure in vitro. *Circulation* 26:1167–1171.

193. Mueller P, Rudin DO, Tien HT, Wescott WC (1963) Methods for the formation of single bimolecular lipid membranes in aqueous solution. *J Phys Chem* 67:534–535.

194. Salay LC, Procopio J, Oliveira E, Nakaie CR, Schreier S (2004) Ion channel-like activity of the antimicrobial peptide tritrpticin in planar lipid bilayers. *FEBS Lett* 565:171–175.

195. Hille B (1968) Pharmacological modifications of the sodium channels of frog nerve. *J Gen Physiol* 51:199–219.

196. Cruickshank C, Minchin R, LeDain A, Martinac B (1997) Estimation of the pore size of the large-conductance mechanosensitive ion channel of Escherichia coli. *Biophys J* 73:1925–1931.

197. Doeven MK et al. (2005) Distribution, lateral mobility and function of membrane proteins incorporated into giant unilamellar vesicles. *Biophys J* 88:1134–1142.

198. Van Den Bogaart G et al. (2008) Dual-color fluorescence-burst analysis to study pore formation and protein-protein interactions. *Methods* 46:123–130.

199. Veldhuis G et al. (2006) The oligomeric state and stability of the mannitol transporter, EnzymeIImtl, from Escherichia coli: A fluorescence correlation spectroscopy study. *Protein science* 15:1977–1986.

200. Bohrer MP, Deen WM, Robertson CR, Troy JL, Brenner BM (1979) Influence of molecular configuration on the passage of macromolecules across the glomerular capillary wall. *J Gen Physiol* 74:583–593.

201. Gregory SM, Cavenaugh A, Journigan V, Pokorny A, Almeida PFF (2008) A quantitative model for the all-or-none permeabilization of phospholipid vesicles by the antimicrobial peptide cecropin A. *Biophys J* 94:1667–1680.

202. Rzepiela AJ, Sengupta D, Goga N, Marrink SJ (2010) Membrane poration by antimicrobial peptides combining atomistic and coarse-grained descriptions. *Faraday Discuss* 144:431–43– discussion 445–81.

203. Ashrafuzzaman M, Andersen OS, McElhaney RN (2008) The antimicrobial peptide gramicidin S permeabilizes phospholipid bilayer membranes without forming discrete ion channels. *Biochim Biophys Acta* 1778:2814–2822.

204. Duclohier H, Molle G, Spach G (1989) Antimicrobial peptide magainin I from Xenopus skin forms anion-permeable channels in planar lipid bilayers. *Biophys J* 56:1017–1021.

205. Epand RM (2003) Fusion peptides and the mechanism of viral fusion. *Biochim Biophys Acta* 1614:116–121.

206. Tamm LK, Han X, Li Y, Lai AL (2002) Structure and function of membrane fusion peptides. *Biopolymers* 66:249–260.

207. Järver P, Langel U (2006) Cell-penetrating peptides--a brief introduction. *Biochim Biophys Acta* 1758:260–263.

208. Wadhwani P, Reichert J, Bürck J, Ulrich AS (2012) Antimicrobial and cell-penetrating peptides induce lipid vesicle fusion by folding and aggregation. *Eur Biophys J* 41:177–187.

209. Nicolas P (2009) Multifunctional host defense peptides: intracellular-targeting antimicrobial peptides. *FEBS J* 276:6483–6496.

210. Almeida PF, Pokorny A (2009) Mechanisms of antimicrobial, cytolytic, and cell-penetrating peptides: from kinetics to thermodynamics. *Biochemistry* 48:8083–8093.

211. Hale JD, Hancock RE (2007) Alternative mechanisms of action of cationic antimicrobial peptides on bacteria. *Expert Rev Anti Infect Ther* 5:951–959.

212. Kozlov MM, McMahon HT, Chernomordik LV (2010) Protein-driven membrane stresses in fusion and fission. 35:699–706.

213. Domingues MM, Castanho MARB, Santos NC (2009) rBPI(21) promotes lipopolysaccharide aggregation and exerts its antimicrobial effects by (hemi)fusion of PG-containing membranes. *PLoS ONE* 4:e8385.

214. Rausch JM, Marks JR, Rathinakumar R, Wimley WC (2007) Beta-sheet pore-forming peptides selected from a rational combinatorial library: mechanism of pore formation in lipid vesicles and activity in biological membranes. *Biochemistry* 46:12124–12139.

215. Wadhwani P et al. (2012) Membrane-active peptides and the clustering of anionic lipids. *Biophys J* 103:265–274.

216. Frolov V, Dunina-Barkovskaya AY, Samsonov A, Zimmerberg J (2003) Membrane permeability changes at early stages of influenza hemagglutinin-mediated fusion. *Biophys J* 85:1725–1733.

217. Marrink SJ, de Vries AH, Tieleman DP (2009) Lipids on the move: simulations of membrane pores, domains, stalks and curves. *Biochim Biophys Acta* 1788:149–168.

218. Bond PJ, Khalid S (2010) Antimicrobial and cell-penetrating peptides: structure, assembly and mechanisms of membrane lysis via atomistic and coarse-grained molecular dynamics simulations. *Protein Pept Lett* 17:1313–1327.

219. Fuertes G, Giménez D, Esteban-Martín S, Sánchez-Muñoz OL, Salgado J (2011) A lipocentric view of peptide-induced pores. *Eur Biophys J* 40:399–415.

220. Mika JT et al. (2011) Structural basis for the enhanced activity of cyclic antimicrobial peptides: the case of BPC194. *Biochim Biophys Acta* 1808:2197–2205.

221. Casadaban MJ, Cohen SN (1980) Analysis of gene control signals by DNA fusion and cloning in Escherichia coli. *J Mol Biol* 138:179–207.

222. Struck DK, Hoekstra D, Pagano RE (1981) Use of resonance energy transfer to monitor membrane fusion. *Biochemistry* 20:4093–4099.

223. Moiset G et al. (2013) Dual Action of BPC194: A Membrane Active Peptide Killing Bacterial Cells. *PLoS ONE* 8:e61541.

224. Melo MN et al. (2011) Prediction of Antibacterial Activity from Physicochemical Properties of Antimicrobial Peptides. *PLoS ONE* 6:e28549.

225. Markvoort AJ, Marrink SJ (2011) Lipid acrobatics in the membrane fusion arena. *Curr Top Membr* 68:259–294.

226. Risselada HJ et al. (2012) Line-tension controlled mechanism for influenza fusion. *PLoS ONE* 7:e38302.

227. Hobot JA, Carlemalm E, Villiger W, Kellenberger E (1984) Periplasmic gel: new concept resulting from the reinvestigation of bacterial cell envelope ultrastructure by new methods. *J Bacteriol* 160:143–152.

228. Bechinger B (2009) Rationalizing the membrane interactions of cationic amphipathic antimicrobial peptides by their molecular shape. *Current Opinion in Colloid & Interface Science* 14:349–355.

229. Smirnova YG, Marrink SJ, Lipowsky R, Knecht V (2010) Solvent-exposed tails as prestalk transition states for membrane fusion at low hydration. *J Am Chem Soc* 132:6710–6718.

230. Mirjanian D, Dickey AN, Hoh JH, Woolf TB, Stevens MJ (2010) Splaying of aliphatic tails plays a central role in barrier crossing during liposome fusion. *J Phys Chem B* 114:11061–11068.

231. Baoukina S, Tieleman DP (2010) Direct simulation of protein-mediated vesicle fusion: lung surfactant protein B. *Biophys J* 99:2134–2142.

232. Risselada HJ, Kutzner C, Grubmüller H (2011) Caught in the act: visualization of SNARE-mediated fusion events in molecular detail. *Chembiochem* 12:1049–1055.

233. Chernomordik LV, Kozlov MM (2008) Mechanics of membrane fusion. *Nat Struct Mol Biol* 15:675–683.

234. Noguchi H, Takasu M (2001) Fusion pathways of vesicles: a Brownian dynamics simulation. *J Chem Phys* 115:9547–9551.

235. Smeijers AF, Markvoort AJ, Pieterse K, Hilbers PAJ (2006) A detailed look at vesicle fusion. *J Phys Chem B* 110:13212–13219.

236. Knecht V, Marrink SJ (2007) Molecular dynamics simulations of lipid vesicle fusion in atomic detail. *Biophys J* 92:4254–4261.

237. Katsov K, Müller M, Schick M (2006) Field theoretic study of bilayer membrane fusion: II. Mechanism of a stalk-hole complex. *Biophys J* 90:915–926.

238. Fuhrmans M, Knecht V, Marrink SJ (2009) A single bicontinuous cubic phase induced by fusion peptides. *J Am Chem Soc* 131:9166–9167.

239. Fuhrmans M, Marrink SJ (2012) Molecular view of the role of fusion peptides in promoting positive membrane curvature. *J Am Chem Soc* 134:1543–1552.

240. Haney EF, Nathoo S, Vogel HJ, Prenner EJ (2010) Induction of non-lamellar lipid phases by antimicrobial peptides: a potential link to mode of action. *Chem Phys Lipids* 163:82–93.

241. Schmidt NW et al. (2011) Criterion for amino acid composition of defensins and antimicrobial peptides based on geometry of membrane destabilization. *J Am Chem Soc* 133:6720–6727.

242. Bayley H, Cremer P (2001) Stochastic sensors inspired by biology. *Nature* 413:226–230.

243. Song L et al. (1996) Structure of staphylococcal alpha-hemolysin, a heptameric transmembrane pore. *Science* 274:1859–1866.

244. Braha O et al. (1997) Designed protein pores as components for biosensors. *Chemistry & Biology* 4:497–505.

245. Braha O et al. (2000) Simultaneous stochastic sensing of divalent metal ions. *Nat Biotechnol* 18:1005–1007.

246. Gu LQ, Braha O, Conlan S, Cheley S, Bayley H (1999) Stochastic sensing of organic analytes by a pore-forming protein containing a molecular adapter. *Nature* 398:686–690.

247. Boersma AJ, Bayley H (2012) Continuous stochastic detection of amino acid enantiomers with a protein nanopore. *Angew Chem Int Edit* 51:9606–9609.

248. Movileanu L, Howorka S, Braha O, Bayley H (2000) Detecting protein analytes that modulate transmembrane movement of a polymer chain within a single protein pore. *Nat Biotechnol* 18:1091–1095.

249. Ashkenasy N, Sánchez-Quesada J, Bayley H, Ghadiri MR (2005) Recognizing a single base in an individual DNA strand: a step toward DNA sequencing in nanopores. *Angew Chem Int Ed Engl* 44:1401–1404.

250. Astier Y, Braha O, Bayley H (2006) Toward single molecule DNA sequencing: direct identification of ribonucleoside and deoxyribonucleoside 5′-monophosphates by using an engineered protein nanopore equipped with a molecular adapter. *J Am Chem Soc* 128:1705–1710.

251. Rhee M, Burns MA (2006) Nanopore sequencing technology: research trends and applications. *Trends Biotechnol* 24:580–586.

252. Cascio M, Wallace BA (1988) Conformation of alamethicin in phospholipid vesicles: implications for insertion models. *Proteins* 4:89–98.

253. Sansom MSP (1993) Alamethicin and related peptaibols—model ion channels. *Eur Biophys J Biophy* 22:105–124.

254. Woolley GA, Wallace BA (1992) Model ion channels: gramicidin and alamethicin. *J Membrane Biol* 129:109–136.

255. Hanke W, Boheim G (1980) The lowest conductance state of the alamethicin pore. *Biochim Biophys Acta* 596:456–462.

256. Duclohier H (2004) Helical kink and channel behaviour: a comparative study with the peptaibols alamethicin, trichotoxin and antiamoebin. *Eur Biophys J* 33:169–174.

257. Duclohier H (2007) Peptaibiotics and peptaibols: an alternative to classical antibiotics? *Chem Biodivers* 4:1023–1026.

258. Leitgeb B, Szekeres A, Manczinger L, Vágvölgyi C, Kredics L (2007) The history of alamethicin: a review of the most extensively studied peptaibol. *Chem Biodivers* 4:1027–1051.

259. Jung G et al. (2003) Template-free self-assembling fullerene and lipopeptide conjugates of alamethicin form voltage-dependent ion channels of remarkable stability and activity. *J Pept Sci* 9:784–798.

260. You S et al. (1996) Engineering stabilized ion channels: covalent dimers of alamethicin. *Biochemistry* 35:6225–6232.

261. Okazaki T, Sakoh M, Nagaoka Y, Asami K (2003) Ion channels of alamethicin dimer N-terminally linked by disulfide bond. *Biophys J* 85:267–273.

262. Jaikaran DC, Biggin PC, Wenschuh H, Sansom MSP, Woolley GA (1997) Structure-function relationships in helix-bundle channels probed via total chemical synthesis of alamethicin dimers: effects of a Gln7 to Asn7 mutation. *Biochemistry* 36:13873–13881.

263. Duclohier H, Alder G, Kociolek K, Leplawy M (2003) Channel properties of template assembled alamethicin tetramers. *J Pept Sci* 9:776–783.

264. Wassner AJ, Hurt JA, Lear JD, Akerfeldt KS (2002) Synthesis and ion conductance behavior of a tetrameric alamethicin ion channel. *Org Lett* 4:1647–1649.

265. Hille B (1968) Charges and potentials at the nerve surface. Divalent ions and pH. *J Gen Physiol* 51:221–236.

266. Hamer WJ, DeWane HJ (1970) Electrolytic conductance and the conductances of the halogen acids in water.

267. Molle G, Dugas J-Y, Duclohier H, Spach G (1988) Conductance properties of des-Aib-Leu-des-Pheol-Phe-alamethicin in planar lipid bilayers. *Biochim Biophys Acta* 938:310–314.

268. Haris PI, Molle G, Duclohier H (2004) Conformational changes in alamethicin associated with substitution of its alpha-methylalanines with leucines: a FTIR spectroscopic analysis and correlation with channel kinetics. *Biophys J* 86:248–253.

269. Davis JT (2004) G-quartets 40 years later: from 5′-GMP to molecular biology and supramolecular chemistry. *Angew Chem Int Ed Engl* 43:668–698.

270. Masiero S et al. (2010) A non-empirical chromophoric interpretation of CD spectra of DNA G-quadruplex structures. *Org Biomol Chem* 8:2683–2692.

271. Clegg JS (2001) Cryptobiosis--a peculiar state of biological organization. *Comp Biochem Physiol B* 128:613–624.

272. Crowe JH, Carpenter JF, Crowe LM (1998) The role of vitrification in anhydrobiosis. *Annu Rev Physiol* 60:73–103.

273. Crowe JH, Oliver AE, Tablin F (2002) Is there a single biochemical adaptation to anhydrobiosis? *Integr Comp Biol* 42:497–503.

274. Rebecchi L, Altiero T, Guidetti R (2007) Anhydrobiosis: the extreme limit of desiccation tolerance. *Invertebr Surv J* 4:65–81.

275. Cacela C, Hincha DK (2006) Low amounts of sucrose are sufficient to depress the phase transition temperature of dry phosphatidylcholine, but not for lyoprotection of liposomes. *Biophys J* 90:2831–2842.

276. Oliver AE et al. (2008) Protecting, patterning, and scaffolding supported lipid membranes using carbohydrate glasses. *Lab Chip* 8:892–897.

277. Ohtake S, Schebor C, de Pablo JJ (2006) Effects of trehalose on the phase behavior of DPPC-cholesterol unilamellar vesicles. *Biochim Biophys Acta* 1758:65–73.

278. Koster KL, Webb MS, Bryant G, Lynch DV (1994) Interactions between soluble sugars and POPC (1-palmitoyl-2-oleoylphosphatidylcholine) during dehydration: vitrification of sugars alters the phase behavior of the phospholipid. *Biochim Biophys Acta* 1193:143–150.

279. Tsvetkova NM, Phillips BL, Crowe LM, Crowe JH, Risbud SH (1998) Effect of sugars on headgroup mobility in freeze-dried dipalmitoylphosphatidylcholine bilayers: solid-state 31P NMR and FTIR studies. *Biophys J* 75:2947–2955.

280. Lambruschini C, Relini A, Ridi A, Cordone L, Gliozzi A (2000) Trehalose interacts with phospholipid polar heads in langmuir monolayers. *Langmuir* 16:5467–5470.

281. Van Den Bogaart G, Hermans N, Krasnikov V, de Vries AH, Poolman B (2007) On the decrease in lateral mobility of phospholipids by sugars. *Biophys J* 92:1598–1605.

282. Lingwood D, Simons K (2010) Lipid rafts as a membrane-organizing principle. *Science* 327:46–50.

283. Marrink SJ, Risselada HJ, Yefimov S, Tieleman DP, de Vries AH (2007) The MARTINI force field: coarse grained model for biomolecular simulations. *J Phys Chem B* 111:7812–7824.

284. López CA et al. (2009) Martini coarse-grained force field: extension to carbohydrates. *J Chem Theory Comput* 5:3195–3210.

285. Risselada HJ, Marrink SJ (2008) The molecular face of lipid rafts in model membranes. *Proc Natl Acad Sci USA* 105:17367–17372.

286. Dimitrov DS, Angelova MI (1988) Lipid swelling and liposome formation mediated by electric fields. *Journal of electroanalytical chemistry and interfacial electrochemistry* 253:323–336.

287. Angelova MI, Dimitrov DS (1986) Liposome electroformation. *Faraday Discuss Chem Soc* 81:303.

288. Burns AR, Frankel DJ, Buranda T (2005) Local mobility in lipid domains of supported bilayers characterized by atomic force microscopy and fluorescence correlation spectroscopy. *Biophys J* 89:1081–1093.

289. O'Shannessy DJ, Voorstad PJ, Quarles RH (1987) Quantitation of glycoproteins on electroblots using the biotin-streptavidin complex. *Anal Biochem* 163:204–209.

290. Hammond AT et al. (2005) Crosslinking a lipid raft component triggers liquid ordered-liquid disordered phase separation in model plasma membranes. *Proc Natl Acad Sci USA* 102:6320–6325.

291. Pines A (1973) Proton-enhanced NMR of dilute spins in solids. *J Chem Phys* 59:569–590.

292. Fung BM, Khitrin AK, Ermolaev K (2000) An improved broadband decoupling sequence for liquid crystals and solids. *J Magn Reson* 142:97–101.

293. Goddard TD, Kneller DG (2006) Sparky—NMR assignment and integration software - Google Scholar. *University of California*.

294. Cukkemane A, Baldus M (2013) Characterization of a cyclic nucleotide-activated k(+) channel and its lipid environment by using solid-state NMR spectroscopy. *Chembiochem* 14:1789–1798.

295. Lee CW, Griffin RG (1989) Two-dimensional 1H/13C heteronuclear chemical shift correlation spectroscopy of lipid bilayers. *Biophys J* 55:355–358.

296. van Leeuwen SS, Leeflang BR, Gerwig GJ, Kamerling JP (2008) Development of a 1H NMR structural-reporter-group concept for the primary structural characterisation of alpha-D-glucans. *Carbohydr Res* 343:1114–1119.

297. Morris GA, Hall LD (1982) Experimental chemical shift correlation maps from heteronuclear two-dimensional nuclear magnetic resonance spectroscopy. II: Carbon-13 and proton chemical shifts of aD-glucopyranose oligomers. *Can J Chem* 60:2431–2441.

298. Marrink SJ, Tieleman DP (2013) Perspective on the Martini model. *Chem Soc Rev* 42:6801–6822.

299. Veatch SL, Keller SL (2003) Separation of liquid phases in giant vesicles of ternary mixtures of phospholipids and cholesterol. *Biophys J* 85:3074–3083.

300. Pereira CS, Hünenberger PH (2008) The influence of polyhydroxylated compounds on a hydrated phospholipid bilayer: a molecular dynamics study. *Molecular Simulation* 34:403–420.

301. Kapla J et al. (2013) Molecular dynamics simulations of membrane-sugar interactions. *J Phys Chem B* 117:6667–6673.

302. Malinsky J, Opekarová M, Tanner W (2010) The lateral compartmentation of the yeast plasma membrane. *Yeast* 27:473–478.

303. Aresta-Branco F et al. (2011) Gel domains in the plasma membrane of Saccharomyces cerevisiae: highly ordered, ergosterol-free, and sphingolipid-enriched lipid rafts. *J Biol Chem* 286:5043–5054.

304. Piao HL, Machado IMP, Payne GS (2007) NPFXD-mediated endocytosis is required for polarity and function of a yeast cell wall stress sensor. *Mol Biol Cell* 18:57–65.

305. Lino R, Koyama I, Kusumi A (2001) Single molecule imaging of green fluorescent proteins in living cells: E-cadherin forms oligomers on the free cell surface. *Biophys J* 80:2667–2677.

306. Saffman PG, Delbrück M (1975) Brownian motion in biological membranes. *Proc Natl Acad Sci USA* 72:3111–3113.

307. Cain NE, Kaiser CA (2011) Transport activity-dependent intracellular sorting of the yeast general amino acid permease. *Mol Biol Cell* 22:1919–1929.

308. Farhan H, Freissmuth M, Sitte HH (2006) Oligomerization of neurotransmitter transporters: a ticket from the endoplasmic reticulum to the plasma membrane. *Handbook of Experimental Pharmacology* 175:233–249.

309. Fang Y et al. (2009) Structure of a prokaryotic virtual proton pump at 3.2 Å resolution. *Nature* 460:1040–1043.

310. Gao X et al. (2010) Mechanism of substrate recognition and transport by an amino acid antiporter. *Nature* 463:828–832.

311. Mitsui K, Yasui H, Nakamura N, Kanazawa H (2005) Oligomerization of the Saccharomyces cerevisiae Na+/H+ antiporter Nha1p: Implications for its antiporter activity. *Biochim Biophys Acta* 1720:125–136.

312. Beese-Sims SE, Lee J, Levin DE (2011) Yeast Fps1 glycerol facilitator functions as a homotetramer. *Yeast* 28:815–819.

313. DNA cloning and engineering by uracil excision (2001) *DNA cloning and engineering by uracil excision* (John Wiley & Sons, Inc., Hoboken, NJ, USA).

314. Sherman F, Fink GR, Hicks JB (1986) *Laboratory course manual for methods in yeast genetics* (Cold Spring Harbor Laboratory, New York).

315. Nørholm MH (2010) A mutant Pfu DNA polymerase designed for advanced uracil-excision DNA engineering. *BMC Biotechnology* 10:21.

316. Sambrook J, Fritsch EF, Maniatis T (1989) *Molecular cloning: A laboratory manual* (Cold Spring Harbor Laboratory, Cold Spring Harbor, New York)Third Edition.

317. Drew D et al. (2008) GFP-based optimization scheme for the overexpression and purification of eukaryotic membrane proteins in Saccharomyces cerevisiae. *Nat Protoc* 3:784–798.

318. Alani E, Cao L, Kleckner N (1987) A method for gene disruption that allows repeated use of URA3 selection in the construction of multiply disrupted yeast strains. *Genetics* 116:541–545.

319. Akada R et al. (2006) PCR-mediated seamless gene deletion and marker recycling inSaccharomyces cerevisiae. *Yeast* 23:399–405.

320. Chen EJ, Kaiser CA (2002) Amino acids regulate the intracellular trafficking of the general amino acid permease of Saccharomyces cerevisiae. *Proc Natl Acad Sci USA* 99:14837–14842.

321. Schneider CA, Rasband WS, Eliceiri KW (2012) NIH Image to ImageJ: 25 years of image analysis. *Nat Methods* 9:671–675.

322. Axelrod D, Koppel DE, Schlessinger J, Elson E, Webb WW (1976) Mobility measurement by analysis of fluorescence photobleaching recovery kinetics. *Biophys J* 16:1055–1069.

323. Phillips R, Kondev J, Theriot J, Garcia HG (2012) *Physical Biology of the Cell* (Garland Pub).

324. Michalet X (2010) Mean square displacement analysis of single-particle trajectories with localization error: Brownian motion in an isotropic medium. *Phys Rev E Stat Nonlin Soft Matter Phys* 82:041914.

325. Kusumi A, Ike H, Nakada C, Murase K, Fujiwara TK (2005) Single-molecule tracking of membrane molecules: plasma membrane compartmentalization and dynamic assembly of raft-philic signaling molecules. *Semin Immunol* 17:3–21.

326. Ritchie K et al. (2005) Detection of non-Brownian diffusion in the cell membrane in single molecule tracking. *Biophys J* 88:2266–2277.

327. Veenhoff LM, Heuberger EHML, Poolman B (2002) Quaternary structure and function of transport proteins. *Trends Biochem Sci* 27:242–249.

328. Ulbrich MH, Isacoff EY (2007) Subunit counting in membrane-bound proteins. *Nat Methods* 4:319–321.

329. Leake MC et al. (2008) Variable stoichiometry of the TatA component of the twin-arginine protein transport system observed by in vivo single-molecule imaging. *Proc Natl Acad Sci USA* 105:15376–15381.

330. Galan JM, Haguenauer-Tsapis R (1997) Ubiquitin lys63 is involved in ubiquitination of a yeast plasma membrane protein. *EMBO J* 16:5847–5854.

331. Lin CH, MacGurn JA, Chu T, Stefan CJ, Emr SD (2008) Arrestin-related ubiquitin-ligase adaptors regulate endocytosis and protein turnover at the cell surface. *Cell* 135:714–725.

Summary

This thesis is not only the result of four years of research but also the reflection of my evolution and growth as a scientist during my PhD. I have divided the thesis into four parts, reflecting different aspects of the study of the molecular basis of membrane stability and dynamics.

I started working on the characterization of the mode of action of membrane-active amphipathic peptides since the first day I came to Groningen, a project in close collaboration with the group of Siewert-Jan Marrink. Later on, I took a synthetic biology approach, making use of amphipathic peptides for the design of new membrane pores (in collaboration with the group of Gerard Roelfes). In parallel, I worked on the interaction of small molecules with membranes, again, with the group of Siewert-Jan Marrink. Finally, I used my expertise in membrane biology to address outstanding questions on the organization and dynamics of amino acid transporters in *Saccharomyces cerevisiae*. Every topic has provided me with further knowledge and understanding of membrane biology, which, together with the beauty of working with different people, made my PhD program a very pleasant and fruitful journey.

Interaction of small molecules with membranes: Amphipathic pore-forming peptides

Chapters 2-4 describe studies on the mechanism of action of antimicrobial peptides. We focused on two small peptides, the cyclic BPC194 and its linear analogue BPC193. Although they have the same amino acid sequence, only the cyclic peptide is able to kill microbial cells. Using a combination of fluorescence-based techniques and molecular dynamic simulations, we have shown that the cyclic peptide adopts a specific conformation upon membrane binding, which allows the molecule to insert deeply into the bilayer and form pores. Remarkably, the cyclic peptide unlike the linear analogue is also able to fuse membranes when two bilayers are in close proximity. We thus present a novel dual-mode of action for an antimicrobial peptide that is active against a wide range of prokaryotic organisms.

Design of novel membrane pores: Applications in synthetic biology

In chapter 5, we describe the design, synthesis and characterization of DNA-peptide hybrids that self-assemble into a membrane pore. In one strategy we used complementary DNA strands to form peptide dimers. In the other strategy we used a G-quadruplex motif to form tetrameric structures. In both cases, the resulting pore had a preference for a specific oligomeric state and a well-defined ion conductance. These first designs of DNA-peptide hybrids suggest great potential for the functionalization of membrane pores on the basis of nucleic acids.

Interaction of small molecules with membranes: reducing *versus* non-reducing sugars

In chapter 6, we describe the effects of carbohydrates on the organization of lipids in synthetic membranes. We combined fluorescence microscopy with molecular dynamic simulations and discovered that non-reducing disaccharides, sucrose and trehalose, have a specific effect on the organization of biological membranes, which results in mixing of lipids that are normally segregated into liquid-ordered and liquid-disordered phases. Our studies offer rationale as to why sucrose and trehalose are frequently used in biology to allow organisms to survive in extreme desiccation

conditions.

Protein dynamics in the plasma membrane of *Saccharomyces cerevisiae*

In chapter 7, we determined the localization, oligomeric state and dynamics of plasma membrane amino acid transporters of *S. cerevisiae*. The distribution of the proteins in the plasma membrane is not homogeneous. We hypothesize that the apparent heterogeneity is due to the extremely slow diffusion of membrane proteins in the plasma membrane together with the low expression levels under native conditions.

Sammenvatting

Dit proefschrift is niet alleen het resultaat van vier jaar onderzoek, maar ook de reflectie van mijn evolutie en groei als wetenschapper tijdens mijn doctoraat. Ik verdeel het proefschrift in vier delen, die overeenkomen met de verschillende onderwerpen waaraan ik heb gewerkt aan de interactie tussen cel membranen en andere biologische moleculen.

Sinds de eerste dag dat ik in Groningen aankwam heb ik gewerkt aan amfipatische peptiden, in nauwe samenwerking met de groep van Siewert-Jan Marrink. Later verschoof mijn aandachtsgebied naar de synthetische biologie waarbij we artificiële membraan kanalen synthetiseerden opgebouwd uit amfipatische peptiden in samenwerking met de groep van Gerard Roelfes. Tegelijkertijd bestudeerde ik de interactie tussen suikers en lipiden membranen wederom, met de groep van Siewert-Jan Marrink. Tot slot heb ik mijn vergaarde kennis in de membraan biologie toegepast op het bestuderen van de complezxe organisatie en dynamiek van aminozuur transporters in het plasma membraan van *S. cerevisiae*. Met elk hoofdstuk heb ik mijn kennis en expertise verbreed evenals de ervaring van het samenwerken met verschillende mensen, wat mijn promotie tot een zeer prettige en vruchtbare reis heeft gemaakt.

Interactie van kleine moleculen met membranen: Amfipathische peptiden

In hoofdstukken 2-4, hebben we gekeken naar het mechanisme van anti-microbiële peptiden met het membraan. We hebben ons gericht op twee korte peptiden, de cyclische BPC194 en zijn lineaire analoog BPC193. Hoewel beide dezelfde aminozuursequentie bezitten, heeft alleen de cyclische vorm een anti-microbiële werking. Met een combinatie van op fluorescentie-gebaseerde technieken en moleculaire dynamica simulaties, hebben we kunnen aantonen dat het cyclisch peptide de juiste conformatie aan neemt bij membraan binding. De daaropvolgende inerstie resulteert in de vorming van porien. Tegelijkertijd hebben we geconstateerd dat het peptide kan ook membraan fusie faciliteert. We omschrijven hier een nieuwe twee component methode voor een antimicrobieel peptide, effectief tegen een groot scala aan prokaryoten.

Membraan kanalen: Toepassingen in de synthetische biologie

In hoofdstuk 5 ontwerpen en synthetiseren we een DNA-peptide hybride om oligomerisatie van een membraan kanaal te moduleren. Daartoe gebruiken we complementaire DNA strengen die resulteren in peptide dimerisatie evenals een G-quadruplex motief voor het vormen van tetrameren. In beide gevallen had het daaruit resulterende kanaal een voorkeur voor een specifieke oligomere toestand met een vaste grootte. Deze Initiële ontwerpen van hybride DNA-peptide suggereren een hoog potentieel voor de basis van membraan porien, gebaseerd op nucleïne zuren.

Interactie van kleine moleculen met membranen: het verminderen versus niet-reducerende suikers

In hoofdstuk 6 hebben we gekeken naar de effecten van koolhydraten op het membraan. We combineerden fluorescentie microscopie met moleculaire dynamica simulaties en ontdekte dat alleen de niet-reducerende koolhydraten, sucrose en trehalose een effect hebben op de organisatie van lipid rafts. Onze studie legt de mogelijke basis waarom deze disachariden door verschillende organismen worden

gesynthetiseerd om te overleven in gevallen van extreme uitdroging.

Eiwitdynamica in het plasmamembraan van *Saccharomyces cerevisiae*

In hoofdstuk 7 bestudeerden we de lokalisatie, oligomerisatie en dynamiek van verschillende plasmamembraan aminozuur transporters van *S. cerevisiae*. De verdeling van deze eiwitten in het plasmamembraan bleek niet homogeen maar gepolariseerd. We hypotetiseren dat deze polarisatie een consequentie is van een extreem trage laterale diffusie evenals een beperkt voorkomen in het plasma membraan.

Epilogue and acknowledgements

I am sitting in the darkness of the microscope room (yes, I am here again, myself and the silence) in the middle of the rainy, cloudy, foggy, cold October, in the Netherlands, where winter starts at the end of August, writing the last words of my thesis. I find these last words very hard to write (I am anxious to see the book finished, printed and unmodifiable, once and for all!) and at the same time extremely essential. One of the reasons is that in this bit of my thesis I can write whatever comes into my mind without caring about the scientific style of writing. Another reason, and the most important one, is the chance to capture in these words all my appreciation to all the people that made it possible for me to be here today writing these last words. It is hard to find a way to put all my thoughts into some lines with a meaningful order, so I decided to mention in a short story all the chronological (and geographical) events and people I encountered.

It all started in Girona (alias "the center of the world"), where my inner scientist, named "Menina", was born in the year 2007. There I had my very first lab colleagues and I even supervised my first students (all of them ended up doing a PhD, at least I didn't make them drop science).

Fel, you have always been "The Mentor", initially for a week (what a supervisor, leaving me a week after my start to "do research" in Lisbon) but afterwards you have been always there, not just scientifically, but most importantly, as a friend. Marta, your positive energy and big heart stayed with me even when I left for the Netherlands. The "cats", Tiffa, Imma and the rest of the UdG people, it was a pleasure spending time with you guys in and out of the lab.

After a couple of years doing research in Girona (and a bit tired already of synthesizing antimicrobial peptides) I started what would be the beginning of a new and exciting period of my life ("The big change"). It was the 31st of January 2009 when Anna and I took the plane that would bring us to Amsterdam. After spending the whole night in the airport we finally arrived in Groningen (not before spending more than 2 hours in the train, though) and lucky for our stomachs and us it was *koopzondag!* (for the ones that don't know, shops are generally closed on Sundays in the Netherlands, but the first Sunday of every month it is an exception and the shops and supermarkets are open).

Diaz, Diaz, Diaz, you have been the inflection point of my scientific career. Thanks to you I came for the first time to the "Poolman's Lab", where our work with Jacek, Durba and Siewert started. You know how enormously thankful I am to you for providing me with the opportunity to come to Groningen and have such a great time. I won't forget our days in the lab, parties in the student house (JieMaaaaaaa, pe-pe-pe-pe-perrrrrrrrrrrrrrrooooo,...), discussing and getting excited about science all the time, meetings, writing together, etc. Thanks for being there. I wish you all the best in your future.

The next day I was already following the lab's rhythm: my first Monday morning group meeting (I still remember Armağan presenting a picture of her daughter, who is now a gorgeous girl, after maternity leave and saying: "this is my new project")

and in the same day, subgroup meeting with Jacek and Bert (I think there I showed my first powerpoint presentation, something that would turn into a routine in our meetings). I was amazed at the way the Dutch do science, at least in my experience, in a very open and collaborative way (I even read once that this comes from the fact that the Dutch had to collaborate together to build the polders, to avoid future floods, all of them working together for a unique purpose). I have had the pleasure to establish lots of collaborations, working with inspiring people and learning a lot on the way.

Bert, you welcomed me in your lab, even though you knew I was from Spain and everybody thought I was drinking wine for breakfast and having "siesta" every day at the university (to make it clear, that is so not true). After one or two months, while you were trying to understand whether I was doing a Masters or a PhD in Girona, you asked me to join the lab to start another PhD, something that, to be honest, I accepted without the need of sleeping on it (well, I did consult with Edu, though). I am hartelijk thankful to you for appointing me (or as some others would say: "stealing me"), giving me the chance to enlist as a PhD student under your guidance, observing and learning from you, something that I will take with me once another bird (as myself) flies from the nest. I also want to express my gratitude to you for all the support that you have shown to Edu, which is also support for me.

Durba, my dear, you have been a role model to follow. You inspired me with your wisdom, experience, and knowledge and I am very thankful to you for that. I know you will become a very successful Professor, and you will give your mustached-students a hard time.

Jacek, with you I started my period in Bert's lab, you taught me lots of things and in the end we had a very productive period working together (our already written chapters saved me so much writing time at the end of my PhD!).

Siewert, I am trying to think whether I have spent more time discussing science with you or preparing you coffee. However, I had a great time working with you during almost five years (we are not yet done with the work, but I hope we can finish our last project together soon). Thanks for being in my committee as well, and sorry for having the defense on Friday at nine, I know it's way too early for you. I would also like to include here Alex, César, Clement, Djurre, Marcelo, Helgi, Tsjerk, Jaakko, Floris, Xavier and all the MD group members I shared some time with, especially having drinks and fun at conferences.

Manel, I didn't know where to mention you since I met you, if I am not mistaken, at the end of 2007 when Marta Ribeiro was in Girona (Marta, eu ainda espero que um dia nossos caminhos se cruzam, em New York ou em outro lugar). Your curiosity and your thirst for knowledge have always amazed me. Thanks for all the help, always, in all areas. I hope to be able to count on you (and vice versa) for many more years.

Joining Bert made me share my days in the lab with a bunch of new colleagues (in "Poolman's Lab" a bunch means around 40 new colleagues). It was the first time having so many workmates and I was a bit frustrated to see I couldn't get close (on a personal level) with all of them, something easily achievable in Girona (in a group of not more than 10). So I had to accept it and keep on going. However, I met great friends and I hope to keep in touch with them.

Josy and Ronnie, you were some of the first I met. Soon we had great times together. Ronnie, thanks for all the cooking during dinners and for always proposing fun activities to do together. Josy, when you left, my cheerful dancing and sports partner was also leaving. However, I am very happy for you two and I wish you the best in this next exciting period of your lives.

JP, thanks for such a great 30-year-old birthday BBQ! Sorry this is what comes to my mind each time I think of you. However, I also remember great funny moments in the lab, especially when you were being annoying to poor Adeline. All the best in your future and I will be waiting for the second BBQ.

I want to mention here other people that also left the group: Adeline (we never coincide in Paris, so sad…), Tejas (great night tour in Zurich, thanks), Inga (thanks for a couple of Feuerzangenbowlen), Andreja, Nadia, Anna Dimitrova (crazy!), Karlien (you were extremely helpful) and all the "ERIBA people": Justyna, Astri, Petra, Anton, Anne, Annemarie, Georges and Liesbeth. To most of you I already told that the lab has never been the same since you left.

Fortunately, not everybody left and more fun was about to come. This was at the time I changed office and joined the "yeast team", working on my last project in the lab together with Dušan, Frans, Stephanie and Joury.

Dušan, ¿qué pasa negro? Thanks to you I started working with yeast and I gained a lot of knowledge (still too much to learn, though) on molecular cell biology and other "angles" of life. All the best in your career and be patient if you end up supervising PhD's.

Stephanie, you are currently having fun in some remote place in Australia while we are here enjoying the rain, but I won't complain because you will be proof reading those lines very soon (maybe from a beach?). Thanks a million for that and for always helping me in anything I asked, in the lab and outside of it (thanks for letting me step on your dining table to fix my suit pants). I wish you all the best, I know your PhD will be a success and whatever you do afterwards you will nail it, as always. I hope you keep on cooking such delicious meals, you are the best!

Andrew, from you I have learnt a lot, you are a great scientist and for the sake of science I hope you never ever quit. Anybody working with you will have a fantastic character to get inspired from, laugh with and, according to my experience, get scared the hell out each time you want to talk to them (not because of your face, you know why…).

Dirk, thanks for all the pressure you put on me (and others) talking about finishing up theses in the coffee corner (always with a lot of humor, though). Thanks for being in my committee as well.

Gea and Ria, I owe you also my gratitude for all the help in the lab. Ria, I am kindly thankful for all the care you had towards me and also Edu. Thanks to you he found his own way in Nijenborgh 4, meeting friends and also clients.

Rianne, bedankt voor het geduld om Nederlans met mij te spreken. Thanks for all the work with the sugars project. I have no doubt you will have a very successful PhD, all the best.

Joury "van het closet", we all had so much fun since you joined the lab. Keep that priceless smile on your face man and all the best in your future. Topie, hoi hoi, mazzel, oing oing, buru buru!

Pranav and Nobina, my dear Indians, I will never ever forget the day we could hold a conversation for an hour (or even more) in Punjabi, Bengali and Catalan without English (especially Pranav that became "English-less"). We have had great times together and have shared lots of stress in the last months of our PhD's but, eventually, we'll all find our successful ways.

Marysia, my dear Maria, you started your PhD just a month before I came, I think, so we have shared lots of years together in the lab, but what I have enjoyed the most are your baking skills and your dinners! Thank you so much and keep on going. Maciek good luck with your "Klussenbedrijf", as well.

Jeanette, initially my officemate and later on my friend, thanks for always being so helpful, such a good listener and a lovely person.

During my days in Groningen I also supervised a couple of students and had the chance to collaborate with great people.

Beata, it was very interesting working with someone that is both a biotechnologist and a psychologist. Łukasz, I really enjoyed the time you were in Groningen. You were (and are) a brilliant student/guy (besides, you handled Dušan's comments very well). I also learned from both of you. All the best in your PhD's!

Armağan, thanks to you I learnt about electrophysiology studies. It was a pleasure working with you. Thanks for always listening and for being always so cheerful (as Alberto once told me and I fully agree with him, you radiate optimism).

Marc Stuart, thanks for all the cryo-EM work. Jan Willem Veening, thanks for providing us with a few slides to perform one last experiment that the referees asked. Manuel Jäger, thanks for giving us one of your synthesized saccharides. Jianwei, it was nice performing with you the microscopy experiment you needed for your project, all the best with your defence.

Lorina, for how long did we work together? I think for about a couple of years. During this time, I must say it was great working with you (and having coffee breaks). I am sure you will find a fantastic job after your Ph.D. (otherwise a rich husband!)

Gerard, it was also very nice working with you, thanks for giving me the opportunity to work "upstairs". I feel sorry for what happen to Beatrix (no, not the former queen, the peptide synthesizer), it was time for her to get retired. Thanks for being in my committee as well.

Tina, I have really enjoyed each time you have come to Groningen for experiments. I am not sure whether Edu thinks the same, though, since each time you were here we stayed in front of the microscope until…almost midnight. It was great working, listening to FFH.de and eating pizza with you!

Abhi, thanks for such a nice collaboration with the sugars. I had a great time visiting your lab. Marc, thank you for being in my committee. I hope our work will be out soon.

Paul, thanks for all the work on the yeast project and for such interesting exchange of opinions and discussions.

Michiel, alias Miguel, I am enormously thankful to you for all the plugins you have made for us, making our data analysis more straightforward.

Antoine, I am very thankful to you and your group in general, without it my last chapter wouldn't exist. Thanks for being in my committee.

The final days in ¨Poolman's Lab" arrived (sooner that I realized, time flies!) and with the end of a PhD in the Netherlands arrives the time one has to choose two faithful, devoted, honorable guardians called "paranimfen" (in English, paranymphs). For those who don't know, here is the explanation from our friend Wikipedia:

"In the Netherlands a pair of paranymphs (*paranimfen*) are present at the doctoral thesis defence. This ritual originates from the ancient concept where obtaining a doctorate was seen as a de facto marriage to the university. Furthermore the paranymphs would also act as a physical shield in case the debate became too heated, or as a backup for the doctoral candidate to ask for advice when answering questions. Today their role is symbolic and seen as a position of honor similar to a best man at a wedding."

The chosen warriors were Duygu, alias paranymph number one, and Frans, alias paranymph number two (for the ones that are wondering, they were enumerated in height order, of course!).

Duygu, guapa, I am not able to write what I would like to tell you in just a few lines. We had great times together, sharing so many things (positive and negative) but everything can be solved (or forgotten) with a good glass of wine. You have been there, and I know you will be always there. We still have too many things to experience together, places to discover and for that we need (and have) a whole life up front. Thanks for everything. Of course with Duygu comes Kıvanç, my lovely piano teacher and friend, it was great meeting you and your sense of humor (I love it!). I hope to travel more with you (if you and I don't plan a trip, who is going to do it? no one!) and have many more unforgettable moments the four of us together.

Frans, my dear lefty (colleague number…something, my blondie friend, Bert of the cake, etc.), there are so many things I also want to say to you. First of all, it has been an immense pleasure working with you. Even though my first impression towards you, when we shared our first office (ages ago…) was a bit, how to say it nicely…not so positive? Later on I discovered a very good friend in you. Despite all the stress around us, making me give talks instead of you with only one day notice, your unstoppable talking and gossiping, I really enjoyed all moments together (especially the sailing with Marijke and the trip to Girona with Marcel, those were the best). Just one last advice: don't lose your optimism!

I wish all the best to the rest of the Enzymology members: Alicja, Faizah, Lotteke, Ruslan, Giorgios, Sonja, Dorith, Arnold, Jonas, Franz, Albert, Michael, Durkje, Katja, Raj, Boqun and Hallie.

Outside I met my "Spanish community", my second family.

Un abrazo enorme para todos, y en especial, a los que habéis compartido conmigo la mayor parte de mi estancia en Groningen: Alberto, Esther y Clara (mis queridos "putu peu", el tío más cojonudo y la mamá más fuerte y guapa del mundo junto con su princesita). Es imposible olvidar a los primeros españoles que conocí en Groningen, no os puedo categorizar solo como amigos, porque os considero mi familia madrileña. ¡Muchas gracias por todos los momentos juntos! Lo mismo va para mi querida Noe, su muelle y su Jason. Cuántas alegrías, fiestas, marshmallows volando, tristezas, separaciones, reunificaciones, cenas, cenas y más cenas. Noe, muchas gracias por todos los ánimos, sobre todo en el final de esta etapa de mi vida. Jeanette, César, André y Tomás os deseo lo mejor en USA, ¡se os echa de menos! Maria, Frank y Tomàs, també us desitjo el millor a Groningen o allà on sigueu (Frank, quick translation: all the best!). Clau, muchos ánimos con tu pequeña, eres una mamá muy valiente.

In Girona I kept my real family and my best friends.

Papa i mama, es pot dir que si he arribat aquí, ha estat en gran part gràcies a vosaltres. Sempre m'heu proporcionat tot el que heu tingut a les mans per fer-me feliç i ho heu aconseguit. Moltes gràcies per tot!

Irene, Juanma i Cristina, sempre diuen que els amics de debò es poden comptar amb una sola mà. Doncs hi estic d'acord. Moltes gràcies per organitzar les vostres agendes i trobar sempre una estona per veure'ns quan l'Edu i jo hem baixat. Irene, moltes gràcies per tots els skype meetings i converses per whatsapp, encara que estiguéssim a gairebé 2000 km de distancia, era com tenir-te al meu costat sempre que t'he necessitat.

Luckily for me, my love decided to join me during this long journey.

Edu, moltes gràcies per venir amb mi a Groningen i fer possible el que, amb aquesta tesis, estic aconseguint. Hem passat quatre anys fantàstics, plens de bons moments i, mentrestant, t'has convertit en un gran dissenyador (i sé que això només és el principi d'una gran trajectòria professional, moltes gràcies per la portada!). Han sigut tantes les coses que hem après i són tantes les que ens queden per descobrir, que ja tinc ganes de saber el futur que ens espera, segurament, amb moments molt durs i difícils i d'altres, plens de felicitat i alegries, però no m'importa sempre i quan els passi amb tu.

It's time to go and I want to finish those lines with the two words every PhD finishes with:

Hora Finita,

Gemma Moiset.

22 October 2013